



Technological University Dublin  
ARROW@TU Dublin

---

Doctoral

Engineering

---

2020-10

## Mode Analysis and Applications of Three-Layer Step-Index and Depressed-Core Optical Fibers

XIAOKANG LIAN

*Technological University Dublin*

Follow this and additional works at: <https://arrow.tudublin.ie/engdoc>

Part of the [Electrical and Computer Engineering Commons](#)

---

### Recommended Citation

Lian, X. (2020) *Mode Analysis and Applications of Three-Layer Step-Index and Depressed-Core Optical Fibers*, Doctoral Thesis, Technological University Dublin. DOI:10.21427/9R2K-R557

This Theses, Ph.D is brought to you for free and open access by the Engineering at ARROW@TU Dublin. It has been accepted for inclusion in Doctoral by an authorized administrator of ARROW@TU Dublin. For more information, please contact [arrow.admin@tudublin.ie](mailto:arrow.admin@tudublin.ie), [aisling.coyne@tudublin.ie](mailto:aisling.coyne@tudublin.ie).



This work is licensed under a [Creative Commons Attribution-Noncommercial-Share Alike 4.0 License](#)



# **Mode Analysis and Applications of Three-Layer Step-Index and Depressed- Core Optical Fibers**

A thesis

Submitted for the degree of Doctor of Philosophy

By

**XIAOKANG LIAN, M.Sc.**



School of Electrical & Electronic Engineering  
College of Engineering & Built Environment  
Technological University Dublin

**Supervisors: Prof. Yuliya Semenova, Prof. Qiang Wu, and  
Prof. Gerald Farrell**

Dublin, Ireland

October, 2020

*“If I have seen further it is by standing on the shoulders of giants.” - Isaac Newton*

*“Ideas do not always come in a flash, but by diligent trial-and-error experiments that take time and thought.” – Charles K. Kao*

*To my wife, daughter, and parents.*

# Abstract

Optical fibers play important roles in telecommunication, imaging, sensing, lasers and amplifiers. The rapid development of fiber optics over the past decades has been underpinned by various designs of the optical fibers and by the rapid improvement of the understanding of the waveguiding mechanisms and associated models. According to the cross-section refractive index distribution, optical fibers can be generally classified into four basic types: two-layer step-index fiber, three-layer step-index fiber, three-layer depressed-core fiber and hollow-core fiber. Among these four basic fiber types, the mode properties and the applications of the three-layer step-index and depressed-core fibers have not been sufficiently investigated. This thesis presents a detailed mode analysis in three-layer step-index and depressed-core fibers and their applications.

A complete dispersion diagram including the core and cladding modes in a three-layer step-index optical fiber has been developed for the first time, using both analytical method and full-vector finite element method. Mode transition from the cladding-type to core-type modes as a function of the core radius was studied as a contribution to deepening the knowledge of conventional step-index optical fibers.

Based on the developed complete dispersion diagram for the three-layer step-index optical fiber, it was found that a small-core fiber with a nano/micro-sized core supports only cladding-type modes. The self-imaging phenomenon of the pure cladding modes in the small-core fiber has been studied, and its comparison to the behaviour of the core-type modes in the conventional multimode fibers has

been carried out. The discrete nature and the exponential growth behaviour of the self-imaging of the cladding-type modes was established for the first time. The results provide new insights and design rules for a number of multimode interference devices such as optical couplers, optical modulators, multimode fiber lasers and space-division multiplexing devices.

The depressed-core fiber, consisting of a low-index solid core and a high-index cladding surrounded by air, is in effect a bridge between the conventional step-index fiber and the tube-type hollow-core fiber from the point of view of the index profile. In the research, a complete dispersion diagram of the depressed-core fiber has been obtained for the first time by solving the full-vector eigenvalue equations. The waveguiding in the depressed-core fiber was analyzed using the theory of anti-resonant and the inhibited coupling guiding mechanisms. An asymmetric planar anti-resonant reflecting optical waveguide model (asymmetric planar ARROW model) was proposed for the depressed-core fiber.

A high-index polymer-coated no-core fiber as an example of the depressed-core fiber has been studied theoretically and experimentally. The appearance of the periodic transmission loss dips in the spectrum of a long or bent polymer-coated no-core fiber samples reflects the anti-resonance nature of the depressed-core fiber. The experiments show that the overall change in spectral loss is greater than 31 dB at the dip position around 1550 nm and the average sensitivity is up to  $14.77 \text{ dB/m}^{-1}$ , as the bend radius changes from  $\infty$  (straight) to 47.48 cm. The results indicate that the polymer-coated no-core fibers have the potential to be used in many devices including curvature sensors and tunable loss filters.

While the superposition of the spectra of multiple modes led to broad dips, it has been found that an individual mode can cause sharp dips in the transmission spectra of a polymer-coated no-core fiber. As a result of this phenomenon and the large thermo-optical and thermal expansion coefficients of the polymer coating, a compact (length < 10 mm), high sensitivity and linear response temperature sensor with the sensitivity as high as -3.784 nm/°C has been demonstrated experimentally.

# **Declaration**

I hereby certify that this thesis which I now submit for examination for the award of PhD is entirely my own work and has not been taken from the work of others, save and to the extent that such work has been cited and acknowledged within the text of my own work.

This thesis was prepared according to the regulations for postgraduate study by research of the Technological University Dublin and has not been submitted in whole or in part for an award in any other third level institution.

The work reported in this thesis conforms to the principles and requirements of University's guidelines for ethics in research.

The University has permission to keep, lend or copy this thesis in whole or in part, on condition that any such use of the material of the thesis be duly acknowledged.

Signature Xiaokang Lian Date 23.10.2020

Candidate

# Acknowledgements

The work presented in this thesis has been carried out within the Photonics Research Centre (PRC) of the Technological University Dublin (TU Dublin).

I would like to thank my main supervisor Prof. Yuliya Semenova, head of the PRC, for her guidance and help in all areas of my research work. Yuliya provided and maintained a comfortable environment for my work in the PRC. She helped me to choose the current research topic of fiber optics and helped to solve every problem encountered in the research. She helped me to write and revise all the journal, conference papers and thesis and taught me the effective way to present research results. Less is more. I would not have gotten so far in my research without her.

I would like to thank my co-supervisor Prof. Qiang Wu, from Northumbria University, UK. Qiang helped me to get the chance to study for PhD degree in TU Dublin when I was working as an engineer in China, which was the beginning of the story here. He helped me to write and revise all the papers and thesis with his professional and rigorous attitude. He encouraged me to do research work with a rigorous attitude. I was happy to discuss with him the problems in the experiments and calculations.

I would like to thank my co-supervisor Prof. Gerald Farrell, Professor Emeritus, former Dean and Director of the College of Engineering & Built Environment and former head of the PRC. Gerry guided me wisely to focus on the research with the available condition in the lab when I was confused at the initial period. He helped me to write and revise all the papers and thesis, and always point out

critical problems and give me profound advice. His wisdom and leadership have a great influence on me, which motivates me to form efficient and effective work habits.

I would like to thank Prof. Gang-Ding Peng from University of New South Wales and Prof. Changyu Shen from China Jiliang University for the valuable discussion and experimental guide during their visit in the PRC.

I would like to thank Prof. Michael Conlon, Head of School of Electrical and Electronic Engineering, Dr. Marek Rebow, head of Research of College of Engineering & Built Environment, and all staffs in Graduate Research School Office for all their supports during my study in TU Dublin.

I would like to thank my colleagues in the PRC, Dr. Manjusha Ramakrishnan, Dr. Vishnu Kavungal, Dr. Arun Kumar Mallik, Dr. Dejun Liu, Mr. Wei Han, Mrs. Fangfang Wei, Mr. Zhe Wang, Mr. Cheng Zhuo and Ms. Anuradha Rout, for the friendship and help in my research works. Many thanks to the former member Dr. Youqiao Ma for his help in simulation works. Many thanks to the visiting students Dr. Lei Sun, Dr. Ke Tian, Mr. Sagar Jinachandran, Mr. Michal Skalsky, Mr. Yuxuan Jiang, and Ms. Yu Yin for the valuable discussion and friendship.

I would like to thank all my friends for their care and support during my study in Ireland.

In addition, I would like to acknowledge the financial support of TU Dublin under Fiosraigh Scholarship Program 2016. I also want to thank the TU Dublin OSA student chapter for supporting me to attend the OSA chapter conference in Xian, China and the Student Leadership Conference in Washington, USA.

Finally, I would like to thank my wife Lin Zhu for her patience and efforts to maintain a well-running family and to raise our daughter Chenyi Lian in China. I would like to express my sincerest respect to my parents for their limitless and endless love since I was born. I would like to thank my parents in law, two sisters, and brothers in law for their sincere help and supports.

X.-K. Lian

# List of Publications

## Journal

1. **Xiaokang Lian**, Qiang Wu, Gerald Farrell, and Yuliya Semenova, “High-sensitivity temperature sensor based on anti-resonance in high-index polymer coated optical fiber interferometers,” Opt. Lett., vol. 45, no. 19, pp. 5385-5388, 2020. DOI: 10.1364/OL.403050.
2. **Xiaokang Lian**, Gerald Farrell, Qiang Wu, Wei Han, Changyu Shen, Youqiao Ma and Yuliya Semenova, “Spectral dependence of transmission losses in high-index polymer coated no-core fibers,” J. Lightw. Technol., vol. 38, no. 22, pp. 6352-6361, 2020. DOI: 10.1109/JLT.2020.3010101.
3. **Xiaokang Lian**, Gerald Farrell, Qiang Wu, Wei Han, Changyu Shen, Youqiao Ma and Yuliya Semenova, “Anti-resonance, inhibited coupling and mode transition in depressed-core fibers,” Opt. Express, vol. 28, no. 11, pp. 16526–16541, 2020. DOI: 10.1364/OE.390371.
4. **Xiaokang Lian**, Qiang Wu, Gerald Farrell, Changyu Shen, Youqiao Ma, and Yuliya Semenova, “Discrete self-imaging in small-core optical fiber interferometers,” J. Lightw. Technol., vol. 37, no. 9, pp. 1873-1884, 2019. DOI: 10.1109/JLT.2019.2894365.
5. Changyu Shen, Dejun Liu, **Xiaokang Lian**, Tingting Lang, Chunliu Zhao, Yuliya Semenova, and Jacques Albert, “Microfluidic flow direction and rate vector sensor based on a partially gold-coated TFBG,” Opt. Lett. vol. 45, no. 10, pp. 2776-2779, 2020. DOI: 10.1364/OL.392511.
6. Wei Han, Marek Rebow, **Xiaokang Lian**, Dejun Liu, Gerald Farrell, Qiang Wu, Youqiao Ma, and Yuliya Semenova, “SNS optical fiber sensor for direct detection of phase transitions in C<sub>18</sub>H<sub>38</sub> n-alkane material,” Exp. Thermal Fluid Sci., vol. 109, p. 109854, 2019. DOI: 10.1016/j.expthermflusci.2019.109854.
7. Changyu Shen, **Xiaokang Lian**, Vishnu Kavungal, Chuan Zhong, Dejun Liu, Yuliya Semenova, Gerald Farrell, Jacques Albert, John F Donegan, “Optical spectral sweep comb liquid flow rate sensor,” Opt. Lett. vol. 43, no. 4, pp. 751-754, 2018. DOI: 10.1364/OL.43.000751.

8. Changyu Shen, Chuan Zhong, Dejun Liu, **Xiaokang Lian**, Jianyao Zheng, Jingjing Wang, Yuliya Semenova, Gerald Farrell, Jacques Albert, John F Donegan, “Measurements of milli-Newton surface tension forces with tilted fiber Bragg gratings,” Opt. Lett., vol. 43, no. 2, pp. 255-258, 2018. DOI: 10.1364/OL.43.000255

## Conference

9. **Xiaokang Lian**, Gerald Farrell, Qiang Wu, and Yuliya Semenova, “Optical fibers and their applications,” in 10<sup>th</sup> Annual Graduate Research Symposium, TU Dublin, Nov. 2019. (**Oral presentation**)
10. **Xiaokang Lian**, Gerald Farrell, Qiang Wu, Wei Han, Fangfang Wei, and Yuliya Semenova, “Mode Transition in Conventional Step-Index Optical Fibers,” in 18<sup>th</sup> International Conference on Optical Communications and Networks, IEEE, Aug. 2019. DOI: 10.1109/ICOQN.2019.8934113.
11. **Xiaokang Lian**, Dejun Liu, Wei Han, Arun Kumar Mallik, Fangfang Wei, Qiang Wu, Gerald Farrell1, and Yuliya Semenova, “Multimode interference fiber structures as curvature sensors,” in Photonics Ireland, Sep. 2017. (Poster presentation)
12. **Xiaokang Lian**, Qiang Wu, Gerald Farrell and Yuliya Semenova, “Analysis of cladding mode interference in bending SMF28-small-core SMF-SMF28 Structure: improving sensitivity of optical fiber bending sensor,” in International OSA Network of Students (IONS) Xi'an, Apr. 2017. (**Oral presentation**)
13. Dejun Liu, **Xiaokang Lian**, Arun Kumar Mallik, Wei Han, Fangfang Wei, Jinhui Yuan, Chongxiu Yu, Gerald Farrell, Yuliya Semenova, Qiang Wu, “Detection of volatile organic compounds using an optical fiber sensor coated with a sol-gel silica layer containing immobilized Nile red,” in 25<sup>th</sup> Optical Fiber Sensors Conference (OFS), IEEE, Apr. 2017. DOI: 10.1117/12.2263671.
14. Arun Kumar Mallik, Dejun Liu, Vishnu Kavungal, **Xiaokang Lian**, Gerald Farrell, Qiang Wu, Yuliya Semenova, “Compact relative humidity sensor based on an Agarose hydrogel coated silica microsphere resonator,” in 25<sup>th</sup>

- Optical Fiber Sensors Conference (OFS), IEEE, Apr. 2017. DOI: 10.1117/12.2263529.
15. Fangfang Wei, Arun Kumar Mallik, Dejun Liu, Wei Han, **Xiaokang Lian**, Gerald Farrell, Qiang Wu, Gang-Ding Peng, Yuliya Semenova, “Simultaneous measurement of both magnetic field strength and temperature with a microfiber coupler based fiber laser sensor,” in 25<sup>th</sup> Optical Fiber Sensors Conference (OFS), IEEE, Apr. 2017. DOI: 10.1117/12.2263678.
  16. Wei Han, Dejun Liu, **Xiaokang Lian**, Arun Kumar Mallik, Fangfang Wei, Lei Sun, Gerald Farrell, Yuliya Semenova, Qiang Wu, “A spherical-structure based fiber sensor for simultaneous measurement of ammonia gas concentration and temperature,” in Proc. SPIE 10025, Advanced Sensor Systems and Applications VII, 100251J, Nov. 2016. DOI: 10.1117/12.2247652.

# Contents

Mode Analysis and Applications of Three-Layer Step-Index and Depressed-Core Optical Fibers .....	I
Abstract .....	IV
Declaration .....	VII
Acknowledgements .....	VIII
List of Publications .....	XI
Journal.....	XI
Conference.....	XII
Contents .....	XIV
List of Figures .....	XVIII
List of Tables .....	XXVII
List of Abbreviations and Symbols.....	XXVIII
Chapter 1 .....	1
Introduction.....	1
1.1 Optical fibers and their applications.....	1
1.1.1 Optical fibers for communication networks .....	2
1.1.2 Optical fibers for lasers and amplifiers .....	5
1.1.3 Optical fibers for imaging applications .....	7
1.1.4 Optical fibers for manipulating micro/nano- particles .....	9
1.1.5 Optical fibers for sensing .....	11
1.2 Optical fiber classification.....	12
1.3 Aim and objectives of the research .....	16
1.4 Research methodology .....	17
1.5 Structure of the thesis .....	19
1.6 Reference .....	20
Chapter 2 .....	31
Waveguiding Mechanisms and Modal Dispersion Diagrams of Optical Fibers..	31
2.1 Light guiding mechanisms and dispersion diagrams .....	31
2.1.1 Total internal reflection in two-layer step-index fibers.....	31
2.1.2 Dispersion diagram of two-layer step-index fibers.....	33
2.1.3 Anti-resonant guiding and dispersion diagram .....	37
2.1.4 Photonic bandgap guiding and dispersion diagram .....	40
2.1.5 Inhibited coupling guiding and dispersion diagram.....	42

2.2 Three-layer fiber waveguide analysis methods .....	44
2.2.1 Ray-optics approach .....	44
2.2.2 Wave-optics approach .....	45
2.2.2.1 Analytical method .....	48
2.2.2.2 Finite element method .....	53
2.2.2.3 Beam propagation method.....	54
2.2.3 Comparison of the waveguide analysis methods .....	55
2.3 Conclusion.....	56
2.4 Reference .....	56
<b>Chapter 3 .....</b>	<b>59</b>
<b>Mode Transition in Conventional Three-Layer Step-Index Optical Fibers .....</b>	<b>59</b>
3.1 Research background.....	59
3.2 Ray trajectories of the core- and cladding-type modes.....	60
3.3 Dispersion diagram of the scalar and vector modes in three-layer step-index fibers .....	62
3.4 Conclusion.....	67
3.5 Reference .....	67
<b>Chapter 4 .....</b>	<b>69</b>
<b>Discrete Self-Imaging in Small-Core Optical Fiber Interferometers.....</b>	<b>69</b>
4.1 Research background.....	70
4.2 Methods .....	73
4.3 Scalar modes in optical fiber interferometers .....	75
4.4 The self-imaging periods .....	80
4.5 Physical interpretation of the discrete self-imaging.....	88
4.6 Experimental investigation .....	94
4.7 Discussion .....	96
4.8 Conclusion.....	98
4.9 Reference .....	99
<b>Chapter 5 .....</b>	<b>104</b>
<b>Anti-Resonance, Inhibited Coupling and Mode Transition in Depressed-Core Optical Fibers .....</b>	<b>104</b>
5.1 Research background.....	105
5.2 Guiding mechanism of the DCFs .....	108
5.2.1 Anti-resonant core mode and asymmetric planar ARROW model.....	108
5.3 Modes in DCFs .....	112
5.3.1 TE/TM modes in DCFs .....	112

5.3.2 HE/EH modes in DCFs .....	118
5.3.3 Mode degeneracy in DCFs .....	122
5.4 Discussion .....	124
5.5 Conclusion.....	127
5.6 Reference .....	128
<b>Chapter 6.....</b>	<b>133</b>
<b>Spectral Dependence of Transmission Losses in High-Index Polymer-Coated No-Core Optical Fibers.....</b>	<b>133</b>
6.1 Research background.....	134
6.2 Method .....	136
6.3 Results.....	139
6.3.1 Modes in straight PC-NCFs.....	139
6.3.2 Analysis of the effects of anti-resonance and multimode interference on the transmission spectra of the PC-NCFs .....	144
6.3.3 Measured transmission spectra of the straight PC-NCFs .....	148
6.3.4 Modal field distortions in bent PC-NCFs.....	150
6.3.5 Measured transmission spectra of the bent PC-NCFs .....	155
6.4 Discussion .....	158
6.5 Conclusion.....	160
6.6 Reference .....	161
<b>Chapter 7 .....</b>	<b>166</b>
<b>High-Sensitivity Temperature Sensor Based on Anti-Resonance in High-Index Polymer-Coated Optical Fiber Interferometers .....</b>	<b>166</b>
7.1 Research motivation .....	167
7.2 The modal properties of the PC-SNCS .....	169
7.3 The transmission spectra of the PC-SNCS.....	171
7.4 Sensing performance of the temperature sensor .....	177
7.5 Conclusion.....	178
7.6 Reference .....	178
<b>Chapter 8 .....</b>	<b>181</b>
<b>Conclusions and Future Research Work .....</b>	<b>181</b>
8.1 Conclusions from the research .....	181
8.2 Future research work.....	186
8.3 Reference .....	188
<b>Appendix A .....</b>	<b>189</b>

Eigenvalue Equations for Vector Modes TE, TM, HE and EH in Three-Layer Optical Fibers .....	189
Reference .....	192
Appendix B .....	193
Eigenvalue Equations for Scalar Modes LP <sub>m,n</sub> in Three-Layer Optical Fibers .	193
Reference .....	195
Appendix C .....	196
Multiple Reflections of an Unpolarized Incident Beam on an Asymmetric Planar Waveguide .....	196
Reference .....	198
Appendix D .....	199
Statement of Contribution.....	199

# List of Figures

- Figure 1.1** (a) Light in optical fibers. Schematic cross section of (b) un-cladded multimode fiber (MMF); (c) cladded MMF, and (d) cladded single-mode fiber (SMF). ..... 3
- Figure 1.2** Different approaches for realization of space-division multiplexing (SDM) to increase the communication bandwidth. (Figure is reproduced from D. J. Richardson *et al.* Nat. Photonics, vol. 7, no. 5, pp. 354-362, 2013; E. Agrell *et al.*, J. Opt., vol. 18, p. 063002, 2016.)..... 4
- Figure 1.3** Schematic of the cladding pumping principle of fiber-laser operation. (Figure is reproduced from the website: [https://en.wikipedia.org/wiki/Double-clad\\_fiber](https://en.wikipedia.org/wiki/Double-clad_fiber))..... 6
- Figure 1.4** Large-mode-area fibers: (a) step-index MMF (reproduced from J. P. Koplow *et al.*, Opt. Lett., vol. 25, no. 7, pp. 442-444, 2000); (b) photonic crystal fiber (reproduced from T. T. Alkeskjold *et al.*, Nanophotonics, vol. 2, no. 5-6, pp. 369-381, 2013); (c) large-pitch fiber (reproduced from F. Stutzki *et al.*, Opt. Lett., vol. 36, no. 5, pp. 689-691, 2011); (d) multi-core fiber (reproduced from M. M. Vogel *et al.*, Opt. Lett., vol. 34, no. 18, pp. 2876-2878, 2009); (e) multi-quench fiber (reproduced from D. Jain *et al.*, Opt. Express, vol. 21, no. 2, pp. 1448-1455, 2013); (f) hollow-core photonic crystal fiber (reproduced from J. P. Uebel *et al.*, Opt. Lett., vol. 41, no. 9, pp. 1961-1964, 2016). ..... 7
- Figure 1.5** Schematic of a MMF-based super-resolution and super-speed endo-microscopy, consisting of three main components: a continuous-wave laser source with a scanning system, a MMF probe, and a single-point detector. Pump light is scanned across the fiber input facet, creating different illumination patterns on the fiber output. The total fluorescent response from the sample is collected by the same fiber probe, propagated back, and measured by the single-point detector. (Figure is reproduced from L. V. Amitonova and J. F. de Boer, Light: Sci. Appl., vol. 9, no. 1 pp. 1-12, 2020)..... 8
- Figure 1.6** Trapping and biosensing: parallel photonic nano-jet array can be used to selectively trap and detect nanoparticles and biological cells.

(Figure is reproduced from Y. Li <i>et al.</i> , ACS Nano, vol. 10, no. 6, pp. 5800-5808, 2016).....	9
<b>Figure 1.7</b> Schemes of the optical fiber tweezer profiles using different fabrication methods: (a) Polishing (b) Heating and Pulling (c) Chemical Etching (d) High Resolution Techniques. (Figure is reproduced from R. S. Rodrigues <i>et al.</i> , J. Lightw. Technol., vol. 33, no. 16, 2015) .....	10
<b>Figure 1.8</b> Schematics of (a) fiber Bragg grating, (b) tapered fiber, (c) coated fiber, and (d) SMF-MMF-SMF hetero-structure. ....	12
<b>Figure 1.9</b> The index profiles of (a) two-layer step-index fiber, (b) three-layer step-index fiber, (c) hollow-core fiber (HCF), and (d) depressed-core fiber (DCF).....	13
<b>Figure 2.1</b> Ray trajectories in a bent silica fiber. ....	33
<b>Figure 2.2</b> Examples of ray trajectories in (a) a multimode fiber and (b) a single-mode fiber. ....	34
<b>Figure 2.3</b> Dispersion diagrams of a two-layer step-index fiber: (a) $n_{\text{eff}}$ vs. $r_1$ , where $n_1 = 1.4504$ , $n_2 = 1.4447$ and $\lambda = 1550$ nm; (b) $n_{\text{eff}}$ vs. $\lambda$ , where $n_1 = 1.4504$ , $n_2 = 1.4447$ and $r_1 = 10 \mu\text{m}$ , $r_2 = \infty$ .....	35
<b>Figure 2.4</b> (a) and (b) show the cross-section of the refractive index profile and the ray trajectories within the tube-type HCF, respectively. (c) and (d) show respectively the ray trajectories and the reflection spectrum of a Fabry-Perot resonator.....	37
<b>Figure 2.5</b> Dispersion curves of the real (a) and imaginary (b) parts of the effective mode index of three lowest-order core modes supported by the tube-type HCF. In both plots, the dark yellow vertical dashed lines indicate the resonances with the corresponding order. (Figure is reproduced from M. Zeisberger and M. A. Schmidt, Sci. Rep., vol. 7, no.1, pp. 1-13, 2017) .....	39
<b>Figure 2.6</b> (a) SEM image of a bandgap fiber. (b) A rod in a hexagonal unit cell. (c) Plots of band structure for the bandgap fiber. The bandgaps are shown in red. The rod modes from which the bands arise are labelled along the top. The yellow curve is the “fundamental” core-guided mode. (d) Transmission spectra of 2 m of the fiber. (Figure is modified from T. A.	

Briks <i>et al.</i> , Opt. Express, vol. 14, no. 12, pp. 5688-5698, 2006 and T. A. Briks <i>et al.</i> Opt. Express, vol. 14, no. 20, pp. 9483-9490).....	41
<b>Figure 2.7</b> (a) The cross-section of a Kagomé-lattice HC-PCF. (b) Optical micrograph of the field intensity pattern at the output of a few cm of the fiber. (c) Primitive unit cell of the Kagomé lattice. (d) Calculated DOPS diagram as a function of the real part of the effective index and normalized frequency. (e) Measured transmission spectrum. Calculated (f) real and (g) imaginary parts of the effective index $n_{\text{eff}}$ of the HE <sub>1,1</sub> -like core mode. (Figure is reproduced from F. Couny <i>et al.</i> , Science, vol. 318, no. 5853, pp. 1118-1121, 2007, supporting online material).....	42
<b>Figure 2.8</b> Nature of the Kagomé lattice HC-PCF cladding modes. (a) The first two columns show the core mode and a cladding mode, respectively, for a frequency $kA = 50$ and $kA = 100$ . The third column shows the mode of an infinite Kagomé lattice, which corresponds to the cladding mode in the second column. (b) Same as in (a) for $kA = 68$ . (Figure is reproduced from F. Couny <i>et al.</i> Science, vol. 318, no. 5853, pp. 1118-1121, 2007)	43
<b>Figure 2.9</b> Cross section of a three-layer optical fiber. The light field in different regions is denoted by different Bessel functions. .....	48
<b>Figure 2.10</b> The FEM analysis region for the calculation of the core and cladding modes in a three-layer optical fiber. The analysis region is meshed by triangular elements.....	53
<b>Figure 2.11</b> The meshing of analysis region in beam propagation method: (a) transverse (x-y) plane, (b) along the z direction. .....	54
<b>Figure 3.1</b> (a) Refractive index profile of a three-layer step-index optical fiber. (b) Ray trajectory of a core-type mode. (c) Ray trajectory of a cladding-type mode ( $0 \leq r_1 \leq 62.5 \mu\text{m}$ , $n_1 = 1.451$ , $r_2 = 62.5 \mu\text{m}$ and $n_2 = 1.445$ , $\lambda = 1550 \text{ nm}$ ). .....	61
<b>Figure 3.2</b> (a) Dispersion curves ( $n_{\text{eff}}$ vs. $r_1$ ) of the modes in step-index optical fibers; (b) is an enlarged part of graph (a), indicated by a black dash rectangle. Scalar LP <sub>m,n</sub> modes indicated by the solid lines are calculated by the analytical method. The vector modes (TE <sub>0,n</sub> , TM <sub>0,n</sub> , HE <sub>m,n</sub> and EH <sub>m,n</sub> ) indicated by the scattered lines are calculated by the full-vector FEM. .....	63

**Figure 3.3** Modal intensities and electric field vector distributions of HE<sub>1,1</sub>, TE<sub>0,1</sub>, HE<sub>2,1</sub> and TM<sub>0,1</sub> modes, with several different  $r_1$  as indicated on the left. The modes in the no-core fibers ( $r_1 = 0 \mu\text{m}$ ), shown in a1, b1 c1 and d1, are core-type modes; the modes shown in a3-a6, b6, c6 and d6 are also core-type modes for  $n_{\text{eff}} > 1.445$ ; the remaining are cladding-type modes with  $n_{\text{eff}} < 1.445$ . (Core-type modes are indicated by the red frames). ..... 66

**Figure 4.1** (a), (b) and (c) are the SMF-NCF-SMF (SNCS), SMF-SCF-SMF (SSCS) and SMF-MMF-SMF (SMS), respectively; (d) transverse intensity profiles of fundamental modes in the input and output SMFs, and partial LP<sub>0,n</sub> modes in the middle fiber section; (e) experimental setup for characterization of the multimode interference spectra; (f) and (g) are respectively the refractive index profiles along the cross-section radius for an optical fiber placed in air without (NCF) and with a fiber core (SMF, SCF and MMF)..... 73

**Figure 4.2** Effective refractive index of LP<sub>0,n</sub> modes as a function of fiber core radius. Solid curves calculated by the analytical method, while the scattered circles are results calculated by the BPM. Inset plot shows that the cutoff of the LP<sub>0,1</sub> mode changing from cladding-type to core-type is  $r_1 = 1.30 \mu\text{m}$  (analytical method) and  $r_1 = 1.35 \mu\text{m}$  (BPM). ..... 76

**Figure 4.3** Field distributions of the modes LP<sub>0,1</sub> (a1-a8), LP<sub>0,2</sub> (b1-b8), and LP<sub>0,3</sub> (a1-c8) for several different  $r_1$  calculated by the BPM. The modes a1, b1 c1, a8, b8 and c8 in the no-core fibers are core-type modes; a4-a7, b7 are also core-type modes for  $n_{\text{eff}} > 1.445$ ; the remaining are cladding-type modes with  $n_{\text{eff}} < 1.445$ . (Core-type modes are indicated by red frames.) ..... 79

**Figure 4.4** Analytical results: (a), (b) and (e) are respectively the transverse intensity profile (TIP), the longitudinal intensity distribution (LID) and the on-axis intensity along the propagation distance inside the NCF of SNCS ( $r_1 = 0 \mu\text{m}$ ). (f), (g) and (h) are respectively the on-axis intensities inside the SCF of SSCS with the  $r_1$  equal to 0.35  $\mu\text{m}$ , 0.45  $\mu\text{m}$  and 0.55  $\mu\text{m}$ . (d), (c) and (i) are respectively the simulated TIPs, the LIDs and the

on-axis intensities inside the SCF of SSCS with the $r_1$ equal to 0.71 $\mu\text{m}$ .	82
<b>Figure 4.5</b> Analytical results: (a)-(h) show the intensity ‘I’ of peak around the positions $Z = nL_s$ , $n = 4, 5, \dots, 11$ as a function of $r_1$ . The peak points in (a)-(g) respectively correspond to the self-imaging points as shown in Figs. 4.4(e), 4.4(i) and 4.6(a)-4.6(e). ..	84
<b>Figure 4.6</b> Analytical results: the on-axis intensities inside the SCF of SSCS with the $r_1$ equal to (a) 0.91 $\mu\text{m}$ , (b) 1.02 $\mu\text{m}$ , (c) 1.11 $\mu\text{m}$ , (d) 1.18 $\mu\text{m}$ and (e) 1.23 $\mu\text{m}$ .....	85
<b>Figure 4.7</b> BPM results: the on-axis intensities inside (a) the NCF of SNCS, the SCF of SSCS with the $r_1$ equal to (b) 0.73 $\mu\text{m}$ , (c) 0.92 $\mu\text{m}$ , (d) 1.04 $\mu\text{m}$ , (e) 1.12 $\mu\text{m}$ , (f) 1.20 $\mu\text{m}$ and (g) 1.27 $\mu\text{m}$ . .....	86
<b>Figure 4.8</b> Discrete and exponential growth of the self-imaging period $L_Z$ for the SNCS ( $r_1 = 0 \mu\text{m}$ ) and the SSCS versus $r_1$ , calculated both analytically and using BPM.....	87
<b>Figure 4.9</b> (a) $L_{Zn}$ calculated by Eq. (4.9): $L_{Zn} = (4n-3)L_n$ with the $n_{\text{eff}}(LP_{0,n})$ determined from the analytical results in Fig. 4.2. The main graph of (b) shows the parts extracted from (a), related to the pure core modes. Inset of (b) shows the part extracted from (a), related to the cladding modes of SCF with $0 \mu\text{m} < r_1 < 1.3 \mu\text{m}$ and the core modes of NCF with $r_1 = 0 \mu\text{m}$ . .....	89
<b>Figure 4.10</b> $L_{Zn}$ calculated by Eqs. (4.9)-(4.15). The violet triangle symbols and the violet dashed line are respectively calculated and exponential fitting values of self-imaging (radius and period) the same as in Fig. 4.8. The color of lines $L_{Zn}$ with the same mode number ‘n’ is consistent with that in Fig. 4.9. ....	93
<b>Figure 4.11</b> (a) and (b) are respectively the on-axis intensities inside the middle fiber section of SNCS ( $r_1 = 0 \mu\text{m}$ ) and SSCS ( $r_1 = 1.1 \mu\text{m}$ ). (c0)-(c8) and (d0)-(d8) show the TIPs in the middle fiber section of the SNCS and SSCS samples at the positions $Z = nL_s$ ( $n = 1, 2, \dots, 8$ ), where the light wavelength was set at 1550 nm. (e1)-(e8) and (f1)-(f8) show the simulated and measured transmission spectra of the samples, where the	

lengths of the middle fiber section are equal to the integer multiples of $L_s$ : $1L_s, 2L_s, \dots, 8L_s$ .....	95
<b>Figure 5.1</b> A depressed-core optical fiber and its cross section and refractive index profile.....	109
<b>Figure 5.2</b> (a) and (b) show the ray trajectory of a mode with $n_1 < n_{\text{eff}} = n_2 \sin \theta_1 < n_2$ in a DCF and an equivalent asymmetric planar waveguide, respectively. (c) and (d) show the ray trajectory of a mode with $n_3 < n_{\text{eff}} = n_1 \sin \theta_1 < n_1$ in the DCF and the equivalent asymmetric planar waveguide, respectively. ....	110
<b>Figure 5.3</b> Dispersion curves ( $n_{\text{eff}}$ vs. $\lambda$ ) of TE modes with $n_{\text{eff}}$ corresponding to (a) $n_1 < n_{\text{eff}} < n_2$ , (b) $n_1 - 0.001 < n_{\text{eff}} < n_1 + 0.001$ , $n_1 = 1.445$ , $n_2 = 1.51$ . (c) shows the modal intensity and electric field vector distributions of TE modes whose positions ( $n_{\text{eff}}, \lambda$ ) are indicated by the black circle dots in (a) and (b). The red vertical dashed lines in (a) and (b) indicate the resonant bands. ....	113
<b>Figure 5.4</b> The left panel (a)-(e) shows the normalized intensity distributions along the $r$ -coordinate for the modes shown at points C-G in Fig. 5.3. The right panel (a')-(e') shows the zoomed-in part of (a)-(e), delineated by the vertical dashed lines.....	115
<b>Figure 5.5</b> Dispersion curves ( $n_{\text{eff}}$ vs. $\lambda$ ) of TM modes with $n_{\text{eff}}$ corresponding to (a) $n_1 < n_{\text{eff}} < n_2$ , (b) $n_1 - 0.001 < n_{\text{eff}} < n_1 + 0.001$ , $n_1 = 1.445$ , $n_2 = 1.51$ . (c) shows the modal intensity and electric field vector distributions of TM modes whose positions ( $n_{\text{eff}}, \lambda$ ) are indicated by the black squares in (a) and (b). The black vertical dashed lines in (a) and (b) indicate the resonant bands.....	117
<b>Figure 5.6</b> Dispersion curves ( $n_{\text{eff}}$ vs. $\lambda$ ) of $\text{HE}_{1,N}$ (red) and $\text{EH}_{1,N}$ (black) modes with $n_{\text{eff}}$ corresponding to $(n_1 - 0.001 < n_{\text{eff}} < n_1 + 0.001)$ , $n_1 = 1.445$ . The black and red vertical dashed lines indicate the resonant bands.....	119
<b>Figure 5.7</b> (a) Dispersion curves ( $n_{\text{eff}}$ vs. $\lambda$ ) of HE modes with $n_{\text{eff}}$ corresponding to (a) $n_1 - 0.001 < n_{\text{eff}} < n_1 + 0.001$ , $n_1 = 1.445$ . (b) partially enlarged image of (a), indicated by a red frame. (c) shows the modal intensity and electric field vector distributions of HE modes whose positions ( $n_{\text{eff}}, \lambda$ ) are	

indicated by the circles in (b). The black and red vertical dashed lines in (a) and (b) indicate the resonant bands. ....	120
<b>Figure 5.8</b> (a) Dispersion curves ( $n_{\text{eff}}$ vs. $\lambda$ ) of a depressed-core fiber. (b) partially enlarged image of (a), indicated by the black dashed frame. The text labels and the corresponding dispersion curves are of the same color. The orange solid lines in (a) and (b) are for $LP_{m,n}$ modes in a conventional step-index fiber ( $n_{\text{co}} = 1.445$ , $n_{\text{cl}} = 1$ , $r_{\text{co}} = 62.5 \text{ um}$ and $r_{\text{cl}} = \infty$ ). The black and red vertical dashed lines indicate the resonant bands.	123
<b>Figure 6.1</b> (a) Microscopic image of a polymer-coated no-core fiber (PC-NCF). (b) Refractive index variations along the cross section of the PC-NCF ( $n_2 > n_1 > n_3$ ). (c) Schematic of the experimental setup for measurements of the straight and bent PC-NCF samples. ....	137
<b>Figure 6.2</b> (a) shows the dispersion curves ( $n_{\text{eff}}$ vs. $\lambda$ ) of modes $HE_{1,N}$ , $N = 34, 35, \dots, 38$ in the PC-NCF, which change into the anti-resonant core modes $HE_{1,n+(N-n)}$ , $n = 1, 2, \dots$ as $\lambda$ increases. The orange lines are the dispersion curves of the $LP_{0,1}$ ( $HE_{1,1}$ ) and $LP_{0,2}$ ( $HE_{1,2}$ ) in the NCF. (b) is the partially enlarged image of (a), indicated by a red dashed frame. The black and red vertical dashed lines indicate the resonant bands. ....	140
<b>Figure 6.3</b> The intensity and electric field vector distributions of modes in PC-NCF, whose positions in dispersion diagram are indicated in Fig. 6.2(b).	142
<b>Figure 6.4</b> Schematic of the ray trajectories of an excited guide mode within the SMF-PC-NCF-SMF hetero-structure.....	144
<b>Figure 6.5</b> The transmission spectra of the SMF-PC-NCF-SMF hetero-structure, calculated by Eq. (6.7) with different intensity coefficients A and B as indicated. (a)-(d) $L = 5.8 \text{ cm}$ ; (e)-(f) $L = 75.8 \text{ cm}$ . The black and red vertical dashed lines indicate the resonant bands.....	147
<b>Figure 6.6</b> Measured transmission spectra of the straight hetero-structures SMF-PC-NCF-SMF with different $L$ . The black and red vertical dashed lines indicate the resonant bands. ....	149
<b>Figure 6.7</b> (a) Dispersion curves ( $n_{\text{eff}}$ vs. $\lambda$ ) and (b) the fractional power in the cladding of $HE_{1,1+(35)}$ and $HE_{1,2+(35)}$ modes with the bend radius $R = \infty$	

and $R = 66.67$ cm. The inset of (b) is an enlarged figure of the part indicated by the black dashed rectangle. $\text{HE}_{1,n+(35)}$ ( $n = 1$ or $2$ ) is a two-fold degeneracy mode of $\text{HE}_{1,n+(35)a}$ and $\text{HE}_{1,n+(35)b}$ . The black and red vertical dashed lines indicate the resonant bands.....	152
<b>Figure 6.8</b> The modal intensity and electric field vector distributions of $\text{HE}_{1,1+(35)}$ and $\text{HE}_{1,2+(35)}$ modes under different bending states as indicated. ....	153
<b>Figure 6.9</b> Measured transmission spectra of the hetero-structure SMF-PC-NCF-SMF with (a) $L = 5.8$ cm and (b) $L = 75.8$ cm, under different bending states as indicated. The black and red vertical dashed lines indicate the resonant bands. ....	156
<b>Figure 7.1</b> Schematic diagrams: (a) SMF-NCF-SMF (SNCS) structure, (b) SMF-polymer coated NCF-SMF (PC-SNCS) structure.....	169
<b>Figure 7.2</b> Dispersion curves for $\text{HE}_{1,1+(N-1)}$ and $\text{HE}_{1,2+(N-2)}$ ( $N = 34, 35, \dots, 38$ ) in the PC-NCF (black lines) and $\text{HE}_{1,1}$ ( $\text{LP}_{0,1}$ ) and $\text{HE}_{1,2}$ ( $\text{LP}_{0,2}$ ) in NCF (red lines).171	
<b>Figure 7.3</b> Simulated transmission spectra of (a) individual modes $\text{LP}_{0,n}$ calculated by Eq. (7.4); (b) straight PC-SNCS calculated by Eq. (7.3) and SNCS with $L = 9$ mm calculated by Eq. (7.2).....	172
<b>Figure 7.4</b> (a) Transmission spectra simulated by BPM for straight PC-SNCSs with $L = 9$ mm and $9.3$ mm. (b) Measured transmission spectra for straight PC-SNCSs with $L = 9$ mm and $9.3$ mm (at $\sim 25^\circ\text{C}$ ).....	173
<b>Figure 7.5</b> Experimental setup for temperature and transmission spectrum measurement.....	175
<b>Figure 7.6</b> Measured transmission spectra for bent and straight PC-SNCSs with (a) and (b) $L = 9.3$ mm, (c) $L = 9$ mm, and (d) $L = 7.5$ mm (at $\sim 25^\circ\text{C}$ , ' $R$ ' = bend radius).....	176
<b>Figure 7.7</b> Measured transmission spectra of (a) the straight, (b) and (c) the bent ( $R = 10$ cm) PC-SNCS with $L = 9.3$ mm, at different temperatures as indicated; (d) shows the spectral shifts and the linear fittings of dip 1 and dip 2 in (b) and (c). .....	177
<b>Figure C.1</b> (a) Ray trajectory of a beam with angle of incidence $\theta_1$ ( $n_1 > n_1 \sin \theta_1 > n_3$ ) impinging on the interface of an asymmetric planar waveguide. (b) Fresnel's refraction and reflection at the interface between regions I and II. (c) Total reflection at the interface between regions II and III,	

where 'z', 'H', and 'h' denote the Goos-Hänchen shift, the deviation of the reflection light, and the penetration depth of the evanescent wave, respectively. .... 196

# List of Tables

<b>Table 2.1</b> Comparison of the waveguide analysis methods. ....	55
<b>Table 4.1</b> The arguments between the discrete self-imaging periods and the constructive interference lengths .....	91
<b>Table 4.2</b> The integer arguments between the discrete self-imaging periods and the constructive interference lengths.....	91

# List of Abbreviations and Symbols

AR	Anti-Resonance
ARROW	Anti-Resonant Reflecting Optical Waveguide
BPM	Beam Propagation Method
DOPS	Density of Photonic States
DCF	Depressed-Core Fiber
EDFA	Erbium-Doped Fiber Amplifier
FBG	Fiber Bragg Grating
FEM	Finite Element Method
HCF	Hollow-Core Fiber
HC-PCF	Hollow-Core Photonic Crystal Fiber
ITO	Indium Tin Oxide
IC	Inhibited Coupling
LMA	Large Mode Area
LP	Linear Polarization
LID	Longitudinal Intensity Distribution
LPFG	Long-Period Fiber Grating
LMR	Lossy Mode Resonance
MPA	Mode Propagation Analysis
MDM	Mode-Division Multiplexing
MMF	Multimode Fiber
MMI	Multimode Interference
MPI	Multi-Path Interference
NCF	No-Core Fiber
OFI	Optical Fiber Interferometer
OSA	Optical Spectrum Analyser
PBG	Photonic Bandgap
PBF	Photonic Bandgap Fiber
PDMS	Polydimethylsiloxane
PC-NCF	Polymer-Coated No-Core Fiber
SMF	Single-Mode Fiber

SCF	Small-Core Fiber
SMS	SMF-MMF-SMF
SNCS	SMF-NCF-SMF
PC-SNCS	SMF-PC-NCF- SMF
SSCS	SMF-SCF-SMF
SDM	Space-Division Multiplexing
SBS	Stimulated Brillouin Scattering
SRS	Stimulated Raman Scattering
TIR	Total Internal Reflection
TIP	Transverse Intensity Profile
WDM	Wavelength-Division Multiplexing

# **Chapter 1**

## **Introduction**

In this chapter the relevant properties and applications of optical fibers are briefly introduced and the aim and objectives of this thesis are formulated.

### **1.1 Optical fibers and their applications**

An optical fiber is a cylindrical waveguide (in a shape of dielectric wire or a rod) with a diameter only slightly larger than a human hair, carrying light along its longitudinal axis. A fundamental element of understanding and applying optical fiber technology, also referred to as “fiber optics” involves the study of the behaviour of light traveling in the fiber typically by an analysis of the optical modes carried by the fiber. The development of laser and optical communications have accelerated progress in the use of fiber optics since the 1960s, particularly in the late 1970s when the first live telecommunications traffic was carried by optical fiber systems. In addition to optical communications, optical fibers have been applied in the fields of fiber lasers and amplifiers, optical imaging, optical manipulation, and fiber optic sensing. Optical fibers offer numerous advantages compared to earlier traditional technologies, including an immunity to electromagnetic interference, small size, light weight, durability, remote operation and multiplexing capabilities. Along with an increasingly wide range of applications, novel fibers and waveguiding theories have also seen a rapid development.

### **1.1.1 Optical fibers for communication networks**

In 1854 John Tyndall, an Irishman, demonstrated that sunlight can be guided by a curved flow of water due to total internal reflection, in effect predicting over a century later the emergence of optical fiber technology. In the early 20<sup>th</sup> century, un-cladded optical fiber bundles were used to collect optical images of body cavities [1,2]. The first cladded optical fiber was proposed in 1954 by Dutch scientist Bram van Heel to improve light transmission through fibers and to reduce the interference from the surrounding medium for the application using fiberscopes [3]. At that time, the very high loss of the optical fibers hindered their application in long-haul optical communications. In 1966, Charles K. Kao (who was awarded Nobel prize in Physics in 2009) theoretically demonstrated that the low-loss single-mode guidance and broad bandwidth can be achieved by reducing the level of impurities in the silica optical fiber [4]. In 1970, F.P. Kapron *et al.* created the first low loss optical fiber (below 20 dB/km) [5]. The first live traffic demonstration of optical fiber transmission took place in the USA in 1977. Since then studies of fiber optics including both fundamental theories and technologies accelerated [6-8]. Fig. 1.1(a) shows a stylised photograph of an optical fiber, while Figs. 1.1(b)-1.1(d) illustrate schematically the cross-sections of an un-cladded multimode fiber (MMF), a cladded MMF and a cladded single-mode fiber (SMF) respectively.

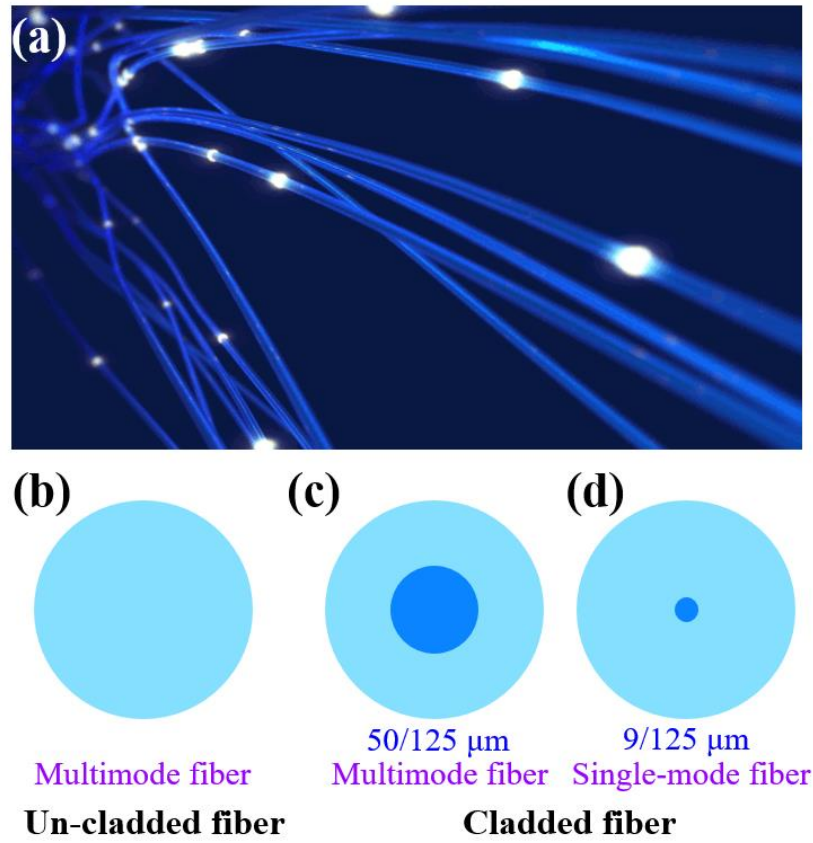


**Figure 1.1** (a) Light in optical fibers. Schematic cross section of (b) un-cladded multimode fiber (MMF); (c) cladded MMF, and (d) cladded single-mode fiber (SMF).

SMF does not suffer from modal dispersion and thus it offers a far higher transmission bandwidth than MMF. For this reason SMF is the dominant type of fiber currently used in optical communication networks, although MMFs are also used in some shorter range cases, for example in building cabling [9,10]. The transmission information capacity of SMF has also been greatly increased by the development of the wavelength-division multiplexing (WDM) [11] and improved dispersion management [12]. However currently conventional SMF technology is approaching its limits [13], for example in the ultimate bandwidth available over a single fiber, the minimum loss possible and the ability to deal with large optical power densities in highly multiplexed environments. In order to overcome such limits new innovations including the few-mode fibers, the

MMFs, and the multi-core fibers have been investigated to increase the capacity of optical communications along with the recent technologies such as the space-division multiplexing (SDM) [14,15] and the mode-division multiplexing (MDM) [16-18]. In addition, the hollow-core photonic crystal fibers such as the photonic bandgap fiber [19], inhibited-coupling fiber [20] and anti-resonant fiber [21] have also been studied intensively due to their intriguing optical properties such as ultralow optical nonlinearity, high mode quality, excellent power handling capabilities, low latency, broad bandwidth, low bending loss, ultralow losses both at conventional wavelengths (e.g., around 1550 nm) and at longer wavelengths (i.e., into the mid-IR and THz) [22,23]. Fig. 1.2 shows the cross sections of several fiber configurations for increasing communication bandwidth [14].

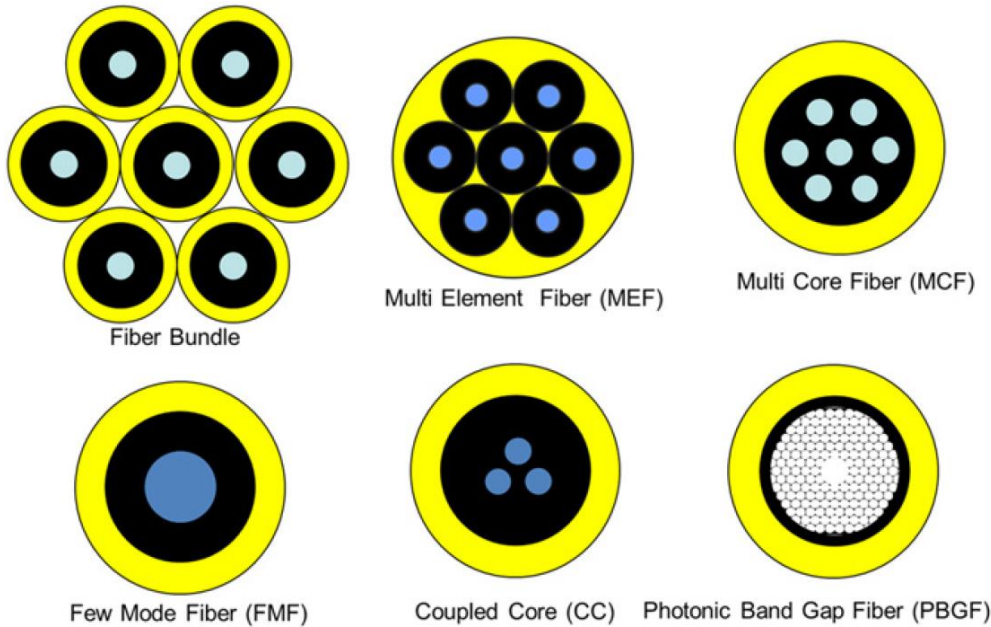


**Figure 1.2** Different approaches for realization of space-division multiplexing (SDM) to increase the communication bandwidth. (Figure is reproduced from D. J. Richardson *et al.* Nat. Photonics, vol. 7, no. 5, pp. 354-362, 2013; E. Agrell *et al.*, J. Opt., vol. 18, p. 063002, 2016.)

### **1.1.2 Optical fibers for lasers and amplifiers**

A wide variety of functional devices have been developed for optical communications and sensing systems. Among the most valuable are devices based on optical fiber itself, not only because such devices are compact in nature but because low attenuation coupling to and from transmission fibers can be easily implemented by comparison to other solutions, such as integrated optics.

Fiber based lasers and amplifiers, fabricated by doping the fiber core with rare earth elements, are an important example of such fiber devices. The first fiber laser was proposed in 1961 [24,25] soon after the first demonstration of the solid-state ruby laser [26]. In the early days performance of fiber lasers was limited by high losses within the active materials in the fiber core [27]. The first low-loss Nd-doped fiber laser was fabricated and demonstrated in 1985 [28].

Soon after that, a low noise erbium-doped fiber amplifier (EDFA) was invented in 1987 [29,30], which offered amplification in the near-IR transmission window of silica fiber circa 1550 nm. Since then, fiber lasers and amplifiers have experienced rapid development, which has enabled all-optical long-haul communication systems and resulted in a revolution in the telecommunication industry, for example EDFA can provide for ultra-long global transmission distances, without the need for complex electronic repeaters and thus fully unlocking the potential of fiber optics for communications [31,32].

Cladding pumping in double clad fiber lasers was proposed in 1988 by E. Snitzer [33] and has proved to be most powerful enabling technique for increasing the power of fiber lasers. The general schematic of a cladding pumping fiber laser is shown in Fig. 1.3, where the pump light is coupled firstly into the inner cladding

and then can be efficiently coupled into the active fiber core [34]. High-power, double-clad fiber amplifiers have similar configurations with the double-cladded fiber laser [32].

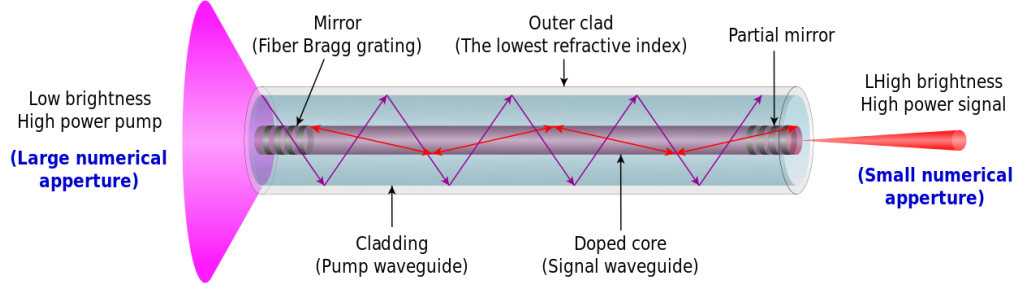


**Figure 1.3** Schematic of the cladding pumping principle of fiber-laser operation. (Figure is reproduced from the website: [https://en.wikipedia.org/wiki/Double-clad\\_fiber](https://en.wikipedia.org/wiki/Double-clad_fiber))

Since 1988, the average output power of continuous-wave, nearly diffraction-limited fiber lasers have been increasing exponentially. Ultrashort-pulse fiber lasers have been developed at a similar rate, attaining average powers of almost 1 kW by 2009 [35]. The increase of the output power of a fiber laser depends on both the pump efficiency and the effectiveness of heat dissipation management [35-37]. Nonlinear effects such as stimulated Brillouin scattering (SBS) [38], stimulated Raman scattering (SRS) [39], self-focusing [40], and thermally induced mode instability [41-43] impose limitations on the average power and peak power output of a fiber laser. One way to reduce the nonlinear effects is to use large-mode-area (LMA) fibers [44-52], some examples of which are shown in Fig. 1.4: such as a step-index MMF [44], photonic crystal fiber [46], large-pitch fiber [47], multi-core fiber [50], multi-quench fiber [51] and hollow-core photonic crystal fiber [52].

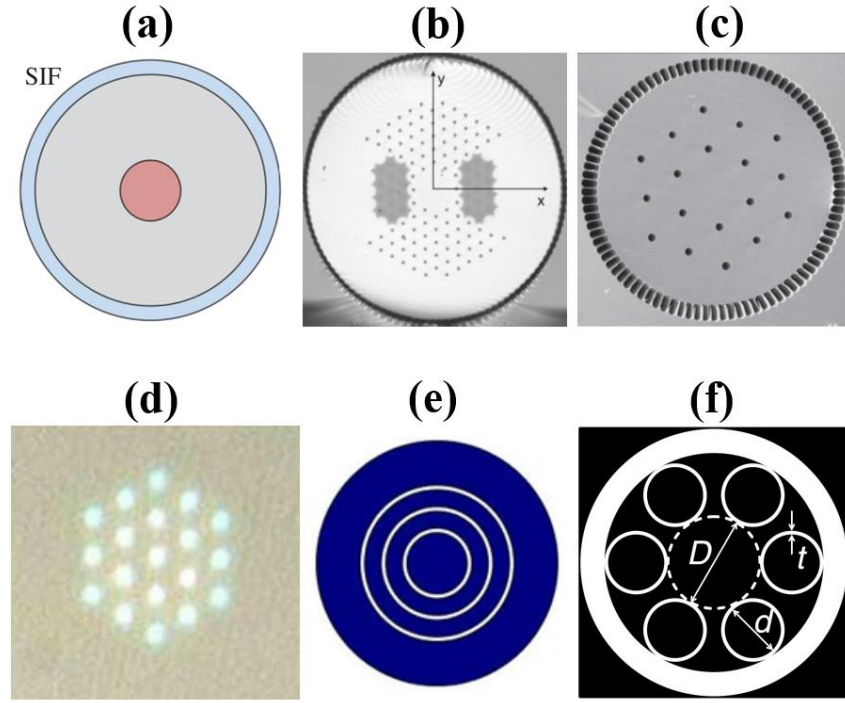


**Figure 1.4** Large-mode-area fibers: (a) step-index MMF (reproduced from J. P. Koplow *et al.*, Opt. Lett., vol. 25, no. 7, pp. 442-444, 2000); (b) photonic crystal fiber (reproduced from T. T. Alkeskjold *et al.*, Nanophotonics, vol. 2, no. 5-6, pp. 369-381, 2013); (c) large-pitch fiber (reproduced from F. Stutzki *et al.*, Opt. Lett., vol. 36, no. 5, pp. 689-691, 2011); (d) multi-core fiber (reproduced from M. M. Vogel *et al.*, Opt. Lett., vol. 34, no. 18, pp. 2876-2878, 2009); (e) multi-quench fiber (reproduced from D. Jain *et al.*, Opt. Express, vol. 21, no. 2, pp. 1448-1455, 2013); (f) hollow-core photonic crystal fiber (reproduced from J. P. Uebel *et al.*, Opt. Lett., vol. 41, no. 9, pp. 1961-1964, 2016).

### 1.1.3 Optical fibers for imaging applications

Optical fibers are excellent tools for optical imaging. As mentioned at the beginning of this chapter, optical fiber bundles started to be used for medical imaging from middle of the 20<sup>th</sup> century [2]. Today, fiber bundles have become well-known standard parts of commercial flexible endoscopes and thus have been widely used for visualizing hard-to-reach areas of the human body [53-56]. However the imaging resolution of a fiber bundle based endoscope is dependent on the number of fibers in the bundle, where one fiber represents a single pixel

and thus there is a tradeoff between the diameter and the resolution of the endoscope, as large pixel counts increase the overall fiber bundle diameter. A MMF supports multiple spatial modes, which can be considered equivalent to the individual fibers in the fiber bundle, and thus MMFs have been intensively studied as the new form of fiber endoscope [57-60]. Fig. 1.5 shows a sketch of a MMF-based super-resolution and super-speed endo-microscope [60]. Compared to a fiber bundle, the diameter of the fiber endoscope can be significantly reduced. However, the quality of imaging with a MMF is more readily affected by the fabrication defects, bends and temperature changes [61]. Therefore a better understanding of the modal behaviour within the MMFs is critically needed [62-65].

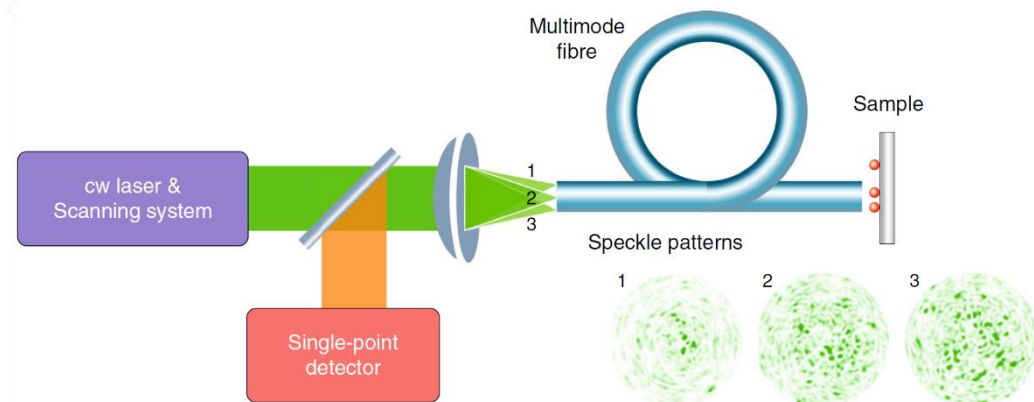


**Figure 1.5** Schematic of a MMF-based super-resolution and super-speed endo-microscopy, consisting of three main components: a continuous-wave laser source with a scanning system, a MMF probe, and a single-point detector. Pump light is scanned across the fiber input facet, creating different illumination patterns on the fiber output. The total fluorescent response from the sample is collected by the same fiber probe, propagated back, and measured by the single-point detector. (Figure is reproduced from L. V. Amitonova and J. F. de Boer, Light: Sci. Appl., vol. 9, no. 1 pp. 1-12, 2020)

### 1.1.4 Optical fibers for manipulating micro/nano- particles

Contactless displacement and levitation of micron-sized dielectric particles by optical tweezers was firstly demonstrated using bulk optics methods in the early 1970s. Light in an optical tweezers provides a very low level force due to the radiation pressure of the light. Optical tweezers based on the bulk optics methods such as axicons [66] and computer-generated holograms [67] have several disadvantages such as the large size of the setup, high cost, difficulties with beam misalignment, etc. All-fiber optical tweezers with their very compact size are attractive due to their capability of being integrated with other equipment, while offering alignment-free operation, high flexibility, and remote delivery [68-71]. Therefore, optical fibers have been widely studied as the optical tweezers to manipulate micro/nano- particles for applications in the biological, medical, and physical fields [66,72-75]. Fig. 1.6 conceptually illustrates trapping of nanoparticles and biological cells with fiber optic tweezers [71].

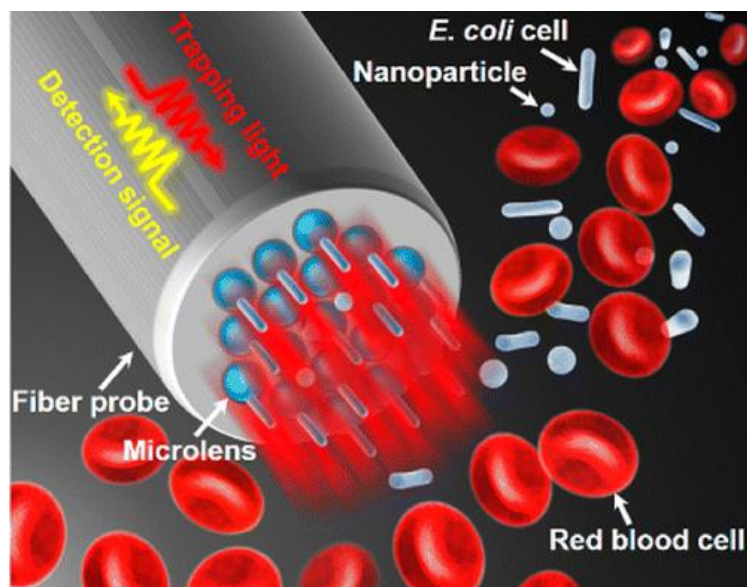


**Figure 1.6** Trapping and biosensing: parallel photonic nano-jet array can be used to selectively trap and detect nanoparticles and biological cells. (Figure is reproduced from Y. Li *et al.*, ACS Nano, vol. 10, no. 6, pp. 5800-5808, 2016)

The balance between light scattering and the light intensity gradient, resulted from reflections and refractions, provides the force to control, trap, and manipulate the neutral dielectric particles and atoms [76]. The mode field profile, polarization, and the on-axis intensity distribution of the beams have proven to be of great importance to the performance of the optical fiber tweezers [77]. Fiber modes modified by a lensed fiber tip or a micro axicon directly written on the fiber core can generate Bessel-like beams in a similar fashion to bulk optic equivalents [78-80]. Bessel-like beams can be generated by on-axis illumination of a MMF via multi-path interference [81], or by higher-order cladding mode excitation in a SMF with a long period fiber grating [68]. In addition, holographic control of light propagation in MMFs has recently been used for the three-dimensional optical manipulation [82,83]. Fig. 1.7 shows several kinds of optical fiber tweezer profiles based on SMFs and multi-core fibers and fabricated with methods such as polishing, thermal pulling, chemical etching and

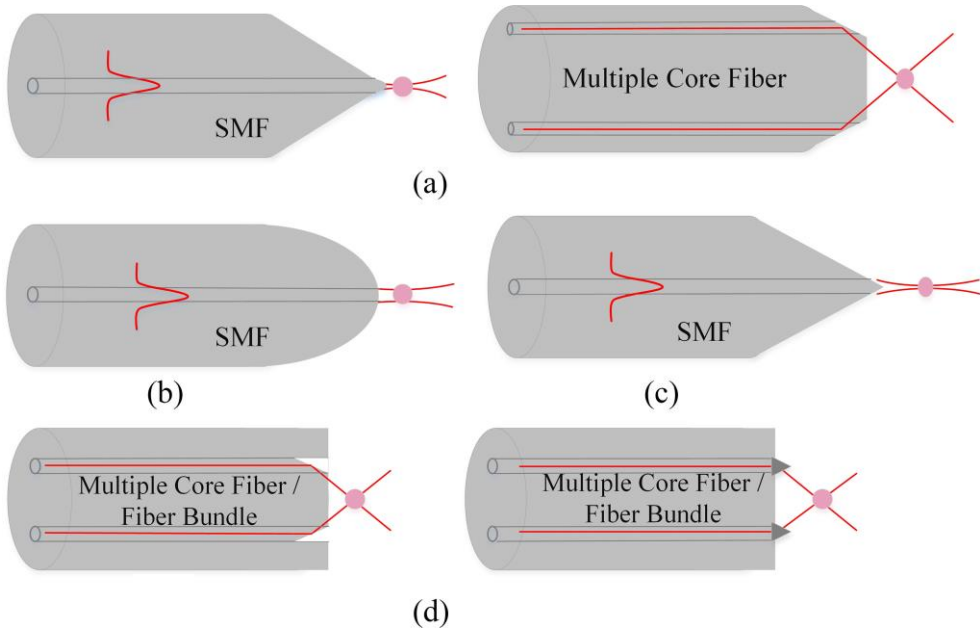


**Figure 1.7** Schemes of the optical fiber tweezer profiles using different fabrication methods: (a) Polishing (b) Heating and Pulling (c) Chemical Etching (d) High Resolution Techniques. (Figure is reproduced from R. S. Rodrigues *et al.*, J. Lightw. Technol., vol. 33, no. 16, 2015)

micromachining [77].

### 1.1.5 Optical fibers for sensing

Changes in fiber parameters such as refractive index and length due to external perturbations lead to variations of the phase and intensity of the output light from an optical fiber, which is the fundamental mechanism underpinning the operation of fiber optic sensors. Fiber optic sensors have been intensively studied for a wide range of applications involving the measurement of physical, chemical, and biological parameters [84,85]. Almost all types of the optical fibers, which at first were designed for other applications such as telecommunications, lasers and amplifiers, imaging and tweezers, can be used for optical sensing. However a key advantage of optical fiber when used for optical communications is its immunity to the local environment but such immunity, while it is essential for reliable communication, is a major disadvantage for sensing which by definition demands interaction with the local environment. Therefore to utilise fibers for sensing with high sensitivity, resolution, and dynamic range, the sensing fibers typically need to be specially modified by optical writing [86,87], tapering [88], twisting [89,90], coating [91,92], hetero-structure splicing [93,94], etc. Fig. 1.8 shows schematically a fiber Bragg grating, a tapered SMF, a coated no-core fiber, and a typical SMF-MMF-SMF (SMS) hetero-structure. It is worth mentioning that fiber optic sensors based on fiber Bragg gratings (FBGs) shown in Fig. 1.8(a) are among the most mature fiber sensing technologies and have been used for real-time in-situ monitoring of bridges, tunnels and airplane structures [95]. Micro/nano-fibers shown in Fig. 1.8(b) can guide light with low optical loss, possess outstanding mechanical flexibilities, tight light confinement, enhanced

evanescent fields and large waveguide dispersions, which makes them a versatile platform for optical sensing on a micro-/nano-meter scale [96]. Coating the no-core fiber with metals or semiconductor materials shown in Fig. 1.8(c) can induce surface plasmon resonance [97] or lossy mode resonance [98], which can be used to design highly sensitive bio-chemical sensors. SMS optical fiber interferometers shown in Fig. 1.8(d) have been widely investigated as refractometers, temperature and curvature sensors [99,100].

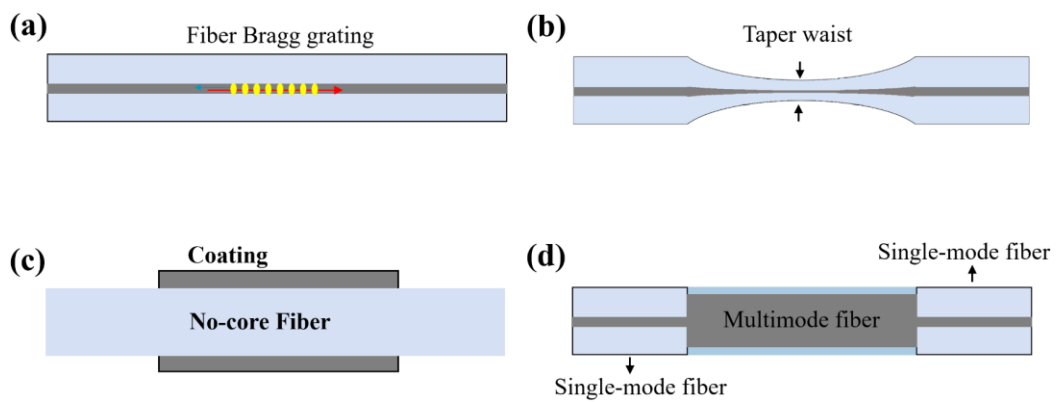


**Figure 1.8** Schematics of (a) fiber Bragg grating, (b) tapered fiber, (c) coated fiber, and (d) SMF-MMF-SMF hetero-structure.

## 1.2 Optical fiber classification

The rapid development of fiber optics over the past decades has been underpinned by various designs of the optical fibers and by the rapid improvement of the understanding of the waveguiding mechanisms and associated models. Although there are many types of optical fibers, with different cross-section profiles, almost all optical fibers can be classified into four basic fiber model types with distinct refractive index profiles as shown in Fig. 1.9.

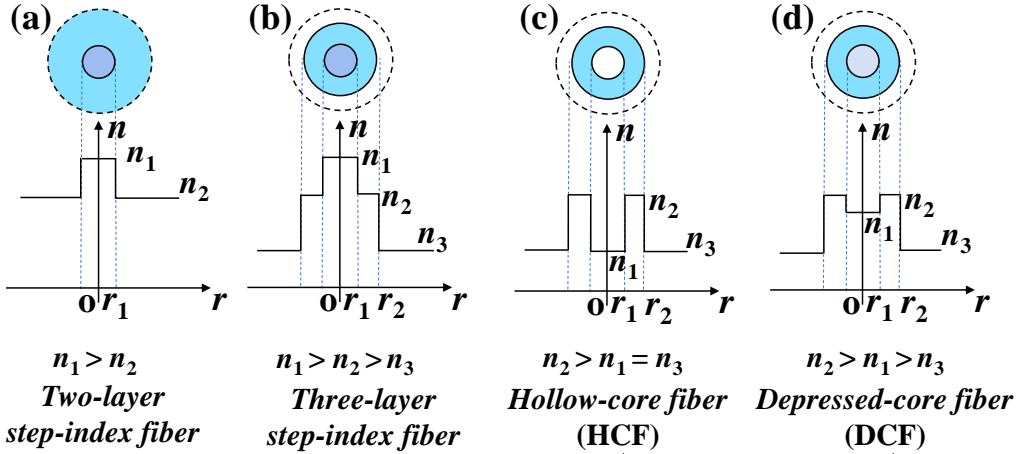


**Figure 1.9** The index profiles of (a) two-layer step-index fiber, (b) three-layer step-index fiber, (c) hollow-core fiber (HCF), and (d) depressed-core fiber (DCF).

- **Two-layer step-index fiber**

Figure 1.9(a) illustrates a two-layer step-index fiber model, consisting of a high-index core and an infinite cladding, where the refractive indices of the core and the cladding region are  $n_1$  and  $n_2$ , with  $n_1 > n_2$ . The two-layer step-index fiber model is a logical starting model for modal analysis, which can be used to represent un-cladded fibers, conventional step-index SMFs and MMFs in the case that only the core modes are considered.

- **Three-layer step-index fiber**

Core modes play a key role in carrying energy or information, while the cladding modes are more important in fiber optic sensing, high-power double-cladded fiber lasers and amplifiers. Therefore, in addition to the core modes, an intuitive interpretation of the qualitative and quantitative characteristics of cladding modes is important. To study the cladding modes, a more complex three-layer step-index fiber model shown in Fig. 1.9(b) is required, where the first finite cladding region with the radius of  $r_2$  is surrounded by an infinite second cladding

region. The relationship between the refractive indices in the three-layer step-index fiber model is  $n_1 > n_2 > n_3$  ( $n_3$  is the refractive index of the second cladding region).

The cladding region of the conventional SMF and MMF (without protective polymer coating) can support multiple cladding modes. Unfortunately, cladding modes usually coexist alongside with the core modes, making it impossible for the cladding modes to be studied independently from the core modes. If the radius of the core in a three-layer step-index fiber is small enough, as in the case of a small-core fiber (SCF), the core mode will be cancelled out leaving only the cladding modes [101,102]. Therefore, the SCF provides a unique opportunity for experimentally investigation of pure cladding modes in fiber optics.

The SCF is in effect a bridge between the no-core fiber (NCF) and the SMF from the point of view of the index profile. The fundamental mode in both no-core fiber and SMF is a core-type mode while in a SCF the fundamental mode is a cladding-type mode. Increasing the core radius of the small-core fiber will lead to transfer of the fundamental mode from a cladding-type to a core-type as the cutoff condition is met.

Overall, the investigation of the three-layer step-index fiber especially the SCF can deepen the understanding of the cladding modes.

- **Three-layer hollow-core fiber**

The refractive index of the core region can be smaller than that of the cladding region, especially for most of novel fibers such as the photonic bandgap fiber

[19], inhibited-coupling fiber [20] and anti-resonant fiber [21]. The fiber with a low-index core and a high-index finite cladding is a three-layer inverted-index fiber. The tube-type hollow-core fiber (HCF) with  $n_2 > n_1 = n_3$  shown in the Fig. 9(c) is the simplest optical fiber with a three-layer inverted-index profile.

The waveguiding in the conventional step-index fibers with  $n_1 > n_2$  shown in Figs. 1.9(a) and 1.9(b) is based on total internal reflection effect. Compared to the conventional step-index fibers, the waveguiding mechanism in the three-layer HCFs is expected to be based on the anti-resonance effect [21].

- **Three-layer depressed-core fiber**

Figure 1.9(d) shows another kind of three-layer inverted-index fiber named as a depressed-core fiber (DCF) with  $n_2 > n_1 > n_3$ . For a DCF the core refractive index is lower than the next outermost region but does not need to take on the lowest or minimum value in a three-layer fiber model as in the HCF shown in Fig. 1.9(c).

DCFs have been studied for various applications including pulse compression in fiber lasers [103-105], generation of supercontinuum [106] and top-hat beams [107], due to their manageable waveguide dispersion and exceptional modal field changes. The DCF can represent a high-index material coated fiber structure, such as the lossy mode resonance (LMR) fiber structures [108]. LMR fiber structures have been extensively studied as a key element of the design of various devices such as optical sensors, filters and modulators. The analysis of the DCF can contribute to a better understanding of the resonant phenomenon in LMR fiber structures.

The three-layer DCF (Fig. 1.9(d)) is in effect a bridge between the conventional three-layer step-index fiber (Fig. 1.9(b)) and the tube-type HCF (Fig. 1.9(c)) from the point of view of the index profile. The investigation of the DCF can deepen the understanding of the mode properties in the three-layer inverted-index fibers and their difference compared to the modes in the conventional step-index fibers and the HCFs.

### **1.3 Aim and objectives of the research**

The investigation of the waveguiding characteristics in these four basic fiber types in Fig. 1.9 is important for the understanding of the fibers with more complex structures. However, a complete modal dispersion diagram for neither the DCF nor the three-layer step-index fiber has ever been reported in the literature to date, although the modal characteristics equations have been derived by several different groups [109-111].

The primary aim of research presented in this thesis is to

**Investigate the three-layer step-index optical fiber and the three-layer depressed-core fiber from a modal and spectral perspective and to develop high performance fiber optic devices based on these types of fibers.**

The objectives of this research are:

- To develop deep understanding of the mode transitions between the core and the cladding type modes of a three-layer step-index fiber by calculating and analyzing the dispersion diagram of such fiber.

- To experimentally investigate the self-imaging characteristics of cladding modes in the SCFs, in comparison with those of the core modes.
- To develop waveguiding mechanisms of inverted-index optical fibers by constructing and simulating dispersion diagram for the three-layer DCFs.
- To experimentally investigate the transmission spectral characteristics of the DCFs in comparison with other type of fibers.
- To investigate the spectral response of the SCFs and DCFs to external stimulus such as temperature and fiber bending for applications.

## **1.4 Research methodology**

The findings presented in this thesis are a result of a combination of numerical and analytical simulations along with experimental investigations. The fiber types employed in the research include NCFs, SCFs and polymer-coated NCFs (PC-NCFs, in effect represents DCFs). The research methodology employed was as follows:

**1) Acquire a fundamental knowledge of the operation of optical waveguides, along with relevant experimental and simulation methods.**

The optical fiber interferometer based on a fiber hetero-structure: SMF-MMF-SMF (SMS) has been widely investigated and applied in sensing and waveguide devices. Therefore the SMS structure was chosen as a good starting point for studies of multimode interference phenomenon and its relation to the modal properties of conventional MMFs.

## **2) Experimental investigations.**

In the experiments a SCF, an NCF and a PC-NCF were used as a replacement for the MMF in an SMS structure, to form the SMF-SCF-SMF (SSCS), the SMF-NCF-SMF (SNCS) and the SMF-PC-NCF-SMF (PC-SNCS) structures.

## **3) Numerical simulations to verify the experimental results and to determine the general rules which describe the experimental phenomenon.**

The numerical simulations for calculating the transmission spectrum of the SSCS and SNCS structures were performed by the scalar Beam Propagation Method (BPM). The scalar BPM simulations were followed by the full-vector Finite Element Method (FEM) simulations in order to calculate the modal dispersion diagrams of the three-layer step-index fibers and the three-layer DCFs.

## **4) Analytical derivation of the corresponding dispersion diagrams with a comparison to the numerical results.**

In order to get a clear understanding of the waveguiding mechanisms in the three-layer SCF and the three-layer DCF, an analytical method of solving the eigenvalue equation of the three-layer fiber was developed and employed.

## **5) Modify the fiber parameters and investigate the corresponding changes of the modal and spectral characteristics.**

The modifications of fiber parameters (states) can change the modal and spectral characteristics, which bring opportunities to the design of fiber optic sensors and devices.

## 1.5 Structure of the thesis

The content of the chapters is briefly outlined below:

- Chapter 2 presents the fundamentals of light guiding mechanisms including total internal reflection, anti-resonance, inhibited coupling, photonic bandgap, and their typical dispersion diagrams. This chapter also briefly describes the different waveguide analysis methods such as the analytical method, the BPM and the FEM.
- Chapter 3 presents the dispersion diagram of a three-layer step-index optical fiber, calculated by both the full-vector FEM and the analytical method. The distributions of the cladding modes and the transitions between the core and cladding modes are analyzed.
- Chapter 4 presents the study of the self-imaging phenomenon for the cladding modes in small-core optical fiber interferometers. The analytical and numerical simulations and experiments show that unlike the self-imaging of core modes, self-imaging of cladding modes only appears at a set of discrete positions along the interferometer axis with an equal spacing corresponding to some discrete values of fiber core radius. This is the first observation of the discrete self-imaging effect in multimode waveguides.
- Chapter 5 presents the dispersion diagram of a DCF obtained by solving the full-vector eigenvalue equations and analyzed using the theory of the anti-resonant and the inhibited coupling mechanisms. An asymmetric planar anti-resonant reflecting optical waveguide (asymmetric planar ARROW) model is proposed.

- Chapter 6 presents the study of the transmission spectra of the straight and bent PC-NCFs, which are measured and analyzed from a modal dispersion perspective. The study details the general principles of the anti-resonant, inhibited coupling and total internal reflection guidance in the formation of the transmission loss dips in fiber optics.
- Chapter 7 presents a high-sensitivity temperature sensor fabricated by a bent SMF-PC-NCF-SMF hetero-structure. It shows that the bending of fiber can suppress the multimode interference and can break the spectral superposition, resulting in the dominance of the anti-resonance of an individual mode and thus periodic sharp transmission dips in the spectrum.
- Chapter 8 presents the key conclusions from the research undertaken and the thesis and suggests some possible future research related to possible practical applications of the three-layer SCFs and DCFs.

## 1.6 Reference

- [1] J. Hecht, *City of Light: The Story of Fiber Optic*, (Oxford University Press, 2004).
- [2] H. H. Hopkins, and N. Singh Kapany, “A flexible fiberscope, using static scanning,” *Nature*, vol. 173, no. 4392, pp. 39-41, 1954.
- [3] V. Heel, A. CS, “A new method of transporting optical images without aberrations,” *Nature*, vol. 173, no. 4392, pp. 39-39, 1954.
- [4] K. C. Kao, and G. A. Hockham, “Dielectric-fiber surface waveguides for optical frequencies,” In *Proceedings of the Institution of Electrical Engineers*, vol. 113, no. 7, pp. 1151-1158, 1966.
- [5] F. P. Kapron, D. B. Keck, and R. D. Maurer, “Radiation losses in glass optical waveguides,” *Appl. Phys. Lett.*, vol. 17, no. 10, pp. 423-425, 1970.
- [6] I. Lee, editor. *Handbook of research on telecommunications planning and management for business*, (IGI Global, 2009).

- [7] S. D. Personick, *Fiber optics: technology and applications*, (Springer Science & Business Media, 2013).
- [8] E. Agrell, M. Karlsson, A. R. Chraplyvy, D. J. Richardson, P. M. Krummrich, P. Winzer, K. Roberts *et al.*, “Roadmap of optical communications,” *J. Opt.*, vol. 18, no. 6, p. 063002, 2016.
- [9] R. Olshansky, and D. B. Keck, “Pulse broadening in graded-index optical fibers,” *Appl. Opt.*, vol. 15, no. 2, pp. 483-491, 1976.
- [10] T. Li, “Advances in optical fiber communications: An historical perspective,” *IEEE J. Sel. Areas in Communications*, vol. 1, no. 3, pp. 356-372, 1983.
- [11] T. Li, “The impact of optical amplifiers on long-distance lightwave telecommunications,” *Proceedings of the IEEE*, vol. 81, no. 11, pp. 1568-1579, 1993.
- [12] A. R. Chraplyvy, A. H. Gnauck, R. W. Tkach, and R. M. Derosier, “8-10 Gb/s transmission through 280 km of dispersion-managed fiber,” *IEEE Photon. Technol. Lett.*, vol. 5, no. 10, pp. 1233-1235, 1993.
- [13] R.-J. Essiambre, G. Kramer, P. J. Winzer, G. J. Foschini, and B. Goebel, “Capacity limits of optical fiber networks,” *J. Lightw. Technol.*, vol. 28, no. 4, pp. 662-701, 2010.
- [14] D. J. Richardson, J. M. Fini, and Lynn E. Nelson, “Space-division multiplexing in optical fibers,” *Nat. Photonics*, vol. 7, no. 5, p. 354, 2013.
- [15] G. Li, N. Bai, N. Zhao, and C. Xia, “Space-division multiplexing: the next frontier in optical communication,” *Adv. Opt. Photon.*, vol. 6, no. 4, pp. 413-487, 2014.
- [16] S. Berdagué, and P. Facq, “Mode division multiplexing in optical fibers,” *Appl. Opt.*, vol. 21, no. 11, pp. 1950-1955, 1982.
- [17] P. Sillard, M. Bigot-Astruc, and D. Molin, “Few-mode fibers for mode-division-multiplexed systems,” *J. Lightw. Technol.*, vol. 32, no. 16, pp. 2824-2829, 2014.
- [18] P. Sillard, D. Molin, M. Bigot-Astruc, A. Amezcua-Correa, K. D. Jongh, and F. Achten, “50  $\mu\text{m}$  multimode fibers for mode division multiplexing,” *J. Lightw. Technol.*, vol. 34, no. 8, pp. 1672-1677, 2016.

- [19] R. F. Cregan, B. J. Mangan, J. C. Knight, T. A. Birks, P. St J. Russell, P. J. Roberts, and D. C. Allan, “Single-mode photonic band gap guidance of light in air,” *Science*, vol. 285, no. 5433, pp. 1537-1539, 1999.
- [20] B. Debord, A. Amsanpally, M. Chafer, A. Baz, M. Maurel, J. M. Blondy, E. Hugonnot *et al.*, “Ultralow transmission loss in inhibited-coupling guiding hollow fibers,” *Optica*, vol. 4, no. 2, pp. 209-217, 2017.
- [21] N. M. Litchinitser, A. K. Abeeluck, C. Headley, and B. J. Eggleton, “Antiresonant reflecting photonic crystal optical waveguides,” *Opt. Lett.*, vol. 27, no. 18, pp. 1592-1594, 2002.
- [22] F. Poletti, M. N. Petrovich, and D. J. Richardson, “Hollow-core photonic bandgap fibers: technology and applications,” *Nanophotonics*, vol. 2, no. 5-6, pp. 315-340, 2013.
- [23] S.-F. Gao, Y-Y Wang, W. Ding, D.-L. Jiang, S. Gu, X. Zhang, and P. Wang, “Hollow-core conjoined-tube negative-curvature fiber with ultralow loss,” *Nat. Commun.*, vol. 9, no. 1, pp. 1-6, 2018.
- [24] E. Snitzer, “Optical maser action of Nd+3 in a barium crown glass,” *Phys. Rev. Lett.*, vol. 7, no. 12, pp. 444–446, 1961.
- [25] E. Snitzer, “Proposed fiber cavities for optical masers,” *J. Appl. Phys.*, vol. 32, no. 1, pp. 36-39, 1961.
- [26] T. H. Maiman, “Stimulated optical radiation in ruby,” *Nature*, vol. 187, no. 4736, pp. 493-494, 1960.
- [27] J. Stone, and C\_A Burrus, “Neodymium-doped silica lasers in end-pumped fiber geometry,” *Appl. Phys. Lett.*, vol. 23, no. 7, pp. 388-389, 1973.
- [28] S. B. Poole, D. N. Payne, and M. E. Fermann, “Fabrication of low-loss optical fibers containing rare-earth ions,” *Electron. Lett.*, vol. 21, no. 17, pp. 737-738, 1985.
- [29] R. Mears, L. Reekie, I. M. Jauncey, and D. N. Payne, “Low-noise erbium-doped fiber amplifier operating at  $1.54\mu\text{m}$ ,” *Electron. Lett.*, vol. 23, pp. 1026–1028, 1987.
- [30] E. Desurvire, J. R. Simpson, and P. C. Becker, “High-gain erbium-doped traveling-wave fiber amplifier,” *Opt. Lett.*, vol. 12, no. 11, pp. 888–890, 1987.

- [31] R. J. Mears, and S. R. Baker, “Erbium fiber amplifiers and lasers,” *Opt. Quantum Electron.*, vol. 24, no. 5, pp. 517-538, 1992.
- [32] M. S. Ab-Rahman, “A review of the configuration and performance limitation parameters in optical amplifiers,” *Optica Applicata*, vol. 44, no. 2, pp. 251-266, 2014.
- [33] E. Snitzer, H. Po, F. Hakimi, R. Tumminelli, and B. C. McCollum, “Double clad, offset core Nd fiber laser,” In *Optical fiber sensors*, p. PD5. OSA, 1988.
- [34] [https://en.wikipedia.org/wiki/Double-clad\\_fiber](https://en.wikipedia.org/wiki/Double-clad_fiber)
- [35] D. J. Richardson, J. Nilsson, and W. A. Clarkson, “High power fiber lasers: current status and future perspectives,” *JOSA B*, vol. 27, no. 11, pp. B63-B92, 2010.
- [36] M. N. Zervas, and C. A. Codemard, “High power fiber lasers: a review,” *IEEE J. Sel. Top. Quantum Electron.*, vol. 20, no. 5, pp. 219-241, 2014.
- [37] C. Jauregui, J. Limpert, and A. Tünnermann, “High-power fiber lasers,” *Nat. Photonics*, vol. 7, no. 11, p. 861, 2013.
- [38] A. Kobyakov, M. Sauer, and D. Chowdhury, “Stimulated Brillouin scattering in optical fibers,” *Adv. Opt. Photon.*, vol. 2, no. 1, pp. 1-59, 2010.
- [39] K. J. Blow, and D. Wood, “Theoretical description of transient stimulated Raman scattering in optical fibers,” *IEEE J. Quantum Electron.*, vol. 25, no. 12, pp. 2665-2673, 1989.
- [40] G. Fibich, and A. L. Gaeta, “Critical power for self-focusing in bulk media and in hollow waveguides,” *Opt. Lett.*, vol. 25, no. 5, pp. 335–337, 2000.
- [41] A. V. Smith, and J. J. Smith. “Mode instability in high power fiber amplifiers,” *Opt. Express*, vol. 19, no. 11, pp. 10180-10192, 2011.
- [42] M. N. Zervas, “Transverse mode instability analysis in fiber amplifiers,” In *Fiber Lasers XIV: Technology and Systems*, vol. 10083, p. 100830M. International Society for Optics and Photonics, 2017.
- [43] C. Jauregui, C. Stihler, and J. Limpert, “Transverse mode instability,” *Adv. Opt. Photon.*, vol. 12, no. 2, pp. 429-484, 2020.

- [44] J. P. Koplow, D. AV Kliner, and L. Goldberg, “Single-mode operation of a coiled multimode fiber amplifier,” Opt. Lett., vol. 25, no. 7, pp. 442-444, 2000.
- [45] J. M. Fini, and S. Ramachandran, “Natural bend-distortion immunity of higher-order-mode large-mode-area fibers,” Opt. Lett., vol. 32, no. 7, pp. 748-750, 2007.
- [46] T. T. Alkeskjold, M. Laurila, J. Weirich, M. M. Johansen, C. B. Olausson, O. Lumholt, D. Noordegraaf, M. D. Maack, and C. Jakobsen, “Photonic crystal fiber amplifiers for high power ultrafast fiber lasers,” Nanophotonics, vol. 2, no. 5-6, pp. 369-381, 2013.
- [47] F. Stutzki, F. Jansen, T. Eidam, A. Steinmetz, C. Jauregui, J. Limpert, and A. Tünnermann, “High average power large-pitch fiber amplifier with robust single-mode operation,” Opt. Lett. vol. 36, no. 5, pp. 689-691, 2011.
- [48] J. Limpert, F. Stutzki, F. Jansen, H.-J. Otto, T. Eidam, C. Jauregui, and A. Tünnermann, “Yb-doped large-pitch fibers: effective single-mode operation based on higher-order mode delocalisation,” Light: Sci. Appl., vol. 1, no. 4, pp. e8-e8, 2012.
- [49] F. Stutzki, F. Jansen, H.-J. Otto, C. Jauregui, J. Limpert, and A. Tünnermann, “Designing advanced very-large-mode-area fibers for power scaling of fiber-laser systems,” Optica, vol. 1, no. 4, pp. 233-242, 2014.
- [50] M. M. Vogel, M. Abdou-Ahmed, A. Voss, and T. Graf, “Very-large-mode-area, single-mode multicore fiber,” Opt. Lett., vol. 34, no. 18, pp. 2876-2878, 2009.
- [51] D. Jain, C. Baskiotis, and J. K. Sahu, “Mode area scaling with multi-trench rod-type fibers,” Opt. Express, vol. 21, no. 2, pp. 1448-1455, 2013.
- [52] P. Uebel, M. C. Günendi, M. H. Frosz, G. Ahmed, N. N. Edavalath, J.-M. Ménard, and P. St J. Russell, “Broadband robustly single-mode hollow-core PCF by resonant filtering of higher-order modes,” Opt. Lett. vol. 41, no. 9, pp. 1961-1964, 2016.
- [53] G. Berci, and K. A. Forde, “History of endoscopy,” Surgical endoscopy, vol. 14, no. 1, p. 5, 2000.

- [54] B. A. Flusberg, E. D. Cocker, W. Piyawattanametha, J. C. Jung, E. LM Cheung, and M. J. Schnitzer, “Fiber-optic fluorescence imaging,” *Nat. Methods*, vol. 2, no. 12, pp. 941-950, 2005.
- [55] M. Hughes, T. P. Chang, and G.-Z. Yang, “Fiber bundle endocytoscopy,” *Biomedical Opt. Express*, vol. 4, no. 12, pp. 2781-2794, 2013.
- [56] A. Orth, M. Plöschner, E. R. Wilson, I. S. Maksymov, and B. C. Gibson, “Optical fiber bundles: Ultra-slim light field imaging probes,” *Science Adv.*, vol. 5, no. 4, p. eaav1555, 2019.
- [57] Y. Choi, C. Yoon, M. Kim, T. D. Yang, C. Fang-Yen, R. R. Dasari, K. J. Lee, and W. Choi, “Scanner-free and wide-field endoscopic imaging by using a single multimode optical fiber,” *Phys. Rev. Lett.*, vol. 109, no. 20, p. 203901, 2012.
- [58] A. M. Caravaca-Aguirre, and R. Piestun, “Single multimode fiber endoscope,” *Opt. Express*, vol. 25, no. 3, pp. 1656-1665, 2017.
- [59] L. V. Amitonova, and J. F. De Boer, “Compressive imaging through a multimode fiber,” *Opt. Lett.*, vol. 43, no. 21, pp. 5427-5430, 2018.
- [60] L. V. Amitonova, and J. F. de Boer, “Endo-microscopy beyond the Abbe and Nyquist limits,” *Light: Sci. Appl.*, vol. 9, no. 1, pp. 1-12, 2020.
- [61] S. Yoon, M. Kim, M. Jang, Y. Choi, W. Choi, S. Kang, and W. Choi, “Deep optical imaging within complex scattering media,” *Nat. Rev. Phys.*, vol. 2, pp. 141-158, 2020.
- [62] T. Čižmár, and K. Dholakia, “Exploiting multimode waveguides for pure fiber-based imaging,” *Nat. Commun.*, vol. 3, no. 1, pp. 1-9, 2012.
- [63] M. Plöschner, T. Tyc, and T. Čižmár, “Seeing through chaos in multimode fibers,” *Nat. Photonics*, vol. 9, no. 8, p. 529, 2015.
- [64] O. Tzang, A. M. Caravaca-Aguirre, K. Wagner, and R. Piestun, “Adaptive wavefront shaping for controlling nonlinear multimode interactions in optical fibers,” *Nat. Photonics*, vol. 12, no. 6, pp. 368-374, 2018.
- [65] N. Borhani, E. Kakkava, C. Moser, and D. Psaltis, “Learning to see through multimode fibers,” *Optica*, vol. 5, no. 8, pp. 960-966, 2018.
- [66] D. McGloin, and K. Dholakia, “Bessel beams: diffraction in a new light,” *Contemporary Phys.*, vol. 46, no. 1, pp. 15-28, 2005.

- [67] K. T. Gahagan, and G. A. Swartzlander, “Simultaneous trapping of low-index and high-index microparticles observed with an optical-vortex trap,” JOSA B, vol. 16, no. 4, pp. 533-537, 1999.
- [68] P. Steinurzel, K. Tantiwanichapan, M. Goto, and S. Ramachandran, “Fiber-based Bessel beams with controllable diffraction-resistant distance,” Opt. Lett., vol. 36, no. 23, pp. 4671-4673, 2011.
- [69] J. Tan, R. Yu, and L. Xiao, “Bessel-like beams generated via fiber-based polymer microtips,” Opt. Lett., vol. 44, no. 4, pp. 1007-1010, 2019.
- [70] S. Sarkar Pal, S. K. Mondal, D. Kumbhakar, R. Kumar, Aparna Akula, Ripul Ghosh, and Randhir Bhatnagar, “Optical fiber antenna generating spiral beam shapes,” Appl. Phys. Lett., vol. 104, no. 3, p. 031105, 2014.
- [71] Y. Li, H. Xin, X. Liu, Y. Zhang, H. Lei, and B. Li, “Trapping and detection of nanoparticles and cells using a parallel photonic nanojet array,” ACS nano, vol. 10, no. 6, pp. 5800-5808, 2016.
- [72] K. T. Gahagan, and G. A. Swartzlander, “Optical vortex trapping of particles,” Opt. Lett., vol. 21, no. 11, pp. 827-829, 1996.
- [73] D. Gao, W. Ding, M. Nieto-Vesperinas, X. Ding, M. Rahman, T. Zhang, C. Lim, and C.-W. Qiu, “Optical manipulation from the microscale to the nanoscale: fundamentals, advances and prospects,” Light: Sci. Appl., vol. 6, no. 9, pp. e17039-e17039, 2017.
- [74] P. Zemánek, G. Volpe, A. Jonáš, and O. Brzobohatý, “Perspective on light-induced transport of particles: from optical forces to phoretic motion,” Adv. Opt. Photonics, vol. 11, no. 3, pp. 577-678, 2019.
- [75] F. M. Fazal, and S. M. Block, “Optical tweezers study life under tension,” Nat. Photonics, vol. 5, no. 6, pp. 318-321, 2011.
- [76] A. Ashkin, J. M. Dziedzic, J. E. Bjorkholm, and Steven Chu, “Observation of a single-beam gradient force optical trap for dielectric particles,” Opt. Lett., vol. 11, no. 5, pp. 288-290, 1986.
- [77] R. S. Rodrigues Ribeiro, O. Soppera, A. G. Oliva, A. Guerreiro, and P. AS Jorge, “New trends on optical fiber tweezers,” J. Lightw. Technol., vol. 33, no. 16, pp. 3394-3405, 2015.
- [78] K. M. Tan, M. Mazilu, T. H. Chow, W. M. Lee, K. Taguchi, B. K. Ng, W. Sibbett, C. S. Herrington, C. T. A. Brown, and K. Dholakia, “In-fiber

- common-path optical coherence tomography using a conical-tip fiber,” Opt. Express, vol. 17, no. 4, pp. 2375-2384, 2009.
- [79] J. K. Kim, J. Kim, Y. Jung, W. Ha, Y. S. Jeong, S. Lee, A. Tünnermann, and K. Oh, “Compact all-fiber Bessel beam generator based on hollow optical fiber combined with a hybrid polymer fiber lens,” Opt. Lett., vol. 34, no. 19, pp. 2973-2975, 2009.
- [80] H. Xin, R. Xu, and B. Li, “Optical trapping, driving, and arrangement of particles using a tapered fiber probe,” Sci. Rep., vol. 2, p. 818, 2012.
- [81] X. Zhu, A. Schülzgen, L. Li, and N. Peyghambarian, “Generation of controllable nondiffracting beams using multimode optical fibers,” Appl. Phys. Lett., vol. 94, no. 20, p. 201102, 2009.
- [82] I. T. Leite, S. Turtaev, X. Jiang, M. Šiler, A. Cuschieri, P. St J. Russell, and T. Čižmár, “Three-dimensional holographic optical manipulation through a high-numerical-aperture soft-glass multimode fiber,” Nat. Photonics, vol. 12, no. 1, pp. 33-39, 2018.
- [83] S. Turtaev, I. T. Leite, T. Altwegg-Boussac, J. MP Pakan, N. L. Rochefort, and T. Čižmár, “High-fidelity multimode fiber-based endoscopy for deep brain *in vivo* imaging,” Light: Sci. Appl., vol. 7, no. 1, pp. 1-8, 2018.
- [84] K. T. V. Grattan, and T. Sun, “Fiber optic sensor technology: an overview,” Sens. Actuators, A, vol. 82, no. 1-3, pp. 40-61, 2000.
- [85] D. A. Krohn, T. MacDougall, and A. Mendez, *Fiber optic sensors: fundamentals and applications*, (SPIE Press, Bellingham, Washington, USA, 2014).
- [86] K. O. Hill, and G. Meltz, “Fiber Bragg grating technology fundamentals and overview,” J. Lightw. Technol., vol. 15, no. 8, pp. 1263-1276, 1997.
- [87] C. Broadway, R. Min, A. G. Leal-Junior, C. Marques, and C. Caucheteur, “Toward commercial polymer fiber Bragg grating sensors: Review and applications,” J. Lightw. Technol., vol. 37, no. 11, pp. 2605-2615, 2019.
- [88] L. Tong, “Micro/nanofiber optical sensors: challenges and prospects,” Sensors, vol. 18, no. 3, p. 903, 2018.
- [89] K. Tian, Y. Xin, W. Yang, T. Geng, J. Ren, Y.-X. Fan, G. Farrell, E. Lewis, and P. Wang, “A curvature sensor based on twisted single-mode–

- multimode-single-mode hybrid optical fiber structure,” J. Lightw. Technol., vol. 35, no. 9, pp. 1725-1731, 2017.
- [90] W. Chen, Z. Chen, Y. Qiu, L. Kong, H. Lin, C. Jia, H. Chen, and H. Li, “Highly sensitive optical fiber curvature sensor based on a seven-core fiber with a twisted structure,” Appl. Opt., vol. 58, no. 32, pp. 8776-8784, 2019.
- [91] C. Elosua, I. R. Matias, C. Bariain, and F. J. Arregui, “Volatile organic compound optical fiber sensors: A review,” Sensors, vol. 6, no. 11, pp. 1440-1465, 2006.
- [92] F. J. Arregui, I. D. Villar, J. M. Corres, J. Goicoechea, C. R. Zamarreño, C. Elosua, M. Hernaez *et al.*, “Fiber-optic lossy mode resonance sensors,” Procedia Engineering, vol. 87, pp. 3-8, 2014.
- [93] L. V. Nguyen, D. Hwang, S. Moon, D. S. Moon, and Y. Chung, “High temperature fiber sensor with high sensitivity based on core diameter mismatch,” Opt. Express, vol. 16, no. 15, pp. 11369-11375, 2008.
- [94] L. Mao, P. Lu, Z. Lao, D. Liu, and J. Zhang, “Highly sensitive curvature sensor based on single-mode fiber using core-offset splicing,” Opt. Laser Technol., vol. 57, pp. 39-43, 2014.
- [95] R. D. Sante, “Fiber optic sensors for structural health monitoring of aircraft composite structures: Recent advances and applications,” Sensors, vol. 15, no. 8, pp. 18666-18713, 2015.
- [96] L. Tong, R. R. G., J. B. Ashcom, S. He, J. Lou, M. Shen, I. Maxwell, and E. Mazur, “Subwavelength-diameter silica wires for low-loss optical wave guiding,” Nature, vol. 426, no. 6968, pp. 816-819, 2003.
- [97] A. K. Sharma, R. Jha, and B. D. Gupta, “Fiber-optic sensors based on surface plasmon resonance: a comprehensive review,” IEEE Sensors J., vol. 7, no. 8, pp. 1118-1129, 2007.
- [98] I. D. Villar, F. J. Arregui, C. R. Zamarreño, J. M. Corres, C. Bariain, J. Goicoechea, C. Elosua *et al.*, “Optical sensors based on lossy-mode resonances,” Sens. Actuators B, vol. 240, pp. 174-185, 2017.
- [99] Q. Wang, and G. Farrell, “All-fiber multimode-interference-based refractometer sensor: proposal and design,” Opt. Lett., vol. 31, no. 3, pp. 317-319, 2006.

- [100] Q. Wu, Y. Semenova, P. Wang, and G. Farrell, “High sensitivity SMS fiber structure based refractometer—analysis and experiment,” *Opt. Express*, vol. 19, no. 9, pp. 7937–7944, 2011.
- [101] A. W. Snyder and J. Love, *Optical waveguide theory*, (Springer Science & Business Media, 2012).
- [102] L. C. Bobb, P. Shankar, and H. D. Krumboltz, “Bending effects in biconically tapered single-mode fibers,” *J. Lightw. Technol.*, vol. 8, no. 7, pp. 1084–1090, 1990.
- [103] A. S. Belanov and S. V. Tsvetkov, “High-index-ring three-layer fibers for mode-locked sub-1.3  $\mu\text{m}$  fiber lasers,” *Quantum Electron.*, vol. 40, no. 2, pp. 160–162, 2010.
- [104] S. S. Aleshkina, M. E. Likhachev, A. K. Senatorov, M. M. Bubnov, M. Y. Salaganskii, and A. N. Guryanov, “Low-loss hybrid fiber with zero dispersion wavelength shifted to 1  $\mu\text{m}$ ,” *Opt. Express*, vol. 21, no. 20, pp. 23838–23843, 2013.
- [105] S. S. Aleshkina, M. V. Yashkov, M. M. Bubnov, A. N. Guryanov, and M. E. Likhachev, “Asymptotically single-mode hybrid fiber for dispersion management near 1  $\mu\text{m}$ ,” *IEEE J. Sel. Topics Quantum Electron.*, vol. 24, no. 3, pp. 1–8, 2017.
- [106] D. Jain, C. Markos, T. M. Benson, A. B. Seddon, and O. Bang, “Exploiting dispersion of higher-order-modes using M-type fiber for application in mid-infrared supercontinuum generation,” *Sci. Rep.*, vol. 9, p. 8536, 2019.
- [107] C. Valentin, P. Calvet, Y. Quiquempois, G. Bouwmans, L. Bigot, Q. Coulombier, M. Douay, K. Delplace, A. Mussot, and E. Hugonnot, “Top-hat beam output of a single-mode microstructured optical fiber: Impact of core index depression,” *Opt. Express*, vol. 21, no. 20, pp. 23250–23260, 2013.
- [108] I. Del Villar, C. R. Zamarreno, M. Hernaez, F. J. Arregui, and I. R. Matias, “Lossy mode resonance generation with indium tin oxide coated optical fibers for sensing applications,” *J. Lightw. Technol.*, vol. 28, pp. 111–117, 2010.

- [109] C. Tsao, *Optical Fiber Waveguide Analysis* (Oxford University Press, New York, 1992).
- [110] T. Erdogan, “Cladding-mode resonances in short- and long-period fiber grating filters,” J. Opt. Soc. Am. A, vol. 14, pp. 1760-1773, 1997.
- [111] Z. Zhang and W. Shi, “Eigenvalue and field equations of three-layered uniaxial fibers and their applications to the characteristics of long-period fiber gratings with applied axial strain,” J. Opt. Soc. Am. A, vol. 22, pp. 2516–2526, 2005.

# **Chapter 2**

## **Waveguiding Mechanisms and Modal Dispersion Diagrams of Optical Fibers**

This chapter describes the fundamental knowledge and insights about waveguiding mechanisms and modal dispersion diagrams in fiber optics needed in subsequent chapters. This chapter also presents computational methods for three-layer fibers including the analytical method, Finite Element Method (FEM) and the Beam Propagation Method (BPM).

### **2.1 Light guiding mechanisms and dispersion diagrams**

As discussed in Chapter 1, in addition to the silica-based step-index fibers such as the SMF and the MMF, a wide variety of new types of optical fibers with generally more complex structures have been developed in recent years. These fiber structures correspond to a variety of waveguiding mechanisms and modal characteristics. In this section the total internal reflection (TIR), photonic bandgap (PBG), inhibited coupling (IC) and the anti-resonant (AR) guiding mechanisms are introduced.

#### **2.1.1 Total internal reflection in two-layer step-index fibers**

Light passing through the interface between two dielectric media obeys the rules of reflection and refraction in ray theory [1-4]. In accordance with Snell's law, the relationship between the angle of incidence ( $\theta_1$ ) for a light beam in the

medium with a refractive index  $n_1$  and the angle of refraction ( $\theta_2$ ) in the medium with  $n_2$  is as follows:

$$\frac{\sin \theta_1}{\sin \theta_2} = \frac{n_2}{n_1} \quad (2.1)$$

If  $n_1 > n_2$ , there is a critical incidence angle  $\theta_c$  making a right angle with the refracted beam ( $\theta_2 = 90^\circ$ ):

$$\theta_c = \sin^{-1} \frac{n_2}{n_1} \quad (2.2)$$

When the incidence angle is greater than  $\theta_c$ , there is no refracted beam and the total internal reflection occurs at the interface between the two dielectric media.

The TIR effect is used as the basis to describe propagation in a conventional step-index optical fiber. As an example Fig. 2.1 shows successive reflections of a beam propagating within a section of a bent unclad silica glass fiber, where the refractive indices of the glass and the surrounding medium are  $n_1$  and  $n_2$ , with  $n_1 > n_2$ . The unclad glass fiber is a two-layer step-index fiber as shown in Fig. 1.9(a). At point P<sub>1</sub>, the incidence angle  $\theta_1$  is equal to the critical angle  $\theta_c$ , the refracted beam travels along the outer boundary of the fiber. At point P<sub>2</sub>, the incidence angle  $\theta_3$  is smaller than  $\theta_c$ , partial light will refract out of the boundary of the fiber. At point P<sub>3</sub>, the incidence angle  $\theta_5$  is larger than  $\theta_c$ , the light will totally reflect into the glass fiber. In this case of TIR, light energy is mainly confined within the fiber. TIR is the fundamental mechanism of light guidance in the conventional step-index optical fibers. Commercial SMF-28, one of the most common fiber types, can maintain TIRs even where the bend radius is small. The

bend loss of the SMF-28 from Corning Inc. is less than 0.5 dB at the wavelength of 1550 nm when the bend radius is equal to 16 mm.

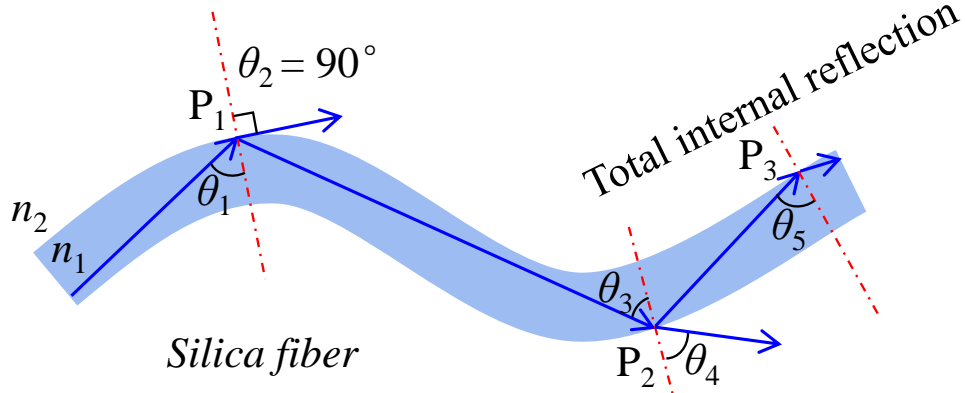


**Figure 2.1** Ray trajectories in a bent silica fiber.

### 2.1.2 Dispersion diagram of two-layer step-index fibers

In conventional MMFs and SMFs, the guided light field in the core region is governed by the TIR at the interface between the core and the cladding of the fibers. The dispersion properties of core modes in MMFs and SMFs can be calculated with a two-layer step-index fiber model as shown in Fig. 1.9(a), where the cladding is considered as an infinite region.

Figure 2.2 shows ray trajectories in a straight MMF and a straight SMF, where one light path represents one optical mode. The MMF can support multiple guided modes represented by multiple light paths, while the SMF supports only one guided mode.

One mode in a 3-dimensional cylindrical fiber can be characterized by one longitudinal propagation constant  $\beta$ , which accounts for the translational invariance of the fiber along its axis. As shown in Fig. 2.2(a), the ray with the

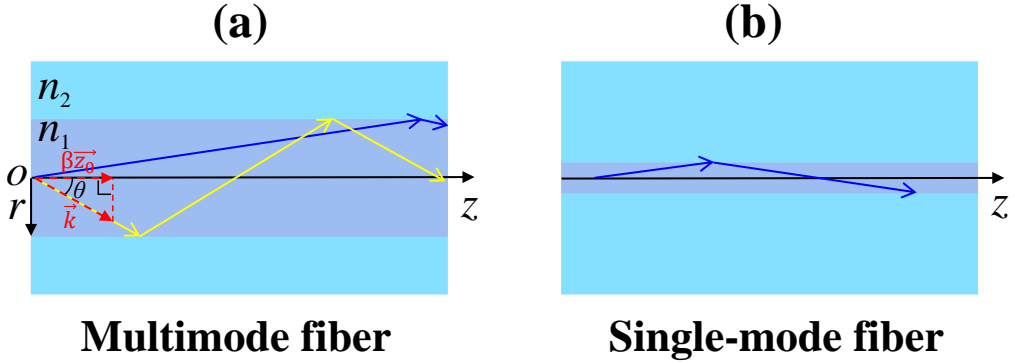


**Figure 2.2** Examples of ray trajectories in (a) a multimode fiber and (b) a single-mode fiber.

wavevector  $\vec{k}$  (shown in yellow) creates a constant angle  $\theta$  with respect to the  $z$ -direction, and its  $\beta$  is determined by:

$$\beta = k \cos \theta = n_1 k_0 \cos \theta \quad (2.3)$$

where  $k_0 = 2\pi/\lambda$  is the wavenumber in vacuum. A mode can also be represented by an effective refractive index  $n_{\text{eff}}$ , defined as

$$n_{\text{eff}} = \frac{\beta}{k_0} = n_1 \cos \theta \quad (2.4)$$

In addition to the longitudinal propagation constant  $\beta$  or  $n_{\text{eff}}$ , in order to fully describe the behaviour of one mode the transverse constants, including the azimuthal mode number ‘m’ and the radial mode number ‘n’, are required. There are four kinds of vector modes to describe the light field in a conventional step-index fiber, known as  $\text{TE}_{0,n}$ ,  $\text{TM}_{0,n}$ ,  $\text{HE}_{m,n}$ , and  $\text{EH}_{m,n}$ . The hybrid HE or EH modes are two-fold degenerate modes. Under the weakly guiding condition ( $n_1 \sim n_2$ ), the longitudinal components of the fields are negligible compared to the transverse ones and the transverse intensity distribution of the degenerated vector modes are almost identical [1-3]. Therefore, the degenerated vector modes can be

simply represented by the linear polarization (LP) scalar modes  $LP_{m,n}$  under the weekly guiding condition.

Figure 2.3(a) shows the dispersion diagram ( $n_{\text{eff}}$  vs.  $r_1$ ) of the core modes in a two-layer step-index fiber, with  $r_2 = \infty$ ,  $n_1 = 1.4504$  and  $n_2 = 1.4447$  at the wavelength of  $\lambda = 1550$  nm (similar to the parameters of SMF-28). In this case,

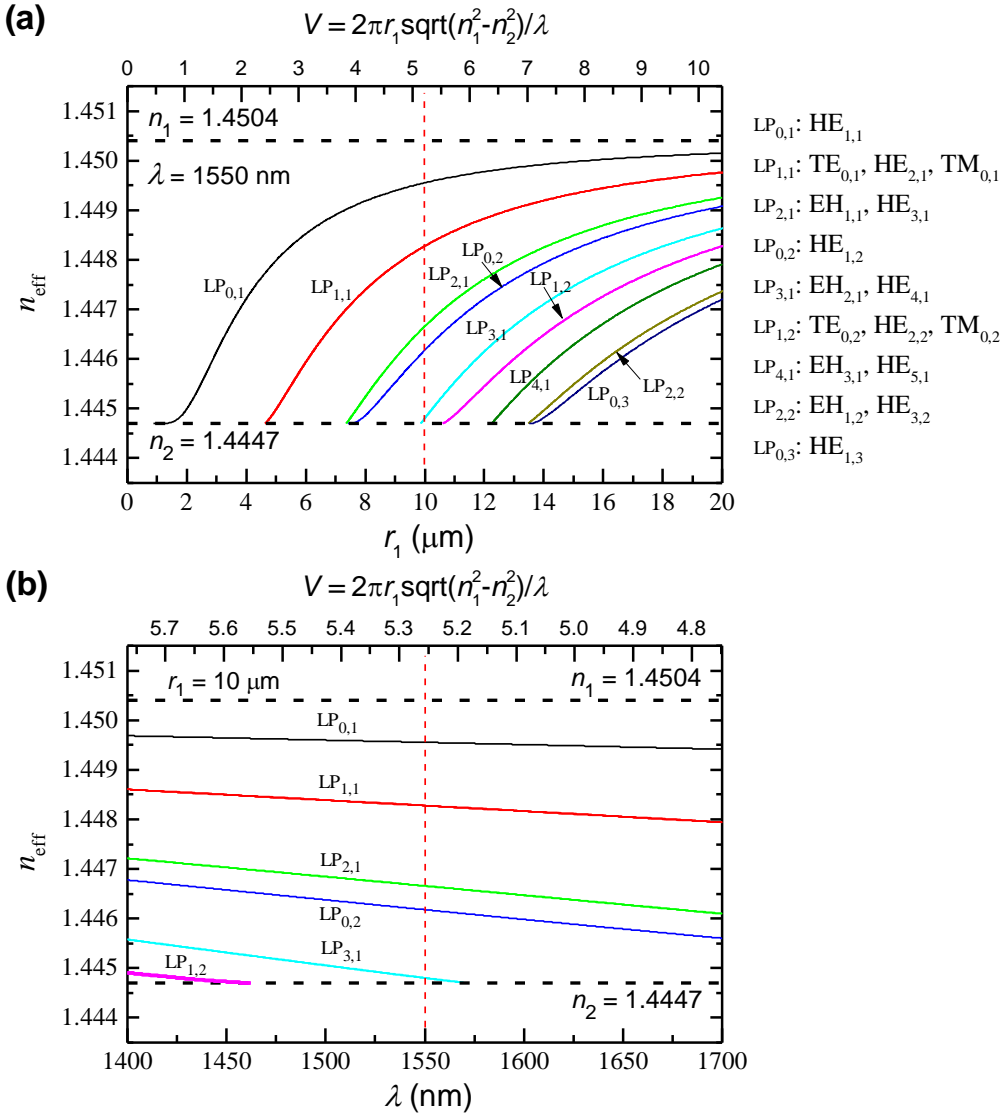


**Figure 2.3** Dispersion diagrams of a two-layer step-index fiber: (a)  $n_{\text{eff}}$  vs.  $r_1$ , where  $n_1 = 1.4504$ ,  $n_2 = 1.4447$  and  $\lambda = 1550$  nm; (b)  $n_{\text{eff}}$  vs.  $\lambda$ , where  $n_1 = 1.4504$ ,  $n_2 = 1.4447$  and  $r_1 = 10 \mu\text{m}$ ,  $r_2 = \infty$ .

the curves of the vector modes overlap with that of scalar LP modes due to weak guiding ( $n_1 \sim n_2$ ). The relationship between the vector and scalar modes is shown on the right from the Fig. 2.3(a).

The  $n_{\text{eff}}$  of the core modes lies between the refractive index of the cladding and the core regions ( $n_2 < n_{\text{eff}} < n_1$ ), as indicated by two black horizontal dashed lines. As the core radius  $r_1$  increases, the number of modes supported by the fiber increases. The total number of core modes ‘N’ in a fiber depends on the  $V$ -parameter, defined as:

$$V = \frac{2\pi r_1}{\lambda} \sqrt{n_1^2 - n_2^2} \quad (2.5)$$

$$N = \frac{V^2}{2} \quad (2.6)$$

The fundamental mode is LP<sub>0,1</sub> or HE<sub>1,1</sub>, which always exists in a two-layer step-index fiber. The cutoff point for LP<sub>1,1</sub> (TE<sub>0,1</sub>, TM<sub>0,1</sub> and HE<sub>2,1</sub>) is at about  $r_1 = 4.618 \mu\text{m}$  ( $V = 2.40483$ ), which is the single-mode condition of the optical fiber. The core radius of the commercial SMF-28 is circa 4.3  $\mu\text{m}$ , smaller than the single-mode cutoff radius. The example of SMF-28 indicates that a modal dispersion diagram plays an important role in the design of optical fibers.

The  $n_{\text{eff}}$  also changes with the wavelength  $\lambda$ . Figure 2.3(b) shows the dispersion diagram ( $n_{\text{eff}}$  vs.  $\lambda$ ) of core modes in a step-index fiber, with  $n_1 = 1.4504$ ,  $n_2 = 1.4447$ , and  $r_1=10 \mu\text{m}$ . As can be seen from the diagram, at 1550 nm, the optical fiber supports 16 vector modes. At 1400 nm, the optical fiber supports 20 vector modes.

### 2.1.3 Anti-resonant guiding and dispersion diagram

Figure 2.4(a) shows a tube-type HCF, consisting of an air core, a tube-type first cladding with an outside air acting as a second cladding, which is one of the simplest fiber designs with a three-layer inverted index profile. Due to the fact that the refractive index of the core is smaller than that of the cladding, TIR is not present in the case of the HCF, as shown in Fig. 2.4(b). Rays incident from the core to the cladding will partially refract into the cladding, regardless of the incident angle  $\theta_1$ . The rays experience multiple successive reflections and refractions at both the inner and outer boundaries of the tube-type (first) cladding.

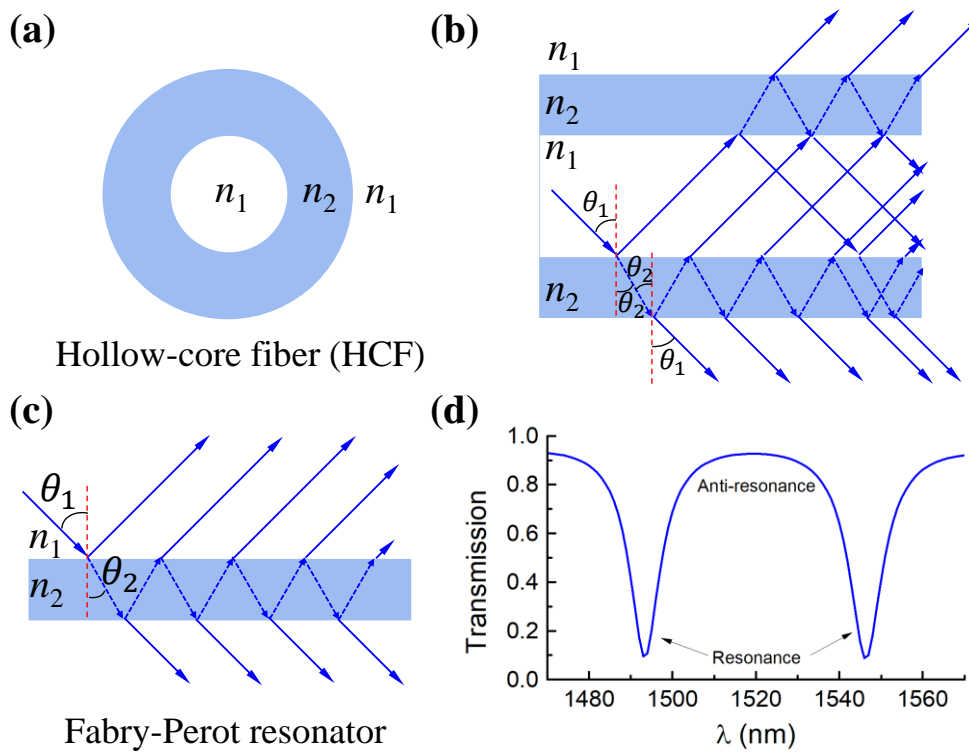


**Figure 2.4** (a) and (b) show the cross-section of the refractive index profile and the ray trajectories within the tube-type HCF, respectively. (c) and (d) show respectively the ray trajectories and the reflection spectrum of a Fabry-Perot resonator.

During this process, the light partially leaks out through the outer boundary of the tube-type cladding with the same angle  $\theta_1$  as the incident ray, due to the presence of the same medium (air) at both sides of the tube-type cladding.

The tube-type cladding of the HCF can be seen as analogous to those in a Fabry-Perot resonator as shown in Fig. 2.4(c) [5,6]. The symmetric planar waveguide acts as a Fabry-Perot resonator, where the anti-resonant light is reflected back while the resonant light is allowed to propagate forward, forming a reflected spectrum with periodic transmission dips and windows, as shown in Fig. 2.4(d).

Similarly, the tube-type HCF can confine the light energy in the air core when the anti-resonance occurs in the high-index tube-type cladding in a range of light wavelength away from the resonance. The guiding mechanism in the tube-type HCFs can be described by the anti-resonant reflecting optical waveguide (ARROW) model [5,6]. In this model, the resonant wavelengths can be determined by Eq. (2.7).

$$\lambda_m = \frac{2d}{m} \sqrt{n_2^2 - n_1^2}, m = 1, 2, \dots \quad (2.7)$$

where  $d$  is the thickness of the first cladding.

Light propagating within a tube-type HCF has a complex propagation constant  $\beta$ , as follows,

$$\beta = \beta_r + j\beta_i \quad (2.8)$$

where the real part  $\beta_r$  represents the longitudinal propagation constant and the imaginary part  $\beta_i$  corresponds to the modal attenuation. The complex propagation constant  $\beta$  corresponds to the complex effective refractive index:

$$n_{\text{eff}} = Re(n_{\text{eff}}) + jIm(n_{\text{eff}}) \quad (2.9)$$

Figure 2.5 shows the dispersion curves of the real and imaginary parts of the  $n_{\text{eff}}$  of three lowest-order core modes in a tube-type HCF with  $r_1 = 20 \mu\text{m}$ ,  $d = 0.7 \mu\text{m}$ ,  $n_1 = 1$  and  $n_2 = 1.45$ , calculated based on the reflection of a wave in a single planar waveguide [7]. These curves have discontinuities at the resonant wavelengths, which is a distinct characteristic compared to that of the step-index optical fiber as shown in Fig. 2.3(b). The resonant bands and the anti-resonant bands correspond to the dips and windows of the transmission spectrum, respectively. The nomenclature and mode profiles of the core modes in the middle region of the anti-resonant bands are similar to those of the step-index optical fibers [8,9].

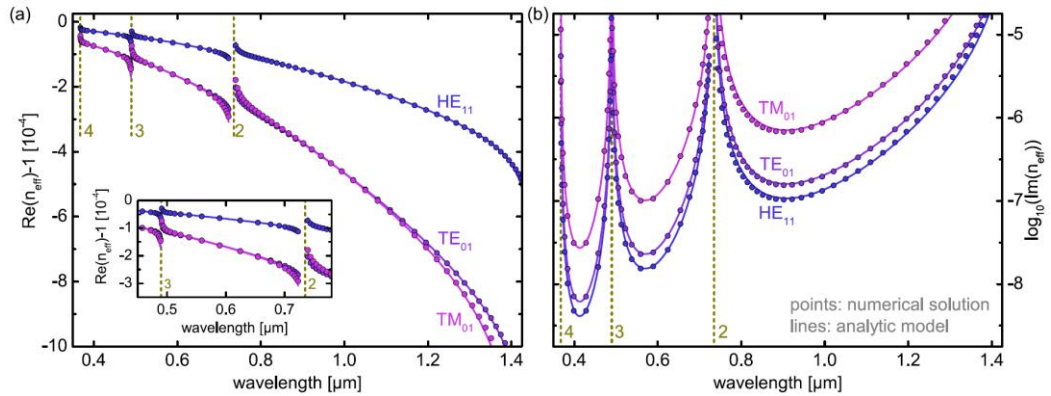


**Figure 2.5** Dispersion curves of the real (a) and imaginary (b) parts of the effective mode index of three lowest-order core modes supported by the tube-type HCF. In both plots, the dark yellow vertical dashed lines indicate the resonances with the corresponding order. (Figure is reproduced from M. Zeisberger and M. A. Schmidt, Sci. Rep., vol. 7, no.1, pp. 1-13, 2017)

## 2.1.4 Photonic bandgap guiding and dispersion diagram

The concept of PBG in optics is analogous to the concept of electronic bandgap in semiconductor physics, which originates from the periodic arrangement of two different dielectrics (namely, photonic crystals) and describes a range of frequencies where the propagation of photons is forbidden in the structure [10-12]. In 1991 Philip Russell conceived the idea of a hollow-core waveguide based on a 2D out-of-plane PBG [13,14]. The PBG formed in the periodic photonic crystal structure of the fiber cladding provides an opportunity to confine the light in a low-index (air) core, avoiding the need for TIR.

The dispersion curves and spectral characteristics of a PBF can be seen in Fig. 2.6. Fig. 2.6(a) shows the cross section of a solid-core PBF, consisting of a cladding region with periodic high-index Ge-doped rods embedded in a low-index pure-glass foundation and a central core region in form of a low-index site resulting from a missing rod [15,16]. Fig. 2.6(b) shows a hexagonal unit cell of the photonic crystal.

Figure 2.6(c) shows the band structure of the solid-core PBF. The grey bands of the density of photonic states (DOPS) are separated by the red bandgaps. The yellow curve in the bandgaps is the “fundamental” guided core mode. The transmission windows and the high-loss dips shown in Fig. 2.6(d) correspond to the periodic bandgaps and the bands of high photonic density of states (Fig. 2.6(c)), respectively.

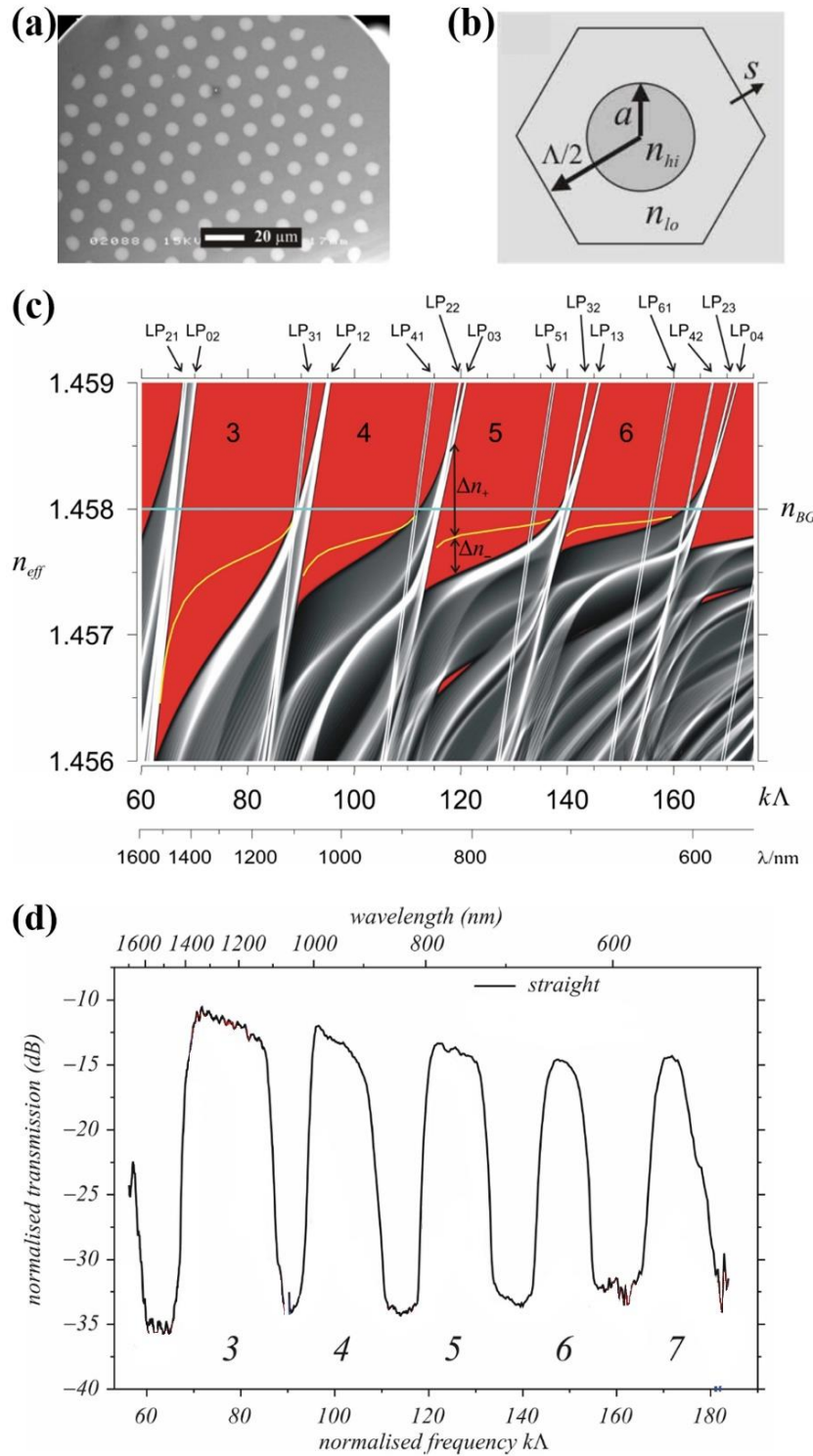


**Figure 2.6** (a) SEM image of a bandgap fiber. (b) A rod in a hexagonal unit cell. (c) Plots of band structure for the bandgap fiber. The bandgaps are shown in red. The rod modes from which the bands arise are labelled along the top. The yellow curve is the “fundamental” core-guided mode. (d) Transmission spectra of 2 m of the fiber. (Figure is modified from T. A. Briks *et al.*, Opt. Express, vol. 14, no. 12, pp. 5688-5698, 2006 and T. A. Briks *et al.* Opt. Express, vol. 14, no. 20, pp. 9483-9490)

### 2.1.5 Inhibited coupling guiding and dispersion diagram

Another guiding mechanism was proposed in the Kagomé lattice hollow-core photonic crystal fibers (HC-PCFs) invented by Benabid *et al.* (2002) [17], as shown in Figs. 2.7(a)-2.7(c) [18]. The Kagomé lattice exhibits no bandgap in its dispersion diagram but does possess periodic low and high DOPS bands, as shown in Fig. 2.7(d). The low and high DOPS bands correspond to low-loss and high-loss transmission bands of the measured spectrum as shown in Fig. 2.7(e). Figs. 2.7(f) and 2.7(g) show the real and imaginary part for the  $n_{\text{eff}}$  of the HE<sub>1,1</sub>-like core mode, respectively. The bands with large imaginary part of  $n_{\text{eff}}$  correspond to high transmission loss bands in Fig. 2.7(e), while the bands with the small imaginary part for  $n_{\text{eff}}$  correspond to low transmission loss bands.

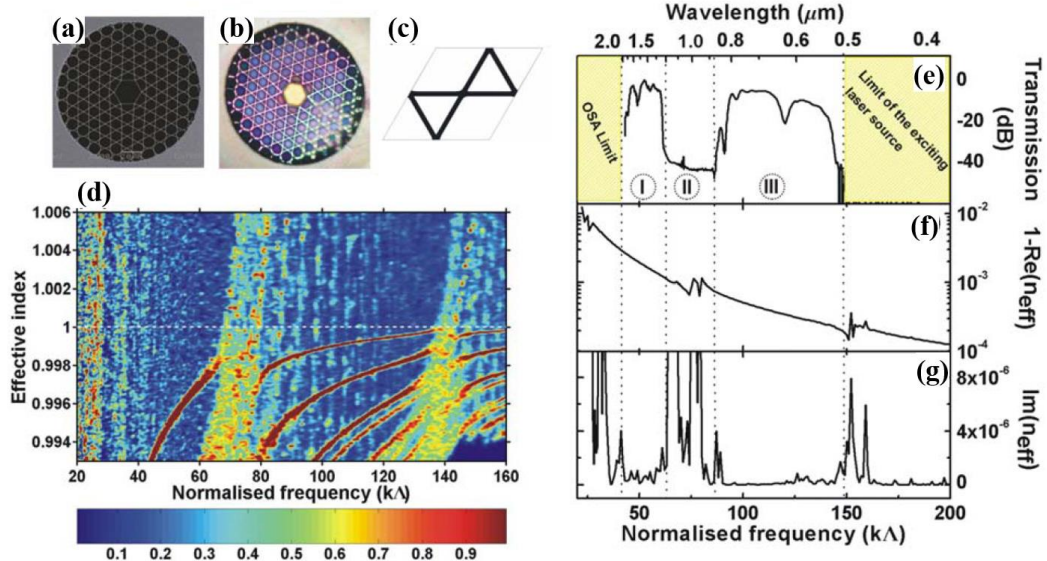


**Figure 2.7** (a) The cross-section of a Kagomé-lattice HC-PCF. (b) Optical micrograph of the field intensity pattern at the output of a few cm of the fiber. (c) Primitive unit cell of the Kagomé lattice. (d) Calculated DOPS diagram as a function of the real part of the effective index and normalized frequency. (e) Measured transmission spectrum. Calculated (f) real and (g) imaginary parts of the effective index  $n_{\text{eff}}$  of the HE<sub>1,1</sub>-like core mode. (Figure is reproduced from F. Courty *et al.*, Science, vol. 318, no. 5853, pp. 1118-1121, 2007, supporting online material)

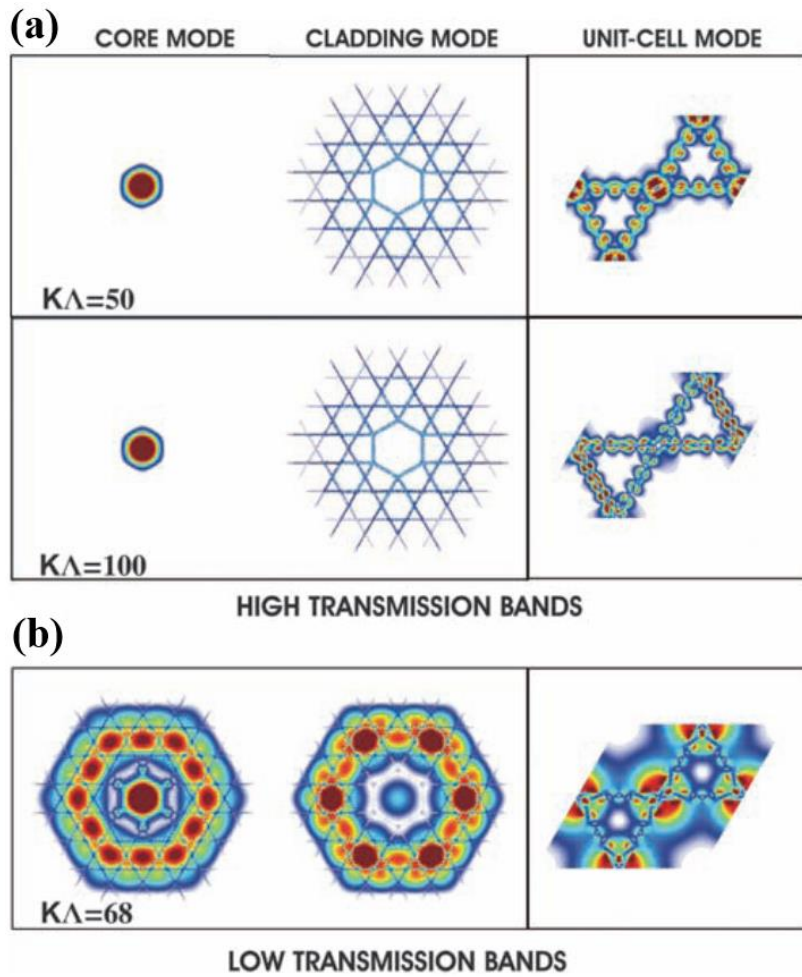


**Figure 2.8** Nature of the Kagomé lattice HC-PCF cladding modes. (a) The first two columns show the core mode and a cladding mode, respectively, for a frequency  $k\Lambda = 50$  and  $k\Lambda = 100$ . The third column shows the mode of an infinite Kagomé lattice, which corresponds to the cladding mode in the second column. (b) Same as in (a) for  $k\Lambda = 68$ . (Figure is reproduced from F. Courty *et al.* Science, vol. 318, no. 5853, pp. 1118-1121, 2007)

The waveguiding in the Kagomé lattice HC-PCF was explained by F. Courty *et al.* as being based on the inhibited coupling effect [18]. In this mechanism, the guided core modes and cladding modes in a Kagomé lattice HC-PCF can coexist even at the same frequency  $k\Lambda$  and effective index  $n_{\text{eff}}$ . The “inhibited interaction” between the hollow-core guided modes and the cladding continuum is explained by the high degree of the transverse-field mismatch between the core and cladding modes, as shown in Fig. 2.8. At the normalised frequencies of 50 and

100 in the high transmission bands, the overlap of the core modes and the cladding modes (silica struts modes) is very small, as shown in Fig. 2.8(a). At the normalised frequency of 68 in the low transmission bands, the overlap of the core modes and the cladding modes (silica struts modes) is very high as shown in Fig. 2.8(b), indicating the high efficiency of mode coupling (resonance) between them and the high loss.

The dispersion diagram of core modes in the AR, PBG, and the IC guiding fibers show periodic characteristics. The reason for this phenomenon is that both the photonic bandgap fibers and the inhibited-coupling fibers have the same anti-resonant nature [18,19]. The AR and IC effects also play a role in the depressed-core fibers (DCFs), for which a completed dispersion diagram will be introduced in Chapter 5.

## 2.2 Three-layer fiber waveguide analysis methods

As discussed in Section 2.1, optical fibers are characterized by the modal dispersion diagrams ( $n_{\text{eff}}$  vs.  $\lambda$  or  $r_1$ ). This section will introduce briefly several waveguide analysis methods to calculate the dispersion diagrams of the three-layer fibers, including the ray-optics approach, analytical method and numerical methods. A comparison of the different methods is also provided and discussed.

### 2.2.1 Ray-optics approach

The ray-optics approach, belonging to the classical geometrical optics, can provide an approximate description of light propagation in a homogeneous optical medium [1]. It is well-known that the most direct and conceptually simple way to describe light propagation in fiber waveguides is by tracing rays

along the core [2]. A ray is reflected from the interface back into the core at an angle regardless of whether partial or total reflection occurs. If this procedure is repeated at successive reflections from the interfaces, the zig-zag paths, or trajectories are constructed, as shown in Figs. 2.1, 2.2, and 2.4(b). Using the laws of ray optics such as the Snell's law, the eigenvalue equations of the mode guidance in some simple waveguides such as a planar waveguide and a two-layer step-index optical fiber can be obtained [1,2].

The ray-optics approach can help to analyse the field distributions of the core and the cladding modes in the three-layer optical fibers. However, it is very difficult to build the eigenvalue equations for complex waveguide structures. For example, the ray-optics approach is generally not suitable for photonic crystal fibers.

### 2.2.2 Wave-optics approach

Light is an electromagnetic wave, whose behaviour in a medium without electric charges can be described exactly by Maxwell's equations, as follows:

$$\nabla \times \vec{E} = -\frac{\partial \vec{B}}{\partial t} \quad (2.10-1)$$

$$\nabla \times \vec{H} = -\frac{\partial \vec{D}}{\partial t} \quad (2.10-2)$$

$$\nabla \cdot \vec{D} = 0 \quad (2.10-3)$$

$$\nabla \cdot \vec{B} = 0 \quad (2.10-4)$$

where  $\vec{E}$  is the electric field (in Volts per meter),  $\vec{H}$  is the magnetic field (in Amperes per meter),  $\vec{D}$  is the electric flux density (in Coulombs for square

meters), and  $\vec{B}$  is the magnetic flux density (in Amperes per square meter). The relationship between  $\vec{E}$ ,  $\vec{D}$ ,  $\vec{H}$  and  $\vec{B}$  is through the equations

$$\vec{D} = \epsilon_0 \epsilon_r \vec{E} \quad (2.11-1)$$

$$\vec{B} = \mu_0 \mu_r \vec{H} \quad (2.11-2)$$

where  $\epsilon_0$  and  $\mu_0$  are the permittivity and permeability of vacuum, and  $\epsilon_r$  and  $\mu_r$  are the relative permittivity and permeability of the material. The velocity of light in vacuum is  $c_0 = 1/\sqrt{\epsilon_0 \mu_0}$ . For non-magnetic materials,  $\mu_r = 1$ . Their relation to the refractive index of the material is  $n = \sqrt{\epsilon_r \mu_r} = \sqrt{\epsilon_r}$ .

For an electromagnetic field oscillating at a single angular frequency  $\omega$  (in radians per second), the phasor expressions for the electric field  $\vec{E}$ , magnetic field  $\vec{H}$ , electric flux density  $\vec{D}$  and magnetic flux density  $\vec{B}$  are as follows:

$$\vec{E}(\vec{r}, t) = \vec{E}(\vec{r}) e^{j\omega t} \quad (2.12-1)$$

$$\vec{H}(\vec{r}, t) = \vec{H}(\vec{r}) e^{j\omega t} \quad (2.12-2)$$

$$\vec{D}(\vec{r}, t) = \vec{D}(\vec{r}) e^{j\omega t} \quad (2.12-3)$$

$$\vec{B}(\vec{r}, t) = \vec{B}(\vec{r}) e^{j\omega t} \quad (2.12-4)$$

Using Eqs. (2.10)-(2.12), the Helmholtz equations for  $\vec{E}$  and  $\vec{H}$  can be deduced as:

$$\nabla^2 \vec{E} + n^2 k_0^2 \vec{E} = 0 \quad (2.13)$$

$$\nabla^2 \vec{H} + n^2 k_0^2 \vec{H} = 0 \quad (2.14)$$

where  $k_0 = \omega\sqrt{\epsilon_0\mu_0} = \omega/c_0$  is the wave number in vacuum.

The boundary conditions required for the light fields in a dielectric waveguide are as follows:

- a) Tangential components of the electric fields are continuous at the interface and hence:

$$E_{1t} = E_{2t} \quad (2.15)$$

- b) Tangential components of the magnetic fields are continuous at the interface and hence:

$$H_{1t} = H_{2t} \quad (2.16)$$

- c) Normal components of the electric flux densities are continuous at the interface and hence:

$$D_{1n} = D_{2n} \quad (2.17)$$

- d) Normal components of the magnetic flux densities are continuous at the interface and hence:

$$B_{1n} = B_{2n} \quad (2.18)$$

In the wave-optics approach, the light field vectors  $\vec{E}$  and  $\vec{H}$  in the waveguide are obtained by using the analytical method or the numerical method to solve the Helmholtz Eqs. (2.13) and (2.14).

### 2.2.2.1 Analytical method

Analytical methods aim to solve problems in “closed form”, that is in terms of standard functions such as polynomial, rational, trigonometric, exponential or logarithmic. Analytical methods usually provide the most meaningful answer because the obtained solution determines an exact behaviour for each variable or parameter. The eigenvalue equations for the guided modes in an optical fiber are derived by employing the Helmholtz equations (2.13) and (2.14) in cylindrical coordinates with boundary conditions as shown by Eqs. (2.15)-(2.18)

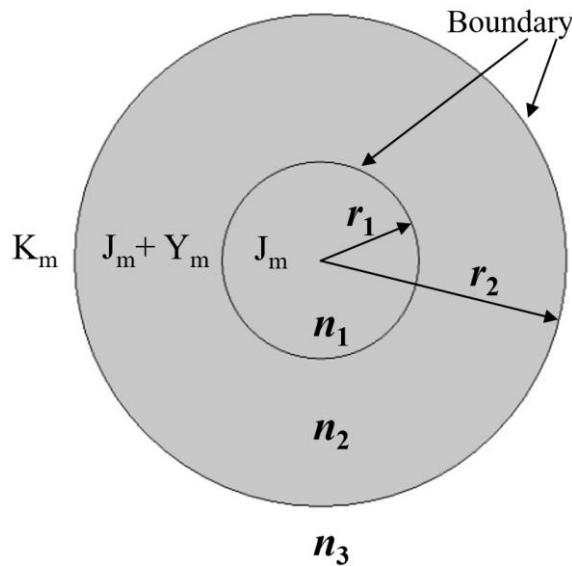


**Figure 2.9** Cross section of a three-layer optical fiber. The light field in different regions is denoted by different Bessel functions.

Figure 2.9 shows a cross section of a three-layer fiber, which can represent both the three-layer step-index fiber with  $n_3 < n_2 < n_1$  shown in Fig. 1.9(b) and the three-layer depressed-core fiber with  $n_3 < n_1 < n_2$  shown in Fig. 1.9(d). The eigenvalue equations and the deduced procedure for these two kinds of fibers are similar.

The electromagnetic fields  $\vec{E} = \vec{e}\exp(j\beta z)$  and  $\vec{H} = \vec{h}\exp(j\beta z)$  can be derived from the scalar potentials  $\Phi = \Phi_a\exp(j\beta z)$  and  $\Psi = \Psi_a\exp(j\beta z)$ , known as the Debye potentials, through the well-known relations [3]:

$$\begin{aligned}\vec{e} = & \left[ \frac{\partial \Psi_a}{r\partial\phi} - \left( \frac{\beta}{\omega\varepsilon_i} \right) \frac{\partial \Phi_a}{\partial r} \right] \vec{r}_0 - \left[ \frac{\partial \Psi_a}{\partial r} + \left( \frac{\beta}{\omega\varepsilon_i} \right) \frac{\partial \Phi_a}{r\partial\phi} \right] \vec{\phi}_0 \\ & - \left[ \left( \frac{1}{j\omega\varepsilon_i} \right) (k_0^2 n_i^2 - \beta^2) \Phi_a \right] \vec{z}_0\end{aligned}\tag{2.19}$$

$$\begin{aligned}\vec{h} = & \left[ \frac{\partial \Phi_a}{r\partial\phi} + \left( \frac{\beta}{\omega\mu} \right) \frac{\partial \Psi_a}{\partial r} \right] \vec{r}_0 - \left[ \frac{\partial \Phi_a}{\partial r} - \left( \frac{\beta}{\omega\mu} \right) \frac{\partial \Psi_a}{r\partial\phi} \right] \vec{\phi}_0 \\ & + \left[ \left( \frac{1}{j\omega\mu} \right) (k_0^2 n_i^2 - \beta^2) \Psi_a \right] \vec{z}_0\end{aligned}\tag{2.20}$$

where  $\vec{r}_0$ ,  $\vec{\phi}_0$ , and  $\vec{z}_0$  is respectively the unit radial, angular, and axial axis in a cylindrical coordinate system. The wavenumber in a vacuum is:  $k_0 = \frac{\omega}{c} = \frac{2\pi}{\lambda}$ , where  $c = \frac{1}{\sqrt{\mu\varepsilon}}$  is light speed,  $\lambda$  is the wavelength. The longitudinal propagation constant is:  $\beta = k_0 n_{\text{eff}}$ . The scalar potentials  $\Phi$  and  $\Psi$  are the solution of the usual Helmholtz wave equation

$$\{\Delta_t + (k_0^2 n_i^2 - \beta^2)\}_{\{\Psi\}}^{\{\Phi\}} = 0\tag{2.21}$$

where  $\Delta_t$  denotes the transverse Laplacian:  $\Delta_t = \frac{\partial^2}{\partial r^2} + \frac{\partial}{\partial r} + \frac{\partial^2}{r^2 \partial\phi^2}$ .

For a three-layer fiber shown schematically in Fig. 2.9, the solution of the Helmholtz wave equation in Eq. (2.21) is as follows:

$$\Phi_a = \begin{cases} A_1 J_m(u_1 r) \exp(jm\phi), & r < r_1 \\ [A_2 J_m(u_2 r) + B_2 Y_m(u_2 r)] \exp(jm\phi), & r_1 < r < r_2 \\ B_3 K_m(w_3 r) \exp(jm\phi), & r > r_2, \end{cases} \quad (2.22)$$

$$\Psi_a = \begin{cases} C_1 J_m(u_1 r) \exp(jm\phi), & r < r_1 \\ [C_2 J_m(u_2 r) + D_2 Y_m(u_2 r)] \exp(jm\phi), & r_1 < r < r_2 \\ D_3 K_m(w_3 r) \exp(jm\phi), & r > r_2 \end{cases} \quad (2.23)$$

where  $u_i^2 = k^2 n_i^2 - \beta^2 = -w_i^2$ ,  $i = 1, 2$ , or  $3$ , the functions  $J_m$ ,  $Y_m$  and  $K_m$  denote the Bessel function of the first kind, the Bessel function of the second kind and the modified Bessel function of the second kind. The field coefficients  $A_i$ ,  $B_i$ ,  $C_i$ , and  $D_i$  are introduced for the purpose of weighting the field at various regions and thus are related to each other.

For TE modes,  $\Phi_a \equiv 0$ , substituting Eqs. (2.22) and (2.23) into Eqs. (2.19) and (2.20), the electromagnetic field components of TE modes are determined as:

Core region:  $r < r_1$

$$e_r = \left(\frac{jm}{r}\right) C_1 J_m(u_1 r) \exp(jm\phi), \quad (2.24-1)$$

$$e_\phi = -u_1 C_1 J'_m(u_1 r) \exp(jm\phi), \quad (2.24-2)$$

$$e_z = 0, \quad (2.24-3)$$

$$h_r = \left(\frac{\beta u_1}{\omega \mu}\right) C_1 J'_m(u_1 r) \exp(j m \phi), \quad (2.24-4)$$

$$h_\phi = \left(\frac{\beta}{\omega \mu}\right) \left(\frac{jm}{r}\right) C_1 J_m(u_1 r) \exp(j m \phi), \quad (2.24-5)$$

$$h_z = \left(\frac{u_1^2}{j \omega \mu}\right) C_1 J_m(u_1 r) \exp(j m \phi), \quad (2.24-6)$$

First cladding region:  $r_1 < r < r_2$

$$e_r = \left(\frac{jm}{r}\right) [C_2 J_m(u_2 r) + D_2 Y_m(u_2 r)] \exp(j m \phi), \quad (2.25-1)$$

$$e_\phi = -u_2 [C_2 J'_m(u_2 r) + D_2 Y'_m(u_2 r)] \exp(j m \phi), \quad (2.25-2)$$

$$e_z = 0, \quad (2.25-3)$$

$$h_r = \left(\frac{\beta u_2}{\omega \mu}\right) [C_2 J'_m(u_2 r) + D_2 Y'_m(u_2 r)] \exp(j m \phi), \quad (2.25-4)$$

$$h_\phi = \left(\frac{\beta}{\omega \mu}\right) \left(\frac{jm}{r}\right) [C_2 J_m(u_2 r) + D_2 Y_m(u_2 r)] \exp(j m \phi), \quad (2.25-5)$$

$$h_z = \left(\frac{u_2^2}{j \omega \mu}\right) [C_2 J_m(u_2 r) + D_2 Y_m(u_2 r)] \exp(j m \phi), \quad (2.25-6)$$

Second cladding region:  $r > r_2$

$$e_r = \left(\frac{jm}{r}\right) D_3 K_m(w_3 r) \exp(j m \phi), \quad (2.26-1)$$

$$e_\phi = -w_3 D_3 K'_m(w_3 r) \exp(j m \phi), \quad (2.26-2)$$

$$e_z = 0, \quad (2.26-3)$$

$$h_r = \left(\frac{\beta w_3}{\omega \mu}\right) D_3 K'_m(w_3 r) \exp(j m \phi), \quad (2.26-4)$$

$$h_\phi = \left(\frac{\beta}{\omega\mu}\right) \left(\frac{jm}{r}\right) D_3 K_m(w_3 r) \exp(jm\phi), \quad (2.26-5)$$

$$h_z = -\left(\frac{w_3^2}{j\omega\mu}\right) D_3 K_m(w_3 r) \exp(jm\phi), \quad (2.26-6)$$

Applying the boundary conditions  $e_\phi|_{r=r_1-} = e_\phi|_{r=r_1+}$ ,  $e_\phi|_{r=r_2-} = e_\phi|_{r=r_2+}$ ,

$h_z|_{r=r_1-} = h_z|_{r=r_1+}$ , and  $h_z|_{r=r_2-} = h_z|_{r=r_2+}$  to Eqs. (2.24)-(2.26), it yields:

$$-u_1 C_1 J'_m(u_1 r_1) = -u_2 [C_2 J'_m(u_2 r_1) + D_2 Y'_m(u_2 r_1)] \quad (2.27-1)$$

$$-u_2 [C_2 J'_m(u_2 r_2) + D_2 Y'_m(u_2 r_2)] = \left(\frac{u_2^2}{j\omega\mu}\right) [C_2 J_m(u_2 r_2) + D_2 Y_m(u_2 r_2)] \quad (2.27-2)$$

$$\left(\frac{u_1^2}{j\omega\mu}\right) C_1 J_m(u_1 r_1) = \left(\frac{u_2^2}{j\omega\mu}\right) [C_2 J_m(u_2 r_1) + D_2 Y_m(u_2 r_1)] \quad (2.27-3)$$

$$\left(\frac{u_2^2}{j\omega\mu}\right) [C_2 J_m(u_2 r_2) + D_2 Y_m(u_2 r_2)] = -\left(\frac{w_3^2}{j\omega\mu}\right) D_3 K_m(w_3 r_2) \quad (2.27-4)$$

The Eqs. (2.27) forms a  $4 \times 4$  matrix and its determinant must be zero:

$$\begin{vmatrix} u_1^2 J_m(u_1 r_1) & -u_2^2 J_m(u_2 r_1) & -u_2^2 Y_m(u_2 r_1) & 0 \\ u_1 J'_m(u_1 r_1) & -u_2 J'_m(u_2 r_1) & -u_2 Y'_m(u_2 r_1) & 0 \\ 0 & u_2 J'_m(u_2 r_2) & u_2 Y'_m(u_2 r_2) & -w_3 K'_m(w_3 r_2) \\ 0 & u_2^2 J_m(u_2 r_2) & u_2^2 Y_m(u_2 r_2) & w_3^2 K_m(w_3 r_2) \end{vmatrix} = 0 \quad (2.28)$$

which yields the eigenvalue equation for the  $\text{TE}_{0,n}$  modes, as shown in Appendix A. Similarly, the eigenvalue equations for the  $\text{TM}_{0,n}$ ,  $\text{HE}_{m,n}$  and  $\text{EH}_{m,n}$  modes can be deduced and shown in Appendix A. These eigenvalue equations can be solved by a graphical method [3] to obtain the longitudinal propagation constant  $\beta$  or  $n_{\text{eff}}$  of modes in a three-layer optical fiber.

Under the weakly guiding approximation, the light field in three-layer step-index fibers can be denoted by scalar modes  $LP_{m,n}$ , whose eigenvalue equations were deduced by M. Monerie, as shown in Appendix B.

### 2.2.2.2 Finite element method

In a finite element method (FEM), the fiber cross-section and wave equation are meshed (divided) into a huge number of elements as shown in Fig. 2.10. Each element has its own function, and the sum of the discretized functionals for all elements form the matrix eigenvalue equations by the variational or the weighted residual methods [20]. In process the boundaries of the inner regions of the fiber do not need to be specially considered, which indicates the FEM can be employed to solve more complex fiber structures.

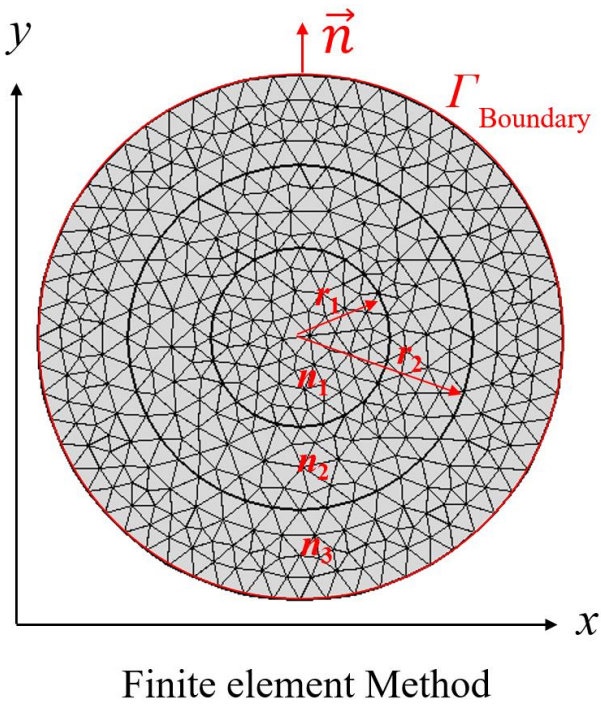


**Figure 2.10** The FEM analysis region for the calculation of the core and cladding modes in a three-layer optical fiber. The analysis region is meshed by triangular elements.

### 2.2.2.3 Beam propagation method

The Beam propagation method (BPM) used in the research is a finite-difference BPM. This technique uses finite-difference methods to solve the well-known parabolic or paraxial approximation of the Helmholtz equation [21,22]. In the finite-difference approach, the field in the transverse ( $x$ - $y$ ) plane is represented only at discrete points on a grid, and at discrete planes along the longitudinal or propagation direction ( $+z$ ), as shown in Fig. 2.11. Given the discretized field at one  $z$  plane, the goal is to derive numerical equations that determine the field at the next  $z$  plane. This elementary propagation step is then repeated to determine the field throughout the structure [22].

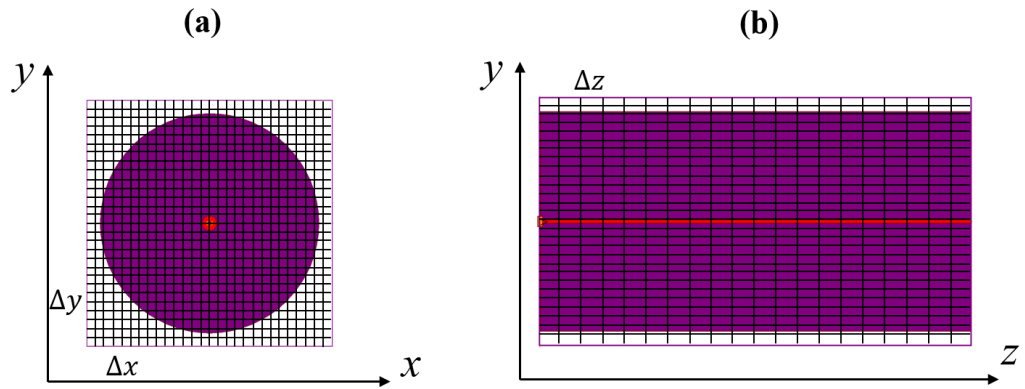


**Figure 2.11** The meshing of analysis region in beam propagation method: (a) transverse ( $x$ - $y$ ) plane, (b) along the  $z$  direction.

Both the FEM and the BPM are numerical methods, where the wave equations are not directly solved, as opposed to the analytical method described in the previous section. These two numerical methods can be used for computing the propagation of light waves in waveguides with arbitrary cross-section.

### 2.2.3 Comparison of the waveguide analysis methods

The waveguide analysis methods are compared in Table 2.1. The ray-optics approach can provide a direct and conceptually simple way to describe the light field in the waveguide, but it is generally inconvenient to build the eigenvalue equations for the modes.

**Table 2.1** Comparison of the waveguide analysis methods.

	<b>Ray Optics Approach</b>	<b>Analytical Method</b>	<b>Finite Element Method</b>	<b>Beam Propagation Method</b>
Pros.	The most direct and conceptually simple way	Solve problems in “closed form”; Provide the most meaningful answer ; Exact solution.	Widely utilized numerical methods; Full-vector; Exact solution.	Relatively faster; Transmission problem; SMS hetero structure.
Cons.	Unsuitable for complex waveguides	Partial solutions; Difficult for complex waveguides.	Time consuming; Lack of meaningful answer.	Time consuming; Lots of approximation; Lack of meaningful answer.

The wave-optics approach uses the electromagnetic wave theory to characterize the light field in optical waveguides. The FEM and the BPM provide a simple way to simulate and calculate the propagation constants of the modes in the waveguide, especially in a complex structure. Therefore, it is easy to use the numerical methods to investigate complex, unknown, or unexplored systems. Compared to the numerical methods, the analytical method that uses specific functions to build the eigenvalue equations, can provide physically meaningful description of the field in a waveguide.

## 2.3 Conclusion

This chapter has reviewed the fundamentals of waveguiding mechanisms, dispersion diagrams, and mode analysis methods in fiber optics. The waveguiding mechanisms include TIR, AR, PBG and IC guiding effects. The fiber mode analysis methods include the ray-optics approach and the wave-optics approach, where the latter includes the analytical method, the FEM and the BPM.

Although the modal characteristics equations for the three-layer fibers have been derived in previous works [3], a complete modal dispersion diagram based on these equations has not been reported in the literature to date. In the following chapters, complete dispersion diagrams of both core and cladding modes in the three-layer step-index fiber and the depressed-core fiber will be introduced.

## 2.4 Reference

- [1] A. W. Snyder, and J. Love, *Optical waveguide theory*, (Springer Science & Business Media, 2012).
- [2] D. Marcuse, *Theory of dielectric optical waveguides*, (Elsevier, 2013).
- [3] C. Tsao, *Optical fiber waveguide analysis*, (Oxford University Press, 1992).
- [4] M. Born, and E. Wolf, *Principles of optics: electromagnetic theory of propagation, interference and diffraction of light*, (Elsevier, 2013).
- [5] M. A. Duguay, Y. Kokubun, T. L. Koch, and L. Pfeiffer, “Antiresonant reflecting optical waveguides in SiO<sub>2</sub>-Si multilayer structures,” *Appl. Phys. Lett.*, vol. 49, no. 1, pp. 13–15, 1986.
- [6] N. M. Litchinitser, A. K. Abeeluck, C. Headley, and B. J. Eggleton, “Antiresonant reflecting photonic crystal optical waveguides,” *Opt. Lett.*, vol. 27, no. 18, pp. 1592–1594, 2002.

- [7] M. Zeisberger and M. A. Schmidt, “Analytic model for the complex effective index of the leaky modes of tubetype anti-resonant hollow core fibers,” *Sci. Rep.*, vol. 7, no. 1, p. 11761, 2017.
- [8] L. Vincetti and V. Setti, “Waveguiding mechanism in tube lattice fibers,” *Opt. Express*, vol. 18, no. 22, pp. 23133–23146, 2010.
- [9] C.-H. Lai, B. You, J.-Y. Lu, T.-A. Liu, J.-L. Peng, C.-K. Sun, and H.-C. Chang, “Modal characteristics of antiresonant reflecting pipe waveguides for terahertz waveguiding,” *Opt. Express*, vol. 18, no. 1, pp. 309–322, 2010.
- [10] E. Yablonovitch, “Inhibited spontaneous emission in solid-state physics and electronics,” *Phys. Rev. Lett.*, vol. 58, no. 20, p. 2059, 1987.
- [11] S. John, “Strong localization of photons in certain disordered dielectric superlattices,” *Phys. Rev. Lett.*, vol. 58, no. 23, p. 2486, 1987.
- [12] J. D. Joannopoulos, P. R. Villeneuve, and S. Fan, “Photonic crystals: putting a new twist on light,” *Nature*, vol. 386, no. 6621, pp. 143-149, 1997.
- [13] P. Russell, “Photonic crystal fibers,” *Science*, vol. 299, no. 5605, pp. 358-362, 2003.
- [14] P. St J. Russell, “Photonic-crystal fibers,” *J. Lightw. Technol.*, vol. 24, no. 12, pp. 4729-4749, 2006.
- [15] T. A. Birks, F. Luan, G. J. Pearce, A. Wang, J. C. Knight, and D. M. Bird, “Bend loss in all-solid bandgap fibers,” *Opt. Express*, vol. 14, no. 12, pp. 5688-5698, 2006.
- [16] T. A. Birks, G. J. Pearce, and D. M. Bird, “Approximate band structure calculation for photonic bandgap fibers,” *Opt. Express*, vol. 14, no. 20, pp. 9483-9490, 2006.
- [17] F. Benabid, J. C. Knight, G. Antonopoulos, and P. St J. Russell, “Stimulated Raman scattering in hydrogen-filled hollow-core photonic crystal fiber,” *Science*, vol. 298, no. 5592, pp. 399-402, 2002.
- [18] F. Couny, F. Benabid, P. J. Roberts, P. S. Light, and M. G. Raymer, “Generation and photonic guidance of multi-octave optical-frequency combs,” *Science*, vol. 318, no. 5853, pp. 1118-1121, 2007.

- [19] R. F. Ando, A. Hartung, B. Jang, and M. A. Schmidt, “Approximate model for analyzing band structures of single-ring hollow-core anti-resonant fibers,” Opt. Express, vol. 27, no. 7, pp. 10009-10021, 2009.
- [20] K. Kawano, and T. Kitoh, *Introduction to Optical Waveguide Analysis: Solving Maxwell's Equation and the Schrödinger Equation*, (John Wiley & Sons, 2004).
- [21] R. Scarmozzino, and R. M. Osgood, “Comparison of finite-difference and Fourier-transform solutions of the parabolic wave equation with emphasis on integrated-optics applications,” JOSA A, vol. 8, no. 5, pp. 724-731, 1991.
- [22] RSoft, C. A. D., *User Guide, Synopsys*, (Inc, RSoft Products, 2014).

# **Chapter 3**

## **Mode Transition in Conventional Three-Layer Step-Index Optical Fibers<sup>1</sup>**

The modal dispersion diagram shown in Section 2.1.2, calculated based on a two-layer step-index fiber model, provides only the information for the core-type modes. Using a three-layer step-index fiber model, the modal behaviour of both the core and the cladding modes can be obtained.

In this chapter, the dispersion diagrams of the vector modes ( $TE_{0,n}$ ,  $TM_{0,n}$ ,  $HE_{m,n}$  and  $EH_{m,n}$ ) and of the related scalar modes  $LP_{m,n}$  for a three-layer step-index optical fiber are calculated using both an analytical method and a full-vector finite element method (full-vector FEM). The cladding mode distributions and the transitions between the core and cladding modes are analyzed. This work aims to enrich the knowledge and understanding of modal characteristics of conventional three-layer step-index optical fibers.

### **3.1 Research background**

Silica-based solid-core step-index optical fibers such as the single-mode optical fiber (SMF) are widely used as the fundamental component in the telecommunications industry. Their single-step index profile is the simplest fiber design and provides a logical starting point for the study of fibers with more complex designs [1-5]. For example, the classification of the modes in the

---

<sup>1</sup>Lian, Xiaokang, Gerald Farrell, Qiang Wu, Wei Han, Fangfang Wei, and Yuliya Semenova, "Mode Transition in Conventional Step-Index Optical Fibers," In 18<sup>th</sup> IEEE International Conference on Optical Communications and Networks (ICOON), pp. 1-3, 2019.

complex hollow-core photonic-bandgap fibers is similar to that in the step-index optical fibers, although the guidance mechanism in the former is the photonic bandgap effect unlike the total internal reflection effect in the latter [6].

Most of the research relating to step-index optical fibers has focused on the studies of the core modes. The two-layer model (the single-step index profile) used in studies of the core modes assumes that the cladding region is infinite, therefore, the information related to the cladding modes cannot be obtained. The cladding modes could be studied with a three-layer model (a double-step index profile) and their modal characteristic equations have been derived by several different groups [2-4]. The cladding modes can be excited by fiber Bragg gratings (FBGs) and long-period fiber gratings (LPFGs), by coupling the energy of core modes into cladding modes. The theory relating to the mode coupling in the fiber gratings has been well described in literature [4,5]. However, an intuitive interpretation of the qualitative and quantitative characteristics of the cladding modes is still lacking. In this chapter, a complete dispersion diagram including the core and cladding modes is developed, which should deepen the understanding of light propagation in the step-index optical fibers.

### 3.2 Ray trajectories of the core- and cladding-type modes

Figure 3.1(a) shows the cross section and the index profile of a three-layer step-index optical fiber. The refractive index of the fiber core  $n_1$  is higher than that of the fiber cladding  $n_2$ , where the radius of the core is  $r_1$  and the cladding radius is  $r_2$ . The surrounding medium is air, with the minimum refractive index  $n_3$ . The effective refractive index  $n_{\text{eff}}$  of the core-type modes lies within a range defined by  $n_1 > n_{\text{eff}} > n_2$  while for the cladding modes it is  $n_2 > n_{\text{eff}} > n_3$ . In the ray optics

model as shown in Figs. 3.1(b) and 3.1(c), the ray of the core mode is confined inside the core region by total internal reflections at the interface between the core and cladding regions. For the cladding modes, the ray can partially penetrate the core-cladding interface in a fashion of multi-path reflections while the total internal reflection only occurs at the interface between the cladding region and the surrounding medium (air).

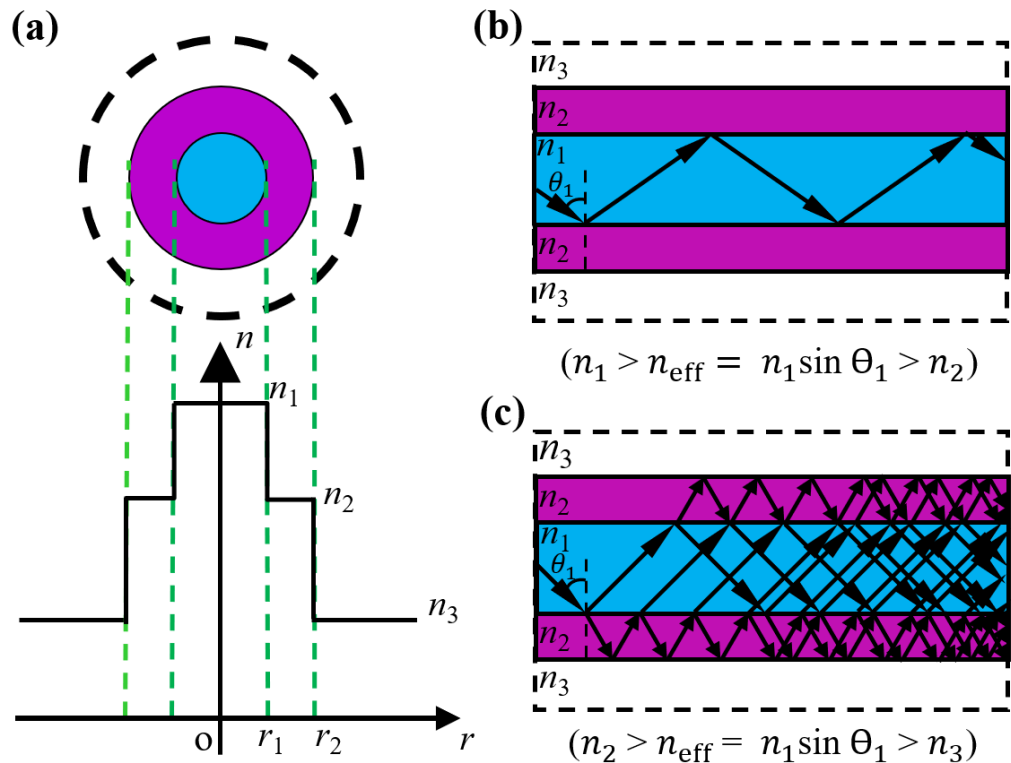


**Figure 3.1** (a) Refractive index profile of a three-layer step-index optical fiber. (b) Ray trajectory of a core-type mode. (c) Ray trajectory of a cladding-type mode ( $0 \leq r_1 \leq 62.5 \mu\text{m}$ ,  $n_1 = 1.451$ ,  $r_2 = 62.5 \mu\text{m}$  and  $n_2 = 1.445$ ,  $\lambda = 1550 \text{ nm}$ ).

In the calculations, the fiber parameters used are:  $n_1 = 1.451$ ,  $n_2 = 1.445$ ,  $r_2 = 62.5 \mu\text{m}$ ,  $n_3 = 1.000$  and the light wavelength is  $\lambda = 1550 \text{ nm}$ . The core radius  $r_1$  is the only variable, covering the range of radii from  $0 \mu\text{m}$  to  $62.5 \mu\text{m}$ . The linear polarization (LP) approximation is reasonable due to a relatively small difference between the core and cladding refractive indices,  $n_1$  (1.451) and  $n_2$  (1.445). It is

also suitable for the no-core fibers (NCFs) due to the mode fields far from cutoff approximation [7], although the difference between  $n_2$  (1.445) and  $n_3$  (1.000) is relatively large. The  $n_{\text{eff}}$  of the scalar  $\text{LP}_{m,n}$  modes are calculated by solving the scalar eigenvalue equations in Appendix B. The  $n_{\text{eff}}$  of the vector modes ( $\text{TE}_{0,n}$ ,  $\text{TM}_{0,n}$ ,  $\text{HE}_{m,n}$  and  $\text{EH}_{m,n}$ ) are calculated by the full-vector FEM. The subscript  $m$  is the azimuthal number and  $n$  is the radial number.

### **3.3 Dispersion diagram of the scalar and vector modes in three-layer step-index fibers**

The calculated dispersion diagrams ( $n_{\text{eff}}$  vs.  $r_1$ ), including the first 17 vector modes ( $\text{TE}_{0,n}$ ,  $\text{TM}_{0,n}$ ,  $\text{HE}_{m,n}$  and  $\text{EH}_{m,n}$ ) and the first 9 scalar  $\text{LP}_{m,n}$  modes, are shown in Fig. 3.2. The  $n_{\text{eff}}$  of the scalar  $\text{LP}_{m,n}$  modes calculated by the analytical method are shown as the solid lines while those of vector modes calculated by the full-vector FEM are shown as the scattered lines. The vector modes are only calculated in a small range of the core radii  $0 \mu\text{m} \leq r_1 \leq 15 \mu\text{m}$  for the sake of conciseness, in order to show the relationship with the scalar  $\text{LP}_{m,n}$  modes.  $\text{LP}_{0,n}$  is a doubly degenerate mode of two  $\text{HE}_{1,n}$  modes; the  $\text{LP}_{1,n}$  is a four-fold degenerate mode of  $\text{TE}_{0,n}$ ,  $\text{TM}_{0,n}$ , and two  $\text{HE}_{2,n}$  modes;  $\text{LP}_{m,n}$  ( $m > 1$ ) is a four-fold degenerate mode of two  $\text{HE}_{m+1,n}$  and two  $\text{EH}_{m-1,n}$  modes. The  $n_{\text{eff}}$  of every vector mode in each group are almost the same as those of the corresponding  $\text{LP}_{m,n}$  modes, as seen from the overlapped scatter lines and the solid lines in Fig. 3.2. The excellent match between the  $n_{\text{eff}}$  of the scalar modes and the vector modes verifies the LP approximation. The mode distribution of the vector modes is the same as for the corresponding  $\text{LP}_{m,n}$  modes.

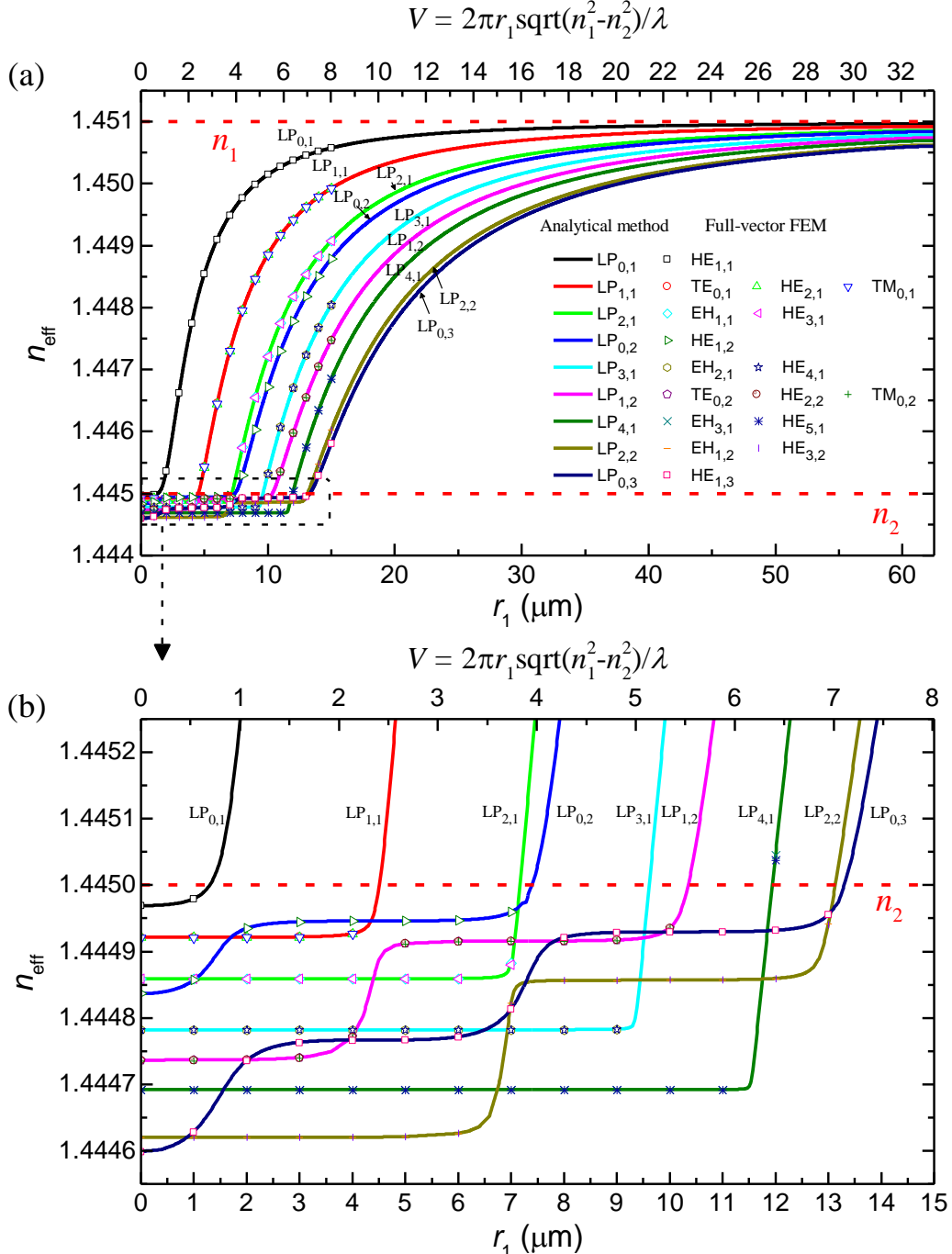


**Figure 3.2** (a) Dispersion curves ( $n_{\text{eff}}$  vs.  $r_1$ ) of the modes in step-index optical fibers; (b) is an enlarged part of graph (a), indicated by a black dash rectangle. Scalar LP<sub>m,n</sub> modes indicated by the solid lines are calculated by the analytical method. The vector modes (TE<sub>0,n</sub>, TM<sub>0,n</sub>, HE<sub>m,n</sub> and EH<sub>m,n</sub>) indicated by the scattered lines are calculated by the full-vector FEM.

Figure 3.2(a) is divided into two regions by the red horizontal dashed lines located at  $n_1$  and  $n_2$ . The region with  $n_2 < n_{\text{eff}} < n_1$  corresponds to the fiber core

modes while the region with  $n_{\text{eff}} < n_2$  ( $r_1 \neq 0 \mu\text{m}$ ) corresponds to the fiber cladding modes. All the modes in NCFs with  $r_1 = 0 \mu\text{m}$  or  $r_1 = 62.5 \mu\text{m}$  are classified as core modes, since there are no guided modes in the infinite air cladding region. The distribution order of core modes does not change throughout the  $r_1$  range as:  $\text{LP}_{0,1}, \text{LP}_{1,1}, \text{LP}_{2,1}, \dots$ , with decreasing  $n_{\text{eff}}$  as shown in the region between two red horizontal dashed lines in Fig. 3.2(a).

The mode reorganization phenomenon for the  $\text{LP}_{0,n}$  mode is shown in Fig. 3.2, where when one cladding-type mode  $\text{LP}_{0,n}$  becomes a core-type mode, the remaining cladding modes  $\text{LP}_{0,n}$  are reorganized (when one  $\text{LP}_{0,n}$  mode transfers to a higher order mode, the lower  $\text{LP}_{0,n}$  mode will take its original  $n_{\text{eff}}$  position). The phenomenon also occurs for the remaining  $\text{LP}_{m,n}$  modes. The mode reorganization causes the step-like changes in the  $n_{\text{eff}}$  values for the cladding modes, as shown in Fig. 3.2(b). Compared to the core modes, the distribution order of the cladding modes changes with the core radius  $r_1$ . It should be noted that only the modes with the same azimuthal number  $m$  are reorganized with the transition of the lower order mode. For example, when the cladding-type  $\text{LP}_{0,1}$  ( $m = 0$ ) becomes a core-type mode, all the  $\text{LP}_{0,n}$  ( $m = 0, n > 1$ ) modes are reorganized while the other  $\text{LP}_{m,n}$  ( $m \neq 0$ ) modes are not affected. In the entire range from  $r_1 = 0 \mu\text{m}$  to the cutoff point as shown in the dispersion region below the red dash horizontal line at  $n_2$ , the number of times such reorganizations occur (the number of  $n_{\text{eff}}$  step changes on the diagram Fig. 3.2(b)) for a single cladding mode  $\text{LP}_{m,n}$  is the same as the radial number  $n$ . For example,  $\text{LP}_{0,1}$  experiences a single mode reorganization process, while the  $\text{LP}_{0,2}$  mode experiences a reorganization twice.

The cutoff point for the  $LP_{0,1}$  ( $HE_{1,1}$ ) mode is at  $r_1 = 1.3 \mu\text{m}$  ( $V = 0.7214$ ), as shown as the point intersection between the dispersion curve and the horizontal line at  $n_{\text{eff}} = n_2$ . Clearly, there is no core-type modes when  $r_1 < 1.3 \mu\text{m}$  ( $V < 0.7214$ ). The cutoff point for  $LP_{1,1}$  ( $TE_{0,1}$ ,  $TM_{0,1}$  and  $HE_{2,1}$ ) is at  $r_1 = 4.5 \mu\text{m}$  ( $V = 2.40456$ ), which is near the value ( $V = 2.40483$ ) calculated with a two-layer step-index fiber model.

Figure 3.3 shows the intensities and electric field vector distributions of the vector modes  $HE_{1,1}$  (corresponding to the scalar mode  $LP_{0,1}$ ),  $TE_{0,1}$ ,  $HE_{2,1}$ , and  $TM_{0,1}$  (corresponding to  $LP_{1,1}$ ) for several core radii, calculated by the full-vector FEM. The core-type mode field distributions are highlighted with red frames, while the remaining unhighlighted contour plots represent cladding-type modes. All the modes in an NCF ( $r_1 = 0 \mu\text{m}$ ) are core-type modes as shown in Figs. 3.3(a1), 3.3(b1), 3.3(c1) and 3.3(d1), where the intensity is extended throughout the whole fiber cross section. As the value of  $r_1$  increases from 0 to 1  $\mu\text{m}$ , the  $n_{\text{eff}}$  of mode  $HE_{1,1}$  increases while its central intensity area reduces as shown in Figs. 3.3(a1) and 3.3(a2). The mode  $HE_{1,1}$  becomes a core-type mode beyond the value of  $r_1 = 1.3 \mu\text{m}$ . As shown in Figs. 3.3(a3)-3.3(a6), the energy of the  $HE_{1,1}$  mode is concentrated mainly inside the fiber core. The intensity distributions of modes  $TE_{0,1}$ ,  $HE_{2,1}$ , and  $TM_{0,1}$  change very little for  $r_1 < 4 \mu\text{m}$ , corresponding to the almost horizontal dispersion line in Fig. 3.2(b). They become core modes as the core radius  $r_1$  increases up to 4.5  $\mu\text{m}$ . Modes  $TE_{0,1}$ ,  $HE_{2,1}$  and  $TM_{0,1}$  have similar intensity distributions and  $n_{\text{eff}}$ , therefore, they can be grouped as an  $LP_{1,1}$  mode.

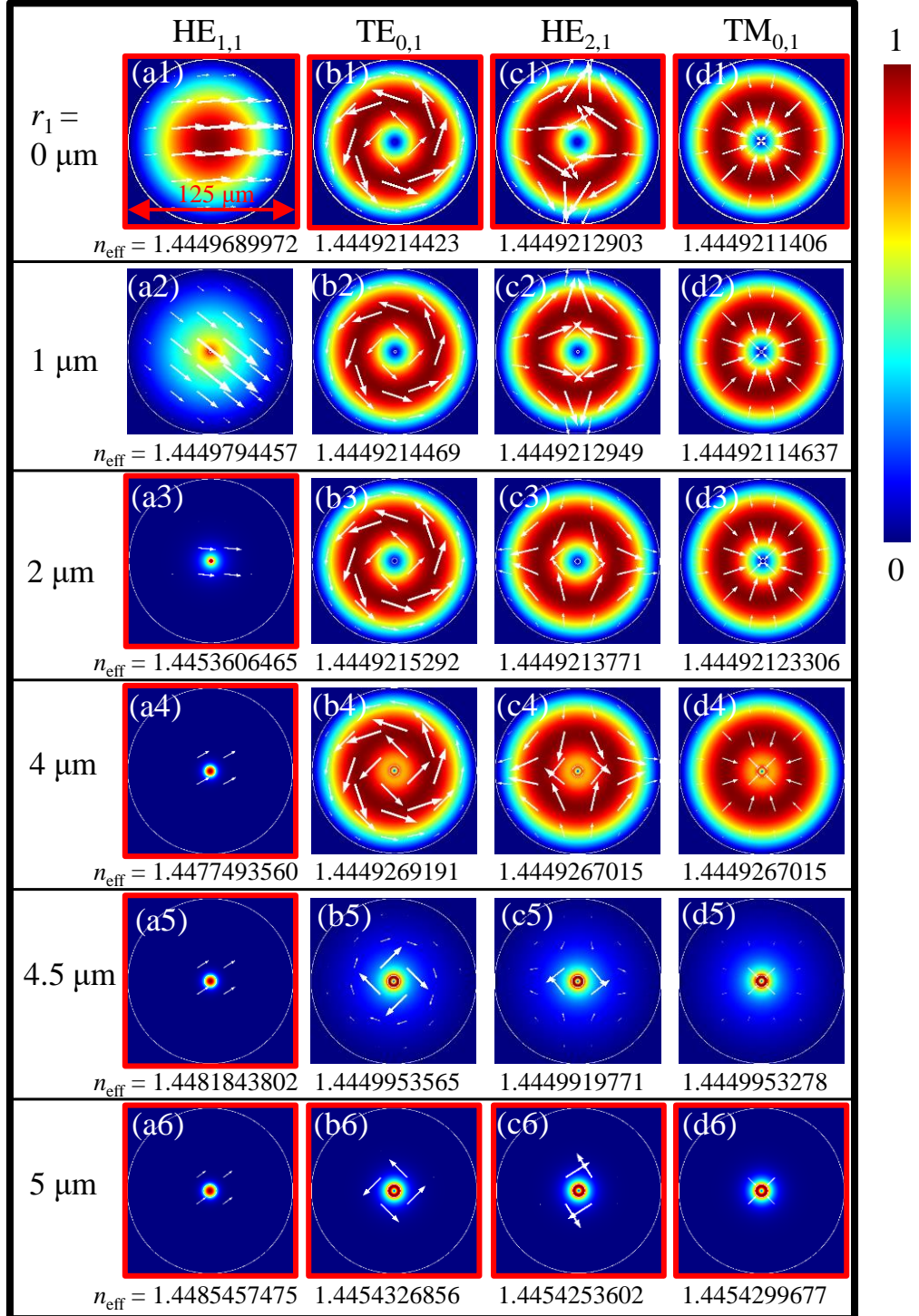


**Figure 3.3** Modal intensities and electric field vector distributions of  $\text{HE}_{1,1}$ ,  $\text{TE}_{0,1}$ ,  $\text{HE}_{2,1}$  and  $\text{TM}_{0,1}$  modes, with several different  $r_1$  as indicated on the left. The modes in the no-core fibers ( $r_1 = 0 \mu\text{m}$ ), shown in a1, b1 c1 and d1, are core-type modes; the modes shown in a3-a6, b6, c6 and d6 are also core-type modes for  $n_{\text{eff}} > 1.445$ ; the remaining are cladding-type modes with  $n_{\text{eff}} < 1.445$ . (Core-type modes are indicated by the red frames).

### 3.4 Conclusion

The effective refractive indices of both core and the cladding modes in three-layer step-index optical fibers as a function of core radius were calculated independently by the analytical method and the full-vector FEM. Due to the fields being far from the cutoff approximation in the case of the no-core fiber and the small index difference between the core and cladding in the other cases, the vector modes ( $TE_{0,n}$ ,  $TM_{0,n}$ ,  $HE_{m,n}$  and  $EH_{m,n}$ ) are perfect degeneracies and can be grouped into the corresponding  $LP_{m,n}$  modes. The transition from a cladding-type to a core-type mode has been studied. Compared to the unchanged distribution order of the core-type modes, the distribution order of cladding-type modes changes with the core radius  $r_1$ .

The cladding modes show mode reorganization characteristics, indicating a different dispersion behaviour compared to that of the core modes. To further investigate the difference between the core and the cladding modes in three-layer step-index optical fibers, a multimode self-imaging phenomenon will be investigated theoretically and experimentally in the next chapter.

### 3.5 Reference

- [1] J. A. Buck, *Fundamentals of Optical Fibers*, (Hoboken, NJ, USA: Wiley, 2004).
- [2] C. Tsao, *Optical Fiber Waveguide Analysis*, (Oxford Univ. Press, London, U.K., 1992).
- [3] M. Monerie, “Propagation in doubly clad single-mode fibers,” IEEE J. Quantum Electron., vol. QE-18, no. 4, pp. 535-542, 1982.
- [4] T. Erdogan, “Cladding-mode resonances in short-and long-period fiber grating filters,” JOSA A, vol. 14, no. 8, pp. 1760-1773, 1997.

- [5] O. V. Ivanov, S. A. Nikitov, and Y. V. Gulyaev, “Cladding modes of optical fibers: properties and applications,” *Phys. Uspekhi*, vol. 49, no. 2, pp. 167–191, 2006.
- [6] M. J. Digonnet, H. K. Kim, G. S. Kino, and S. Fan, “Understanding air-core photonic-bandgap fibers: Analogy to conventional fibers,” *J. Lightw. Technol.*, vol. 23, no. 12, pp. 4169-4177, 2005.
- [7] W. Xu, J. Shi, X. Yang, D. Xu, F. Rong, J. Zhao, and J. Yao, “Improved numerical calculation of the single-mode-no-core-single-mode fiber structure using the fields far from cutoff approximation,” *Sensors*, vol. 17, no. 10, p. 2240, 2017.

# **Chapter 4**

## **Discrete Self-Imaging in Small-Core Optical Fiber Interferometers<sup>2</sup>**

As demonstrated by the calculations presented in Chapter 3, the cladding modes show a different dispersion behaviour to that of core modes in three-layer step-index fibers. A small-core three-layer step-index fiber can support pure cladding-type modes, providing an opportunity to study the properties of cladding modes. In this chapter, the difference between the core and the cladding modes is further investigated.

In this chapter, a study of the self-imaging of the cladding modes in small-core optical fiber interferometers is presented. The results of the analytical and numerical simulations and experiments show that unlike the self-imaging of core modes, self-imaging of cladding modes only appears at a set of discrete positions along the interferometer axis with an equal spacing corresponding to some discrete values of the fiber core radius. This is the first observation of a discrete self-imaging effect in multimode waveguides. More strikingly, the self-imaging period of cladding modes grows exponentially with the fiber core radius, unlike the quadratic relationship in the case of core modes. The findings bring new insights into mode propagation in an optical fiber with a core at the micro/nanoscale, which may open new avenues for exploring MMF technologies in both linear and non-linear optics.

---

<sup>2</sup> Lian, Xiaokang, Qiang Wu, Gerald Farrell, Changyu Shen, Youqiao Ma, and Yuliya Semenova, “Discrete self-imaging in small-core optical fiber interferometers,” *J. Lightw. Technol.*, vol. 37, no. 9, pp. 1873-1884, 2019.

## 4.1 Research background

Multimode fibers (MMFs) have acquired significant popularity in telecommunications [1,2], microscopic imaging [3], optical manipulation [4,5], fiber lasers and amplifiers [6,7]. Moreover, MMFs provide new degrees of freedom and opportunities in linear and the non-linear optics, which are not possible with single-mode fibers (SMFs) [8-10]. Most of the research relating to single-core step-index MMFs [3,4], no-core fibers (NCFs) [5], graded-index fibers [2,10] and multicore fibers [1] has focused on studies of the core modes, which propagate mainly in the core region. In fact, the cladding region of an optical fiber can also act as a waveguide and can support multiple cladding modes, which can be excited in a standard SMF by a fiber Bragg grating (FBG) or a long-period grating [11]. Cladding modes are useful in many applications such as sensing and integrated optical devices [12,13]. For example, in sensing cladding modes can interact much more readily with the surrounding environment. Mathematically the core modes and the cladding modes are characterized by different functions arising from different solutions of the Bessel equations [11,14]:  $J_m$  and  $K_m$  for the core modes and functions  $J_m$ ,  $Y_m$  and  $K_m$  for the cladding modes. Therefore, the cladding modes may have some distinct characteristics compared to core modes. Unfortunately, cladding modes excited by FBGs usually coexist alongside with the core modes, making it impossible for the cladding modes to be studied independently from the core modes [11,15], [16]. It is a commonly held belief that there are no principal differences between the cladding modes and the core modes in optical fibers, except that they have different transverse intensity distributions [11].

The modal distribution in a step-index optical fiber depends on the value of the  $V$ -parameter, defined by Eq. (2.5) in Chapter 2. When  $V < 1$ , the core modes are cancelled out leaving only the cladding modes, and thus create a unique opportunity for the investigation of pure cladding modes [17-19]. To satisfy the condition  $V < 1$ , the core radius  $r_1$  should reach micro/nanoscale, which occurs in a small-core fiber (SCF). In an SCF, a very small core surrounded by a much larger silica cladding is analogous to optical microfibers and nanofibers which in effect possess an air cladding. Microfibers and nanofibers can offer numerous favorable properties such as strong evanescent fields, tight light confinement and large and manageable waveguide dispersion for manipulating light at micro/nanoscale, which has shown to be advantageous in a wide range of applications such as optical communications, sensors, lasers and non-linear optics [20-22]. An SCF with a core at micro/nanoscale may have different properties than those of the commonly used SMF and MMF. However it has not been sufficiently explored in literature to date [23,24].

The fundamental mode in both NCF and SMF is a core-type mode. However in an SCF the fundamental mode is a cladding-type mode because the core radius in the SCF is too small to support any core modes. Increasing the core radius of the SCF will lead to transfer of the fundamental mode from a cladding-type to a core-type as the cutoff condition is met. The mode transition phenomenon is usually relevant to many techniques such as single-mode operation, mode selective excitation and evanescent coupling, which are important to the design of fiber lasers, sensors and devices for optical networks [25-31].

Self-imaging is a property of multimode waveguides by which an input field profile is reproduced as single or multiple images at periodic lengths along the propagation direction of the waveguide [32]. The self-imaging effect is widely employed in design of multimode waveguide devices such as power splitters/combiners, Mach-Zehnder switches/modulators, high power laser diodes and semiconductor optical amplifiers [32-40]. Self-imaging is also important for studies of the exciting physical phenomena recently found in multimode nonlinear fiber optics such as the geometric parameter instability [41], spatial beam self-cleaning [10], multimode solitons and ultrabroadband dispersive radiation [42]. Self-imaging in multimode waveguides is closely related to the propagation constants of the guided modes. Based on the approximate expression for the propagation constants of the core modes, the self-imaging period ( $L_Z$ ) for an optical fiber interferometer (OFI) utilizing a fiber hetero-structure SMF-MMF-SMF (SMS) is a quadratic function of the  $r_1$  of the MMF section, presented by W. S. Mohammed *et al.* in Ref. [33] as:

$$L_Z = \frac{8n_1 k_0 r_1^2}{\pi} \quad (4.1)$$

where  $k_0 = 2\pi/\lambda$  is the wavenumber. This quadratic relationship is also suitable in the case of the OFI consisting of the fiber combination SMF-NCF-SMF (SNCS) [34-37]. Studies of self-imaging in a small-core optical fiber interferometer SMF-SCF-SMF (SSCS) may be an effective way to investigate the properties of cladding modes.

In this chapter, a comparative study of the self-imaging of core modes and cladding modes in SSCS, SNCS and SMS structures is presented. The modal characteristics of core modes and cladding modes are analyzed. The discrete

nature and exponential growth behaviour of the self-imaging in the SSCS are predicted independently by both analytical and numerical simulations and verified by spectral measurements. The discrete nature is analyzed based on the constructive interference of adjacent radial modes. The implications of the results for linear and non-linear MMF optics are discussed.

## 4.2 Methods

Figure 4.1 shows three different types of OFIs: SNCS (a), SSCS (b) and SMS (c).

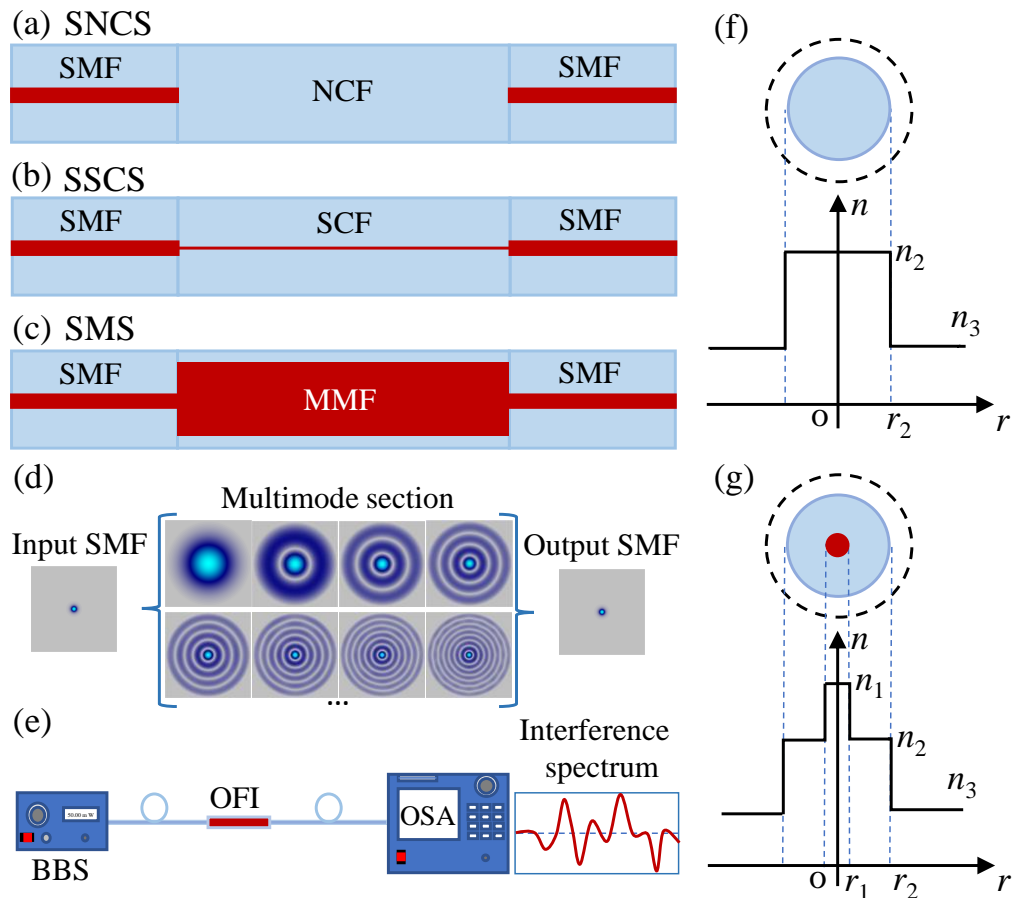


**Figure 4.1** (a), (b) and (c) are the SMF-NCF-SMF (SNCS), SMF-SCF-SMF (SSCS) and SMF-MMF-SMF (SMS), respectively; (d) transverse intensity profiles of fundamental modes in the input and output SMFs, and partial  $LP_{0,n}$  modes in the middle fiber section; (e) experimental setup for characterization of the multimode interference spectra; (f) and (g) are respectively the refractive index profiles along the cross-section radius for an optical fiber placed in air without (NCF) and with a fiber core (SCF and MMF).

In an OFI, the fundamental mode of the input SMF is at first coupled into the guided modes in the middle fiber section and after propagating through the middle fiber section light is then re-coupled into the output SMF. The guided modes in the middle fiber section can be represented as radial  $LP_{0,n}$  modes for the on-axis excitation, as shown in Fig. 4.1(d). Due to the difference in the propagation constants (phase) of  $LP_{0,n}$ , constructive or destructive modal interferences occur along the middle fiber section. At the periodic self-imaging positions, the input field is replicated along the middle fiber section in both amplitude and phase. The structure and material features of the middle fiber section can be determined by measuring its transmission spectrum using an experimental setup shown in Fig. 4.1(e).

The cross-sectional view of the NCF is shown in Fig. 4.1(f) while a general model for the SMF, SCF and MMF is shown in Fig. 4.1(g), where we have assumed that the fibers are placed in air. In the simulations, the  $r_1$  of the middle fiber section of the OFI is the only variable, covering the range of radii from 0  $\mu\text{m}$  to 62.5  $\mu\text{m}$ . The other parameters for the middle section fiber are:  $r_2 = 62.5 \mu\text{m}$ ,  $n_1 = 1.451$  and  $n_2 = 1.445$  ( $\lambda = 1550 \text{ nm}$ ). The parameters of the input/output SMFs are  $r_1 = 4.15 \mu\text{m}$ ,  $r_2 = 62.5 \mu\text{m}$ ,  $n_1 = 1.4504$  and  $n_2 = 1.4447$ . The refractive index of the surrounding medium (air) is  $n_3 = 1$ . It should be noted that both the fibers with  $r_1$  equal to 0  $\mu\text{m}$  and 62.5  $\mu\text{m}$  are NCFs (bare fibers, which in effect possess an air cladding). In this work, the refractive index of NCF with  $r_1 = 0 \mu\text{m}$  is equal to  $n_2 = 1.445$  (same as the  $n_2$  of SCF) as shown in Fig. 4.1(f), while the one with  $r_1 = 62.5 \mu\text{m}$  is equal to 1.451 (the  $n_1$  of SCF).

The simulations were carried out by both analytical and numerical methods, including the effective refractive index ( $n_{\text{eff}}$ ), the transverse intensity profile (TIP), the longitudinal intensity distribution (LID), the on-axis intensity, and the transmission spectra. In the analytical method, a mode propagation analysis (MPA) was employed, with the field functions and the eigenvalue equations for three-layer step-index optical fibers (shown in Fig. 4.1(g)). In the numerical method, a 3-dimensional finite difference beam propagating method (FD-BPM) was used. All the simulations were performed in the scalar mode, under the assumption that the linear polarization (LP) approximation is valid for the fiber due to a relatively small difference between the core and cladding  $n_1$  (1.451) and  $n_2$  (1.445). The LP approximation is also suitable for the NCF (SNCS), due to the fields far from cutoff approximation [35], although the difference between  $n_1$  and  $n_3$  is relatively large. In the BPM simulation of the  $n_{\text{eff}}$ , TIP, LID and on-axis intensity, the mesh size is 0.05  $\mu\text{m}$  along the X and Y directions and 1  $\mu\text{m}$  along the Z direction. In the BPM simulation of transmission spectra, the mesh size is 0.2  $\mu\text{m}$  along the X and Y direction and 4  $\mu\text{m}$  along the Z direction.

In the experiments, the broadband light source (Thorlabs S5FC1005s, 1030 nm–1660 nm) and the optical spectrum analyser (OSA, Agilent 86142B) were used. The middle fiber section in the OFIs were cleaved and the length was measured manually. The error of the length between calculated and experimental value was controlled to within 0.5 mm. The OFIs were fabricated by automated fusion splicing.

### 4.3 Scalar modes in optical fiber interferometers

The first 10  $\text{LP}_{0,n}$  modes, calculated by solving the eigenvalue equations in

Appendix B, are shown as a functions of  $r_1$  in Fig. 4.2 (solid curves). The  $n_{\text{eff}}$  ( $\text{LP}_{0,n}$ ) ( $n = 1, 2, \dots, 8$ ) calculated by BPM are also shown in Fig. 4.2 (scattered circles). Clearly, the results from the analytical method and the BPM are consistent with each other. The corresponding V-parameter values are shown as

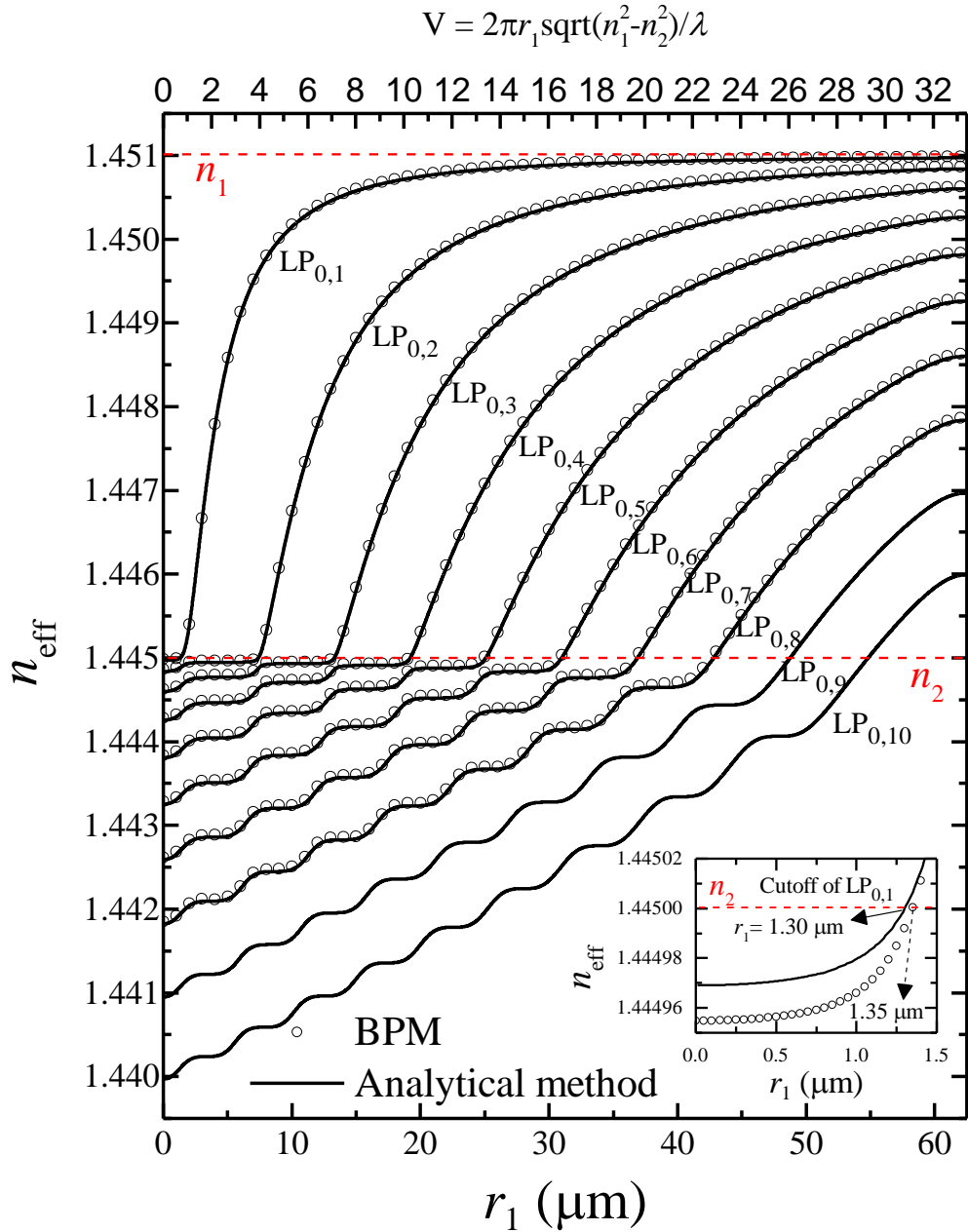


**Figure 4.2** Effective refractive index of  $\text{LP}_{0,n}$  modes as a function of fiber core radius. Solid curves calculated by the analytical method, while the scattered circles are results calculated by the BPM. Inset plot shows that the cutoff of the  $\text{LP}_{0,1}$  mode changing from cladding-type to core-type is  $r_1 = 1.30 \mu\text{m}$  (analytical method) and  $r_1 = 1.35 \mu\text{m}$  (BPM).

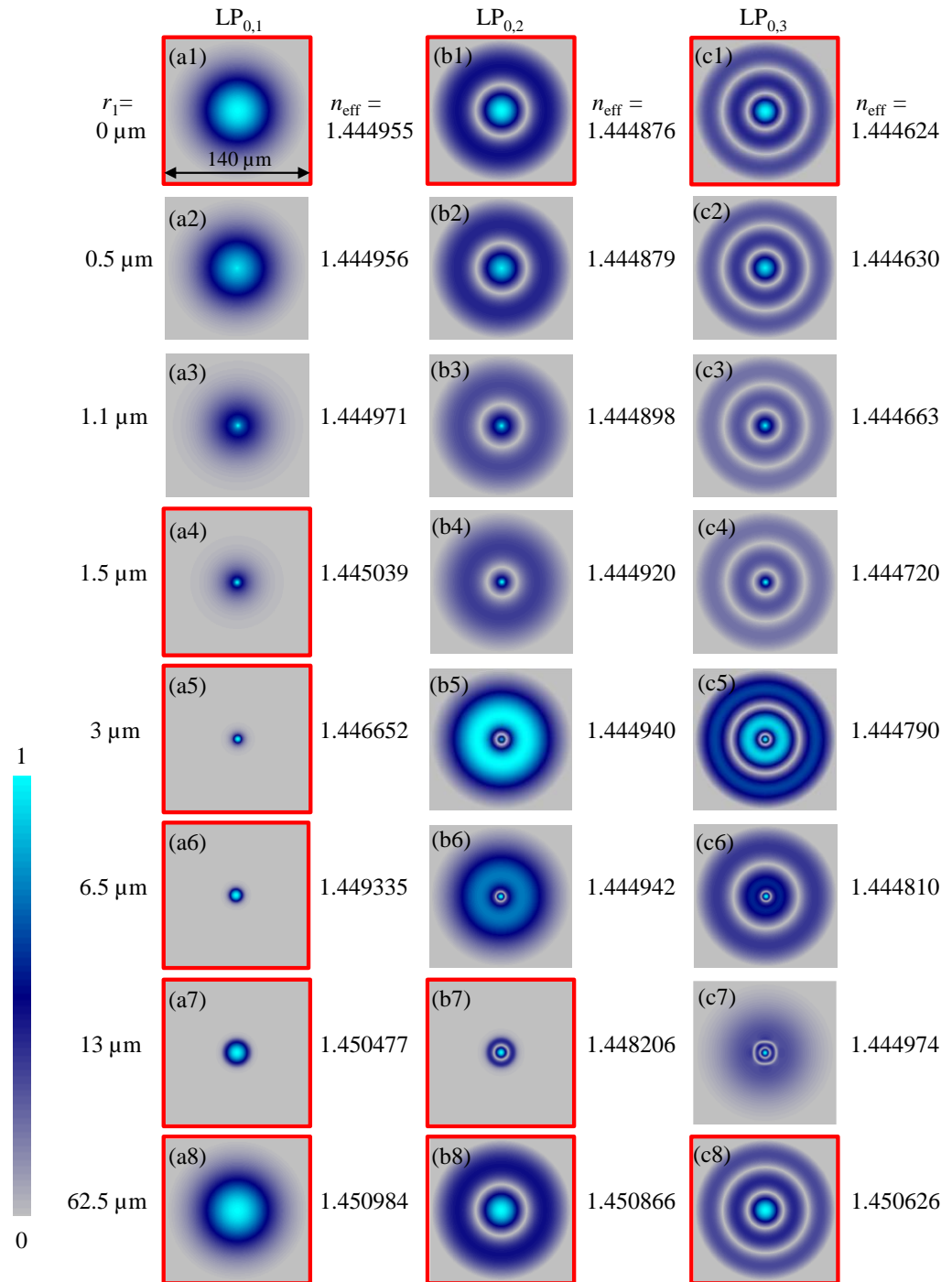
the top axis of the graph.

Figure 4.2 is divided into two parts by the red horizontal dashed lines located at  $n_1$  and  $n_2$ . The region with  $n_2 < n_{\text{eff}} < n_1$  corresponds to the fiber core modes while the region with  $n_{\text{eff}} < n_2$  ( $r_1 \neq 0 \mu\text{m}$ ) corresponds to the cladding modes. All the modes in no-core fibers (NCFs) with  $r_1 = 0 \mu\text{m}$  or  $r_1 = 62.5 \mu\text{m}$  are classified as core-type modes, since no guided mode can exist in an infinite air cladding region. The difference in their values of  $n_{\text{eff}}$  is due to the different refractive indices of the bare fiber, as mentioned in Section 4.2. When a micro/nano- core exists in the central region of the fiber, the fiber is SCF. The SCF studied in this work has a core radius smaller than the cutoff radius of  $\text{LP}_{0,1}$ , where all the guided modes  $\text{LP}_{0,n}$  are cladding-type modes due to  $n_{\text{eff}} < n_2$ . As the  $r_1$  increases, the  $\text{LP}_{0,n}$  modes change from cladding-type modes to core-type modes following the order from low to high. The behaviour of curves in the region  $n_{\text{eff}} < n_2$  shows a feature of mode reorganization (as one cladding mode becomes a core-type mode, the remaining cladding modes are reorganized), which is similar to the mode reorganization in overlay-coated long-period gratings and SMS [25,26].

The cutoff of  $\text{LP}_{0,1}$  calculated by the BPM is found at about  $r_1 = 1.35 \mu\text{m}$  as seen in the inset graph of Fig. 4.2. This is slightly larger than the value calculated by the analytical method ( $r_1 = 1.30 \mu\text{m}$ ). The difference between these two results may be attributed to the mesh size used in the former method. The mesh size in the numerical simulation may affect the accuracy. In this work, several different mesh sizes were tried but in the end the value that provided the best tradeoff between accuracy and computational time was selected. It should be noted that the mesh size in the simulation here is the same as that in the simulation of on-

axis intensity, from which the self-imaging period is determined. The  $V$ -parameter is smaller than 0.7214 for the optical fibers with  $r_1 < 1.35 \mu\text{m}$ .

Figure 4.3 shows the field distributions for the modes  $\text{LP}_{0,1}$ ,  $\text{LP}_{0,2}$ , and  $\text{LP}_{0,3}$  for several core radii, calculated by the BPM. The core-type modes are indicated by red frames, while the remaining modes are cladding-type modes. The field profiles in Fig. 4.3 show that the energy of core modes is concentrated mainly inside the fiber core while the part distributed inside the cladding region decreases exponentially with increasing distance from the core as demonstrated in Ref. [27]. The field energy in the cladding modes can extend throughout the core and cladding regions. All the modes in the NCF indicated by  $r_1 = 0 \mu\text{m}$  are core-type modes as shown in Figs. 4.3(a1), 4.3(b1) and 4.3(c1), where the field is extended throughout the whole fiber cross section. As the  $r_1$  increases from 0 to  $1.1 \mu\text{m}$ , the  $n_{\text{eff}}$  of modes  $\text{LP}_{0,1}$ ,  $\text{LP}_{0,2}$  and  $\text{LP}_{0,3}$  increase while their central intensity (bright circle) area reduces. The  $\text{LP}_{0,1}$  becomes a core-type mode beyond the value of  $r_1$  around  $1.3 \mu\text{m}$ . As shown in Figs. 4.3(a4)-4.3(a7), the energy of  $\text{LP}_{0,1}$  is concentrated mainly inside the fiber core. The  $\text{LP}_{0,2}$  changes into a core-type mode as soon as the core radius becomes large enough. Fig. 4.3(b7) shows the field distribution of the core-type  $\text{LP}_{0,2}$  mode with  $r_1 = 13 \mu\text{m}$ , where the energy distribution area including both the central circle and the outer ring is concentrated mainly inside the fiber core. When  $r_1$  increases to  $62.5 \mu\text{m}$ , the fiber becomes an NCF again, for which all the modes belong to core-type modes similar to NCF with  $r_1 = 0 \mu\text{m}$ , shown in Figs. 4.3(a8), 4.3(b8) and 4.3(c8).



**Figure 4.3** Field distributions of the modes  $LP_{0,1}$  (a1-a8),  $LP_{0,2}$  (b1-b8), and  $LP_{0,3}$  (a1-c8) for several different  $r_1$  calculated by the BPM. The modes a1, b1 c1, a8, b8 and c8 in the no-core fibers are core-type modes; a4-a7, b7 are also core-type modes for  $n_{\text{eff}} > 1.445$ ; the remaining are cladding-type modes with  $n_{\text{eff}} < 1.445$ . (Core-type modes are indicated by red frames.)

## 4.4 The self-imaging periods

The field of the fundamental mode of the input SMF is denoted by  $E_s(r)$ . The excited optical field in the middle fiber section of OFIs can be represented by the superposition of  $E_{0,n}(LP_{0,n})$  and shown as:

$$E_s(r, 0) = \sum_{n=1}^N c_n E_{0,n}(r) \quad (4.2)$$

where  $E_{0,n}$  is expressed by Eqs. (B.1) and (B.2) in Appendix B, and  $c_n$  is the excitation coefficient between the fundamental mode of SMF and the  $LP_{0,n}$  in the middle fiber section, which is calculated as follows:

$$c_n = \sqrt{\eta_n} \quad (4.3)$$

$$\eta_n = \frac{\left| \int_0^\infty E_s(r) E_{0,n}(r) r dr \right|^2}{\int_0^\infty |E_s(r)|^2 r dr \int_0^\infty |E_{0,n}(r)|^2 r dr} \quad (4.4)$$

The field propagating along the middle fiber section can be written as follows:

$$E(r, z) = \sum_{n=1}^N c_n E_{0,n}(r) \exp(j\beta_{0,n}z) \quad (4.5)$$

where  $\beta_{0,n} = k_0 n_{\text{eff}}(LP_{0,n})$  is the longitudinal propagation constant of  $LP_{0,n}$ . The starting point along the Z-axis is at the splice between the input SMF and the middle fiber section. The on-axis intensity (normalized to the input power) along the propagation distance ‘Z’ inside the middle fiber section can be calculated as follows:

$$I(z) = \frac{\left| \int_0^\infty E_s(r, 0) E(r, z) r dr \right|^2}{\int_0^\infty |E_s(r, 0)|^2 r dr \int_0^\infty |E(r, z)|^2 r dr}. \quad (4.6)$$

Figures 4.4(a), 4.4(b) and 4.4(e) show respectively the TIP of the optical field in X-Y plane, the LID in X-Z plane and the on-axis intensity along the propagation

distance in the middle fiber section (NCF) of the SNCS. The light field is focused at the center of the TIP at the position  $Z = 58.64$  mm, coinciding with the profile of the input field (the fundamental mode of the input SMF) at the position  $Z = 0$ , as shown in Fig. 4.4(a). The on-axis intensity peak at the position  $Z = 58.64$  mm (indicated by the black diamond symbol in Fig. 4.4(e)) is equal to 0.98 of the input power, which is clearly larger than those of the neighboring maxima, corresponding to bright points at the same position in Figs. 4.4(a) and 4.4(b). It should be noted that achieving 100% perfect self-imaging (the normalized power is equal to 1) is impossible due to phase mismatches [36]. These features are consistent with the results in Refs. [34,35], indicating that an explicit self-imaging of the input field is formed and the self-imaging period  $L_Z$  for SNCS is equal to 58.64 mm. The result of  $L_Z = 58.64$  mm is in reasonable agreement with the result of  $L_Z = 58.24$  mm calculated by Eq. (4.1).

One self-imaging period of the SNCS can be divided into four segments with equal lengths of  $L_s$  ( $= L_Z/4$ ). Unlike the light field focused at the center of the TIP (point-like image) at the self-imaging position ( $Z = 4L_Z$ ) shown in Fig. 4.4(a), light fields at positions  $Z = 1L_s$ ,  $2L_s$  and  $3L_s$  are mainly focused within a ring area with a certain width (ring-like image), according to the results of lateral field profiles calculated analytically in Ref. [34].

Similarly, it can be deduced from Figs. 4.4(c), 4.4(d) and 4.4(i) that the other explicit self-imaging point is formed at  $Z = 5L_s$  (73.12 mm) in the case of SSCS

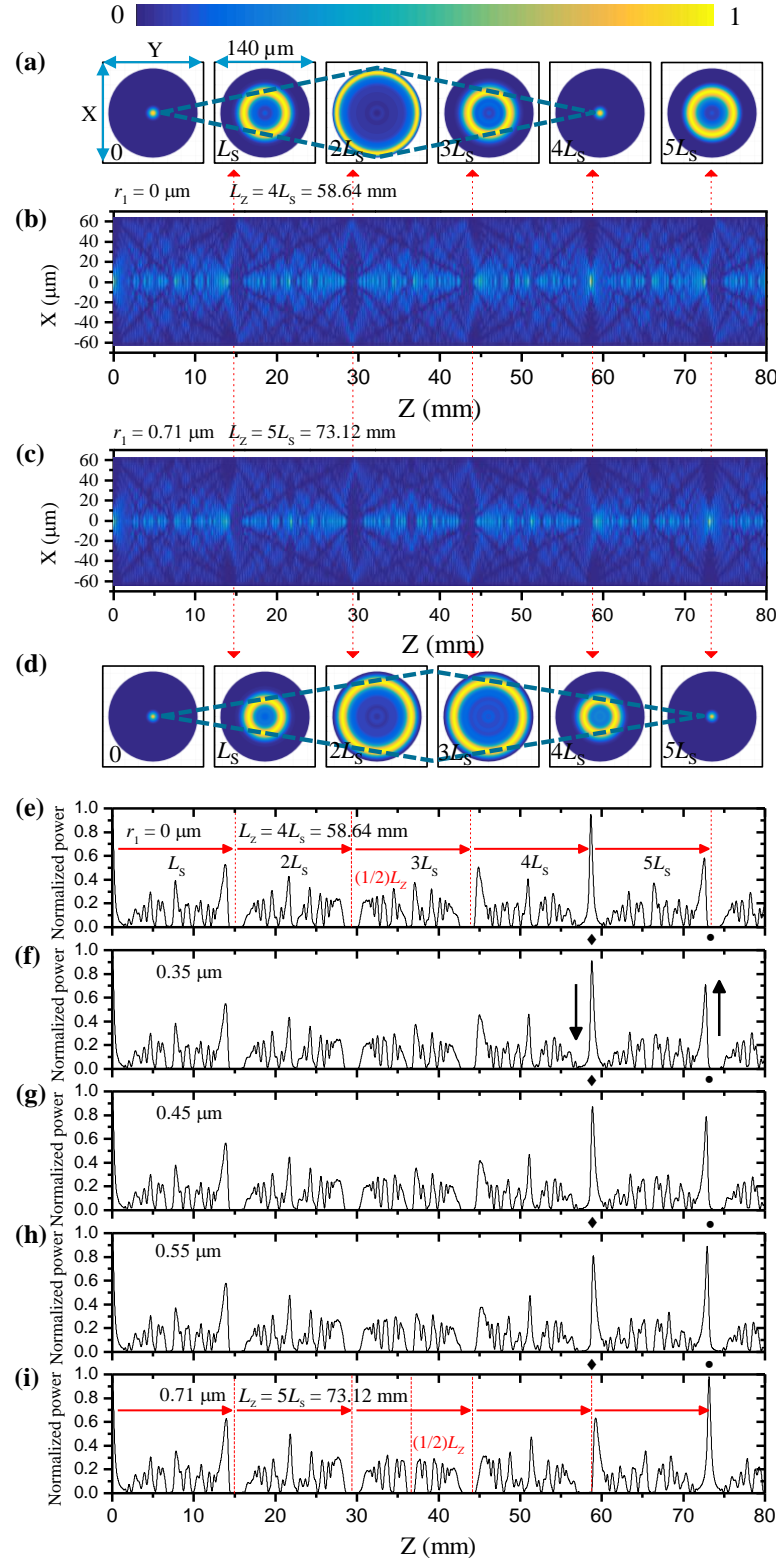


**Figure 4.4** Analytical results: (a), (b) and (e) are respectively the transverse intensity profile (TIP), the longitudinal intensity distribution (LID) and the on-axis intensity along the propagation distance inside the NCF of SNCS ( $r_1 = 0 \mu\text{m}$ ). (f), (g) and (h) are respectively the on-axis intensities inside the SCF of SSCS with the  $r_1$  equal to  $0.35 \mu\text{m}$ ,  $0.45 \mu\text{m}$  and  $0.55 \mu\text{m}$ . (d), (c) and (i) are respectively the simulated TIPs, the LIDs and the on-axis intensities inside the SCF of SSCS with the  $r_1$  equal to  $0.71 \mu\text{m}$ .

with  $r_1 = 0.71 \mu\text{m}$ . For the intermediate transition state where  $0 \mu\text{m} < r_1 < 0.71 \mu\text{m}$  as shown in Figs. 4.4(f)-4.4(h), no self-imaging point exists. The decision was based on the following considerations. As the  $r_1$  increases above  $0 \mu\text{m}$ , the intensity of the peak at the position  $Z = 4L_s$  (indicated by the black diamond symbols) decreases monotonically while the value of the peak at  $Z = 5L_s$  (indicated by the black dot symbols) increases monotonically, as shown in Figs. 4.4(e)-4.4(i). When the critical point ( $r_1 = 0.71 \mu\text{m}$ ) is reached, the intensity value at  $Z = 5L_s$  achieves its maximum while the value at  $Z = 4L_s$  decreases as shown in Fig. 4.4(i).

For clarity, the intensities of the peaks around the positions  $Z = 4L_s$  and  $Z = 5L_s$  as shown in Figs. 4.4(e)-4.4(i) are respectively redrawn in Figs. 4.5(a) and 4.5(b) as a function of  $r_1$ . The  $r_1$  of the peak point for the curve in Fig. 4.5(b) corresponds to the self-imaging radius ( $r_1 = 0.71 \mu\text{m}$ ). Based on the monotonic and deterministic evolution of the on-axis intensity, it can be deduced that the explicit self-imaging is only formed at a critical core radius such as  $r_1 = 0.71 \mu\text{m}$ . In other words, the explicit self-imaging in the SSCS only occurs at certain discrete values of the core radius of the SCF.

As the  $r_1$  increases, the  $L_z$  will also increase. Another set of values for  $r_1$  allowing one to achieve explicit self-imaging are shown in Fig. 4.6, where the  $L_z$  grows up to  $6L_s$ ,  $7L_s$ ,  $8L_s$ ,  $9L_s$  and  $10L_s$  for  $r_1$  equal to  $0.91 \mu\text{m}$  (Fig. 4.6(a)),  $1.02 \mu\text{m}$  (Fig. 4.6(b)),  $1.11 \mu\text{m}$  (Fig. 4.6(c)),  $1.18 \mu\text{m}$  (Fig. 4.6(d)) and  $1.23 \mu\text{m}$  (Fig. 4.6(e)). These self-imaging points respectively correspond to the peak points for the curves shown in Figs. 4.5(c), 4.5(d), 4.5(e), 4.5(f) and 4.5(g). Beyond the value of  $r_1 = 1.23 \mu\text{m}$ , the intensity of the peak around  $Z = 10L_s$

decreases as the  $r_1$  increases, as shown in Fig. 4.5(g). The intensity of the peak around the position  $Z = 11L_s$  shown in Fig. 4.5(h) is always smaller than the value at position  $Z = 10L_s$  in Fig. 4.5(g). These features indicate that there is no explicit self-imaging at the position  $Z = 11L_s$ .

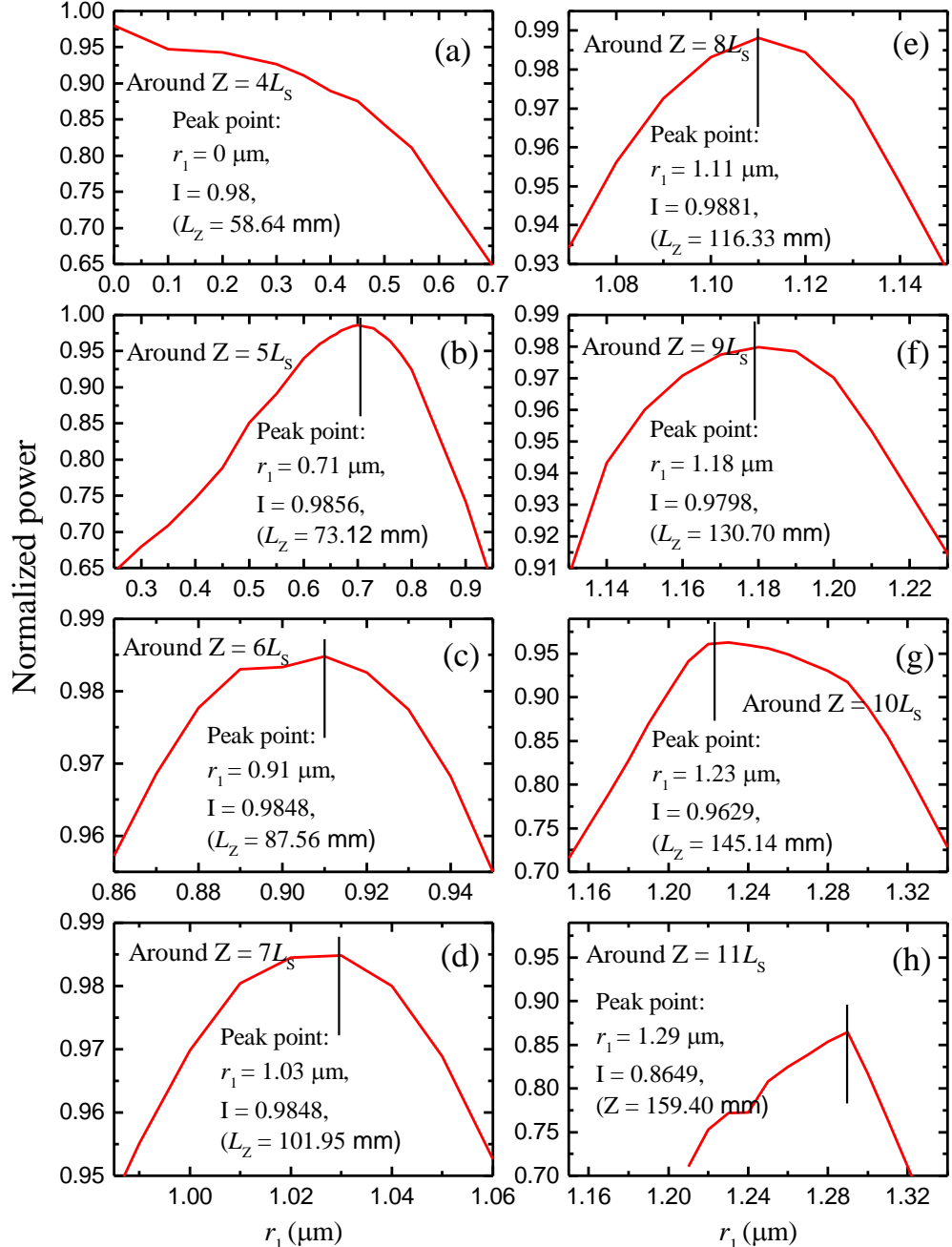


**Figure 4.5** Analytical results: (a)-(h) show the intensity 'I' of peak around the positions  $Z = nL_s$ ,  $n = 4, 5, \dots, 11$  as a function of  $r_1$ . The peak points in (a)-(g) respectively correspond to the self-imaging points as shown in Figs. 4.4(e), 4.4(i) and 4.6(a)-4.6(e).

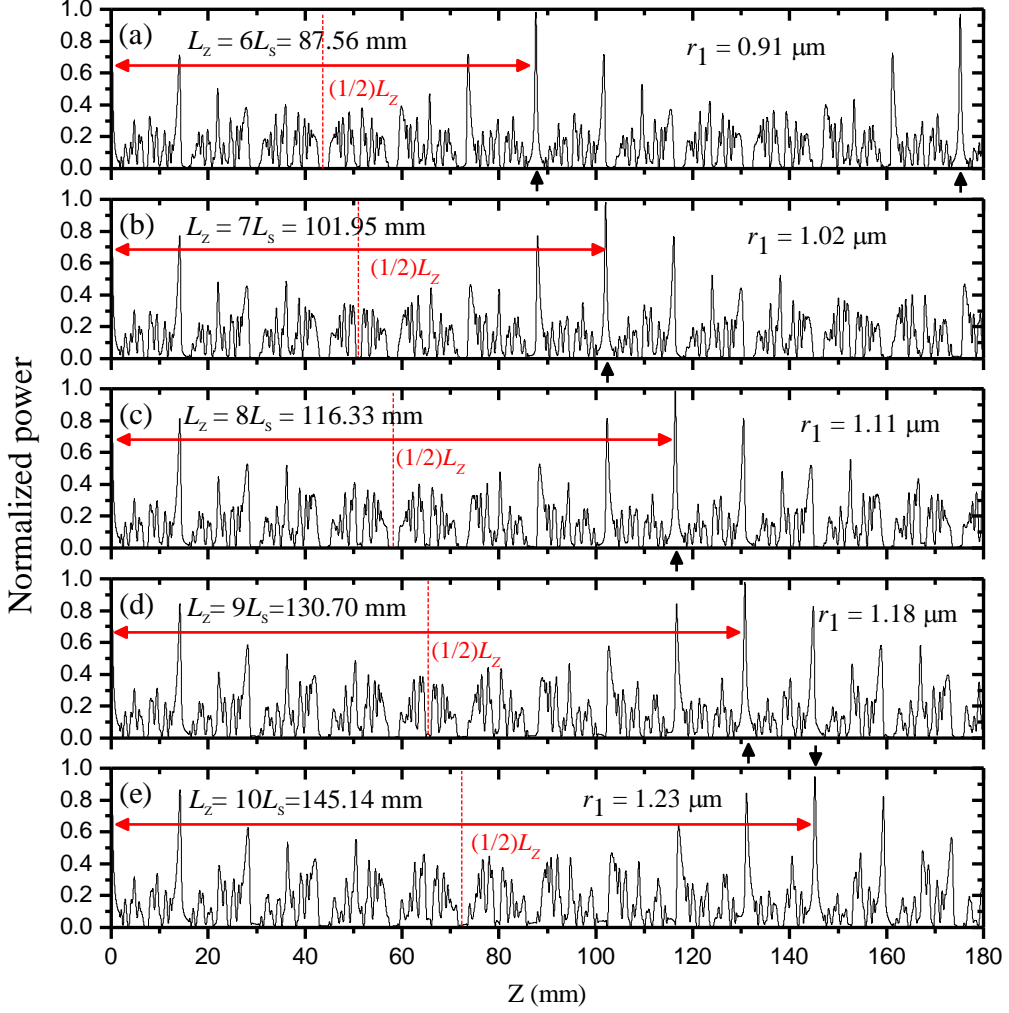


**Figure 4.6** Analytical results: the on-axis intensities inside the SCF of SSCS with the  $r_1$  equal to (a) 0.91  $\mu\text{m}$ , (b) 1.02  $\mu\text{m}$ , (c) 1.11  $\mu\text{m}$ , (d) 1.18  $\mu\text{m}$  and (e) 1.23  $\mu\text{m}$ .

The discrete self-imaging phenomenon was also confirmed by the BPM. The results are shown in Fig. 4.7, where the  $L_z$  grows as  $4L_s$ ,  $5L_s$ ,  $6L_s$ ,  $7L_s$ ,  $8L_s$ ,  $9L_s$  and up to  $10L_s$  for  $r_1$  equal to 0  $\mu\text{m}$  (SNCS, Fig. 4.7(a)), 0.73  $\mu\text{m}$  (Fig. 4.7(b)), 0.92  $\mu\text{m}$  (Fig. 4.7(c)), 1.04  $\mu\text{m}$  (Fig. 4.7(d)), 1.12  $\mu\text{m}$  (Fig. 4.7(e)), 1.20  $\mu\text{m}$  (Fig. 4.7(f)) and 1.27  $\mu\text{m}$  (Fig. 4.7(g)). Both the analytical and the BPM results indicate that the self-imaging period of the SSCS is discrete and is closely related to that of the SNCS ( $r_1 = 0 \mu\text{m}$ ):  $L_z(\text{SSCS}) = (1+q/4)L_z(\text{SNCS}) = (4+q)L_s$ , where “q” is a positive integer and  $1 \leq q \leq 6$ .

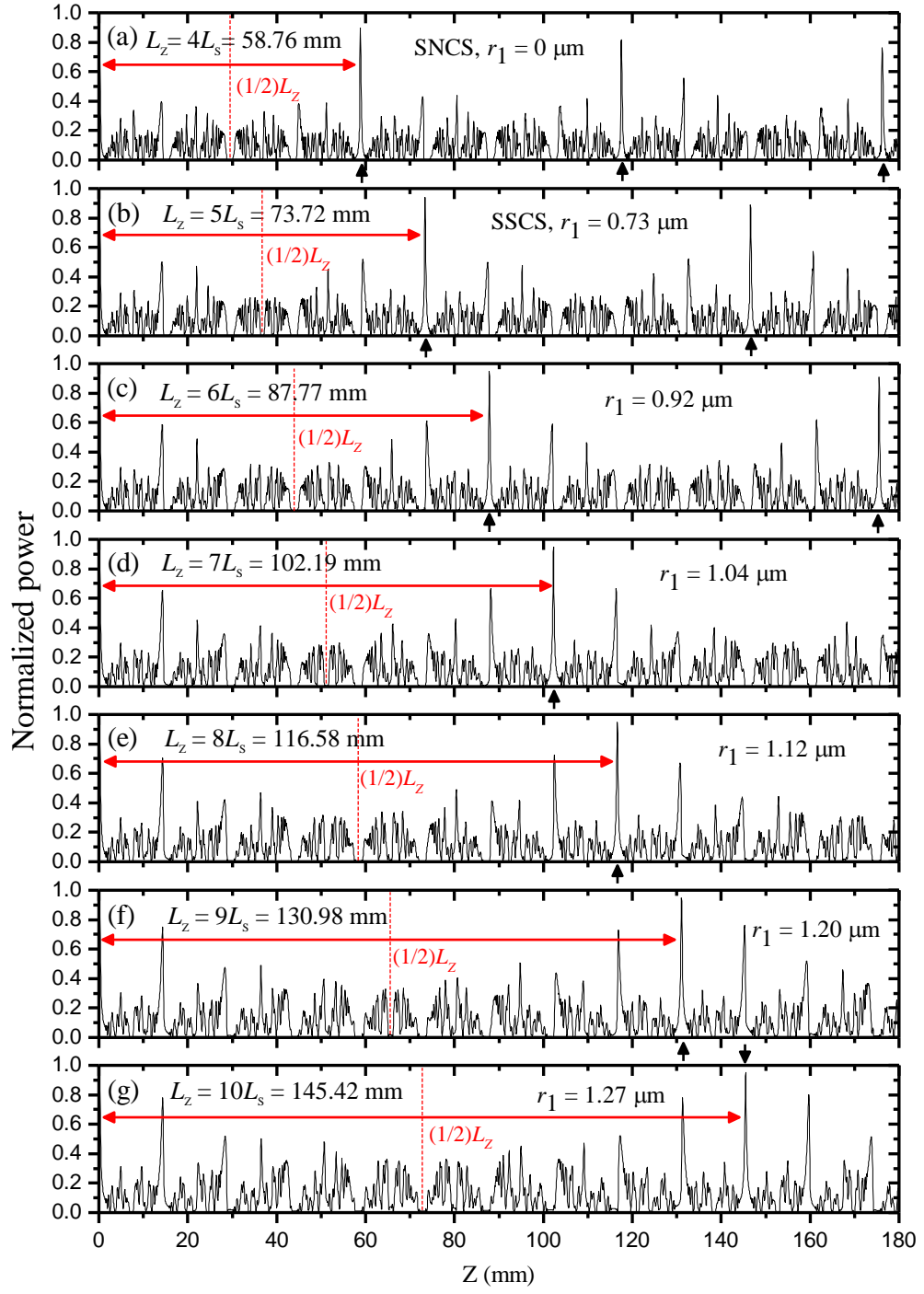


**Figure 4.7** BPM results: the on-axis intensities inside (a) the NCF of SNCS, the SCF of SSCS with the  $r_1$  equal to (b)  $0.73 \mu\text{m}$ , (c)  $0.92 \mu\text{m}$ , (d)  $1.04 \mu\text{m}$ , (e)  $1.12 \mu\text{m}$ , (f)  $1.20 \mu\text{m}$  and (g)  $1.27 \mu\text{m}$ .

The values of the discrete self-imaging periods calculated both analytically and using BPM were extracted and fitted with an exponential function, as shown in Fig. 4.8. The fitting function can be written as:

$$L_Z = L_{Z0} + B_1 \exp\left(\frac{r_1}{t_1}\right) \quad (4.7)$$

For the case of analytical method, the R-squared value is 0.99976;  $B_1 = 1.53093 \pm 0.10829$ ;  $t_1 = 0.30396 \pm 0.00511$ ;  $L_{Z0} = 57.15441 \pm 0.54124$  mm. For the case of BPM, the R-squared value is 0.99804;  $B_1 = 2.17781 \pm 0.40074$ ;  $t_1 = 0.3404 \pm 0.01606$ ;  $L_{Z0} = 55.92114 \pm 1.62183$  mm. In both cases,  $r_1$  is a set of discrete values. The  $L_{Z0}$  in both cases is close to the  $L_Z$  of SNCS ( $r_1 = 0 \mu\text{m}$ ). The results calculated independently by two different methods are highly consistent, although there is a slight difference between the results at the relatively large  $r_1$ . The difference may be due to the mesh size, which affects the accuracy of the numerical results.

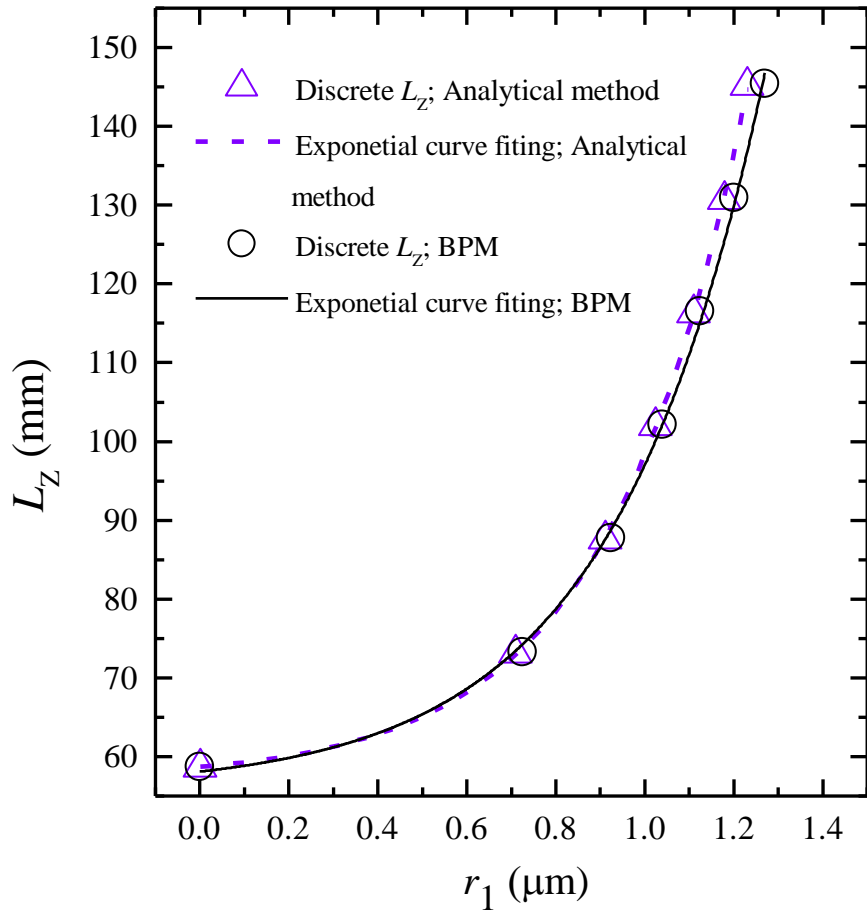


**Figure 4.8** Discrete and exponential growth of the self-imaging period  $L_Z$  for the SNCS ( $r_1 = 0 \mu\text{m}$ ) and the SSCS versus  $r_1$ , calculated both analytically and using BPM.

## 4.5 Physical interpretation of the discrete self-imaging

The light field in the middle fiber section of the OFI is a superposition of all the guided modes  $LP_{0,n}$ . At a self-imaging position, constructive interference occurs for all of the modes. The self-imaging period  $L_Z$  in SMS is closely related to the constructive interference length  $L_n$  of two adjacent guided modes [33].  $L_n$  is calculated for two adjacent modes ( $LP_{0,n-1}$  and  $LP_{0,n}$ ) when their phase difference equals  $2\pi$ :

$$L_n = \frac{2\pi}{(\beta_{n-1} - \beta_n)} = \frac{\lambda}{[n_{\text{eff}}(LP_{0,n-1}) - n_{\text{eff}}(LP_{0,n})]}, n = 2, 3, \dots \quad (4.8)$$

These two adjacent guided modes will also experience constructive interference at the position  $qL_n$  ( $q = 1, 2, \dots$  is an integer number). It is noted that the  $L_Z$  is an integer multiple of  $L_p$ :  $L_Z = (4p-3)L_p$ , where the mode number  $p$  is related to the mode  $LP_{0,p}$  holding the highest coupling efficiency [33]. However, the  $L_Z$  may be not restricted to the mode with the highest coupling efficiency. Using  $L_n$  of any two adjacent modes, the corresponding length  $L_{Zn}$  is calculated as:

$$L_{Zn} = (4n - 3)L_n, n = 2, 3, \dots \quad (4.9)$$

Applying the  $n_{\text{eff}}$  calculated by the analytical method, the results for  $L_{Zn}$  are shown in Fig. 4.9(a), with a comparison to  $L_Z$  calculated by Eq. (4.1) (indicated by the diamonds). It is interesting that the part of the curves below the red dashed line overlaps with the  $L_Z$  calculated by Eq. (4.1). The overlapped part as redrawn in Fig. 4.9(b) corresponds to the pure core modes (the range of  $n_2 < n_{\text{eff}} < n_1$  in Fig. 4.2). The equation (4.1) is derived from the 2-layer fiber model, where only the core modes are considered. The results indicate that the superposition of the pure core modes obeys the quadratic relationship between  $L_Z$  and  $r_1$  shown in Eq.

(4.1) and the rule of  $L_{Zn} = (4n - 3)L_n$ .

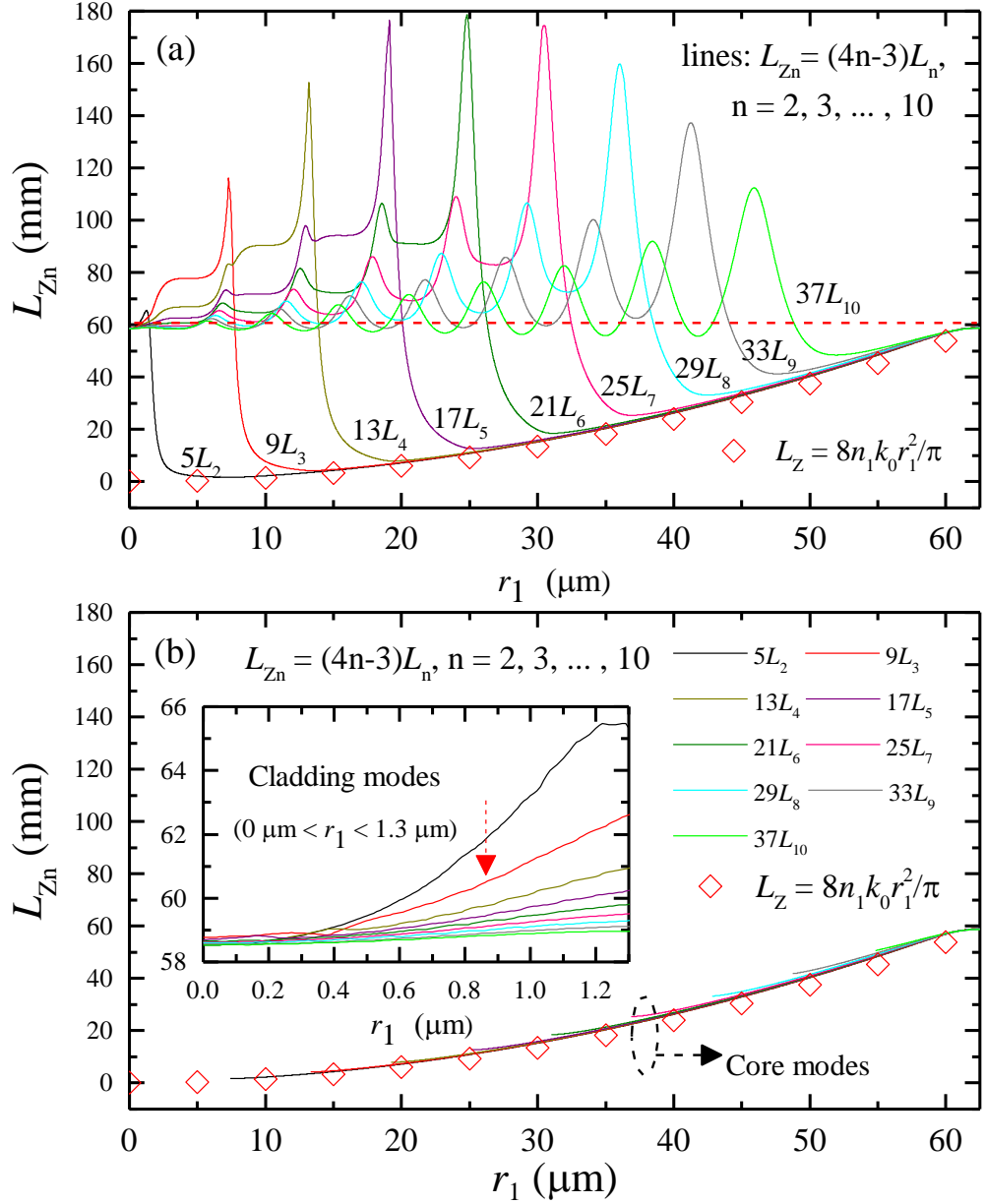


**Figure 4.9** (a)  $L_{Zn}$  calculated by Eq. (4.9):  $L_{Zn} = (4n - 3)L_n$  with the  $n_{\text{eff}}(\text{LP}_{0,n})$  determined from the analytical results in Fig. 4.2. The main graph of (b) shows the parts extracted from (a), related to the pure core modes. Inset of (b) shows the part extracted from (a), related to the cladding modes of SCF with  $0 \mu\text{m} < r_1 < 1.3 \mu\text{m}$  and the core modes of NCF with  $r_1 = 0 \mu\text{m}$ .

On the other hand, those parts of the curves in Fig. 4.9(a) that deviate from the  $L_Z$  represented by Eq. (4.1) correspond to the cladding modes. The curves above

the red dash line are separated from each other and these phenomena may be due to the mode transition and the mode reorganization shown in Fig. 4.2. The part of Fig. 4.9(a) for  $r_1 < 1.3 \mu\text{m}$  is shown in the inset of Fig. 4.9(b), where the lines of  $L_{zn}$  ( $n = 2, 3, \dots, 10$ ) become closer as the  $r_1$  decreases. At the point ( $r_1 = 0 \mu\text{m}$ ), the lines converge to the value of  $L_z = (4n - 3)L_n$ , the self-imaging period of NCF. The results indicate that the cladding modes in SCF with the micro/nano-core ( $0 \mu\text{m} < r_1 < 1.3 \mu\text{m}$ ) do not obey the quadratic relationship between the self-imaging period of the core modes and the core radius.

The derivation of Eqs. (4.1) and (4.9) is based on an approximate expression for the  $n_{\text{eff}}$  of the core modes related to the roots of equation  $J_0 = 0$  [33]. Although there are some improvements, the simulations of SMS and SNCS in most publications are still based on approximate expressions for the core modes [35], [37]. To the best of author's knowledge, there has been no (approximate) analytical expression for the cladding modes in optical fibers to date. The reason may be due to the complexity of the field function and the eigenvalue equation for the cladding modes as discussed in Appendix B, which is closely related to the function  $Y_0$  in addition to  $J_0$  and  $K_0$ .

Although there has been no explicit analytical expression for  $n_{\text{eff}}$  of cladding modes until now, some indications can be obtained from the simulation results. The arguments  $D_n$  ( $L_z = D_n L_n$ ), between the value of self-imaging period  $L_z$  from analytical results in Fig. 4.8 and the  $L_n$  calculated by Eq. (4.8), are shown in Table 4.1. Clearly,  $D_n$  is close to an integer ‘*round* ( $D_n$ )’ as shown in Table 4.2, where the degree of deviation:  $|D_n - \text{round}(D_n)| / D_n < 1\%$ . The degree of deviation (the difference between  $D_n$  and ‘*round* ( $D_n$ )’) may be attributed to two

**Table 4.1** The arguments between the discrete self-imaging periods and the constructive interference lengths

$r_1$ (μm)	$L_Z$ (mm)	$D_2 = L_Z/L_2$	$D_3 = L_Z/L_3$	$D_4 = L_Z/L_4$	$D_5 = L_Z/L_5$	$D_6 = L_Z/L_6$	$D_7 = L_Z/L_7$	$D_8 = L_Z/L_8$	$D_9 = L_Z/L_9$	$D_{10} = L_Z/L_{10}$
0	58.636	5.00941	8.97887	12.99934	16.98053	20.99547	25.00504	29.02002	33.04142	37.06998
0.71	73.116	6.03221	10.99033	15.9949	20.99286	25.99331	31.00182	36.0065	41.03591	46.04113
0.91	87.562	7.0293	12.98382	19.0031	24.99515	30.99758	36.99459	43.00676	49.0406	55.05314
1.02	101.953	8.04557	14.97467	22.00988	29.00472	35.99829	42.99714	50.00864	57.03445	64.05008
1.11	116.331	9.01812	16.97317	25.01795	32.99923	40.99165	48.99595	57.00807	65.01083	73.03617
1.18	130.702	10.03411	18.95392	28.0204	37.01572	45.9954	54.98189	63.98647	73.01578	82.03356
1.23	145.141	11.08954	20.92305	31.00198	41.01084	50.99464	61.00377	71.01788	81.03748	91.07236

**Table 4.2** The integer arguments between the discrete self-imaging periods and the constructive interference lengths

$r_1$ (μm)	<i>Round</i> ( $D_2$ )	<i>Round</i> ( $D_3$ )	<i>Round</i> ( $D_4$ )	<i>Round</i> ( $D_5$ )	<i>Round</i> ( $D_6$ )	<i>Round</i> ( $D_7$ )	<i>Round</i> ( $D_8$ )	<i>Round</i> ( $D_9$ )	<i>Round</i> ( $D_{10}$ )	<i>Round</i> ( $D_n$ )
0	5	9	13	17	21	25	29	33	37	(4n-3)
0.71	6	11	16	21	26	31	36	41	46	(5n-4)
0.91	7	13	19	25	31	37	43	49	55	(6n-5)
1.02	8	15	22	29	36	43	50	57	64	(7n-6)
1.11	9	17	25	33	41	49	57	65	73	(8n-7)
1.18	10	19	28	37	46	55	64	73	82	(9n-8)
1.23	11	21	31	41	51	61	71	81	91	(10n-9)

causes: one is the errors in the calculation of the effective refractive index; the other is the phase mismatches among the excited modes, which always exist although they are quite small [36]. The 100% perfect self-imaging is impossible due to phase mismatches [36], therefore 100% integer may be also impossible.

From Table 4.2, it is easy to obtain the expressions similar to Eq. (4.9), as follows:

$$L_{Zn} = (5n - 4)L_n, n = 2, 3, \dots, 10, \text{ for } L_Z = 5L_S \quad (4.10)$$

$$L_{Zn} = (6n - 5)L_n, n = 2, 3, \dots, 10, \text{ for } L_Z = 6L_S \quad (4.11)$$

$$L_{Zn} = (7n - 6)L_n, n = 2, 3, \dots, 10, \text{ for } L_Z = 7L_S \quad (4.12)$$

$$L_{Zn} = (8n - 7)L_n, n = 2, 3, \dots, 10, \text{ for } L_Z = 8L_S \quad (4.13)$$

$$L_{Zn} = (9n - 8)L_n, n = 2, 3, \dots, 10, \text{ for } L_Z = 9L_S \quad (4.14)$$

$$L_{Zn} = (10n - 9)L_n, n = 2, 3, \dots, 10, \text{ for } L_Z = 10L_S \quad (4.15)$$

The groups of lines calculated by Eqs. (4.9)-(4.15) are plotted together in Fig. 4.10. As with the group of lines converged at the position ( $r_1 = 0 \mu\text{m}$ ,  $L_Z = 58.64 \text{ mm}$ ) characterized by  $(4n-3)L_n$ , each of other groups also has one intersect point indicated by a violet triangle symbol. The violet triangle symbols and the violet dashed line are respectively the calculated and the exponential fitting values of the self-imaging points (radius and period) shown in the Fig. 4.8.

The difference between any two adjacent  $L_{Zn}$  among Eqs. (4.9)-(4.15) is equal to:

$$\Delta L_{Zn} = (n - 1)L_n, n = 2, 3, \dots, 10. \quad (4.16)$$

For  $n = 2$ ,  $\Delta L_{Zn} = L_2$ , which is one constructive interference length of  $\text{LP}_{0,1}$  and  $\text{LP}_{0,2}$ .  $L_2$  is longer than  $L_n$  ( $n > 2$ ), deduced from Eq. (4.8). As shown in Eqs.

(4.10)-(4.16) and Table 4.2, the self-imaging period grows as  $5L_2$ ,  $6L_2$ , ..., and up to  $11L_2$ . Therefore, it can be deduced that  $L_2$  is the shortest distance change possible if self-imaging is to occur. Larger distance changes of the self-imaging period must be an integer multiple of  $L_2$ . The results indicate that there is no other self-imaging position between any two adjacent periods indicated by Eqs. (4.9)-(4.15). For example, there is no self-imaging with a period between  $L_z = 4L_s = 5L_2$  and  $L_z = 5L_s = 6L_2$ , from Eqs. (4.9) and (4.10). Therefore, the self-imaging of pure cladding modes in SSCS is discrete.

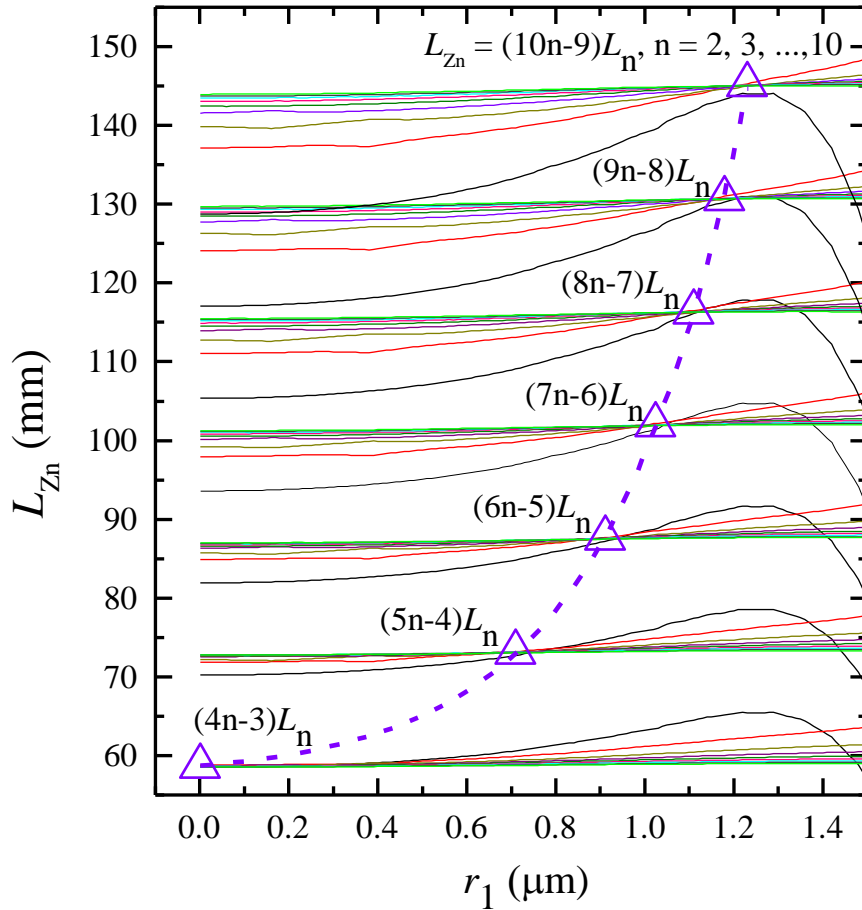


**Figure 4.10**  $L_{Zn}$  calculated by Eqs. (4.9)-(4.15). The violet triangle symbols and the violet dashed line are respectively calculated and exponential fitting values of self-imaging (radius and period) the same as in Fig. 4.8. The color of lines  $L_{Zn}$  with the same mode number ‘ $n$ ’ is consistent with that in Fig. 4.9.

## 4.6 Experimental investigation

To verify the above results, simulations and the experimental measurements of the transmission spectra were carried out for both the SSCS and the SNCS structures. The BPM were used in this part for its convenience and straightforward simulation of the spectrum. In the experiments, fiber type SMF28<sup>TM</sup> (from Corning) was used as the SMF, fiber type FG125LA (from Thorlabs) was used as the NCF ( $r_1 = 0 \mu\text{m}$ ) and fiber type SM450 (Thorlabs) was used as the SCF. The  $r_1$  of SM450 is about  $1.1 \mu\text{m}$ , which is close to the discrete value of self-imaging radius  $r_1 = 1.12 \mu\text{m}$  (in BPM results), of which the self-imaging period is  $L_z = 8L_s$  as shown in Fig. 4.7(e). The remaining fiber parameters for the SMF28<sup>TM</sup>, the FG125LA and the SM450 are same as those used in simulations, shown in Section 4.2. Figs. 4.11(a) and 4.11(b) are the on-axis intensity along the propagation distance inside the middle fiber section of the SNCS ( $r_1 = 0 \mu\text{m}$ ) and SSCS ( $r_1 = 1.1 \mu\text{m}$ ), respectively. The  $L_z$  of the SSCS ( $r_1 = 1.1 \mu\text{m}$ ) is equal to  $116.66 \text{ mm}$  ( $8L_s$ ,  $L_s = 14.58 \text{ mm}$ ), which is nearly double the  $L_z$  for the SNCS equal to  $58.76 \text{ mm}$  ( $4L_s$ ,  $L_s = 14.69 \text{ mm}$ ). 16 samples were studied in two groups for the SNCS/SSCS with the lengths of the middle fiber sections (NCF/SCF) equal to the integer multiples of  $L_s$ :  $1L_s$ ,  $2L_s$ , ...,  $8L_s$ . The TIPs of the middle fiber section were also calculated for the SNCS/SSCS at the positions  $L = nL_s$  ( $n = 1, 2, \dots, 8$ ), where the light wavelength was set at  $1550 \text{ nm}$ , as shown in the Figs. 4.11(c0)-4.11(c8) and 4.11(d0)-4.11(d8). The transmission spectra were simulated (red lines) and measured (black lines and circles) in the wavelength range from  $1450 \text{ nm}$  to  $1650 \text{ nm}$ , as shown in Figs. 4.11(e1)-4.11(e8) and 4.11(f1)-4.11(f8).

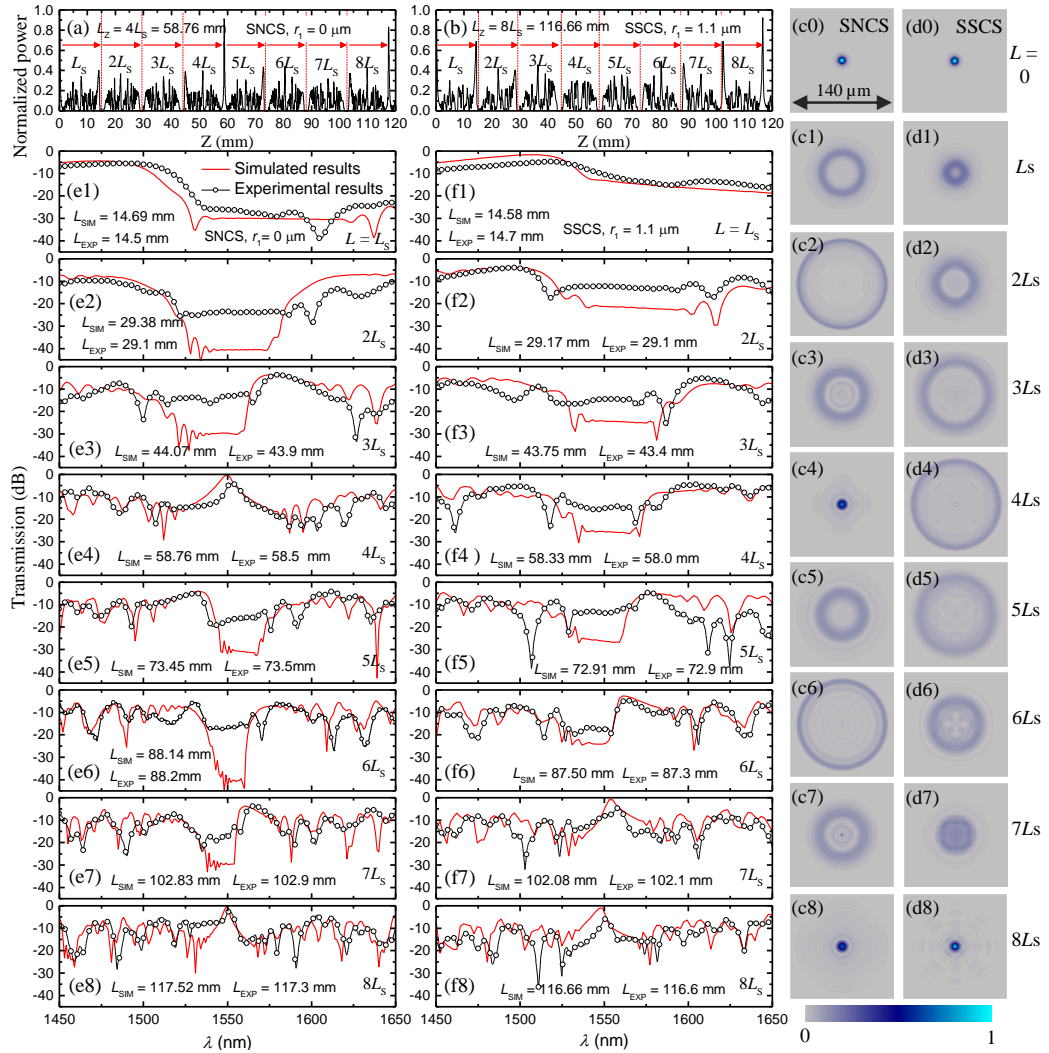


**Figure 4.11** (a) and (b) are respectively the on-axis intensities inside the middle fiber section of SNCS ( $r_1 = 0 \mu\text{m}$ ) and SSCS ( $r_1 = 1.1 \mu\text{m}$ ). (c0)-(c8) and (d0)-(d8) show the TIPs in the middle fiber section of the SNCS and SSCS samples at the positions  $Z = nL_S$  ( $n = 1, 2, \dots, 8$ ), where the light wavelength was set at 1550 nm. (e1)-(e8) and (f1)-(f8) show the simulated and measured transmission spectra of the samples, where the lengths of the middle fiber section are equal to the integer multiples of  $L_S$ :  $1L_S, 2L_S, \dots, 8L_S$ .

The presence of self-imaging means that the input field profile is reproduced at periodic lengths along the middle fiber section of an OFI. For the SNCS, the reproduced input profile (single point-like image) can be found in Figs. 4.11(c4) and 4.11(c8) for the lengths  $L = 4L_S$  and  $L = 8L_S$ , respectively, corresponding to the transmission peak appearing around the 1550 nm as shown in Figs. 4.11(e4) and 4.11(e8). At the other lengths  $L = L_S, 2L_S, 3L_S, 5L_S, 6L_S$  and  $7L_S$ , a single

ring-like image is observed as shown in Figs. 4.11(c1)-4.11(c3) and 4.11(c5)-4.11(c7), corresponding to the transmission notch appearing around the 1550 nm in Figs. 4.11(e1)-4.11(e3) and 4.11(e5)-4.11(e7). The transmission peak and the notch result from the constructive and destructive interference of the  $LP_{0,n}$  modes. There are more dips and peaks in the transmission spectra along the second periodic interval in Figs. 4.11(e5)-4.11(e8) compared to the first periodic interval in Figs. 4.11(e1)-4.11(e4), due to more dense interference among the guided modes along the longer length of the NCF. Similarly, from the analysis of Figs. 4.11(b), 4.11(d0)-4.11(d8) and 4.11(f1)-4.11(f8), we can see that self-imaging appears at about  $L = 8L_s$  for the SSCS ( $r_1 = 1.1 \mu\text{m}$ ). The experimental results of the transmission spectra in Figs. 4.11(e1)-4.11(e8) and 4.11(f1)-4.11(f8) match well with the simulation results.

## 4.7 Discussion

The results show two prime characteristics of self-imaging in a SSCS structure: one is its discrete nature, the other is the exponential growth of the self-imaging period with the fiber core radius. The explicit self-imaging occurs only at the distinct sites along the propagation direction, for only a specific set of  $r_1$  values, hence it is discrete. The  $L_Z$  in an SSCS is an exponential function of the (discrete) values of  $r_1$ , while in SMS and SNCS structures the  $L_Z$  is a quadratic function of  $r_1$ . Nevertheless, the self-imaging of the SSCS retains some features similar to those for the SNCS. Firstly, the  $L_s$  is approximately the same in both the SNCS and SSCS structures. Secondly, the lengths for the generation of the single ring-like images or point-like images are still integer multiples of  $L_s$ . Moreover, there exists a relationship:  $L_Z(\text{SSCS}) = (1+q/4)L_Z(\text{SNCS})$ . It can be

deduced that the approximately constant  $L_s$  in both SNCS and SSCS is associated with the function  $J_0$  while the discrete growth behaviour of  $L_z$  solely in the SSCS is attributed to the additional function  $Y_0$ . The  $n_{\text{eff}}$  of the core modes, obtained by solving equation  $J_0 = 0$ , define the general characteristics of the self-imaging in SMS and SNCS: the relationship between  $L_z$  and  $L_s$  ( $L_z = 4L_s$ ) is satisfied for all the continuous core radii. The modulation between  $J_0$  and  $Y_0$  in the description of the cladding modes in a SSCS not only reflects the observed mode reorganization behaviour, but also results in a more complex mode superposition compared to that of core modes.

The discrete self-imaging effect in an SSCS can be regarded as the first discrete self-imaging phenomenon found in multimode waveguides. As a counterpart in one-dimensional waveguide arrays, the discrete Talbot self-imaging effect was first found in 2005 by Robert Iwanow *et al.*, who stated that the self-imaging of the input field pattern is only possible for a specific set of periodicities [44]. The waveguide arrays consisted of a large number (infinite in principle) of periodic evanescently coupled single-mode channel waveguides, which is a form of discrete system where the field evolution equation is effectively discretized (discrete diffraction) and is capable of nonlinear effects and even the discrete optical solitons [45,46]. Analogously, the discrete self-imaging effect in SSCS indicates that the SCF may be also a discrete multimode physical system. The SCF with pure cladding modes may be a valuable platform for studying multimode nonlinear fiber optics. It is also expected that the multimode solitons, which so far have been only experimentally observed in the graded-index multimode fiber [2], could be achieved in an SCF.

The unique light field of multiple cladding-type modes in the SCF, distinct from that of multiple core-type modes in the commonly used MMF and NCF, can be further explored in many applications. For example, compared to the Bessel beams generated by NCF or MMF and characterized by the function  $J_0$  [4,5], the pure cladding modes in a SCF can be used to generate a new kind of Bessel beams characterized by the combinations of  $J_0$  and  $Y_0$ . Bessel beams based on a truncation of  $Y_0$  having higher energy over a longer range than that of  $J_0$  Bessel beams were theoretically predicted in Ref. [47]. Indeed, the micro/nano- core in SCFs can strongly modify the on-axis intensity, which is critically important to the performance of Bessel beams in the optical manipulation [48,49]. Therefore the  $Y_0$  modulated  $J_0$  Bessel beams generated with SCFs may offer a better performance in optical manipulation applications.

## 4.8 Conclusion

In this chapter the effective refractive index of both the core-type and cladding-type modes  $LP_{0,n}$  in three-layer step-index optical fibers as a function of core radius, was calculated independently by the analytical method and the BPM. The cladding modes show mode reorganization characteristics, indicating a behaviour different from that of core modes. The self-imaging of cladding modes in an SSCS was analytically and numerically calculated and confirmed by experiments for the first time. The self-imaging in the SSCS shows the discrete nature and the behaviour of exponential growth with the core radius of the middle fiber section. An analysis of the constructive interference of adjacent guided modes shows that the self-imaging must be discrete since the change in distance of the self-imaging period must be an integer multiple of  $L_2$  (constructive interference length of  $LP_{0,1}$

and LP<sub>0,2</sub>). The discrete nature and exponential growth behaviour found in this work indicate that the propagation properties of cladding modes in an SCF are distinct from those of the core modes in the commonly used NCF and MMF. The SCF may be a discrete multimode physical system, which deserves further study in the context of nonlinear multimode fiber optics. The distinctive physical characteristics of the self-imaging in the SSCS may provide new insights and rules in the design of the multimode interference devices such as optical couplers, optical modulators, multimode fiber lasers and space-division multiplexing systems.

## 4.9 Reference

- [1] D. Richardson, J. Fini, and L. Nelson, “Space-division multiplexing in optical fibers,” Nat. Photonics, vol. 7, no. 5, p. 354, 2013.
- [2] W. H. Renninger and F. W. Wise, “Optical solitons in graded-index multimode fibers,” Nat. Commun., vol. 4, p. 1719, 2013.
- [3] M. Plöschner, T. Tyc, and T. Čižmár, “Seeing through chaos in multimode fibers,” Nat. Photonics, vol. 9, no. 8, p. 529, 2015.
- [4] Y. Zhang, X. Tang, Y. Zhang, Z. Liu, E. Zhao, X. Yang, J. Zhang, J. Yang, and L. Yuan, “Multiple particles 3-d trap based on all-fiber bessel optical probe,” J. Lightw. Technol., vol. 35, no. 18, pp. 3849–3853, 2017.
- [5] S. R. Lee, J. Kim, S. Lee, Y. Jung, J. K. Kim, and K. Oh, “All-silica fiber bessel-like beam generator and its applications in longitudinal optical trapping and transport of multiple dielectric particles,” Opt. Express, vol. 18, no. 24, pp. 25299–25305, 2010.
- [6] M. N. Zervas and C. A. Codemard, “High power fiber lasers: a review,” IEEE J. Sel. Top. Quantum Electron., vol. 20, no. 5, pp. 219–241, 2014.
- [7] H. Chen, C. Jin, B. Huang, N. Fontaine, R. Ryf, K. Shang, N. Grégoire, S. Morency, R.-J. Essiambre, G. Li *et al.*, “Integrated cladding-pumped multicore few-mode erbium-doped fiber amplifier for space-division-multiplexed communications,” Nat. Photonics, vol. 10, no. 8, p. 529, 2016.

- [8] L. G. Wright, Z. M. Ziegler, P. M. Lushnikov, Z. Zhu, M. A. Eftekhar, D. N. Christodoulides, and F. W. Wise, “Multimode nonlinear fiber optics: Massively parallel numerical solver, tutorial, and outlook,” *IEEE J. Sel. Top. Quantum Electron.*, vol. 24, no. 3, pp. 1–16, 2018.
- [9] J. Carpenter, B. J. Eggleton, and J. Schröder, “Observation of eisenbud–wigner–smith states as principal modes in multimode fiber,” *Nat. Photonics*, vol. 9, no. 11, p. 751, 2015.
- [10] K. Krupa, A. Tonello, B. M. Shalaby, M. Fabert, A. Barthélémy, G. Millot, S. Wabnitz, and V. Couderc, “Spatial beam self-cleaning in multimode fibers,” *Nat. Photonics*, vol. 11, no. 4, p. 237, 2017.
- [11] O. V. Ivanov, S. A. Nikitov, and Y. V. Gulyaev, “Cladding modes of optical fibers: properties and applications,” *Physics-Uspekhi*, vol. 49, no. 2, pp. 167–191, 2006.
- [12] C. Caucheteur, T. Guo, F. Liu, B.-O. Guan, and J. Albert, “Ultrasensitive plasmonic sensing in air using optical fiber spectral combs,” *Nat. Commun.*, vol. 7, p. 13371, 2016.
- [13] Y. Li and T. Erdogan, “Cladding-mode assisted fiber-to-fiber and fiber-to-free-space coupling,” *Opt. Commun.*, vol. 183, no. 5-6, pp. 377–388, 2000.
- [14] C. Tsao, *Optical fiber waveguide analysis*, (Oxford University Press, 1992).
- [15] M. Z. Alam and J. Albert, “Selective excitation of radially and azimuthally polarized optical fiber cladding modes,” *J. Lightw. Technol.*, vol. 31, no. 19, pp. 3167–3175, 2013.
- [16] R. Guyard, D. Leduc, C. Lupi, and Y. Lecieux, “Critical cladding radius for hybrid cladding modes,” *Opt. Laser Technol.*, vol. 101, pp. 116–126, 2018.
- [17] A. W. Snyder and J. Love, *Optical waveguide theory*, (Springer Science & Business Media, 2012).
- [18] L. C. Bobb, P. Shankar, and H. D. Krumboltz, “Bending effects in biconically tapered single-mode fibers,” *J. Lightw. Technol.*, vol. 8, no. 7, pp. 1084–1090, 1990.
- [19] Q. Wu, Y. Semenova, P. Wang, and G. Farrell, “A comprehensive analysis verified by experiment of a refractometer based on an smf28–

- small-core singlemode fiber (scsmf)–smf28 fiber structure,” J. Opt., vol. 13, no. 12, p. 125401, 2011.
- [20] L. Tong, F. Zi, X. Guo, and J. Lou, “Optical microfibers and nanofibers: A tutorial,” Opt. Commun., vol. 285, no. 23, pp. 4641–4647, 2012.
  - [21] F. Xu, Z.-X. Wu, and Y.-Q. Lu, “Nonlinear optics in optical-fiber nanowires and their applications,” Progress in Quantum Electronics, vol. 55, pp. 35–51, 2017.
  - [22] L. Tong, R. R. Gattass, J. B. Ashcom, S. He, J. Lou, M. Shen, I. Maxwell, and E. Mazur, “Subwavelength-diameter silica wires for low-loss optical wave guiding,” Nature, vol. 426, no. 6968, p. 816, 2003.
  - [23] D. Marcuse, *Theory of Dielectric Optical Waveguides*, (Academic press Inc., 1991).
  - [24] J. A. Buck, *Fundamentals of optical fibers*, (John Wiley & Sons, 2004).
  - [25] I. Del Villar, I. R. Matías, F. J. Arregui, and P. Lalanne, “Optimization of sensitivity in long period fiber gratings with overlay deposition,” Opt. Express, vol. 13, no. 1, pp. 56–69, 2005.
  - [26] A. B. Socorro, I. Del Villar, J. M. Corres, F. J. Arregui, and I. R. Matias, “Mode transition in complex refractive index coated single-mode–multimode–single-mode structure,” Opt. Express, vol. 21, no. 10, pp. 12668–12682, 2013.
  - [27] D. Marcuse, “Mode conversion in optical fibers with monotonically increasing core radius,” J. Lightw. Technol., vol. 5, no. 1, pp. 125–133, 1987.
  - [28] J. Kerttula, V. Filippov, V. Ustimchik, Y. Chamorovskiy, and O. G. Okhotnikov, “Mode evolution in long tapered fibers with high tapering ratio,” Opt. Express, vol. 20, no. 23, pp. 25461–25470, 2012.
  - [29] Y. Jung, G. Brambilla, and D. J. Richardson, “Broadband single-mode operation of standard optical fibers by using a sub-wavelength optical wire filter,” Opt. Express, vol. 16, no. 19, pp. 14661–14667, 2008.
  - [30] X. Jiang, L. Shao, S.-X. Zhang, X. Yi, J. Wiersig, L. Wang, Q. Gong, M. Lončar, L. Yang, and Y.-F. Xiao, “Chaos-assisted broadband momentum transformation in optical microresonators,” Science, vol. 358, no. 6361, pp. 344–347, 2017.

- [31] L. Tong, J. Lou, and E. Mazur, “Single-mode guiding properties of subwavelength-diameter silica and silicon wire waveguides,” *Opt. Express*, vol. 12, no. 6, pp. 1025–1035, 2004.
- [32] L. B. Soldano and E. C. Pennings, “Optical multi-mode interference devices based on self-imaging: principles and applications,” *J. Lightw. Technol.*, vol. 13, no. 4, pp. 615–627, 1995.
- [33] W. S. Mohammed, A. Mehta, and E. G. Johnson, “Wavelength tunable fiber lens based on multimode interference,” *J. Lightw. Technol.*, vol. 22, no. 2, p. 469, 2004.
- [34] Q. Wang, G. Farrell, and W. Yan, “Investigation on single-mode–multimode–single-mode fiber structure,” *J. Lightw. Technol.*, vol. 26, no. 5, pp. 512–519, 2008.
- [35] W. Xu, J. Shi, X. Yang, D. Xu, F. Rong, J. Zhao, and J. Yao, “Improved numerical calculation of the single-mode-no-core-single-mode fiber structure using the fields far from cutoff approximation,” *Sensors*, vol. 17, no. 10, p. 2240, 2017.
- [36] X. Zhu, A. Schülzgen, H. Li, L. Li, L. Han, J. Moloney, and N. Peyghambarian, “Detailed investigation of self-imaging in large core multimode optical fibers for application in fiber lasers and amplifiers,” *Opt. Express*, vol. 16, no. 21, pp. 16632–16645, 2008.
- [37] J. Zheng, J. Li, T. Ning, L. Pei, S. Jian, and Y. Wen, “Improved self-imaging for multi-mode optical fiber involving cladding refractive index,” *Opt. Commun.*, vol. 311, pp. 350–353, 2013.
- [38] K. Hamamoto and H. Jiang, “Active mmi devices: concept, proof, and recent progress,” *J. Phys. D: Appl. Phys.*, vol. 48, no. 38, p. 383001, 2015.
- [39] N. Li, M. Liu, X. Gao, L. Zhang, Z. Jia, Y. Feng, Y. Ohishi, G. Qin, and W. Qin, “All-fiber widely tunable mode-locked thulium-doped laser using a curvature multimode interference filter,” *Laser Phys. Lett.*, vol. 13, no. 7, p. 075103, 2016.
- [40] X. Zhao, G. Bai, Y. Zheng, X. Chen, Y. Yang, K. Liu, C. Zhao, Y. Qi, B. He, J. Zhou *et al.*, “Mode suppression employing periodical large-small-core (plsc) filter in strongly pumped large mode area fiber amplifier,” *J. Opt.*, vol. 19, no. 6, p. 065801, 2017.

- [41] K. Krupa, A. Tonello, A. Barthélémy, V. Couderc, B. M. Shalaby, A. Bendahmane, G. Millot, and S. Wabnitz, “Observation of geometric parametric instability induced by the periodic spatial self-imaging of multimode waves,” *Phys. Rev. Lett.*, vol. 116, no. 18, p. 183901, 2016.
- [42] L. G. Wright, S. Wabnitz, D. N. Christodoulides, and F. W. Wise, “Ultrabroadband dispersive radiation by spatiotemporal oscillation of multimode waves,” *Phys. Rev. Lett.*, vol. 115, no. 22, p. 223902, 2015.
- [43] M. Monerie, “Propagation in doubly clad single-mode fibers,” *IEEE J. Quantum Electron.*, vol. QE-18, no. 4, pp. 535–542, 1982.
- [44] R. Iwanow, D. A. May-Arrioja, D. N. Christodoulides, G. I. Stegeman, Y. Min, and W. Sohler, “Discrete talbot effect in waveguide arrays,” *Phys. Rev. Lett.*, vol. 95, no. 5, p. 053902, 2005.
- [45] I. L. Garanovich, S. Longhi, A. A. Sukhorukov, and Y. S. Kivshar, “Light propagation and localization in modulated photonic lattices and waveguides,” *Phys. Reps.*, vol. 518, no. 1-2, pp. 1–79, 2012.
- [46] F. Lederer, G. I. Stegeman, D. N. Christodoulides, G. Assanto, M. Segev, and Y. Silberberg, “Discrete solitons in optics,” *Phys. Reps.*, vol. 463, no. 1-3, pp. 1–126, 2008.
- [47] L. Vicari, “Truncation of non-diffracting beams,” *Opt. Commun.*, vol. 70, no. 4, pp. 263–266, 1989.
- [48] D. McGloin and K. Dholakia, “Bessel beams: diffraction in a new light,” *Contemporary Phys.*, vol. 46, no. 1, pp. 15–28, 2005.
- [49] T. Čižmár, V. Kollárová, Z. Bouchal, and P. Zemánek, “Sub-micron particle organization by self-imaging of non-diffracting beams,” *New J. Phys.*, vol. 8, no. 3, p. 43, 2006.

# **Chapter 5**

## **Anti-Resonance, Inhibited Coupling and Mode Transition in Depressed-Core Optical Fibers<sup>3</sup>**

Compared to the three-layer step-index fiber studied in the last two chapters, a three-layer depressed-core fiber (DCF) has an inverted refractive index profile, where the refractive index of the core is smaller than that of the first cladding but still larger than the second cladding as discussed in Section 1.2. The three-layer DCF is in effect a bridge between the three-layer step-index fiber and the tube-type hollow-core fiber (HCF) from the point of view of the index profile.

In this chapter the dispersion diagram of a DCF is obtained by solving the full-vector eigenvalue equations and analyzed using the theory of anti-resonant and the inhibited coupling mechanisms. While light propagation in tube-type HCFs is commonly described by the symmetric planar waveguide model, here it is proposed that an asymmetric planar waveguide for the DCFs in an anti-resonant reflecting optical waveguide (ARROW) model. It is found that the anti-resonant core modes in the DCFs have real effective indices, compared to that with complex effective indices in the tube-type HCFs. The anti-resonant core modes in the DCFs exhibit similar qualitative and quantitative behaviour as that in the conventional step-index fibers. The full-vector analytical results for the simple-

---

<sup>3</sup>Lian, Xiaokang, Gerald Farrell, Qiang Wu, Wei Han, Changyu Shen, Youqiao Ma, and Yuliya Semenova, “Anti-resonance, inhibited coupling and mode transition in depressed-core fibers,” Opt. Express, vol. 28, no. 11, pp. 16526–16541, 2020.

structure DCFs can contribute to a better understanding of the anti-resonant and inhibited coupling guidance mechanisms in other complex inverted-index fibers.

## 5.1 Research background

Inversed-index fibers with a low-index core and a high-index cladding such as the tube-type hollow-core fibers and hollow-core photonic crystal fibers have attracted a lot of interest in the fields of high-capacity telecommunication networks [1-5], high-power/supercontinuum/ultrafast lasers [6-11], terahertz waveguiding [12,13] and high sensitivity optical sensing [14,15]. In contrast to conventional step-index fibers where the light is guided in the high-index core region by total internal reflections, light guidance in the low-index core region of the inverted-index fibers can be explained by other mechanisms such as the photonic bandgap effect, inhibited coupling effect and the anti-resonant effect. Generally, all optical fibers can be grouped into two types based on the effective refractive index ( $n_{\text{eff}}$ ) -wavelength ( $\lambda$ ) dispersion diagram [2]. For the first type, the  $n_{\text{eff}} - \lambda$  of the core modes lies outside any cladding mode continuum. The photonic bandgap fibers belong to this type, as their photonic bandgaps are formed in the periodic dielectric cladding region, the coupling between the core modes, which have  $n_{\text{eff}}$  within the bandgaps, and cladding modes are forbidden due to their separation in the  $n_{\text{eff}} - \lambda$  space [3]. The second type is inhibited coupling fibers, for which the  $n_{\text{eff}} - \lambda$  of the core modes lies inside the cladding mode continuum, but the coupling between them is minimized due to the high degree of transverse-field mismatch [6]. Both the photonic bandgap fibers and the inhibited-coupling fibers have the same anti-resonant nature, which can be described by an anti-resonant reflecting optical waveguide (ARROW) model

[2,3,6]. In this model, the planar waveguide acts as a Fabry-Perot resonator, which allows the anti-resonant light to be reflected back while allowing forward transmission of the resonant light [16-19].

In a manner similar to photonic bandgap fibers, conventional step-index fibers belong to the first type since the  $n_{\text{eff}}$  of the core modes are higher than that of the cladding modes, in other words, their modal dispersion space is separated [2]. Compared to conventional step-index fibers, inverted-index fibers have generally a more complex structure and modal characteristics. However, there exists a close relationship between them. It has been stated that the photonic bandgap fibers exhibit strikingly similar modal behaviour with that of the conventional fibers, including dispersion curves and field profiles [20,21]. The analogy to conventional fibers provides a convenient tool to model the modes of photonic bandgap fibers. The question is whether there is a connection between the inhibited-coupling fibers and the conventional fibers in addition to the photonic bandgap fibers.

A recent publication Ref. [22] shows that the mode density of anti-resonant elements in an inhibited-coupling guiding single-ring hollow-core photonic crystal fiber is similar to the behaviour of conventional multimode fibers. The single-ring hollow-core photonic crystal fiber studied in Ref. [22] has a ring of 6-8 detached thin tube-type hollow-core waveguides/fibers surrounding the hollow core. However, the results of the work were obtained using a scalar semi-analytical model, which does not give sufficiently rigorous vector modal analysis. The tube-type hollow-core fiber has a simple structure, where the leaky core-type modes are supported by the anti-resonant effect [17-19]. In most of the

previous works, only the fundamental mode or few low-order modes of the tube-type hollow-core fibers were obtained with different approximation methods [17,23-25].

A depressed-core fiber (DCF) is a type of inverted-index fibers, described by a three-layer fiber model with a low-index solid core, a finite high-index cladding, and surrounding air. This fiber structure is different from the M-type fiber [26], although in some papers it has been referred to as M-type fiber [27]. The refractive index of the central region of the M-type fiber has a minimum value set by the need for the core to have a refractive index equal to or lower than that of the surrounding medium, which if the surrounding region is air means that the core must also be air. For a DCF the core refractive index is lower than the next outermost region but does not need to take on the lowest or minimum value in a three-layer fiber model. The M-type fiber can be considered as a leaky waveguide with the anti-resonant structure, in which the core mode is leaky with a complex effective refractive index, similar to the case of the hollow-core fiber [17,28]. Compared to the M-type fiber, the core mode of the DCF is guided by both total internal reflection and anti-resonance guidance, and its core mode has a real effective refractive index [27,29-32]. The DCFs have been studied for various applications including pulse compression in fiber lasers [29-31], generation of supercontinuum [27] and top-hat beams [32], due to their manageable waveguide dispersion and exceptional modal field changes. However, these studies in regard to DCFs [27,29-32] were limited to the analysis of a few modes in the strong dispersion region.

In this chapter, the modal dispersion and field distributions of a DCF are calculated and analyzed with the vector field functions and eigenvalue equations for the three-layer fiber as given in Refs. [33-35]. To the best of the author's knowledge, this is the first report providing a complete full-vector modal dispersion diagram for the DCFs. In Section 5.2, the ray method is used to analyze the mode characteristics in the DCFs, in comparison to asymmetric planar waveguides. The possibility of anti-resonant core modes and the positions of the mode coupling (resonances) is analyzed using the ARROW model. In Section 5.3, the dispersion curves and mode field distributions of the vector modes TE, TM, HE and EH are analyzed, along with their comparison for the case of conventional step-index fibers. It is found that the waveguiding mechanism of core-type modes in DCFs with a simple structure can be explained by the anti-resonant and inhibited coupling effects, similarly to the complex single-ring hollow-core photonic crystal fibers discussed in Ref. [22]. In Section 5.4, the implications of the analytical results for the tube-type hollow-core fibers and single-ring hollow-core fibers are discussed.

## 5.2 Guiding mechanism of the DCFs

### 5.2.1 Anti-resonant core mode and asymmetric planar ARROW model

Figure 5.1 shows a DCF and its cross section and refractive index profile. The radii of the rod core and the tube cladding are  $r_1$  and  $r_2$  while the surrounding medium (air) is unlimited. The refractive index of the rod core region  $n_1$  is smaller than the refractive index of the tube cladding region  $n_2$  but greater than that of the surrounding air  $n_3$ , as  $n_3 < n_1 < n_2$ .

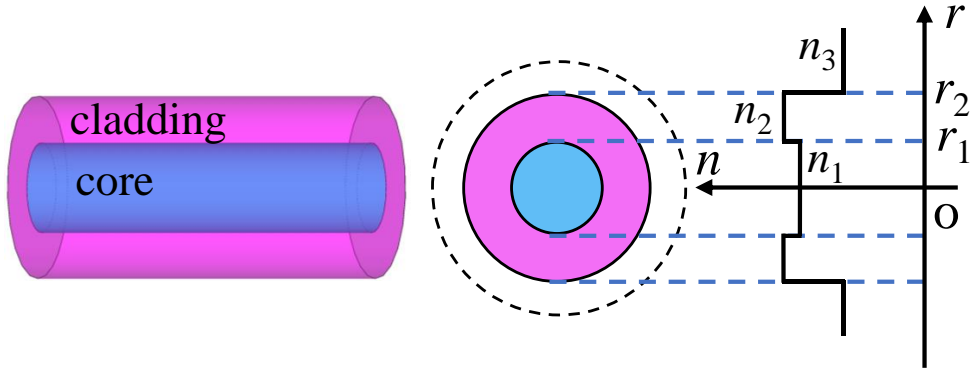


**Figure 5.1** A depressed-core optical fiber and its cross section and refractive index profile.

The high-index tube cladding region of the DCF can be considered as an asymmetric planar waveguide, where a high-index core region with the same thickness ( $d = r_2 - r_1$ ) as the cladding of the DCF is sandwiched between two different low-index regions, as shown in Fig. 5.2. It is useful to analyze the DCFs using a ray optics approach, which help to analyse the field distributions of the core and the cladding modes as discussed in Section 2.2.1. Since the asymmetric planar waveguide supports core modes with  $n_1 < n_{\text{eff}} = n_2 * \sin\theta_1 < n_2$  [36] shown in Fig. 5.2(b), it can be deduced that a DCF can support the annular-like (transverse field profile) cladding modes with  $n_1 < n_{\text{eff}} = n_2 * \sin\theta_1 < n_2$  guided by the total internal reflections at the inner and outer boundaries of the cladding region as shown in Fig. 5.2(a). The modes with  $n_3 < n_{\text{eff}} = n_1 * \sin\theta_1 < n_1$  in the asymmetric planar waveguide are radiation modes with power escaping into the higher-index (upper) region (where will form a standing wave field) [36], as shown in Fig. 5.2(d). In the DCF an incident ray representing a mode with  $n_3 < n_{\text{eff}} = n_1 * \sin\theta_1 < n_1$ , partially reflected at the inner boundary of the cladding region and totally reflected at the outer boundary of the cladding region, excites multiple-path rays reflecting into the core region. The light field of these modes with  $n_3 < n_{\text{eff}} < n_1$  is distributed in across the entire cross section of the DCF,

which is similar to the cladding modes in conventional three-layer step-index fibers [37,38].

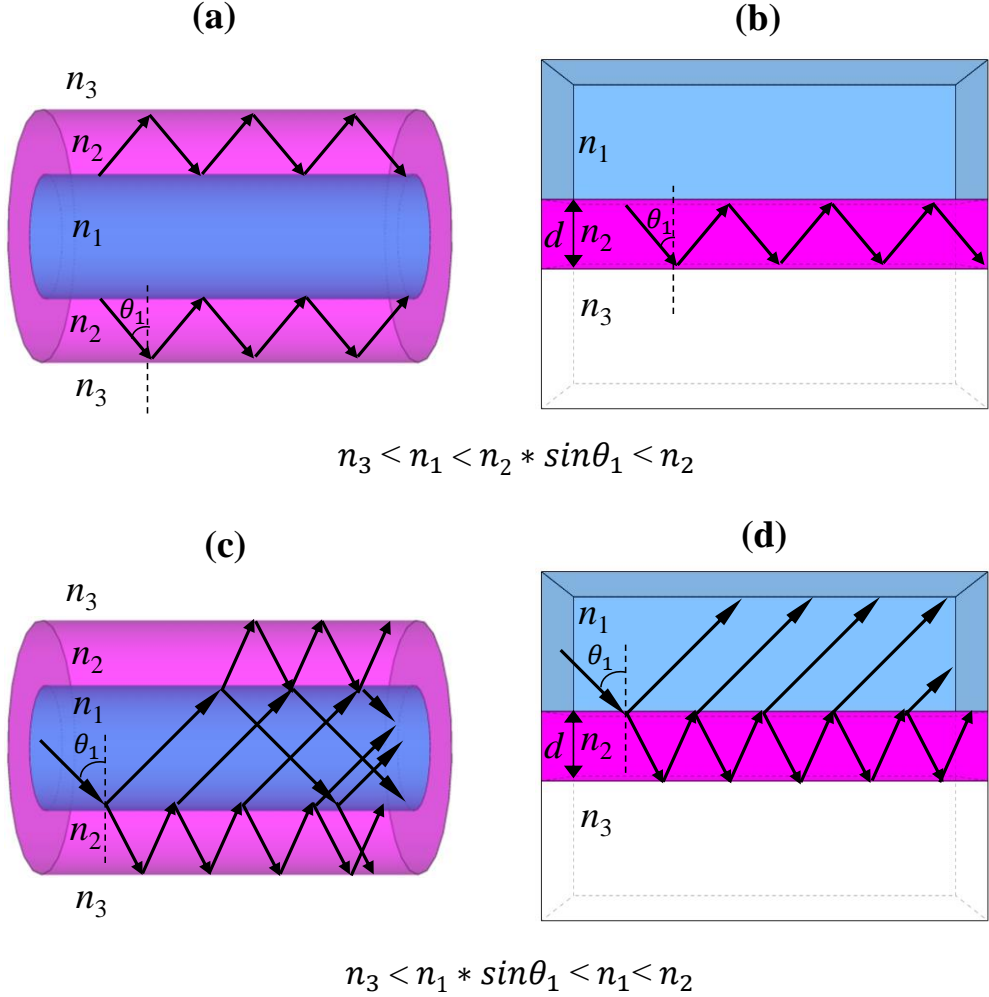


**Figure 5.2** (a) and (b) show the ray trajectory of a mode with  $n_1 < n_{\text{eff}} = n_2 \sin\theta_1 < n_2$  in a DCF and an equivalent asymmetric planar waveguide, respectively. (c) and (d) show the ray trajectory of a mode with  $n_3 < n_{\text{eff}} = n_1 \sin\theta_1 < n_1$  in the DCF and the equivalent asymmetric planar waveguide, respectively.

Due to the inverted-index distribution in the DCF, the total internal reflection effect does not work at the inner boundary of the cladding region. Therefore, there is no core modes guided by the total internal reflections like those in conventional step-index fibers.

The high-index layers can be considered as Fabry-Perot resonators in the ARROW model [16]. Analogous to a symmetric planar waveguide in the ARROW model for the tube-type hollow-core fibers [18,19], an asymmetric planar waveguide is proposed for the DCFs. Indeed, the characteristics of multi-path reflections formed in the DCF shown in Fig. 5.2(c) indicate that the cladding region of the DCF acts as a Fabry-Perot resonator, corresponding to an asymmetric planar waveguide shown in Fig. 5.2(d). In a Fabry-Perot resonator the resonances usually occur over a narrow band of wavelengths while the antiresonances are spectrally broad [16,39]. The energy of the incident ray can be strongly reflected back to the core region at the anti-resonant wavelengths, forming anti-resonant core modes in the anti-resonant reflecting optical waveguides [16] and the tube-type hollow-core fibers [18]. Similarly, it can be concluded that DCFs have anti-resonant core modes with the light field mainly confined in the core region, with disc-like transverse field profiles.

The resonant wavelengths of an asymmetric planar waveguide-like Fabry-Perot resonator shown in Fig. 5.2(d), corresponding to the minimal total energy of all the reflected rays, are equal to the cutoff wavelengths of the guided core modes. The cutoff wavelengths for the guided core modes  $TE_N$  and  $TM_N$  in the asymmetric waveguide can be written as [36]:

$$\lambda_{N,c} = \frac{2d\sqrt{n_2^2 - n_1^2}}{\left[N - 1 + \frac{1}{\pi}\tan^{-1}\left(\kappa\sqrt{\frac{n_1^2 - n_3^2}{n_2^2 - n_1^2}}\right)\right]}, \quad \kappa = \begin{cases} 1, & TE_N \\ \frac{n_2^2}{n_3^2}, & TM_N \end{cases} \quad (5.1)$$

where  $N$  is the mode number. The second term in the denominator of Eq. (5.1) arises from the asymmetry of the waveguide and vanishes for the symmetric case as shown in Ref. [19].

## 5.3 Modes in DCFs

Similar to the conventional step-index fibers, the modes in a DCF are denoted as  $\text{TE}_{0,N}$ ,  $\text{TM}_{0,N}$ ,  $\text{HE}_{m,N}$  and  $\text{EH}_{m,N}$ , where the numbers ‘0’ and ‘m’ on the left side of the comma in the subscript positions are the azimuthal mode number while the number symbols ‘N’ on the right side are the radial mode number. The eigenvalue equations for the vector modes in the DCFs are shown in Appendix A, which were solved by a graphical method. In the calculations, the fiber parameters of the studied DCF are assumed to be  $n_1 = 1.445$ ,  $n_2 = 1.51$ ,  $n_3 = 1$ ,  $r_1 = 62.5 \mu\text{m}$  and  $r_2 = 125 \mu\text{m}$ .

### 5.3.1 TE/TM modes in DCFs

Figure 5.3(a) shows the dispersion diagram ( $n_{\text{eff}}$  vs.  $\lambda$ ) for the modes  $\text{TE}_{0,N}$  with  $n_1 < n_{\text{eff}} < n_2$ . There are 38  $\text{TE}_{0,N}$  modes, from upper to lower as the radial mode number N increases, as indicated by a black arrow. All the dispersion curves of the  $\text{TE}_{0,N}$  modes with the purple dashed line at  $n_1$ , but only the modes  $\text{HE}_{0,N}$ ,  $N = 34, 35, 36, 37$  and  $38$  have their cutoffs in the investigated spectral range. The wavelengths of the intersect points are approximated as the cutoff wavelengths of the  $\text{TE}_N$  modes in the asymmetric planar waveguide calculated by Eq. (5.1), indicated by the red vertical dashed lines. The difference between the wavelength of the intersect point for the  $\text{TE}_{0,N}$  mode and the cutoff wavelength of the  $\text{TE}_N$  mode is less than 1 nm. Compared to the curves above the horizontal line at  $n_1$ , the curves below  $n_1$  show a step-like decrease as the  $\lambda$  increases, showing periodic strong and moderate index dispersion bands. The slopes of the dispersion curves with a strong index dispersion are similar to those of the curves above the horizontal line at  $n_1$  and that in the equivalent asymmetric waveguide

(not shown). The slopes of the dispersion curves with a moderate index dispersion in DCFs are similar to those of the dispersion curves of the core modes in the conventional step-index fiber, as shown in Fig. 2.3(b).

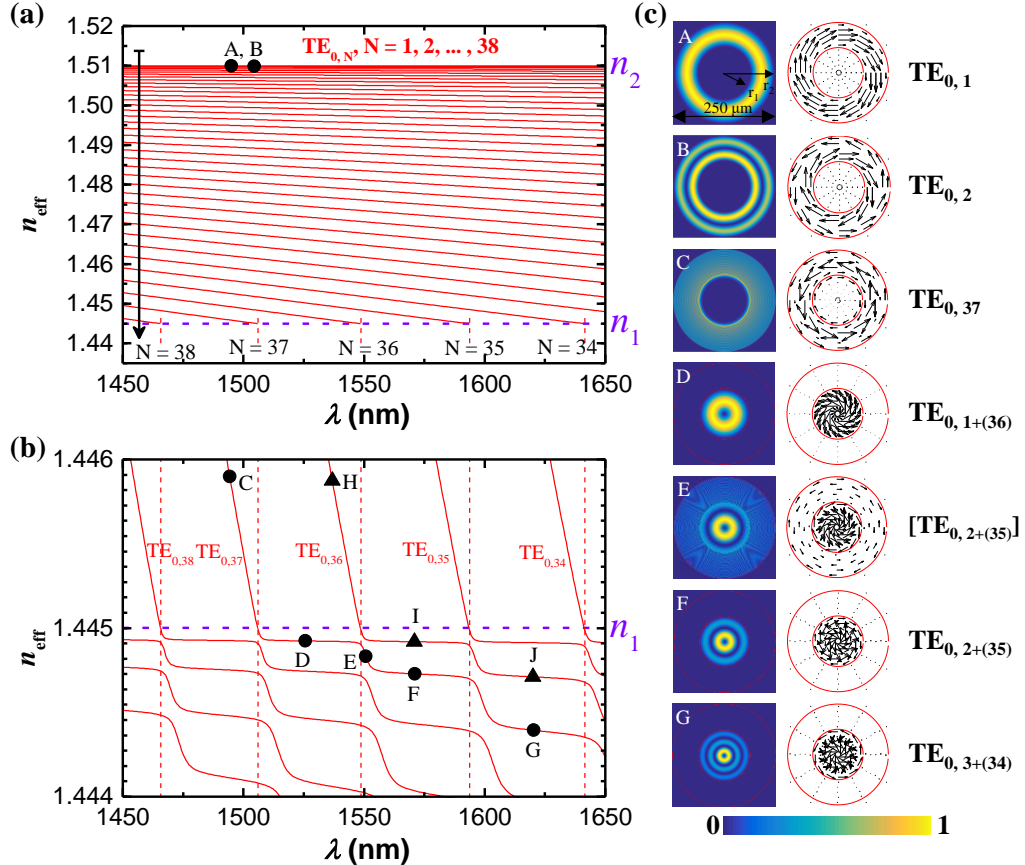


**Figure 5.3** Dispersion curves ( $n_{\text{eff}}$  vs.  $\lambda$ ) of TE modes with  $n_{\text{eff}}$  corresponding to (a)  $n_1 < n_{\text{eff}} < n_2$ , (b)  $n_1 - 0.001 < n_{\text{eff}} < n_1 + 0.001$ ,  $n_1 = 1.445$ ,  $n_2 = 1.51$ . (c) shows the modal intensity and electric field vector distributions of TE modes whose positions ( $n_{\text{eff}}, \lambda$ ) are indicated by the black circle dots in (a) and (b). The red vertical dashed lines in (a) and (b) indicate the resonant bands.

Figure 5.3(c) shows the modal intensities and electric field vector distributions at seven different points marked A-G (black circle dots) in Figs. 5.3(a) and 5.3(b). The electric field vector helps to distinguish between different kinds of vector modes and helps to compare the modes in the DCF and the conventional step-index fiber, as discussed in following parts. The radial maxima in the modal field profiles represent intensity oscillations, and the number of the radial maxima is

equal to the radial mode number  $N$ . In Fig. 5.3(c) the modal field profile of the mode  $TE_{0,1}$  at point A shows one radial maxima in the fiber cladding region  $r_1 < r < r_2$ . The  $TE_{0,2}$  at point B shows two radial maxima in the fiber cladding region.

In order to count the number of radial maxima in the distributions corresponding to points C-G in Fig. 5.3(c), the normalized intensity distribution along the  $r$ -coordinate is drawn, as seen in Fig. 5.4. One oscillation peak on a curve in Fig. 5.4 corresponds to one radial maxima in a modal field profile. Similar to the modal field profiles at points A and B, all 37 radial maxima are distributed within the fiber cladding region for the mode at point C. The oscillation peaks shift from the cladding region to the core region one by one along the points C-G. The modes at points D, F and G exhibit 1, 2 and 3 maxima in the core and 36, 35 and 34 maxima in the cladding, respectively. The energy is mainly confined in the core region of the modes at points D, F and G, as seen in Figs. 5.4(b), 5.4(d) and 5.4(e), where the field intensity in the cladding region is almost negligible compared to that in the core region. The mode at point E with a very strong index dispersion represents a mode in a transition state from the mode at point D to the mode at point F, where the energy is more evenly distributed between the core and the cladding regions as seen in Fig. 5.4(c). There are two peaks in the core region and 35 peaks in the cladding region for the mode at point E.

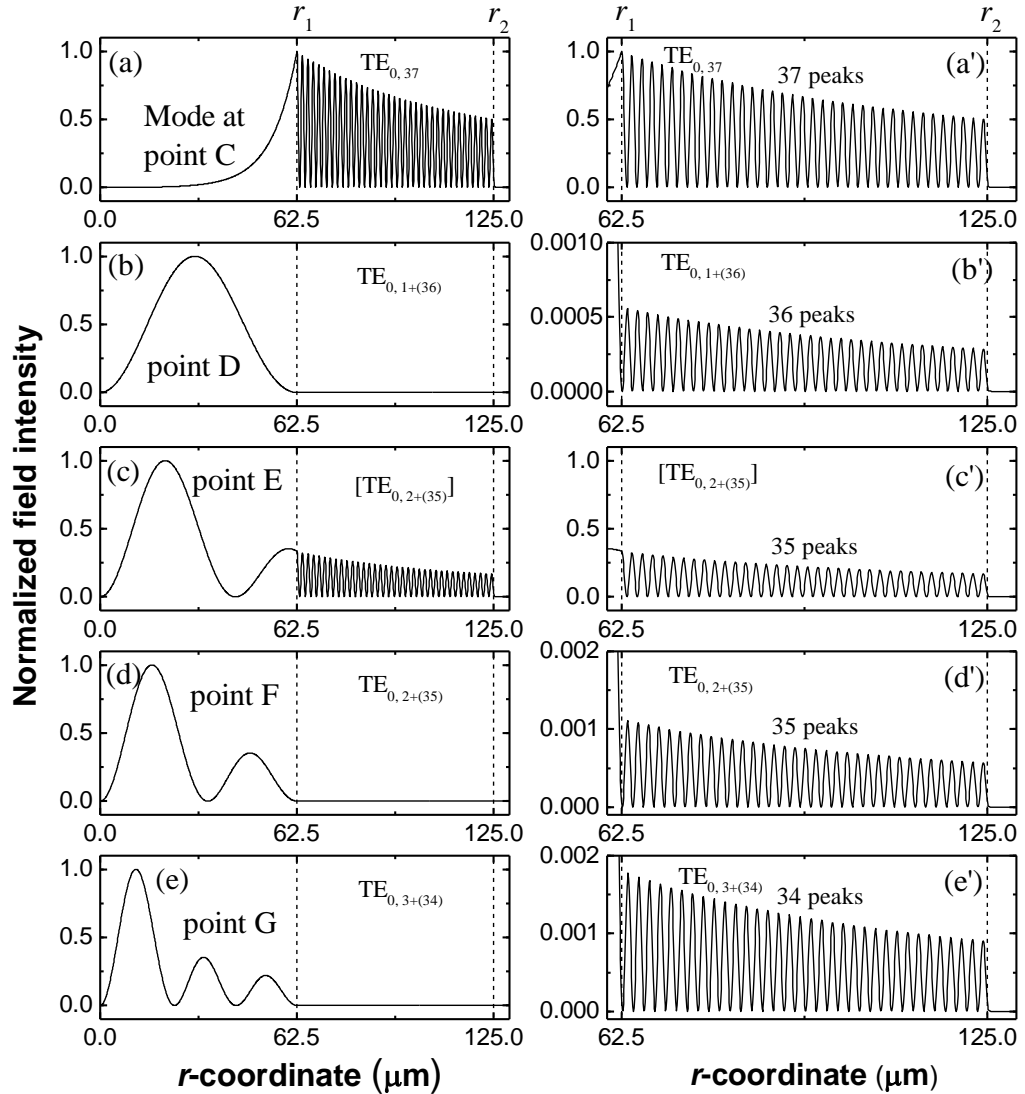


**Figure 5.4** The left panel (a)-(e) shows the normalized intensity distributions along the *r*-coordinate for the modes shown at points C-G in Fig. 5.3. The right panel (a')-(e') shows the zoomed-in part of (a)-(e), delineated by the vertical dashed lines.

The following nomenclature for the modes with  $n_{\text{eff}} < n_1$ , identified as  $\text{TE}_{0,n+(N-n)}$  has been proposed here as follows. The subscript ‘*n*’ denotes the radial number in the core region, while the number ‘*N-n*’ denotes the radial number in the cladding region. Therefore, the modes at points D, F and G in Fig. 5.3(b) with moderate index dispersion can be named as  $\text{TE}_{0,1+(36)}$ ,  $\text{TE}_{0,2+(35)}$  and  $\text{TE}_{0,3+(34)}$ . The mode at point E in Fig. 5.3(b) can be named as  $[\text{TE}_{0,2+(35)}]$ , where the brackets indicate that the mode is with a strong effective index dispersion and is in a transition state. It is clear that the field profiles of the modes  $\text{TE}_{0,1+(36)}$ ,

$\text{TE}_{0,2+(35)}$  and  $\text{TE}_{0,3+(34)}$  are similar to that of the modes  $\text{TE}_{0,1}$ ,  $\text{TE}_{0,2}$  and  $\text{TE}_{0,3}$  in conventional step-index fibers, respectively. As discussed, the  $\text{TE}_{0,1+(36)}$ ,  $\text{TE}_{0,2+(35)}$  and  $\text{TE}_{0,3+(34)}$  in the DCF are formed by the anti-resonant effect of the high-index cladding region, therefore, they represent anti-resonant core modes.

According the above nomenclature, the modes at points I and J on the dispersion curve of  $\text{TE}_{36}$  indicated by the black triangle dots in Fig. 5.3(b) are both anti-resonant core modes and named as  $\text{TE}_{0,1+(35)}$  and  $\text{TE}_{0,2+(34)}$ , respectively. The mode transition from the core mode  $\text{TE}_{0,1+(35)}$  at point I to the cladding mode  $\text{TE}_{0,36}$  at point H and the mode transition from the higher-order core mode  $\text{TE}_{0,2+(35)}$  at point F to the lower-order core mode  $\text{TE}_{0,1+(36)}$  at point D leads to an anti-crossing phenomenon near the mode [ $\text{TE}_{0,2+(35)}$ ] at point E around the resonant bands indicated by the red vertical dashed line. Due to mode reorganization [38,40-42], the anti-crossing phenomenon also takes place for the higher order modes. A similar phenomenon is also observed for the TM, HE and EH modes. The anti-crossing phenomenon originates from the resonant coupling between the core and the cladding modes, leading to the exceptional waveguide dispersion and modal field changes compared to that in the anti-resonant bands (similar to the conventional step-index fiber). As shown in Figs. 5.3 and 5.4 the modal field distribution and effective refractive index dispersion change drastically from the points D or F to the point E. The mode [ $\text{TE}_{0,2+(35)}$ ] at point E shows similar strong dispersion with the cladding modes in the DCF and the modes in the equivalent asymmetric waveguide. Therefore, the wavelength position and the dispersion shape of the anti-crossing are related to the thickness and the refractive index of the high-index cladding, in accordance with the ARROW model and Eq. (5.1) as discussed in the theory section. Due to the

manageable waveguide dispersion and modal field changes in a DCF, the generation of supercontinuum [27] and top-hat beams [32] can be achieved.

The dispersion diagram of  $\text{TM}_{0,N}$  modes is similar to that of  $\text{TE}_{0,N}$  modes, as seen in Fig. 5.5. The positions of the intersect points between the dispersion curves of the  $\text{TM}_{0,N}$  and the horizontal line at  $n_1$  can be approximated as the cutoff wavelengths of the  $\text{TM}_N$  modes in the asymmetric planar waveguide calculated by Eq. (5.1), indicated by the black vertical dashed lines in Figs. 5.5(a) and 5.5(b). Fig. 5.5(c) shows the modal intensity and electric field vector distributions of TM modes at points A'-G' indicated by the black squares in Figs.

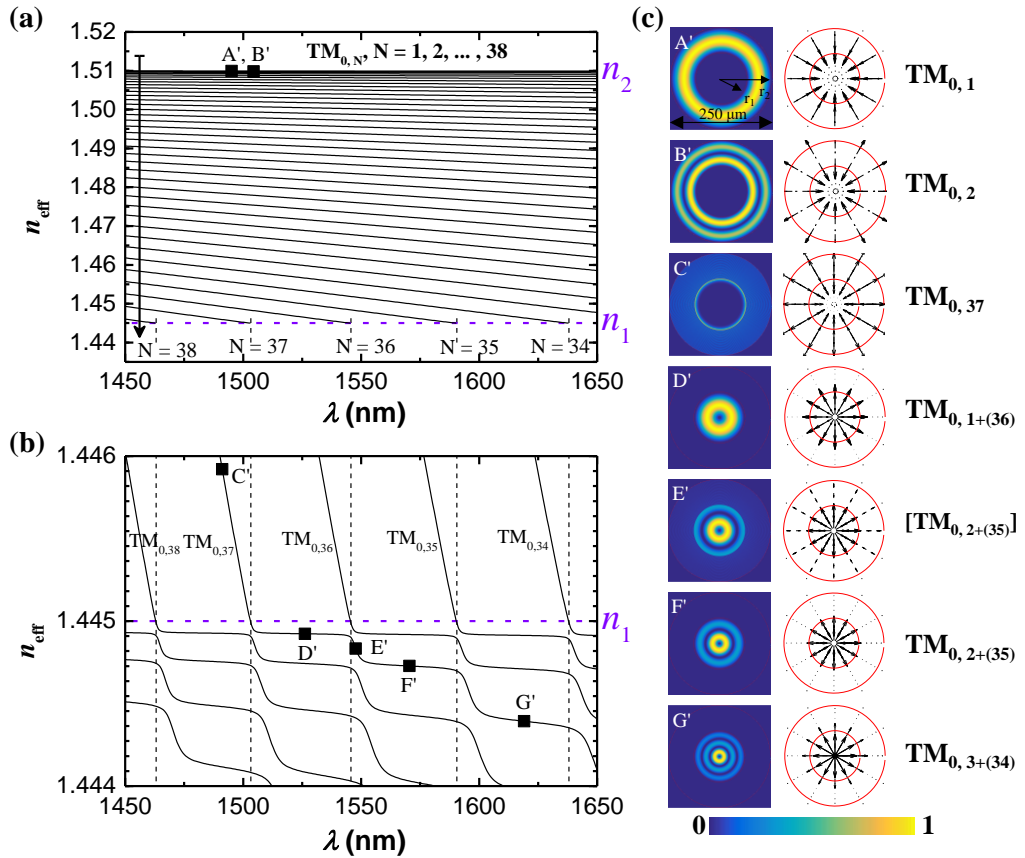


**Figure 5.5** Dispersion curves ( $n_{\text{eff}}$  vs.  $\lambda$ ) of TM modes with  $n_{\text{eff}}$  corresponding to (a)  $n_1 < n_{\text{eff}} < n_2$ , (b)  $n_1 - 0.001 < n_{\text{eff}} < n_1 + 0.001$ ,  $n_1 = 1.445$ ,  $n_2 = 1.51$ . (c) shows the modal intensity and electric field vector distributions of TM modes whose positions ( $n_{\text{eff}}, \lambda$ ) are indicated by the black squares in (a) and (b). The black vertical dashed lines in (a) and (b) indicate the resonant bands.

5.5(a) and 5.5(b).

The modes at points A' and B' are TM<sub>0,1</sub> and TM<sub>0,2</sub>, respectively. The points C'-G' are on the dispersion curve of TM<sub>0,3</sub>.<sup>37</sup> The field intensity distributions of TM modes in Fig. 5.5(c) are similar with those of TE modes shown in Fig. 5.3(c). However, the directions of the electric field vector of TM and TE modes are different: the former is parallel to the radial direction while the latter is normal in the radial direction.

Similarly to the nomenclature of the TE modes, the TM modes with  $n_{\text{eff}} < n_1$  can be named as TM<sub>0,n+(N-n)</sub>. Therefore, the anti-resonant core modes at points D', F' and G' in Fig. 5.5(b) with a moderate effective index dispersion can be named as TM<sub>0,1+(36)</sub>, TM<sub>0,2+(35)</sub> and TM<sub>0,3+(34)</sub>, respectively. The mode at point E' in Fig. 5.5(b) can be named as [TM<sub>0,2+(35)</sub>]. From the modal field distributions, it is clear that the anti-resonant core modes TM<sub>0,1+(36)</sub>, TM<sub>0,2+(35)</sub> and TM<sub>0,3+(34)</sub> are similar to the core modes TM<sub>0,1</sub>, TM<sub>0,2</sub> and TM<sub>0,3</sub> in the conventional step-index fibers, respectively.

### 5.3.2 HE/EH modes in DCFs

The HE or EH are two-fold degenerate modes with the same effective refractive index but different field vector directions, similar to the HE/EH modes in conventional step-index fibers. Here the modal intensity and electric field vector distributions for one of these two-fold degenerate modes are shown.

Figure 5.6 illustrates the dispersion curves of the modes HE<sub>1,N</sub> and EH<sub>1,N</sub> ( $N = 34, 35, \dots, 38$ ). Similar with the TE and TM modes in Figs. 5.3(b) and 5.5(b), the  $n_{\text{eff}}$  of HE<sub>1,N</sub> and EH<sub>1,N</sub> decrease linearly with the increase of  $\lambda$  when  $n_{\text{eff}} > n_1$ .

while below  $n_1$  the  $n_{\text{eff}}$  decrease in a step-like fashion as  $\lambda$  increases. The curves show periodic strong and moderate index dispersion bands. The positions of the intersect points between the dispersion curves of modes  $\text{HE}_{1,N}$  ( $\text{EH}_{1,N}$ ) and the horizontal line at  $n_1$  can be approximated as the cutoff wavelengths of the  $\text{TE}_N$  ( $\text{TM}_N$ ) modes in the asymmetric planar waveguide calculated by Eq. (5.1), indicated by the red (black) vertical dashed lines in Fig. 5.6.

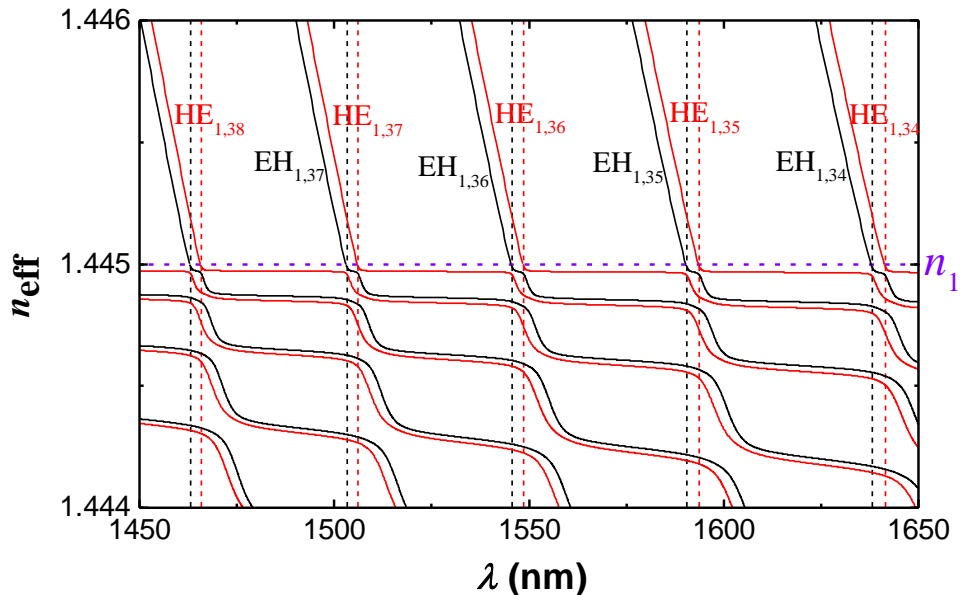


**Figure 5.6** Dispersion curves ( $n_{\text{eff}}$  vs.  $\lambda$ ) of  $\text{HE}_{1,N}$  (red) and  $\text{EH}_{1,N}$  (black) modes with  $n_{\text{eff}}$  corresponding to  $(n_1 - 0.001 < n_{\text{eff}} < n_1 + 0.001)$ ,  $n_1 = 1.445$ . The black and red vertical dashed lines indicate the resonant bands.

For  $\text{HE}_{m,N}$  or  $\text{EH}_{m,N}$  modes, each radial mode order ‘N’ supports a larger number of azimuthal mode orders ‘m’. Fig. 5.7(a) as an example shows a dispersion diagram of the  $\text{HE}_{m,N}$  modes with  $m = 1, 2, \dots$  and  $N = 34, 35, \dots, 38$ . The curves with the same radial mode order ‘N’ are shown in the same color. For the sake of clarity, the transparency of the curves has been increased toward higher azimuthal mode orders in each group. All these curves form a very dense dispersion diagram, where the curves with moderate slopes intersect with those having steeper slopes.

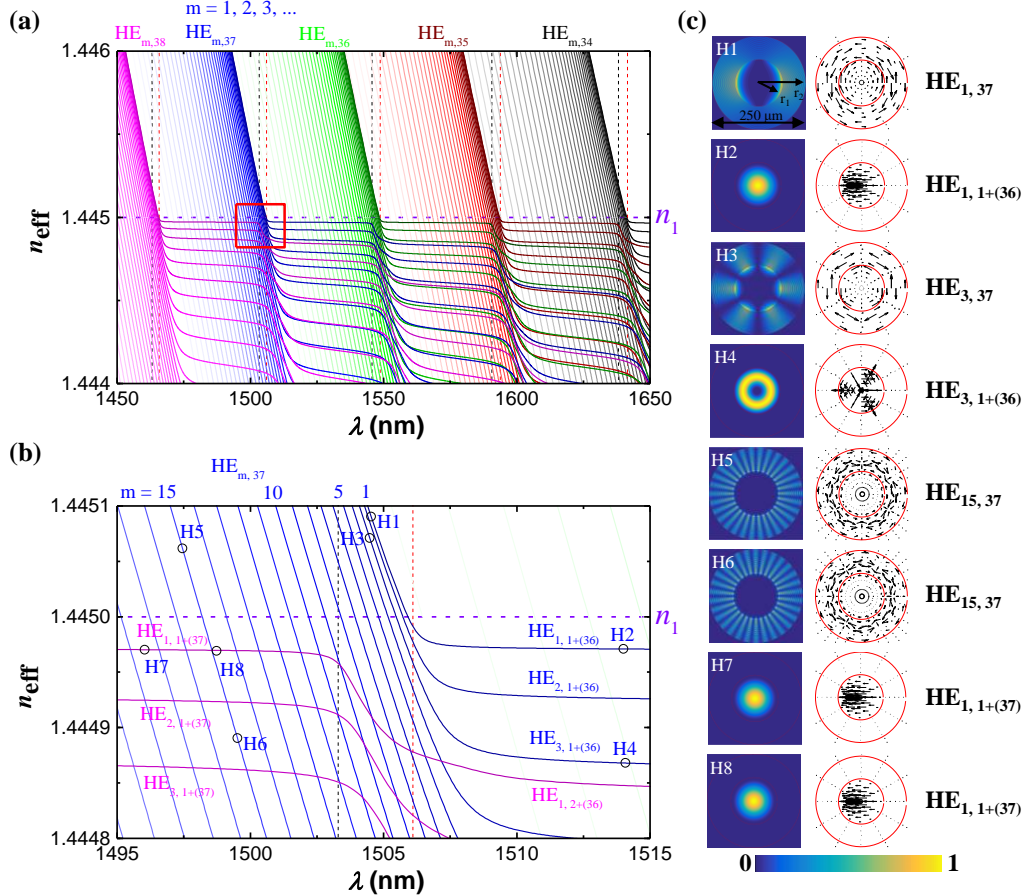


**Figure 5.7** (a) Dispersion curves ( $n_{\text{eff}}$  vs.  $\lambda$ ) of HE modes with  $n_{\text{eff}}$  corresponding to (a)  $n_1 - 0.001 < n_{\text{eff}} < n_1 + 0.001$ ,  $n_1 = 1.445$ . (b) partially enlarged image of (a), indicated by a red frame. (c) shows the modal intensity and electric field vector distributions of HE modes whose positions ( $n_{\text{eff}}, \lambda$ ) are indicated by the circles in (b). The black and red vertical dashed lines in (a) and (b) indicate the resonant bands.

Figure 5.7(b) shows the zoomed view of the part indicated by a red rectangle in Fig. 5.7(a), showing the transition of modes  $\text{HE}_{m,37}$ ,  $m = 1, 2, \dots$ . The dispersion curve of the mode  $\text{HE}_{m,37}$  changing from a steep slope to a moderate slope indicates the formation of an anti-resonant core-type mode  $\text{HE}_{m,1+(36)}$  (the nomenclature similar to TE/TM modes). For example, the modes  $\text{HE}_{1,37}$  at point H1 and  $\text{HE}_{3,37}$  at point H3 are transferred into the modes  $\text{HE}_{1,1+(36)}$  at point H2 and  $\text{HE}_{3,1+(36)}$  at point H4, respectively. Their modal field intensity and electric vector distributions are shown in Fig. 5.7(c). As the azimuthal mode order ‘ $m$ ’ increases, the transition of the cladding-type  $\text{HE}_{m,37}$  to anti-resonant core-type

$\text{HE}_{m,1+(36)}$  will occur at a longer wavelength and a smaller effective index at the point where the slope of the dispersion curve changes. Therefore, the transition process for the modes with large azimuthal mode orders ‘ $m$ ’ may not be visible in the given range of the dispersion diagram. As an example, although the dispersion curve of the mode  $\text{HE}_{15,37}$  in Fig. 5.7(b) intersects the horizontal line corresponding to the value  $n_1$ , it does not change direction abruptly, indicating no mode transition in the given range. Two modes at points H5 and H6 on this dispersion curve of the mode  $\text{HE}_{15,37}$  show similar modal field intensity and electric vector distributions as seen in Fig. 5.7(c). These two modes are both cladding-type modes with energy confined in the cladding region, however, their formation mechanisms are likely different. Compared to the cladding mode at point H5 with  $n_{\text{eff}} > n_1$  guided by the total internal reflections at both the inner and outer boundaries of the cladding region, the cladding mode at point H6 with  $n_{\text{eff}} < n_1$  cannot be guided by the total internal reflections at the inner boundary of the cladding region. The existence of the cladding modes in the dispersion space below the horizontal line at  $n_1$  in Figs. 5.7(a) and 5.7(b) is likely attributed to the inhibited coupling effects as per following discussion.

The modal field intensity and electric vector distributions of two anti-resonant core modes  $\text{HE}_{1,1+(37)}$  at points H7 and H8 are presented in Fig. 5.7(c), showing that for both of the modes the field energy is confined in the fiber core region. The intersection of the dispersion curve of  $\text{HE}_{1,1+(37)}$  with that of  $\text{HE}_{15,37}$  indicates that the disc-like core modes and the annular-like cladding modes can exist in the same dispersion space ( $n_{\text{eff}}$  vs.  $\lambda$ ). The same  $n_{\text{eff}}$  indicates that the modes have the same longitudinal components of the light field. However, they cannot couple

with each other since their transverse components of the light field are different, corresponding to the inhibited coupling effect [6].

### 5.3.3 Mode degeneracy in DCFs

The dispersion curves of several lower order TE, TM, HE and EH modes in the DCF are drawn together in the same dispersion diagram, shown in Fig. 5.8(a). Other higher order modes in the DCF are not shown in order to preserve clarity of the diagram. The dispersion diagram shows periodic resonant and anti-resonant bands corresponding to the strong and moderate index dispersion, and the resonant bands are indicated by the black and red vertical dashed lines. Fig. 5.8(b) displays one of such periodic bands, indicated by a black dashed rectangle. The dispersion curves of the anti-resonant core modes in the DCF such as  $\{\text{HE}_{1,1+(36)}\}$ ,  $\{\text{TE}_{0,1+(36)}, \text{HE}_{2,1+(36)}$  and  $\text{TM}_{0,1+(36)}\}$  and  $\{\text{EH}_{1,1+(36)}$  and  $\text{HE}_{3,1+(36)}\}$  can be respectively grouped together. In the calculation, the longitudinal components of the light field are very small compared to the transverse components of the light field for the anti-resonant core modes. Therefore, the modes in each group can be grouped into a single degenerate scalar mode or a linear polarized mode, similar to that in the conventional step-index fibers. These degeneracies are broken in the resonant bands, where dispersion curves of TE, TM, HE and EH modes are separated.

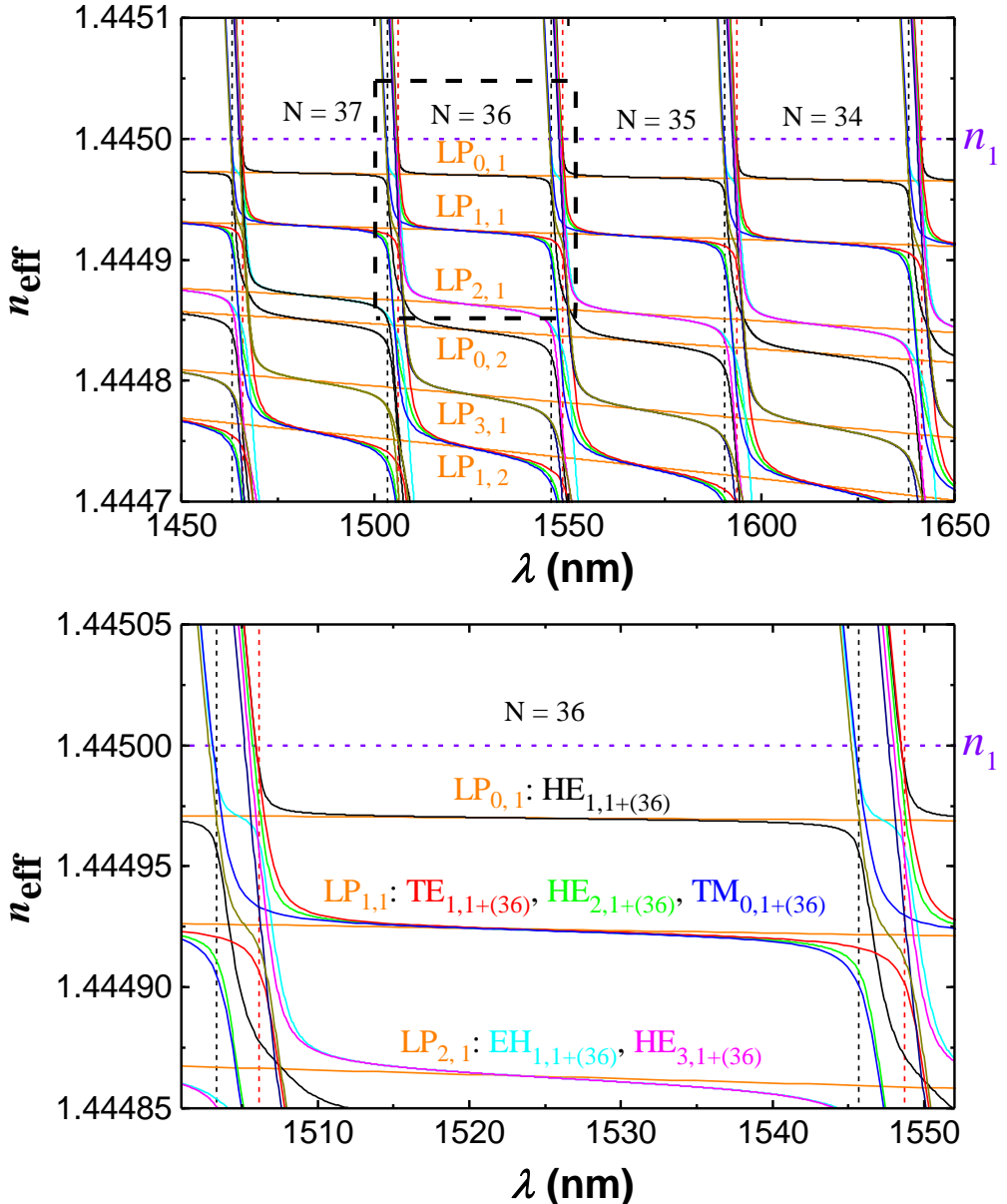


**Figure 5.8** (a) Dispersion curves ( $n_{\text{eff}}$  vs.  $\lambda$ ) of a depressed-core fiber. (b) partially enlarged image of (a), indicated by the black dashed frame. The text labels and the corresponding dispersion curves are of the same color. The orange solid lines in (a) and (b) are for  $LP_{m,n}$  modes in a conventional step-index fiber ( $n_{\text{co}} = 1.445$ ,  $n_{\text{cl}} = 1$ ,  $r_{\text{co}} = 62.5 \mu\text{m}$  and  $r_{\text{cl}} = \infty$ ). The black and red vertical dashed lines indicate the resonant bands.

If the high-index cladding region is removed, the fiber becomes a conventional step-index fiber (a no-core fiber as discussed in Chapter 4), consisting of a bare core and the surrounding air acting as the fiber cladding, where  $n_{\text{co}} = 1.445$ ,  $n_{\text{cl}} = 1$ ,  $r_{\text{co}} = 62.5 \mu\text{m}$  and  $r_{\text{cl}} = \infty$ . The dispersion curves of the core modes in such a step-index fiber were calculated by analytical method. The vector modes in the

fiber such as  $\{\text{HE}_{1,1}\}$ ,  $\{\text{TE}_{0,1}, \text{HE}_{2,1} \text{ and } \text{TM}_{0,1}\}$  and  $\{\text{EH}_{1,1} \text{ and } \text{HE}_{3,1}\}$  can be respectively grouped into linear polarization modes  $\text{LP}_{0,1}$ ,  $\text{LP}_{1,1}$  and  $\text{LP}_{2,1}$ , due to their mode fields being far from cutoff [37,38]. Fig. 5.8 shows the dispersion curves of modes  $\text{LP}_{m,n}$  in the step-index fiber in orange color, which are overlapped with the moderate dispersion curves of the anti-resonant core modes in the DCF. The results indicate that the anti-resonant core modes  $\{\text{HE}_{1,1+(36)}\}$ ,  $\{\text{TE}_{0,1+(36)}, \text{HE}_{2,1+(36)} \text{ and } \text{TM}_{0,1+(36)}\}$  and  $\{\text{EH}_{1,1+(36)} \text{ and } \text{HE}_{3,1+(36)}\}$  in the DCF show similar qualitative and quantitative behaviour with the corresponding core modes  $\{\text{HE}_{1,1}\}$ ,  $\{\text{TE}_{0,1}, \text{HE}_{2,1} \text{ and } \text{TM}_{0,1}\}$  and  $\{\text{EH}_{1,1} \text{ and } \text{HE}_{3,1}\}$  in a conventional step-index fiber. In addition, the effective refractive index of the anti-resonant core modes in the DCF can be approximated as that of the corresponding  $\text{LP}_{m,n}$  modes in a conventional step-index fiber.

## 5.4 Discussion

The dispersion diagram of the DCF shows some similar characteristics to the dispersion diagram of a single-ring hollow-core anti-resonant fiber reported in Ref. [22]. Firstly, they both show periodic resonant and anti-resonant bands. Secondly, they both show the inhibited coupling phenomenon between the core modes and the cladding modes. However, due to the complex structure of the single-ring hollow-core anti-resonant fibers, only an approximate scalar method was used in Ref. [22]. Using the full-vector analytical method in this work, the transition between the cladding modes and the anti-resonant core modes has been demonstrated. The degeneracy in the anti-resonant bands and the loss of degeneracy around the resonant bands make the dispersion curves of anti-

resonant core modes merge together or separate, which may correspond to the narrow and wide variations in bands of anti-resonant modes in Ref. [22].

Although the inhibited-coupling fiber is different with the photonic bandgap fiber from the modal dispersion perspective, both fibers can be viewed as analogous to the conventional step-index fibers. Ref. [20] shows that the density of core modes in the bandgap fibers is similar to that of the conventional step-index multimode fibers. The work presented in this chapter verified that the density of the anti-resonant core modes in the DCF (a inhibited-coupling fiber) is equal to that of the core modes in the equivalent conventional step-index fiber, since the anti-resonant core modes in the former have a one-to-one correspondence to the core modes in the latter.

The core modes in both DCFs and tube-type hollow-core fibers are formed by the anti-resonant effect, yet their properties are different. The  $n_{\text{eff}}$  of the core modes in DCFs is higher than the refractive index of the surrounding air, therefore they are guided by total internal reflections at the outer boundary of the cladding region and they are non-leaky modes with a real  $n_{\text{eff}}$ . Compared to the DCFs, the core modes in a tube-type hollow-core fiber are usually treated as leaky modes with a complex  $n_{\text{eff}}$ . The leaky modes can be solved by the eigenvalue equations in the complex plane, but it is extremely cumbersome. In most of the previous works, only the fundamental mode or a few low-order modes of the hollow-core fibers were obtained with different approximation methods [17,23-25]. However, the available results for the tube-type hollow-core fibers show some similar characteristics with those for the DCFs. Ref. [17] reports step-like dispersion curves for the modes  $\text{HE}_{1,n+(N-n)}$  ( $n = 1, 2, 3, 4$ , where

the radial number ‘N-n’ in the cladding is not clear), which is similar to the behaviour of the  $HE_{1,n+(N-n)}$  modes in the DCFs presented here. Therefore, it can be concluded that all other modes for the tube-type hollow-core fibers are similar to those in DCFs. Since the tube-type hollow-core fiber has a dispersion diagram similar to that of the DCF, a tube-type hollow-core fiber should be considered as an inhibited-coupling fiber.

The anti-resonance derived anti-crossing phenomenon takes place both in the DCF and in the hollow-core photonics crystal fibers (for either the photonic bandgap guiding or inhibited-coupling guiding). The anti-crossing phenomenon has been intensively studied in hollow-core photonic crystal fibers for applications such as generation of the multi-octave supercontinuum [10], ultrafast nonlinear dynamics optics [11] and the broadband robustly single-mode guidance [12]. Therefore, given that DCFs can readily provide manageable waveguide dispersion and exceptional modal field changes, they are worthy further study for a wide range of applications, in addition to the few existing works such as the generation of the supercontinuum [27] and top-hat beams [32]. Furthermore high refractive index coated step-index fibers have been used for sensing of organic vapors, humidity, voltage, pH, and chemical/bio analytes [43] and have a similar refractive index profile to that of DCF which suggests the possibility that DCF might also be useful for sensing. Probably because the thickness of the coating in these structures is small, the inverted refractive index profile and the anti-resonant effect were not observed.

## 5.5 Conclusion

DCFs were studied analytically in comparison with the conventional step-index fibers and the tube-type hollow-core fibers and were found to be a form of anti-resonant and inhibited-coupling fibers. In this chapter an asymmetric planar waveguide approach was proposed for the DCFs in the ARROW model. It has been shown that the DCFs support annular-like cladding modes in the tube cladding region and disc-like anti-resonant core modes in the rod core region and both of them were obtained by solving a same group of full-vector eigenvalue equations using a graphical method. The calculated dispersion diagram shows periodic resonant and anti-resonant bands, where the dispersion curves of the anti-resonant core modes intersect with those of the cladding modes. The formation of core-type modes in a low-index core region can be explained by both the anti-resonant and inhibited coupling mechanisms. The anti-resonant core modes exhibit similar qualitative and quantitative behaviours as those of the conventional step-index fibers. The analogy to conventional step-index fibers may provide a convenient tool to model the modes of the DCFs (the inhibited-coupling fibers). To the author's knowledge, it is the first report on the complete full-vector modal dispersion diagram calculated analytically for an inversed-index fiber. The results presented in this chapter provide better understanding of the anti-resonant and inhibited-coupling guidance mechanisms in complex inversed-index fibers such as hollow-core photonic-bandgap fibers, tube-type hollow-core fibers and single-ring hollow-core fibers.

## 5.6 Reference

- [1] S. F. Gao, Y. Y. Wang, W. Ding, D. L. Jiang, S. Gu, X. Zhang, and P. Wang, “Hollow-core conjoined-tube negative-curvature fiber with ultralow loss,” *Nat. Commun.*, vol. 9, no. 1, pp. 1-6, 2018.
- [2] B. Debord, A. Amsanpally, M. Chafer, A. Baz, M. Maurel, J. M. Blondy, E. Hugonnot, F. Scol, L. Vincetti, F. Gérôme, and F. Benabid, “Ultralow transmission loss in inhibited-coupling guiding hollow fibers,” *Optica*, vol. 4, no. 2, pp. 209-217, 2017.
- [3] F. Poletti, M. N. Petrovich, and D. J. Richardson, “Hollow-core photonic bandgap fibers: technology and applications,” *Nanophotonics*, vol. 2, no. 5-6, pp. 315-340, 2013.
- [4] F. Yu and J. C. Knight, “Negative curvature hollow-core optical fiber,” *IEEE J. Sel. Top. Quantum Electron.*, vol. 22, no. 2, p. 4400610, 2016.
- [5] Y. Chen, Z. Liu, S. R. Sandoghchi, G. T. Jasion, T. D. Bradley, E. N. Fokoua, J. R. Hayes, N. V. Wheeler, D. R. Gray, B. J. Mangan, R. Slavík, S. Member, F. Poletti, M. N. Petrovich, S. Member, and D. J. Richardson, “Multi-kilometer long, longitudinally uniform hollow core photonic bandgap fibers for broadband low latency data transmission,” *J. Lightw. Technol.*, vol. 34, no. 4, pp. 104-113, 2016.
- [6] F. Courty, F. Benabid, P. J. Roberts, P. S. Light, and M. G. Raymer, “Generation and photonic guidance of multioctave optical-frequency combs,” *Science*, vol. 318, no. 5853, pp. 1118-1121, 2007.
- [7] A. F. Kosolapov, A. D. Pryamikov, A. S. Biriukov, V. S. Shiryaev, M. S. Astapovich, G. E. Snopatin, V. G. Plotnichenko, M. F. Churbanov, and E. M. Dianov, “Demonstration of CO<sub>2</sub>-laser power delivery through chalcogenide-glass fiber with negative-curvature hollow core,” *Opt. Express*, vol. 19, no. 25, pp. 25723-25728, 2011.
- [8] A. D. Pryamikov, A. S. Biriukov, A. F. Kosolapov, V. G. Plotnichenko, S. L. Semjonov, and E. M. Dianov, “Demonstration of a waveguide regime for a silica hollow--core microstructured optical fiber with a negative curvature of the core boundary in the spectral region > 3.5 μm,” *Opt. Express*, vol. 19, no. 2, pp. 1441-1448, 2011.

- [9] P. S. J. Russell, P. Hölzer, W. Chang, A. Abdolvand, and J. C. Travers, “Hollow-core photonic crystal fibers for gas-based nonlinear optics,” *Nat. Photonics*, vol. 8, no. 4, pp. 278-286, 2014.
- [10] R. Sollapur, D. Kartashov, M. Zürch, A. Hoffmann, T. Grigorova, G. Sauer, A. Hartung, A. Schwuchow, J. Bierlich, J. Kobelke, M. Chemnitz, M. A. Schmidt, and C. Spielmann, “Resonance-enhanced multi-octave supercontinuum generation in antiresonant hollow-core fibers,” *Light: Sci. Appl.*, vol. 6, no. 12, p. e17124, 2017.
- [11] F. Tani, F. Köttig, D. Novoa, R. Keding, and P. S. Russell, “Effect of anti-crossings with cladding resonances on ultrafast nonlinear dynamics in gas-filled photonic crystal fibers,” *Photon. Res.*, vol. 6, no. 2, pp. 84–88, 2018.
- [12] P. Uebel, M. C. Günendi, M. H. Frosz, G. Ahmed, N. N. Edavalath, J.-M. Ménard, and P. St. J. Russell, “Broadband robustly single-mode hollow-core PCF by resonant filtering of higher-order modes,” *Opt. Lett.*, vol. 41, no. 9, pp. 1961-1964, 2016.
- [13] C.-H. Lai, B. You, J.-Y. Lu, T.-A. Liu, J.-L. Peng, C.-K. Sun, and H.-C. Chang, “Modal characteristics of antiresonant reflecting pipe waveguides for terahertz waveguiding,” *Opt. Express*, vol. 18, no. 1, pp. 309-322, 2010.
- [14] S. Liu, Y. Ji, L. Cui, W. Sun, J. Yang, and H. Li, “Humidity-insensitive temperature sensor based on a quartz capillary anti-resonant reflection optical waveguide,” *Opt. Express*, vol. 25, no. 16, pp. 18929-18939, 2017.
- [15] D. Liu, Q. Wu, C. Mei, J. Yuan, X. Xin, A. K. Mallik, F. Wei, W. Han, R. Kumar, C. Yu, S. Wan, X. He, B. Liu, G.-D. Peng, Y. Semenova, and G. Farrell, “Hollow Core Fiber Based Interferometer for High Temperature (1000 °C) Measurement,” *J. Lightw. Technol.*, vol. 36, no. 9, pp. 1583-1590, 2018.
- [16] M. A. Duguay, Y. Kokubun, T. L. Koch, and L. Pfeiffer, “Antiresonant reflecting optical waveguides in SiO<sub>2</sub>-Si multilayer structures,” *Appl. Phys. Lett.*, vol. 49, no. 1, pp. 13-15, 1986.
- [17] J. L. Archambault, R.J. Black, S. Lacroix, and J. Bures, “Loss calculations for antiresonant waveguides,” *J. Lightw. Technol.*, vol. 11, no. 3, pp. 416-423, 1993.

- [18] N. M. Litchinitser, A. K. Abeeluck, C. Headley, and B. J. Eggleton, “Antiresonant reflecting photonic crystal optical waveguides,” *Opt. Lett.*, vol. 27, no. 18, pp. 1592-1594, 2002.
- [19] N. M. Litchinitser, S. C. Dunn, B. Usner, B. J. Eggleton, T. P. White, R. C. McPhedran, and C. M. de Sterke, “Resonances in microstructured optical waveguides,” *Opt. Express*, vol. 11, no. 10, pp. 1243-1251, 2003.
- [20] M. J. F. Digonnet, H. K. Kim, G. S. Kino, and S. Fan, “Understanding air-core photonic-bandgap fibers: analogy to conventional fibers,” *J. Lightw. Technol.*, vol. 23, no. 12, pp. 4169-4177, 2005.
- [21] K. Z. Aghaie, V. Dangui, M. J. F. Digonnet, S. H. Fan, and G. S. Kino, “Classification of the core modes of hollow-core photonic-bandgap fibers,” *IEEE J. Quantum Electron.*, vol. 45, no. 9, pp. 1192-1200, 2009.
- [22] R. F. Ando, A. Hartung, B. Jang, and M. A. Schmidt, “Approximate model for analysing band structures of single-ring hollow-core anti-resonant fibers,” *Opt. Express*, vol. 27, no. 7, pp. 10009-10021, 2019.
- [23] L. Vincetti and V. Setti, “Waveguiding mechanism in tube lattice fibers,” *Opt. Express*, vol. 18, no. 22, pp. 23133-23146, 2010.
- [24] M. Zeisberger and M. A. Schmidt, “Analytic model for the complex effective index of the leaky modes of tubetype anti-resonant hollow core fibers,” *Sci. Rep.*, vol. 7, no. 1, p. 11761, 2017.
- [25] M. Bache, M. S. Habib, C. Markos, and J. Lægsgaard, “Poor-man’s model of hollow-core anti-resonant fibers,” *J. Opt. Soc. Am. B*, vol. 36, no. 1, pp. 69-80, 2018.
- [26] V. I. Neves and A. S. C. Fernandes, “Modal characteristics for W-type and M-type dielectric profile fibers,” *Micro. & Opt. Tech. Lett.*, vol. 22, no. 6, pp. 398-405, 1999.
- [27] D. Jain, C. Markos, T. M. Benson, A. B. Seddon, and O. Bang, “Exploiting dispersion of higher-order-modes using M-type fiber for application in mid-infrared supercontinuum generation,” *Sci. Rep.*, vol. 9, no. 1, p. 8536, 2019.
- [28] M. Hautakorpi and M. Kaivola, “Modal analysis of M-type-dielectric-profile optical fibers in the weakly guiding approximation,” *J. Opt. Soc. Am. A*, vol. 22, no. 6, pp. 1163-1169, 2005.

- [29] A. S. Belanov and S. V. Tsvetkov, “High-index-ring three-layer fibers for mode-locked sub-1.3  $\mu\text{m}$  fiber lasers,” *Quantum Electron.*, vol. 40, no. 2, pp. 160-162, 2010.
- [30] S. S. Aleshkina, M. E. Likhachev, A. K. Senatorov, M. M. Bubnov, M. Y. Salaganskii, and A. N. Guryanov, “Low-loss hybrid fiber with zero dispersion wavelength shifted to 1  $\mu\text{m}$ ,” *Opt. Express*, vol. 21, no. 20, pp. 23838-23843, 2013.
- [31] S. S. Aleshkina, M. V. Yashkov, M. M. Bubnov, A. N. Guryanov, and M. E. Likhachev, “Asymptotically single-mode hybrid fiber for dispersion management near 1  $\mu\text{m}$ ,” *IEEE J. Sel. Topics Quantum Electron.*, vol. 24, no. 3, pp. 1-8, 2017.
- [32] C. Valentin, P. Calvet, Y. Quiquempois, G. Bouwmans, L. Bigot, Q. Coulombier, M. Douay, K. Delplace, A. Mussot, and E. Hugonnot, “Top-hat beam output of a single-mode microstructured optical fiber: Impact of core index depression,” *Opt. Express*, vol. 21, no. 20, pp. 23250-23260, 2013.
- [33] C. Tsao, *Optical Fiber Waveguide Analysis* (Oxford University Press, New York, 1992).
- [34] T. Erdogan, “Cladding-mode resonances in short- and long-period fiber grating filters,” *J. Opt. Soc. Am. A*, vol. 14, no. 8, pp. 1760-1773, 1997.
- [35] Z. Zhang and W. Shi, “Eigenvalue and field equations of three-layered uniaxial fibers and their applications to the characteristics of long-period fiber gratings with applied axial strain,” *J. Opt. Soc. Am. A*, vol. 22, no. 11, pp. 2516-2526, 2005.
- [36] D. Marcuse, *Theory of Dielectric Optical Waveguides*, 2nd ed. (Academic, New York, 1991).
- [37] X. K. Lian, G. Farrell, Q. Wu, W. Han, F. F. Wei, and Y. Semenova, “Mode Transition in Conventional Step-Index Optical Fibers,” in 2019 IEEE 18th International Conference on Optical Communications and Networks (ICOON), pp. 1-3, 2019.
- [38] X. K. Lian, Q. Wu, G. Farrell, C. Y. Shen, Y. Q. Ma, and Y. Semenova, “Discrete self-imaging in small-core optical fiber interferometers,” *J. Lightw. Technol.*, vol. 37, no. 9, pp. 1873-1884, 2019.

- [39] M. Born, and E. Wolf. *Principles of Optics*, (Cambridge University Press, 1999).
- [40] I. Del Villar, I. R. Matías, F. J. Arregui, and P. Lalanne, “Optimization of sensitivity in Long Period Fiber Gratings with overlay deposition,” *Opt. Express*, vol. 13, no. 1, pp. 56-69, 2005.
- [41] A. Cusano, A. Iadicicco, P. Pilla, L. Contessa, S. Campopiano, A. Cutolo, and M. Giordano, “Mode transition in high refractive index coated long period gratings,” *Opt. Express*, vol. 14, no. 1, pp. 19-34, 2006.
- [42] L. L. Xue and Y. Li, “Sensitivity enhancement of RI sensor based on SMS fiber structure with high refractive index overlay,” *J. Lightw. Technol.*, vol. 30, no. 10, pp. 1463-1469, 2012.
- [43] I. D. Villar, F. J. Arregui, C. R. Zamarreño, J. M. Corres, C. Bariain, J. Goicoechea, C. Elosua, M. Hernaez, P. J. Rivero, A. B. Socorro, A. Urrutia, P. Sanchez, P. Zubiate, D. Lopez, N. De Acha, J. Ascorbe, and I. R. Matias, “Optical sensors based on lossy-mode resonances,” *Sens. Actuators B Chem.*, vol. 240, pp. 174-185, 2017.

# **Chapter 6**

## **Spectral Dependence of Transmission Losses in High-Index Polymer-Coated No-Core Optical Fibers<sup>4</sup>**

Chapter 5 demonstrated that the light field in a depressed-core fiber is guided by the anti-resonant, inhibited coupling and total internal reflection effects, and its dispersion diagram shows periodic resonant and anti-resonant bands. In this chapter experimental works are carried out to verify the theoretical results in Chapter 5.

A high-index polymer-coated no-core fiber (PC-NCF) is effectively a depressed-core fiber and in this chapter, the transmission spectra of the straight and bent PC-NCFs (length > 5 cm) are measured and analyzed from a modal dispersion perspective. For the purpose of the study, the PC-NCFs are contained within a fiber hetero-structure using two single-mode fiber (SMF) pigtails forming a SMF-PC-NCF-SMF structure. The anti-resonant spectral characteristics are suppressed by the multimode interference in the PC-NCF with a short fiber length. The increase of the length or fiber bending (bend radius > 28 cm) can make the anti-resonance dominate and result in the periodic transmission loss dips and variations in the depth of these loss dips, due to the different modal intensity distributions in different bands and the material absorption of the

---

<sup>4</sup>Lian, Xiaokang, Gerald Farrell, Qiang Wu, Wei Han, Youqiao Ma, and Yuliya Semenova, “Spectral dependence of transmission losses in high-index polymer coated no-core fibers,” J. Lightw. Technol., vol. 38, no. 22, pp. 6352-6361, 2020.

polymer. The PC-NCFs are expected to be used in many devices including curvature sensors and tunable loss filters, as the experiments show that the change of loss dip around 1550 nm is over 31 dB and the average sensitivity is up to 14.77 dB/m<sup>-1</sup> in the bend radius range from  $\infty$  to 47.48 cm. The study details the general principles of the effect of high-index layers in the formation of the transmission loss dips in fiber optics.

## 6.1 Research background

Coating of optical fibers has been extensively studied as a key element of the design of various devices such as optical sensors [1-10], filters [11,12] and modulators [13]. Fiber coating materials include metals, metal oxides, graphene, polymers, and many others. These materials are either chosen to be sensitive to specific physical, chemical and bio- parameters in order to enhance the sensitivity of the sensor [14-19] or to facilitate particular waveguiding mechanisms [2,3,20]. For example, thin films of silver or gold deposited on an optical fiber can result in surface plasmon resonances due to the coupling between light and the surface electrons of the metal films [2]. Lossy films (i.e., indium-tin oxide (ITO) [20]) on the surface of no-core fibers (NCFs) can cause lossy mode resonance (LMR), due to the coupling between the guided modes in the optical fiber and the lossy modes in the fiber coating [3].

The high refractive index coated fibers show exceptional modal characteristics. The high-index coating can cause mode reorganization [14-16], when a core mode in the fiber is coupled into the modes of the high-index coating and other fiber modes are reorganized. The mode reorganization phenomenon along with drastic changes of the modal field distributions have also been observed

numerically in a LMR fiber structure [21,22], where the real part of the complex refractive index of the lossy coating is higher than that of the fiber and the surrounding medium. The energy of the lossy modes was demonstrated numerically to be distributed both in the fiber core and the lossy coating along with a mode splitting phenomenon near the resonant wavelength [23]. Although a number of methods have been employed to investigate the high-index coated fiber structure [14-23], it was rarely mentioned that a high-index coating changes the index distribution within a fiber. For example, an NCF is a typical conventional two-layer step-index fiber, which consists of a silica core surrounded by the low-index air acting as its cladding. Light guiding within the NCF is based on the total internal reflection effect. If an NCF is coated with a high-index material, its original index distribution changes to the inversed-index distribution with the high-index coating acting as the new fiber cladding, and the light guiding mechanism in such a fiber is also changed. This inversed-index structure can be considered as a depressed-core fiber [24].

In Chapter 5, a dispersion diagram of the depressed-core fiber was obtained by solving the full-vector eigenvalue equations [25]. Analysis of the dispersion diagram suggests that the light guiding mechanism in the fiber core is supported by the anti-resonant, inhibited coupling and total internal reflection effects. The anti-resonant effect is typically described by an anti-resonant reflecting optical waveguide (ARROW) model [26]. In this model, the high-index cladding region of the depressed-core fiber is treated as a Fabry-Perot resonator, which allows the anti-resonant light to be reflected back while allowing forward transmission of the resonant light. The inhibited coupling mechanism explains the coexistence of cladding- and core-type modes in the same effective refractive index-

wavelength ( $n_{\text{eff}} - \lambda$ ) dispersion space. To date the anti-resonant and inhibited-coupling guiding nature of the high refractive index coated fiber structure, has not been exploited.

In this chapter, a high-index polymer-coated no-core fiber (PC-NCF) is studied, which consists of an NCF with acrylate polymer coating. Compared to a semiconductor coating with a complex refractive index in the LMR fiber structure [20], the refractive index of the acrylate polymer is a real number [27-29]. The PC-NCF can be used as a model for studies of the waveguiding properties of the depressed-core fiber, since the refractive index of the polymer coating (as a cladding region) is higher than that of the silica core. In Section 6.3, the spectra of the straight and bent PC-NCFs with several different lengths were measured and periodic transmission loss dips were found in the spectra of straight PC-NCFs with long lengths and in bent PC-NCFs. The effects of the multimode interference and the anti-resonance on the spectral characteristics of the PC-NCFs are analyzed. With the knowledge of the anti-resonant and inhibited-coupling guiding mechanisms, the relationship between the modal field distribution and the transmission loss is studied. In Section 6.4, the implications of the results for the LMR fiber structures are discussed.

## 6.2 Method

The PC-NCF used in this study is FG125LA from Thorlabs, which is an NCF coated with a layer of acrylate polymer. The microscopic image and the cross-sectional view of the PC-NCF are shown in Fig. 6.1(a) and Fig. 6.1(b), respectively. The PC-NCF is described by a three-layer fiber model, where the silica NCF plays the role of a core region, the polymer coating serves as the

cladding region and the surrounding medium air acting in effect as a second cladding region. The refractive indices of the three layers are  $n_1$ ,  $n_2$  and  $n_3$  respectively, with  $n_2 > n_1 > n_3$ . The transmission spectra of the straight and bent PC-NCFs are studied, where the PC-NCF is spliced with two single-mode fiber (SMF) pigtails forming a fiber hetero-structure SMF-PC-NCF-SMF as shown in Fig. 6.4. The experimental setup is shown in Fig. 6.1(c), where the fiber is fixed on two translation stages and the bending curvature of the PC-NCF is controlled by moving the two stages toward one another. The bend radius is calculated based on the displacement of the translation stages [30].

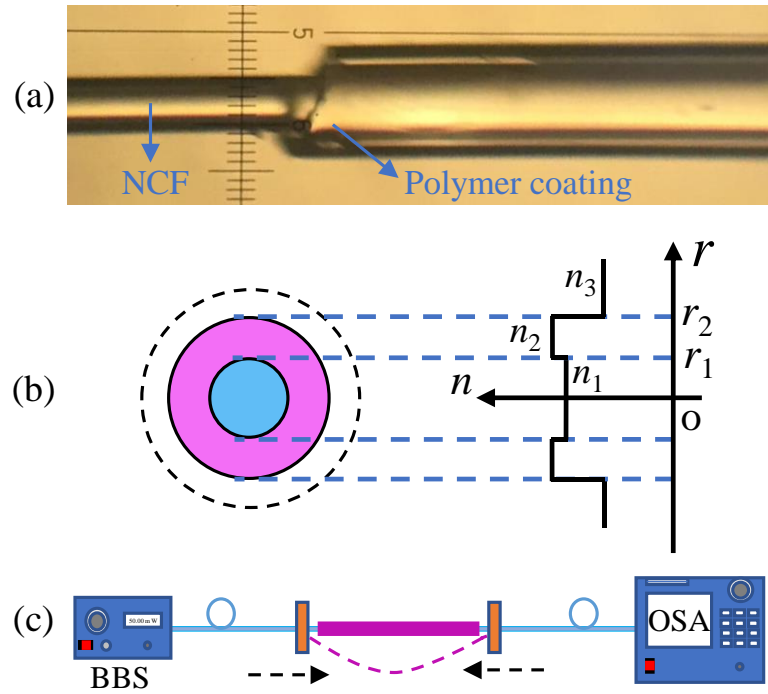


**Figure 6.1** (a) Microscopic image of a polymer-coated no-core fiber (PC-NCF). (b) Refractive index variations along the cross section of the PC-NCF ( $n_2 > n_1 > n_3$ ). (c) Schematic of the experimental setup for measurements of the straight and bent PC-NCF samples.

In this chapter the calculations for both the straight and bent PC-NCFs were carried out by the full-vector finite element method, where the maximum mesh size is  $0.4\lambda$  and the relative error in the computed eigenvalues is smaller than  $10^{-4}$ .

<sup>12</sup>. The numerical results obtained agree well with the analytical results in chapter 5 for the straight PC-NCF. Furthermore, the waveguiding in the straight PC-NCF was analyzed using the ray optics approach and the transmission loss spectra were simulated analytically based on an asymmetric planar reflection model.

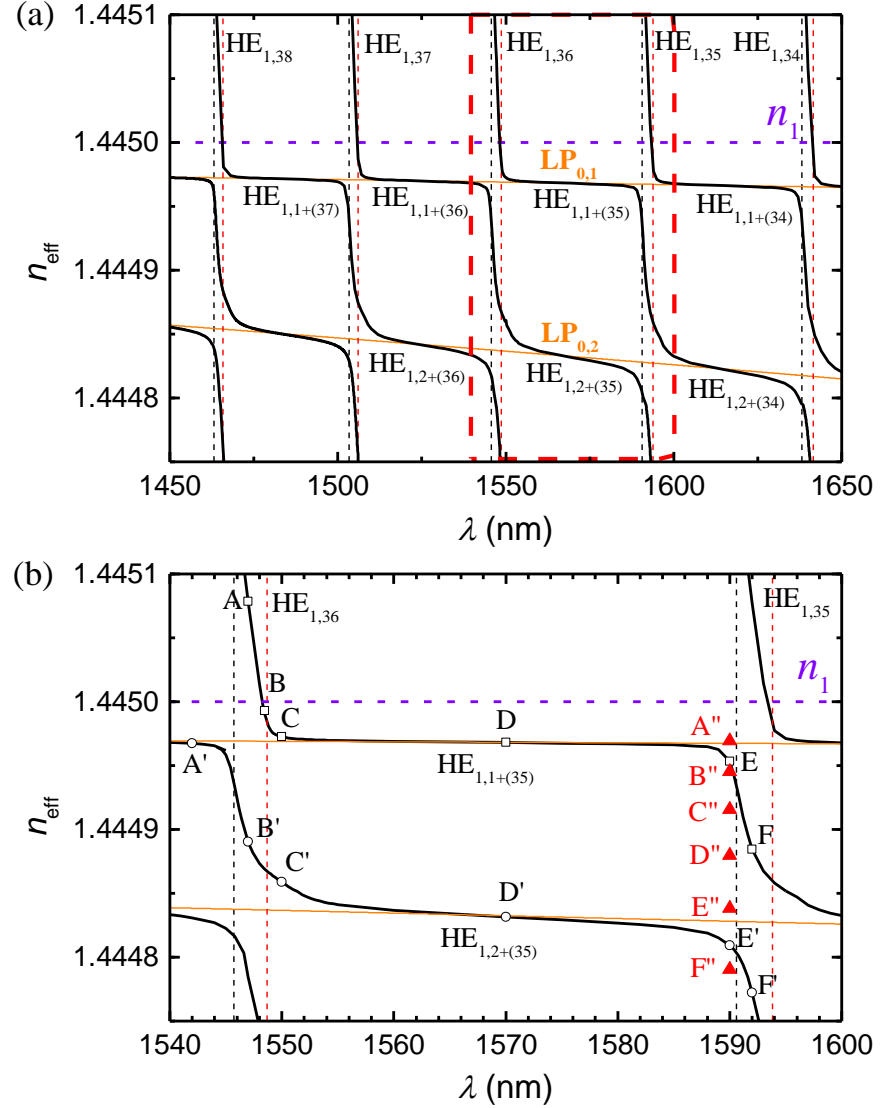
In the calculations, the refractive indices of the silica NCF and the polymer coating are assumed as  $n_1 = 1.445$  and  $n_2 = 1.51$  at  $\lambda = 1550$  nm, respectively. The radii of the silica NCF and the polymer coating are  $r_1 = 62.5$   $\mu\text{m}$  and  $r_2 = 125$   $\mu\text{m}$  respectively. The thickness of the polymer coating is  $d = 62.5$   $\mu\text{m}$ . The surrounding medium is air with the refractive index of  $n_3 = 1$ . The radii and the refractive indices of the core (co) and cladding (cl) regions of the input/output SMF-28 (from Corning) are  $r_{\text{co}} = 4.15$   $\mu\text{m}$ ,  $r_{\text{cl}} = 62.5$   $\mu\text{m}$ ,  $n_{\text{co}} = 1.4504$  and  $n_{\text{cl}} = 1.4447$ . The material dispersion was not considered in the calculations for the sake of conciseness.

In the experiments, a broadband light source (Thorlabs S5FC1005s, 1030 nm-1660 nm) and an optical spectrum analyzer (OSA, Agilent 86142B) were used. The polymer coating with the length of about 0.5 cm at both ends of the PC-NCF was removed before splicing with the SMFs, as shown in Fig. 6.1(a). Any slight unevenness at the end points of the remaining polymer coating does not affect the experimental results for the transmission spectral loss. The ends of the bare NCF and the SMF have the same diameter as shown in Fig. 6.4 and were axially aligned and spliced using a Fujikura 70S splicer in automatic mode.

## 6.3 Results

### 6.3.1 Modes in straight PC-NCFs

The modes in PC-NCFs include  $TE_{0,N}$ ,  $TM_{0,N}$ ,  $HE_{m,N}$  and  $EH_{m,N}$ , where ‘0’ and ‘m’ on the left side of the comma in the subscript positions are the azimuthal mode numbers and ‘N’ on the right side are the radial mode numbers. Fig. 6.2(a) shows the dispersion diagram ( $n_{\text{eff}}$  vs.  $\lambda$ ) for the modes  $HE_{1,N}$ ,  $N = 34, 35, \dots, 38$ . The cladding modes, which are guided in the cladding region by total internal reflections, are depicted within the top part of the graph where  $n_{\text{eff}} > n_1$ . On the same dispersion curve, as  $\lambda$  increase the cladding modes  $HE_{1,N}$  can change into anti-resonant core modes  $HE_{1,n+(N-n)}$ ,  $n = 1, 2, \dots$ , where the subscript ‘n’ denotes the radial number in the core region while the number ‘ $N-n$ ’ denotes the radial number in the cladding region [25]. The total radial number does not change for each of the dispersion curves. The step-like dispersion curves are consistent with the mode reorganization phenomenon [14-16]. The  $HE_{1,n+(N-n)}$  exhibit similar qualitative and quantitative behaviour as the  $HE_{1,n}$  modes of conventional step-index fibers and can be approximated as the linear polarization modes  $LP_{0,n}$  in the NCF [25]. As shown in the Fig. 6.2(a), the dispersion curves of the modes  $LP_{0,n}$  shown in orange color are overlapped with that of the modes  $HE_{1,n+(N-n)}$ .



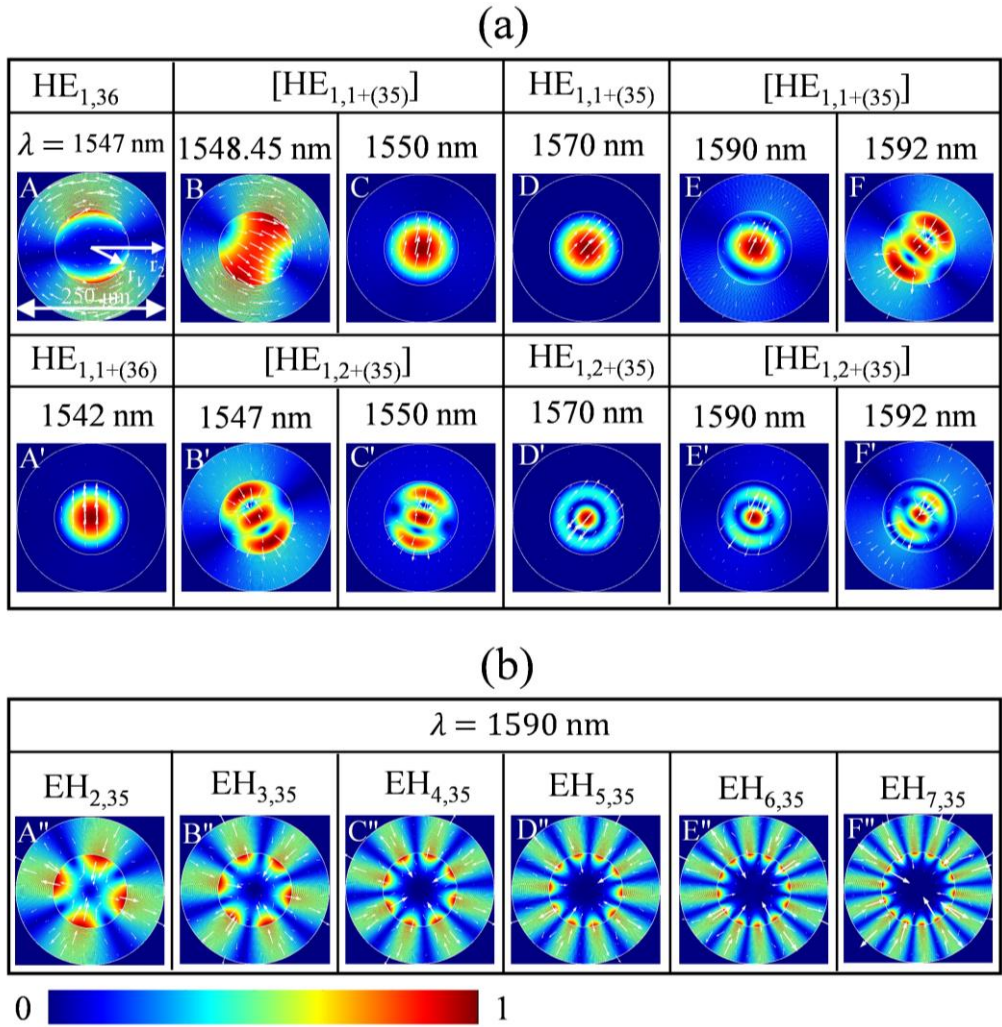
**Figure 6.2** (a) shows the dispersion curves ( $n_{\text{eff}}$  vs.  $\lambda$ ) of modes  $\text{HE}_{1,N}$ ,  $N = 34, 35, \dots, 38$  in the PC-NCF, which change into the anti-resonant core modes  $\text{HE}_{1,n+(N-n)}$ ,  $n = 1, 2, \dots$  as  $\lambda$  increases. The orange lines are the dispersion curves of the  $\text{LP}_{0,1}$  ( $\text{HE}_{1,1}$ ) and  $\text{LP}_{0,2}$  ( $\text{HE}_{1,2}$ ) in the NCF. (b) is the partially enlarged image of (a), indicated by a red dashed frame. The black and red vertical dashed lines indicate the resonant bands.

Figure 6.2(a) exhibits periodic strong and moderate index dispersion bands, corresponding to resonant and anti-resonant bands. The resonant bands are indicated by the vertical black and red dashed lines, which intersect with the horizontal purple dashed line corresponding to the value of  $n_1$ . The intersect points can be approximated as the cutoff positions of the  $\text{TM}_N$  and  $\text{TE}_N$  modes in an equivalent asymmetric planar waveguide, calculated by [25,31]:

$$\lambda_{N,c} = \frac{2d\sqrt{n_2^2 - n_1^2}}{\left[N-1 + \frac{1}{\pi}\tan^{-1}\left(\kappa\sqrt{\frac{n_1^2 - n_3^2}{n_2^2 - n_1^2}}\right)\right]}, \quad \kappa = \begin{cases} 1, & \text{TE}_N \\ \frac{n_2^2}{n_3^2}, & \text{TM}_N \end{cases} \quad (6.1)$$

where,  $N = 34, 35, \dots, 38$ .

In order to analyze the modal field distributions in different dispersion bands, one dispersion period indicated by the red dashed rectangle in Fig. 6.2(a) is enlarged and shown in Fig. 6.2(b). The modal intensity and electric field vector distributions at several points indicated in Fig. 6.2(b) are shown in Fig. 6.3. It should be noted that the HE mode is a two-fold degeneracy mode, including the modes  $\text{HE}_a$  and  $\text{HE}_b$ , whose modal intensity distributions are identical except for a  $\pi/2$  rotation of the electric vector as shown later in Fig. 6.8. Fig. 6.3 shows only one of the two degenerate modes for simplicity. For the cladding mode  $\text{HE}_{1,36}$  at point A the modal energy is mainly confined in the fiber cladding region, for the anti-resonant core mode  $\text{HE}_{1,1+(35)}$  at point D the modal energy is mainly confined in the fiber core region, as discussed in Chapter 5. The modes at B and C are denoted as  $[\text{HE}_{1,1+(35)}]$ , where the brackets indicate that the modes are in a transition state and their modal energy is evenly distributed both in the fiber core and cladding regions. The modes at points E and F are also in transition states and denoted as  $[\text{HE}_{1,1+(35)}]$  or  $[\text{HE}_{1,2+(34)}]$ . Similarly, the modes at points A' and D' represent the low-order and high-order anti-resonant core modes  $\text{HE}_{1,1+(36)}$  and  $\text{HE}_{1,2+(35)}$ , respectively. The modes at points B', C', E' and F' are in transition states.



**Figure 6.3** The intensity and electric field vector distributions of modes in PC-NCF, whose positions in dispersion diagram are indicated in Fig. 6.2(b).

Another modal characteristic of the PC-NCF is the coexistence of the core and cladding modes in the dispersion space [25]. Some cladding modes exist in the dispersion space below the horizontal purple dashed line corresponding to the value of  $n_1$  in Fig. 6.2. For example, the modes  $\text{EH}_{m,35}$ ,  $m = 2, 3, \dots 7$  at points A''- F'' with the wavelength of 1590 nm, whose modal intensities and electric field vector distributions are shown in Fig. 6.3(b). Although the energy of these cladding modes at points A''- F'' with  $n_{\text{eff}} < n_1$  is mainly confined in the cladding region, they differ from the cladding modes with  $n_{\text{eff}} > n_1$ , since the total internal reflection does not apply at the inner boundary of the cladding region. The

confinement of energy in the cladding region for the modes at points A"- F" is attributed to the anti-resonant and inhibited coupling effects.

If the material dispersion is considered, the refractive index of the polymer coating will decrease smoothly as the wavelength increases according to the Cauchy–Schott equation [27]. Based on Eq. (6.1), the resonant coupling position is mainly dependent on the thickness and the refractive index of the coating. Therefore, the anti-resonance condition is maintained if an inversed-index profile (the refractive index of the cladding is higher than that of the fiber core) is maintained. The changes of the index due to material dispersion will only modify the resonant wavelength positions (period), which may cause the discrepancies between the simulated and measured results. If the inversed-index profile is unchanged, then the modal field distributions in both the resonant and anti-resonant bands will not be affected by changes in the refractive index of the polymer coating.

The process of mode coupling in the LMR and PC-NCF structures is different and depends on the overlap of modal fields and the phase-matching conditions (equality of real parts of the effective refractive index). As shown in the dispersion diagram and the mode profiles for the PC-NCF in Figs. 6.2 and 6.3 and Ref. [25], the coupling between the cladding modes and the anti-resonant core modes takes place in accordance with the order of the modes and the symmetry of the modal field distributions, that is the fundamental core modes are at first coupled to the corresponding cladding modes and then the high-order core modes become low-order core modes due to mode reorganization. The field of the core modes in both fiber structures is distributed throughout the entire fiber

cross section. However, the parts of modal field of the core modes which propagate in the high-loss coating layer of the LMR structure may be absorbed and changed based on their symmetries. As a result, in the LMR structure mode coupling occurs in a less predictable manner and some high-order modes may couple to cladding modes before the low-order modes, as shown in the Refs. [21,22].

### 6.3.2 Analysis of the effects of anti-resonance and multimode interference on the transmission spectra of the PC-NCFs

The complex modal dispersion diagram indicates the actual light field in the PC-NCF is very complex, possessing both anti-resonance (AR) and multimode interference (MMI) properties. Fig. 6.4 shows ray trajectories within the SMF-PC-NCF-SMF hetero-structure. The light in the lead-in SMF excites multiple LP<sub>0,n</sub> (HE<sub>1,n</sub>) modes in the NCF. An individual guided LP<sub>0,n</sub> mode indicated by the red arrows in the NCF will progressively reflect between the polymer coatings at a certain angle  $\theta_1$ , forming the multiple reflections and multi-path interference at the inner boundary of the polymer coating region, which corresponds to the anti-resonance property. All the black and red arrows in the

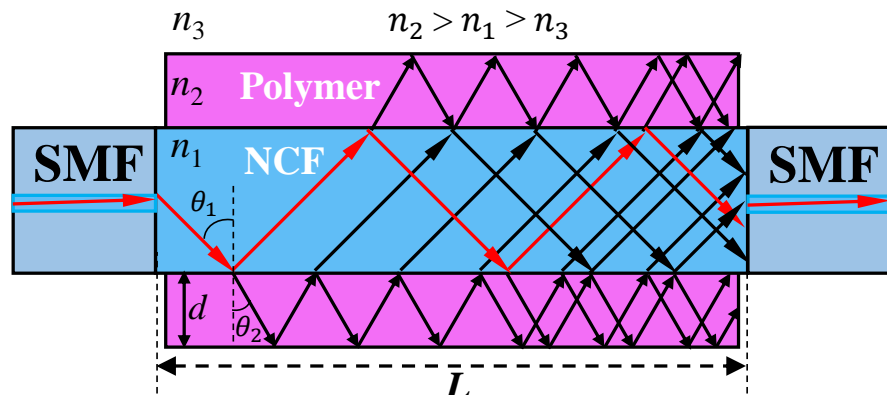


**Figure 6.4** Schematic of the ray trajectories of an excited guide mode within the SMF-PC-NCF-SMF hetero-structure.

middle section fiber represent the ray trajectories of an guided mode  $\text{HE}_{1,n+(N-n)}$  in the PC-NCF. After propagation within the PC-NCF the light will couple into the lead-out SMF. The transmitted power in the lead-out SMF is dependent on the coupling between its modal field and the field in the NCF.

The  $n_{\text{eff}}(\text{LP}_{0,n})$  can be written as [31,32]:

$$n_{\text{eff}}(\text{LP}_{0,n}) = \frac{1}{k_0} \sqrt{k_0^2 n_1^2 - \frac{1}{r_1^2} \left[ \left( 2n - \frac{1}{2} \right) \frac{\pi}{2} \right]^2} \quad (6.2)$$

where  $k_0 = 2\pi/\lambda$  is wavenumber in vacuum. The angle  $\theta_{0,n}$  (equal to  $\theta_1$  in Fig. 6.4) between the incident direction of the mode  $\text{LP}_{0,n}$  (at the boundary) and the radial direction can be calculated with  $n_1 \sin \theta_{0,n} = n_{\text{eff}}(\text{LP}_{0,n})$ , as:

$$\theta_{0,n} = \sin^{-1} \left( \frac{n_{\text{eff}}(\text{LP}_{0,n})}{n_1} \right) \quad (6.3)$$

The energy coupling coefficient  $\eta_{0,n}$  between the fundamental mode in the SMF and the guided mode  $\text{LP}_{0,n}$  in the NCF can be calculated as [32-34]:

$$\eta_{0,n} = \frac{\left| \int_0^\infty E_s(r) E_{0,n}(r) r dr \right|^2}{\int_0^\infty |E_s(r)|^2 r dr \int_0^\infty |E_{0,n}(r)|^2 r dr} \quad (6.4)$$

where  $E_s$  and  $E_{0,n}$  represent the field profiles of the fundamental mode in the SMF and the  $\text{LP}_{0,n}$  mode in the NCF, respectively.

The multiple reflections of a ray ( $\text{LP}_{0,n}$ ) from the high-index polymer coating of the PC-NCF can be approximated as the multiple reflections of an unpolarized incident beam on an equivalent asymmetric planar waveguide as explained in more detail in the Appendix C. The ratio of the reflection intensity ( $\bar{R}$ ) of the unpolarized incident beam is calculated by Eq. (C.8). Using Eqs. (6.2)-(6.4) and

(C.8), the transmission efficiency of the hetero-structure SMF-PC-NCF-SMF induced by the multiple reflections (the AR effect) can be calculated as:

$$I_{\text{AR}} = 10 \log_{10} \left( \sum \eta_{0,n}^2 \bar{R}_{0,n} \right) \quad (6.5)$$

where  $\bar{R}_{0,n}$  is corresponding to the mode  $\text{LP}_{0,n}$ . Eq. (6.5) is a scalar superposition of the transmission efficiency of all individual modes  $\text{HE}_{1,n+(N-n)}$  in the PC-NCF.

In Eq. (6.5), the interference between different guided modes is not considered, which is a superposition of both the intensity and the phase of different guided modes  $\text{HE}_{1,n+(N-n)}$  in the PC-NCF. The interference between different guided modes  $\text{HE}_{1,n+(N-n)}$  in the PC-NCF is similar to and can be approximated as the multimode interference of  $\text{LP}_{0,n}$  ( $\text{HE}_{1,n}$ ) modes in an SMF-NCF-SMF [32-34], since the  $n_{\text{eff}}$  and the mode field distribution of  $\text{HE}_{1,n+(N-n)}$  modes in PC-NCF can be approximated by that of the  $\text{LP}_{0,n}$  ( $\text{HE}_{1,n}$ ) modes in the NCF as discussed in Section 6.3.1 and Ref. [25].

The transmission efficiency of the straight SMF-NCF-SMF based on the MMI effect can be calculated by [33]:

$$I_{\text{MMI}} = 10 \log_{10} \left( \left| \sum \eta_{0,n} \exp \left( j \frac{2\pi n_{\text{eff}}(\text{LP}_{0,n}) L}{\lambda} \right) \right|^2 \right) \quad (6.6)$$

which is related to the length  $L$ . Combining Eqs. (6.5) and (6.6), the transmission efficiency of the SMF-PC-NCF-SMF including both the AR and the MMI effects can be calculated as:

$$I = 10 \log_{10} \left( A \sum \eta_{0,n}^2 \bar{R}_{0,n} + B \left| \sum \eta_{0,n} \exp \left( j \frac{2\pi n_{\text{eff}}(\text{LP}_{0,n}) L}{\lambda} \right) \right|^2 \right) \quad (6.7)$$

where A and B ( $A + B = 1$ ) are defined as intensity coefficients for the AR and MMI effects, respectively. These coefficients are used to set the relative levels of AR interference and MMI for the purpose of discussion below.

Figures 6.5(a)-6.5(d) show the simulated transmission spectra of the hetero-structure SMF-PC-NCF-SMF with  $L = 5.8$  cm (approximately one self-imaging distance), calculated by Eq. (6.7). The spectrum in Fig. 6.5(a) calculated with  $A = 0$  and  $B = 1$  is as expected similar to the simulated and measured results for an SMF-NCF-SMF in Chapter 4, where the transmission peaks and dips are solely due to the MMI effect. As the intensity coefficient A increases to 0.5 in Fig.

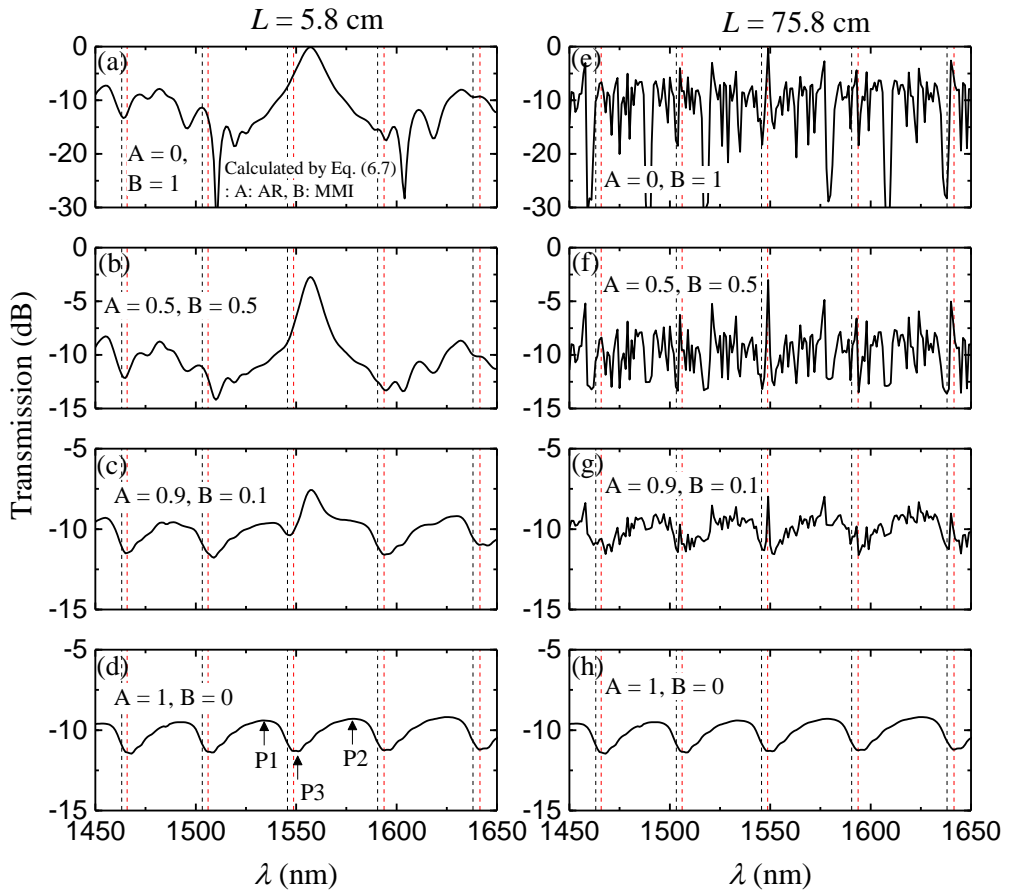


**Figure 6.5** The transmission spectra of the SMF-PC-NCF-SMF hetero-structure, calculated by Eq. (6.7) with different intensity coefficients A and B as indicated. (a)-(d)  $L = 5.8$  cm; (e)-(f)  $L = 75.8$  cm. The black and red vertical dashed lines indicate the resonant bands.

6.5(b) and then to 1 in Fig. 6.5(d), the AR characteristics in the spectrum become more and more pronounced, showing periodic transmission dips aligned with the vertical black and red dashed lines. The results are similar for the hetero-structure SMF-PC-NCF-SMF with  $L = 75.8$  cm, as shown in Figs. 6.5(e)-6.5(h). It should be noted that the spectra for different values of  $L$  in Figs. 6.5(d) and 6.5(h) are the same, indicating the AR effect ( $A = 1$ ,  $B = 0$ ) is independent of the value of length  $L$ .

The depth of the transmission loss dip around 1550 nm in Fig. 6.5(d) and Fig. 6.5(h) is 1.97 dB in both cases, this is calculated as the difference between the minimum value of the transmission loss taken at the dip labelled P3 and the average of the two adjacent transmission levels at the points labelled P1 and P2, as shown in Fig. 6.5(d).

The above analysis indicates that the MMI effect can be suppressed to obtain a periodic transmission spectrum due to AR. This can be achieved either by increasing the length of the PC-NCF or by bending the fiber as discussed in the sections which follow below.

### **6.3.3 Measured transmission spectra of the straight PC-NCFs**

Figure 6.6 shows the experimentally recorded spectra for a straight SMF-PC-NCF-SMF with different values of  $L$  increasing from 5.8 cm to 85.8 cm. The spectra as a function of length in the range from 5.8 cm to 38 cm shown in Figs. 6.6(a)-6.6(c) display irregular shapes, where the differences are consistent with the presence of multimode interference. For the sample with a longer PC-NCF length  $L = 75.8$  cm in Fig. 6.6(d), the transmission spectrum exhibits periodic

transmission dips and windows, similar to those in the simulated spectrum shown in Figs. 6.5(d) and 6.5(h) in terms of the spectral positions of the transmission dips and their depth, consistent with AR interference. The slight difference in the spectral period of the simulated and experimental results is due to the material dispersion (the refractive index changes with wavelength), which has not been considered in the simulation. The periodic spectral characteristics are maintained while the intensity of the transmission windows is reduced for the PC-NCF with a longer  $L$  of 85.8 cm as shown in Fig. 6.6(e). The progressive increase of loss in the transmission window as the length increases is related to the modal attenuation due to the material absorption.

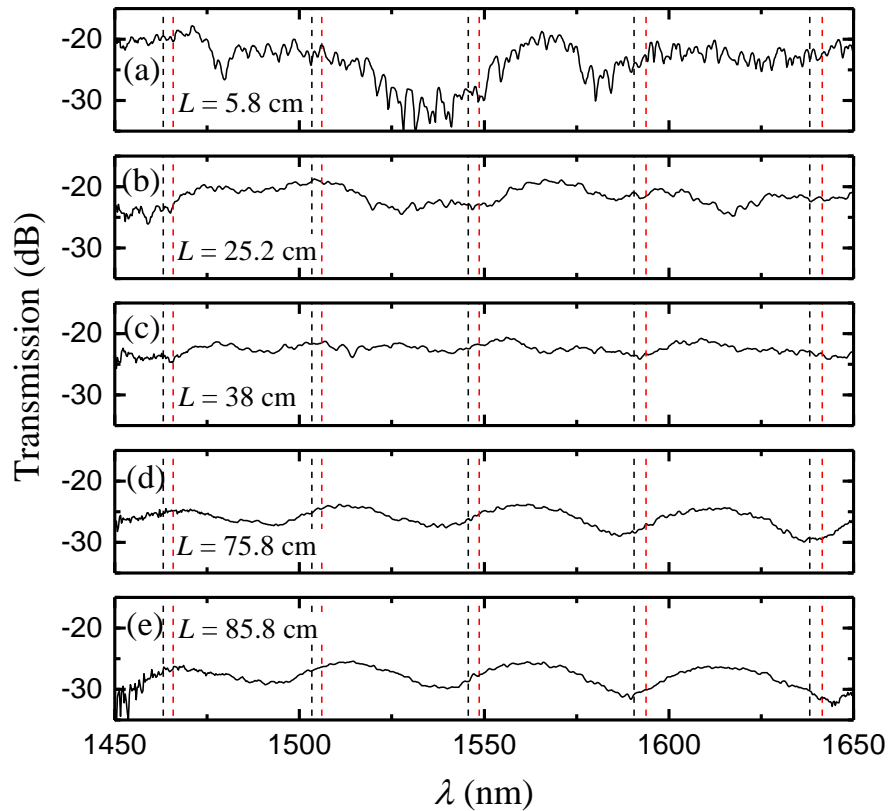


**Figure 6.6** Measured transmission spectra of the straight hetero-structures SMF-PC-NCF-SMF with different  $L$ . The black and red vertical dashed lines indicate the resonant bands.

The experimental results imply that the multimode interference effect is suppressed in the hetero-structures with a sufficiently large  $L$ , which can be

explained as follows. There are multiple modes in both the anti-resonant and resonant bands shown in Fig. 6.2(a), therefore in principle the multimode effects can occur in all the bands with the result that the spectrum is dependent on the length  $L$ . However, the field distributions of modes in different bands are different, as discussed in Section 6.3.1. The energy of anti-resonant core modes is mainly confined in the silica core region while that of the transition modes is distributed in both the silica core and the cladding regions. The modes propagating in the fiber suffer attenuation due to the material absorption, which is significantly larger in the polymer cladding (with a propagation loss level of  $0.6 \text{ dB cm}^{-1}$  [35]) than in the silica core (a loss level of  $0.2 \times 10^{-5} \text{ dB cm}^{-1}$ ). Therefore, the transition modes suffer greater attenuation as a function of distance than the anti-resonant core modes. The transition modes will fade earlier than the anti-resonant core modes during the propagation process, due to the increase of attenuation with the length  $L$ . For larger values of  $L$ , the higher attenuation of the transition modes compared to the anti-resonant core modes leads to the suppression of the multimode interference in the resonant bands and the appearance of periodic transmission dips, as shown in Figs. 6.6(d) and 6.6(e). For shorter values of  $L$ , the difference in the modal attenuation in the resonant and anti-resonant bands is minor, therefore the multimode property is present for both bands, which in turn is why the transmission spectrum in Figs. 6.6(a)-6.6(c) is dependent on the length  $L$ .

### 6.3.4 Modal field distortions in bent PC-NCFs

In this section and the following Section 6.3.5 the effect of bending induced mode field distortions on propagation and the relative strength of AR

interference and MMI are considered. In the simulations, a bent PC-NCF is transformed to an equivalent, straight fiber by the process of conformal mapping [36]. The refractive index distribution in the equivalent straight PC-NCF is expressed as [36]:

$$n'_i(x, y) = n_i(x, y) \exp\left(\frac{x}{R}\right), i = 1 \text{ or } 2 \quad (6.8)$$

where  $n_i(x, y)$  is the refractive index of the bent fiber cross section, which can be approximated as that of the straight fiber if the stress-optic effect is not considered.  $x$  is a transverse coordinate, with its origin in the center of the fiber and a positive value indicating the magnitude of the distance along a line joining the center of curvature and the center of the fiber.  $R$  is the bend radius. In the simulation of the bent fiber structure by the finite element method, a perfectly matched layer is set at the outer boundary of the polymer coating to absorb the possible outgoing energy. In practice, the energy loss from the outer boundary of the polymer coating can be neglected for the studied range ( $R > 28$  cm), since the imaginary part of  $n_{\text{eff}}$  is  $10^{10}$  times smaller than the real part in the simulated results.

Figure 6.7(a) shows two groups of dispersion curves for the modes in the PC-NCF with different bend radii: the upper group is for the mode  $\text{HE}_{1,1+(35)}$  while the lower group is for the mode  $\text{HE}_{1,2+(35)}$ . Fig. 6.8 shows the modal intensity and electric field vector distributions of the  $\text{HE}_{1,1+(35)}$  and  $\text{HE}_{1,2+(35)}$  modes with  $R = \infty$  (infinite, represents the fiber straight state) and  $R = 66.67$  cm at the wavelengths of 1550 nm, 1570 nm, and 1590 nm. The HE mode is two-fold degeneracy of modes  $\text{HE}_a$  and  $\text{HE}_b$ . In a straight PC-NCF the dispersion curves of the modes  $\text{HE}_a$  and  $\text{HE}_b$  are overlapped as shown in Fig. 6.7(a). The modal intensity

distributions for these modes are identical except for a  $\pi/2$  rotation of the electric vector as shown in Fig. 6.8. Under the influence of bending, the electric field directions of the modes HE<sub>a</sub> and HE<sub>b</sub> will change to be odd or even along the

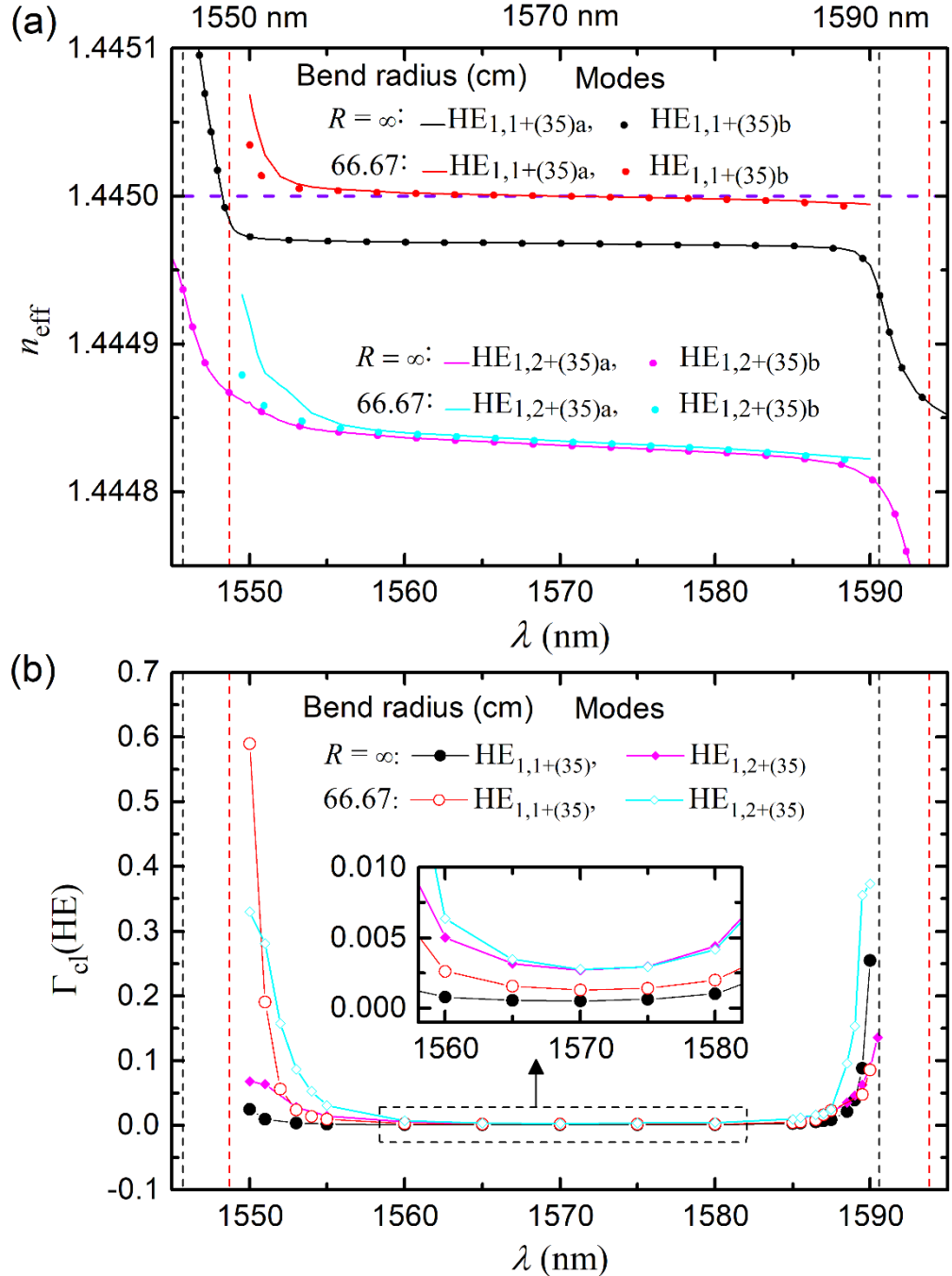


**Figure 6.7** (a) Dispersion curves ( $n_{\text{eff}}$  vs.  $\lambda$ ) and (b) the fractional power in the cladding of HE<sub>1,1+(35)</sub> and HE<sub>1,2+(35)</sub> modes with the bend radius  $R = \infty$  and  $R = 66.67$  cm. The inset of (b) is an enlarged figure of the part indicated by the black dashed rectangle. HE<sub>1,n+(35)</sub> ( $n = 1$  or 2) is a two-fold degeneracy mode of HE<sub>1,n+(35)a</sub> and HE<sub>1,n+(35)b</sub>. The black and red vertical dashed lines indicate the resonant bands.

bending direction, as shown by the  $\text{HE}_{1,n+(35)a}$  and  $\text{HE}_{1,n+(35)b}$  ( $n = 1$  or  $2$ ) with  $R = 66.67$  cm. The bending breaks the degeneracy between the  $\text{HE}_{1,n+(35)a}$  and  $\text{HE}_{1,n+(35)b}$  modes as evident by the separated dispersion curves, which is obvious near the resonant bands while less obvious far from them. The  $n_{\text{eff}}$  of modes increases as the bend radius decreases, where the increasing amplitude is higher near the resonant bands (around 1550 nm and 1590 nm) compared to those in the anti-resonant band (around 1570 nm).

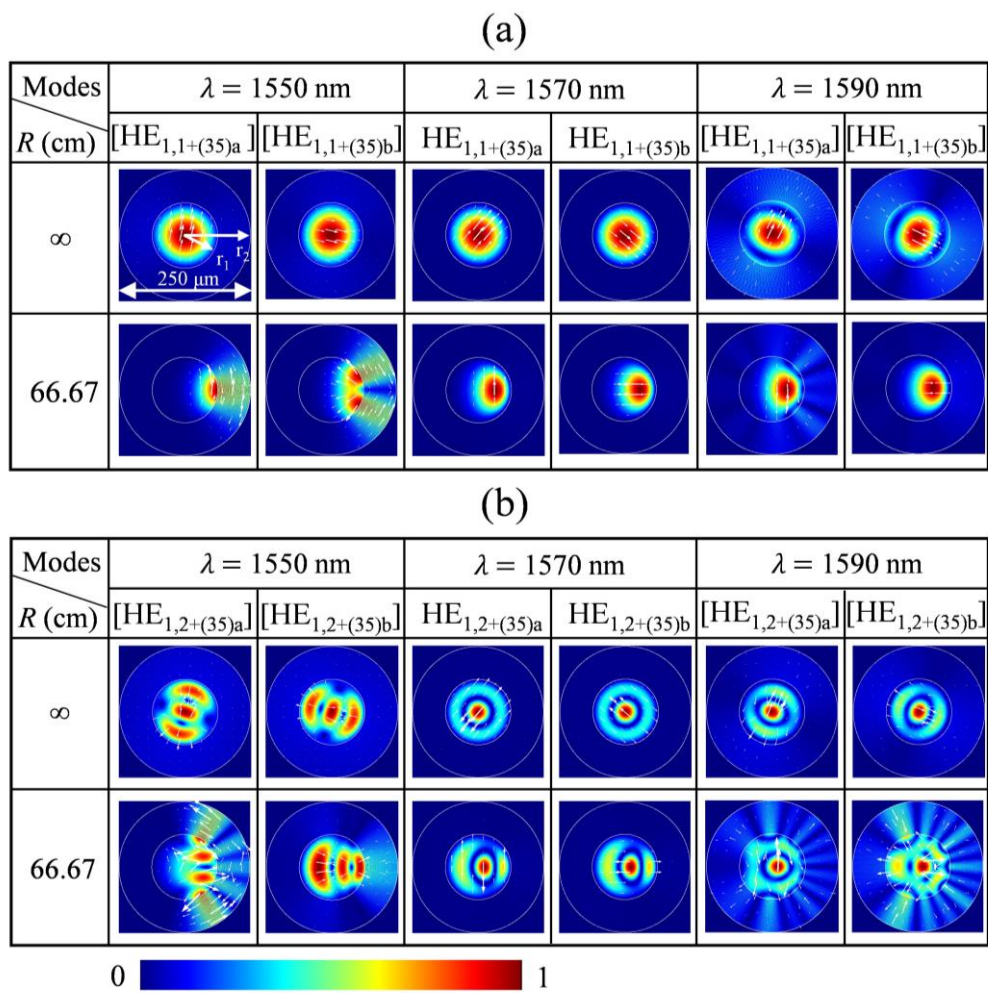


**Figure 6.8** The modal intensity and electric field vector distributions of  $\text{HE}_{1,1+(35)}$  and  $\text{HE}_{1,2+(35)}$  modes under different bending states as indicated.

Fiber bending skews the modal intensity distribution toward the outer edge of the fiber bend, with the result that light leaks from the core region into the cladding

region at the bend, as shown by the modes  $\text{HE}_{1,n+(35)}$  ( $n = 1$  or  $2$ ) with  $R = 66.67$  cm in Fig. 6.8. The modal field distortions are obvious at wavelengths of 1550 nm and 1590 nm around the resonant bands while less obvious at the wavelength of 1570 nm in the middle of the anti-resonant band, which is consistent with the change of the dispersion curves shown in Fig. 6.7(a). The modes in the bending states show strong hybridization with the cladding modes. For example, the azimuthal field distribution in the cladding region of the  $\text{HE}_{1,2+(35)}$  mode at the wavelength of 1590 nm with  $R = 66.67$  cm has a pattern with six radial dark lines. The characteristics of the intensity distribution in the cladding region are similar to those of the cladding mode  $\text{EH}_{6,35}$  shown in Fig. 6.3(b). The hybridization phenomenon was also found in a hypocycloid-shaped hollow-core photonic crystal fiber [37], which indicates the resonant coupling between the core and the cladding modes.

To quantify the change in modal intensity distribution and to compare the responses of different order modes to fiber bending, the fractional power in the fiber cladding region is calculated numerically using the following expression:

$$\Gamma_{\text{cl}} = \frac{\iint P_z \cdot d\mathbf{s}_{\text{cl}}}{\iint P_z \cdot d\mathbf{s}_{\text{cl}} + \iint P_z \cdot d\mathbf{s}_{\text{co}}} \quad (6.9)$$

where  $s_{\text{cl}}$  and  $s_{\text{co}}$  represent the cross-section areas of the fiber cladding and core, respectively.  $P_z$  is the z component of Poynting vector, calculated by:

$$P_z = \frac{1}{2} \text{Re}(H_y^* E_x - H_x^* E_y) \quad (6.10)$$

Since the HE is a two-fold degeneracy mode, the fractional power in the cladding is the average of the modes  $\text{HE}_a$  and  $\text{HE}_b$ , as follows:

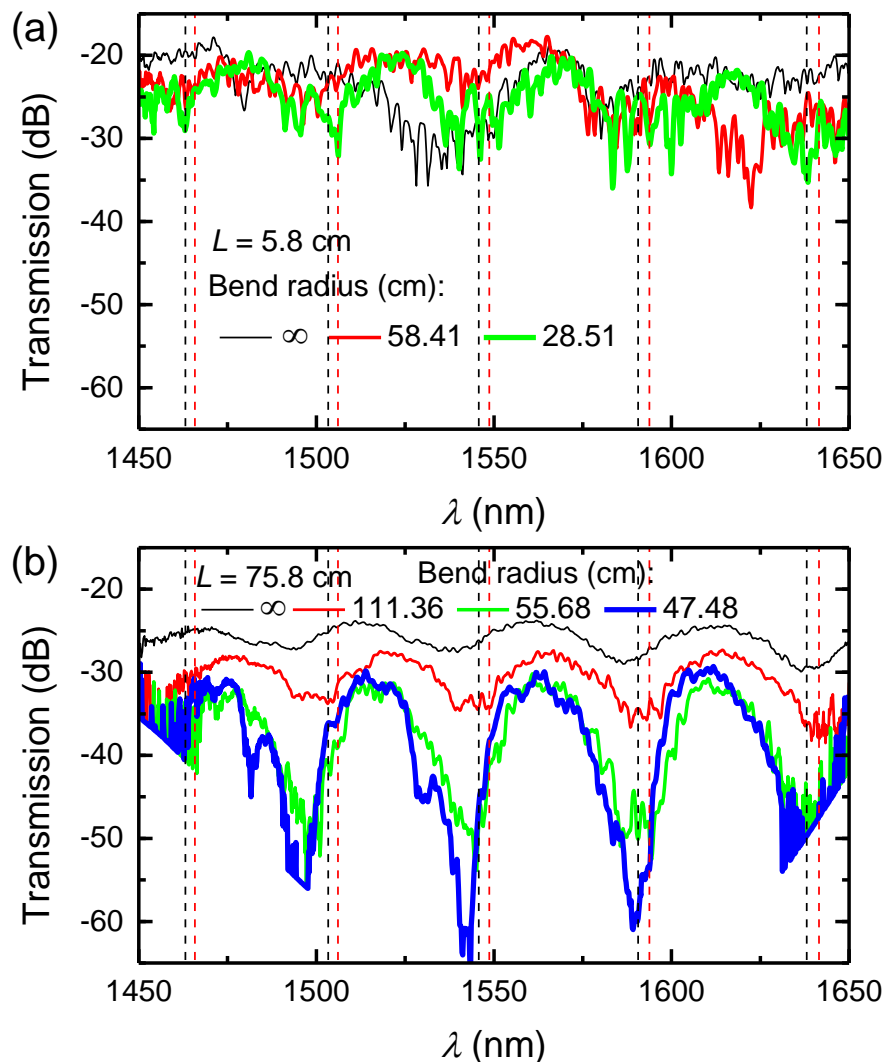
$$\Gamma_{\text{cl}}(\text{HE}) = \frac{1}{2}(\Gamma_{\text{cl}}(\text{HE}_a) + \Gamma_{\text{cl}}(\text{HE}_b)) \quad (6.11)$$

Figure 6.7(b) shows that the fractional power in the cladding  $\Gamma_{\text{cl}}(\text{HE})$  for the  $\text{HE}_{1,1+(35)}$  and  $\text{HE}_{1,2+(35)}$  modes, with  $R = \infty$  and  $R = 66.67$  cm. The  $\Gamma_{\text{cl}}(\text{HE})$  of modes in the middle region of the anti-resonant band is smaller than that near the resonant bands indicated by the vertical black and red dashed lines, for the straight PC-NCF with  $R = \infty$ . The modes near the resonant bands are more sensitive to the fiber bending than those in the anti-resonant bands, where the  $\Gamma_{\text{cl}}(\text{HE})$  of both the  $\text{HE}_{1,1+(35)}$  and  $\text{HE}_{1,2+(35)}$  modes increases significantly near the resonant bands. The enlarged insert figure in Fig. 6.7(b) shows that the  $\Gamma_{\text{cl}}(\text{HE})$  of the high-order mode  $\text{HE}_{1,2+(35)}$  is larger than that of the low-order mode  $\text{HE}_{1,1+(35)}$  in the anti-resonant bands, which means that the confinement loss of the former is larger than that of the latter.

### 6.3.5 Measured transmission spectra of the bent PC-NCFs

Figure 6.9 shows the measured transmission spectra for SMF-PC-NCF-SMF with  $L = 5.8$  cm and  $75.8$  cm under different bending states, using the previously described experimental setup in Fig. 6.1(c). The spectrum of the structure with  $L = 5.8$  cm and  $R = \infty$  shows irregular interference dips in Fig. 6.9(a). The fiber bending changes the spectrum with irregular interference dips to a spectrum with periodic transmission dips, although the intensity of the transmission windows is inconsistent, as one can see for the curve with  $R = 58.41$  cm in Fig. 6.9(a). The depths of the transmission dips marginally increase and the intensities of the transmission windows become relatively consistent as the bend radius decreases to  $R = 28.51$  cm in Fig. 6.9(a). The appearance of periodic transmission dips in the spectrum of the bent PC-NCF with the short length  $L$  can be explained in two

steps. Firstly, fiber bending shifts the modal intensity distribution from the silica core region into the polymer cladding region, which causes an increase of loss in all bands since the material absorption in the polymer is higher than that in the silica. Secondly, the fractional power in the cladding is larger in the resonant bands than in the anti-resonant bands, which indicates that there is more loss in the former bands than in the latter bands. Therefore, fiber bending can lead to the formation of the periodic transmission dips and an increase of the depths in PC-NCFs with a short length.



**Figure 6.9** Measured transmission spectra of the hetero-structure SMF-PC-NCF-SMF with (a)  $L = 5.8 \text{ cm}$  and (b)  $L = 75.8 \text{ cm}$ , under different bending states as indicated. The black and red vertical dashed lines indicate the resonant bands.

Similarly, the depth of the transmission dips increases as the bend radius decreases for the PC-NCF with a large length of  $L=75.8$  cm, as shown in Fig. 6.9(b). For similar bend radii, the depth of the transmission dips for the PC-NCF with  $L = 5.8$  cm (around 5 dB,  $R = 58.41$  cm, in Fig. 6.9(a)) is smaller than that for the PC-NCF with  $L = 75.8$  cm (around 20 dB,  $R = 55.68$  cm, in Fig. 6.9(b)). The larger depth of the transmission dips for the longer PC-NCF is caused by a larger propagation loss, provided that the confinement losses (the fractional power in the cladding) of the modes are similar for both the long and short PC-NCFs. The intensity of the transmission windows of the PC-NCF with  $L = 75.8$  cm decreases strongly as the bend radius decreases from  $R = \infty$  to  $R = 113.36$  cm as shown in Fig. 6.9(b). The situation is different for the PC-NCF with  $L = 5.8$  cm as shown in Fig. 6.9(a), where the intensity of the transmission window does not decrease noticeably within the studied range of bend radius. The decreased intensity of the transmission windows is related to the attenuation of the anti-resonant core modes, especially for the higher order. The fractional power in the cladding of the high-order modes is larger than that of the low-order modes, as discussed in Section 6.3.4.

The consequence of introducing a fiber bend is that compared to the low-order modes, the high-order modes are more easily affected by bending, which shifts the modal field into the fiber cladding. Therefore, the higher-order modes propagating in a bent PC-NCF experience higher loss and some of them will fade with the decrease of the bend radius, leading to a decrease in the intensity of the transmission windows. The shorter the propagation length the lower the attenuation of the anti-resonant core modes, therefore, there is no significant

reduction in the intensity of the transmission windows for the short PC-NCF within a certain range of bend radius.

The depth of the transmission loss dip around 1550 nm for the PC-NCF with  $L = 75.8$  cm increases over 31 dB from 3.54 dB to 34.65 dB as the bend radius decreases from  $R = \infty$  to  $R = 47.48$  cm (the bending curvature increases from 0 to  $2.106 \text{ m}^{-1}$ ). The average change rate of the depth in the studied range is up to  $14.77 \text{ dB/m}^{-1}$ .

## 6.4 Discussion

A PC-NCF has been studied as an example of the depressed-core fiber in this Chapter. Compared to the more frequently studied anti-resonant guiding hollow-core fibers, whose core modes have a leaky nature [26,38,39], the depressed-core fiber has the non-leaky anti-resonant core modes. The energy of the core modes in the hollow-core fibers tends to leak out from both the core and the cladding regions at the resonant bands while that of the depressed-core fibers are totally reflected back at the outer boundary of the cladding region although they can leak from the core region. Therefore, the hollow-core fibers generally show periodic transmission loss dips [26,39,40] while the depressed-core fiber with multiple non-leaky core modes are prone to showing multimode interference characteristics of the transmission spectrum. However, the appearance of the periodic transmission dips and windows in the long or bent PC-NCFs demonstrated in this work reflect the anti-resonant nature of the depressed-core fibers.

The LMR fiber structures are similar with the PC-NCFs, although the coating materials (i.e. ITO in Ref. [20]) of the former are strongly lossy and usually have a complex refractive index. The generation of the loss dips is related to the resonant coupling of the core modes and cladding modes in both the PC-NCF and the LMR fiber structures. The resonant coupling in both structures causes similar changes to the modal field distributions in the resonant bands, where the modal energy is evenly distributed in both the core and the cladding regions [22]. If the high-index coating in the LMR structure is treated as a Fabry-Perot resonator in the ARROW model, it is easy to understand the general rules of the LMR with the help of Eq. (6.1). For example, the resonant wavelengths are dependent on the thickness and the refractive index of the high-index layer (if other parameters are constant), which is near to the cutoff of the TE and TM modes in the high-index layer [20]. In addition, Eq. (6.1) also helps to explain the generation of the multiple LMRs with the thick coating and the excitation of the LMR by both TE and TM light [20]. It should be note that the coating materials such as semiconductor ITO in LMR fiber structures are usually much more lossy compared to the acrylate polymer in PC-NCF, therefore the loss dips can be formed with a much shorter length for the coating (for example the ITO-coated fiber region is 4 cm in Ref. [20]).

The sensing mechanism for the PC-NCF is similar to that for the LMR structure and relies on the change of the thickness and refractive index contrast of the high-index coating and the intensity of the evanescent wave generated at the outer boundary of the coating layer [3,5,6]. Based on the theoretical analysis in this work, several methods of reducing the length of the PC-NCF in practical devices such as curvature sensors and optical filters exist. As discussed above,

one method of achieving periodic transmission dips in the PC-NCF with a short length  $L$  is to introduce deliberate well-defined bending of the fiber, which leads to an increase of the fractional power in the polymer coating and consequently to an increase of losses in the coating. In a similar fashion, reducing the mode confinement by tapering the silica fiber can increase the fractional power in the cladding, which may allow one to shorten the length of the device. Increasing the losses within the polymer coating may also allow a reduction in the length of the fiber. In addition, previous experiments have indicated that bending of any short part of the PC-NCF while keeping the rest of the structure straight also allows for the formation of periodic transmission dips, which could reduce the length of the device.

## 6.5 Conclusion

Light propagation in PC-NCFs was studied experimentally and theoretically. The periodic loss dips were found in the transmission spectra of the PC-NCFs with a longer length or under bending states. The wavelength positions of the transmission dips can be predicted based on the ARROW model, with the knowledge of the anti-resonant and inhibited-coupling guiding mechanisms. The fractional power in the fiber cladding (polymer coating) for the modes in the resonant bands is higher than that for the modes in the anti-resonant bands, and the fiber bending can enhance this difference. Therefore, the modes in the resonant bands experience higher attenuation due to the material absorption within the polymer coating, which suppresses the multimode interference and displays anti-resonant characteristics. The obtained results indicate that the PC-NCFs or the depressed-core fibers can be used in many devices including

bend/curvature sensors and tunable loss filters. The analysis carried out, regardless of the specific refractive index dispersion properties of the high-index fiber layers, may contribute to a better understanding of the resonant phenomenon in fiber optics such as the LMR in lossy film coated fiber structures.

The transmission spectrum experiments of the PC-NCF in this chapter not only verify the theoretical results in Chapter 5, but also point out their distinct spectral characteristics compared to that of three-layer step-index fibers and hollow-core fibers.

## 6.6 Reference

- [1] X.-d. Wang and S. W. Otto, “Fiber-optic chemical sensors and biosensors (2013–2015),” *Analytical Chem.*, vol. 88, no. 1, pp. 203-227, 2015.
- [2] C. Caucheteur, T. Guo, and J. Albert, “Review of plasmonic fiber optic biochemical sensors: Improving the limit of detection,” *Anal. Bioanal. Chem.*, vol. 407, no. 14. pp. 3883-3897, 2015.
- [3] I. D. Villar, F. J. Arregui, C. R. Zamarreño, J. M. Corres, C. Bariain, J. Goicoechea, C. Elosua, M. Hernaez, P. J. Rivero, A. B. Socorro, A. Urrutia, P. Sanchez, P. Zubiate, D. Lopez, N. D. Acha, J. Ascorbe, I. R. Matiasa, “Optical sensors based on lossy-mode resonances,” *Sens. Actuators B Chem.*, vol. 240, pp. 174-185, Mar. 2017.
- [4] K. M. Tripathi, T. Y. Kim, D. Losic, and T. T. Tung, “Recent advances in engineered graphene and composites for detection of volatile organic compounds (VOCs) and non-invasive diseases diagnosis,” *Carbon*, vol. 110, pp. 97-129, 2016.
- [5] A. Ozcariz, D. A. Piña-Azamar, C. R. Zamarreño, R. Dominguez, and F. J. Arregui, “Aluminum doped zinc oxide (AZO) coated optical fiber LMR refractometers—An experimental demonstration,” *Sens. Actuators B*, vol. 281, pp. 698-704, 2019.
- [6] M. Śmietana, M. Koba, P. Sezemsky, K. Szot-Karpińska, D. Burnat, V. Stranak, J. Niedziółka-Jönsson, and R. Bogdanowicz, “Simultaneous optical

- and electrochemical label-free biosensing with ITO-coated lossy-mode resonance sensor,” Biosensors and Bioelectronics, vol. 154, pp. 112050, 2020.
- [7] Y. Wang, C. Shen, W. Lou, F. Shentu, C. Zhong, X. Dong, and L. Tong, “Fiber optic relative humidity sensor based on the tilted fiber Bragg grating coated with graphene oxide,” Appl. Phys. Lett., vol. 109, no. 3, p. 031107, 2016.
  - [8] Q. Wu, Y. Semenova, J. Mathew, P. Wang, and G. Farrell, “Humidity sensor based on a single-mode hetero-core fiber structure,” Opt. Lett., vol. 36, no. 10, pp. 1752-1754, 2011.
  - [9] D. Liu, W. Han, A. K. Mallik, J. Yuan, C. Yu, G. Farrell, Y. Semenova, and Q. Wu, “High sensitivity sol-gel silica coated optical fiber sensor for detection of ammonia in water,” Opt. Express, vol. 24, pp. 24179-24187, 2016
  - [10] J. Ascorbe, J. M. Corres, F. J. Arregui, and I. R. Matías, “Optical fiber current transducer using lossy mode resonances for high voltage networks,” J. Lightw. Technol., vol. 33, no. 12, pp. 2504-2510, 2015.
  - [11] J. M. Corres, J. Ascorbe, F. J. Arregui, and I. R. Matías, “Tunable electro-optic wavelength filter based on lossy-guided mode resonances,” Opt. Express, vol. 21, no. 25, pp. 31668-31677, 2013
  - [12] Y. Zhang, H. Li, C. Dai, L. Xu, C. Gu, W. Chen, Y. Zhu, P. Yao, and Q. Zhan, “All-fiber high-order mode laser using a metal-clad transverse mode filter,” Opt. Express, vol. 26, no. 23, pp. 29679-29686, 2018.
  - [13] H. Zhang, N. Healy, L. Shen, C. C. Huang, D. W. Hewak, and A. C. Peacock, “Enhanced all-optical modulation in a graphene-coated fiber with low insertion loss,” Sci. Rep., vol. 6, p. 23512, 2016.
  - [14] I. D. Villar, I. R. Matias, F. J. Arregui, and P. Lalanne, “Optimization of sensitivity in long period fiber gratings with overlay deposition,” Opt. Express, vol. 13, no. 1, pp. 56–69, 2005.
  - [15] A. Cusano, A. Iadicicco, P. Pilla, L. Contessa, S. Campopiano, A. Cutolo, and M. Giordano, “Mode transition in high refractive index coated long period gratings,” Opt. Express, vol. 14, no. 1, p. 8237, 2006.
  - [16] L.-L. Xue and L. Yang, “Sensitivity enhancement of RI sensor based on SMS fiber structure with high refractive index overlay,” J. Lightw. Technol., vol. 30, no. 10, pp. 1463-1469, 2012.

- [17] N. D Rees, S. W James, R. P. Tatam, and G. J Ashwell, “Optical fiber long period gratings with Langmuir Blodgett thin film overlays,” Opt. Lett., vol. 27, no. 9, pp. 686-688, 2002.
- [18] A. Socorro, I. D. Villar, J. Corres, F. Arregui, and I. Matias, “Sensitivity enhancement in a multimode interference-based SMS fiber structure coated with a thin-film: Theoretical and experimental study,” Sens. Actuators B, Chem., vol. 190, pp. 363-369, 2014.
- [19] C. R. Zamarreno, M. Hernaez, I. D. Villar, I. R. Matias, and F. J. Arregui, “Optical fiber pH sensor based on lossy-mode resonances by means of thin polymeric coatings,” Sens. Actuators B Chem., vol. 155, no. 1, pp. 290-297, 2011.
- [20] I. D. Villar, C. R. Zamarreno, M. Hernaez, F. J. Arregui, and I. R. Matias, “Lossy mode resonance generation with indium tin oxide coated optical fibers for sensing applications,” J. Lightw. Technol., vol. 28, pp. 111-117, 2010.
- [21] J. M. Corres, I. D. Villar, F. J. Arregui, and I. R. Matias. “Analysis of lossy mode resonances on thin-film coated cladding removed plastic fiber,” Opt. Lett., vol. 40, no. 21, pp. 4867-4870, 2015.
- [22] I. D. Villar, I. R. Matias, F. J. Arregui, and M. Achaerandio, “Nanodeposition of materials with complex refractive index in long-period fiber gratings,” J. Lightw. Technol., vol. 23, no. 23, pp. 4192-4199, 2005.
- [23] W. M. Zhao, Q. Wang, J. Y. Jing, and X. Z. Wang, “Discoveries and explorations of mode splitting phenomenon in lossy dielectric waveguide,” Plasmonics, vol. 15, no. 2, pp. 481-487, 2020.
- [24] C. Tsao, *Optical Fiber Waveguide Analysis*. (Oxford Univ. Press, London, U.K.,1992).
- [25] X. Lian, G. Farrell, Q. Wu, W. Han, C. Shen, Y. Ma, and Y. Semenova, “Anti-resonance, inhibited coupling and mode transition in depressed-core fibers.” Opt. Express, vol. 28, no. 11, pp. 16526–16541, 2020.
- [26] M. Duguay, Y. Kokubun, T. Koch, and L. Pfeiffer, “Antiresonant reflecting optical wave-guides in SiO<sub>2</sub>-Si multilayer structures,” Appl. Phys. Lett., vol. 49, no. 1, pp. 13–15, 1986.
- [27] N. Sultanova, S. Kasarova, and I. Nikolov, “Dispersion properties of optical polymers,” Acta. Phys. Pol. A, vol. 116, no. 4, pp. 585–587, 2009.

- [28] T. Eiselt, J. Preinfalk, U. Gleißner, U. Lemmer, and T. Hanemann, “Development and characterization of adjustable refractive index scattering epoxy acrylate polymer layers,” In Light Manipulating Organic Materials and Devices III, vol. 9939, p. 99390Q. International Society for Optics and Photonics, 2016.
- [29] K. Tian, G. Farrell, E. Lewis, X. Wang, H. Liang, and P. Wang, “A high sensitivity temperature sensor based on balloon-shaped bent SMF structure with its original polymer coating,” Meas. Sci. Technol., vol. 29, no. 8, p. 085104, 2018.
- [30] Y. P. Wang, D. Richardson, G. Brambilla, X. Feng, M. Petrovich, M. Ding, and Z. Q. Song, “Intensity measurement bend sensors based on periodically tapered soft glass fibers,” Opt. Lett., vol. 36, no. 4, pp. 558–560, 2011.
- [31] D. Marcuse, *Theory of Dielectric Optical Waveguides*, (Elsevier, 2013).
- [32] W. S. Mohammed, A. Mehta, and E. G. Johnson, “Wavelength tunable fiber lens based on multimode interference,” J. Lightw. Technol., vol. 22, no. 2, p. 469, 2004.
- [33] Q. Wang, G. Farrell, and W. Yan, “Investigation on single-mode–multimode–single-mode fiber structure,” J. Lightw. Technol., vol. 26, no. 5, pp. 512–519, Mar. 2008.
- [34] X. Lian, Q. Wu, G. Farrell, C. Shen, Y. Ma, and Y. Semenova, “Discrete self-imaging in small-core optical fiber interferometers,” J. Lightw. Technol., vol. 37, no. 9, pp. 1873-1884, 2019.
- [35] H. Ma, A. K.-Y. Jen, and L. R. Dalton, “Polymer-based optical waveguides: Materials, processing, and devices,” Adv. Mater., vol. 14, no. 19, pp. 1339-1365, 2002.
- [36] M. Heiblum and J. Harris, “Analysis of curved optical waveguides by conformal transformation,” IEEE J. Quantum Electron., vol. QE-11, no. 2, pp. 75–83, Feb. 1975.
- [37] B. Debord, M. Alharbi, T. Bradley, C. Fourcade-Dutin, Y. Y. Wang, L. Vincetti, F. Gérôme, and F. Benabid, “Hypocycloid-shaped hollow-core photonic crystal fiber Part I: Arc curvature effect on confinement loss,” Opt. Express, vol. 21, no. 23, pp. 28597-28608, 2013.

- [38] J. L. Archambault, R. J. Black, S. Lacroix, and J. Bures, “Loss calculations for antiresonant waveguides,” *J. Lightw. Technol.*, vol. 11, no. 3, pp. 416-423, Mar. 1993.
- [39] N. M. Litchinitser, A. K. Abeeluck, C. Headley, and B. J. Eggleton, “Antiresonant reflecting photonic crystal optical waveguides,” *Opt. Lett.*, vol. 27, no. 18, pp. 1592-1594, 2002.
- [40] M. Born, and E. Wolf, *Principles of Optics: Electromagnetic Theory of Propagation, Interference and Diffraction of Light*. (Elsevier, 2013).

# **Chapter 7**

## **High-Sensitivity Temperature Sensor Based on Anti-Resonance in High-Index Polymer-Coated Optical Fiber Interferometers<sup>5</sup>**

Chapter 6 demonstrated that an appropriate control of fiber length and the external stimulus such as the fiber bending can modify the light field and change the transmission spectral characteristics of a depressed-core fiber. Therefore, the depressed-core fibers deserves a further investigation for the design of fiber optic devices. In this chapter, an example of employing a depressed-core fiber as the basis of a temperature sensing is demonstrated.

Compared to the multimode interference (MMI) effect, the anti-resonance (AR) effect does not rely on the multimode property of the optical waveguide. This chapter shows that fiber bending can suppress the MMI and can break the superposition of AR spectra of multiple modes in a high-index polymer-coated optical fiber interferometer based on a single-mode fiber-polymer-coated no-core fiber-single-mode fiber hetero-structure. This results in the dominance of the AR spectrum of an individual mode and consequently in periodic sharp transmission dips. As a result of this phenomenon and large thermo-optical and thermal expansion coefficients of the polymer, a compact, high-sensitivity and linear

---

<sup>5</sup> Lian, Xiaokang, Qiang Wu, Gerald Farrell, and Yuliya Semenova, “High-sensitivity temperature sensor based on anti-resonance in high-index polymer-coated optical fiber interferometers,” Opt. Lett., vol. 45, no. 19, pp. 5385-5388, 2020.

response temperature sensor with the sensitivity as high as -3.784 nm/°C has been demonstrated experimentally.

## 7.1 Research motivation

Fiber temperature sensors based on the anti-resonance (AR) effect have gained significant popularity owing to their simple structure, periodic transmission dips, high spectral extinction ratio, large free spectral range and multiplexing capability [1-3]. The simplest design for an AR-based fiber sensor is a fiber hetero-structure, such as a single-mode fiber (SMF)-hollow-core fiber (HCF)-SMF (SHCS). The light guiding in the low-index air core of the HCF is based on the AR effect, which allows the anti-resonant light to be reflected back from the high-index cladding while allowing forward transmission of the resonant light [4]. The resonant coupling between the core and the cladding modes in the HCF results in periodic transmission dips in the spectra of the SHCS [5]. The typical temperature sensitivity of a silica based SHCS is around 30 pm/°C in the range from room temperature to over 850 °C[1]. With a polydimethylsiloxane (PDMS) coating on the middle section HCF, a sensitivity of -201 pm/°C in the range from -30 °C to 45 °C was achieved, owing to the large thermo-optical coefficient and thermal expansion coefficient of the polymer coating [3]. These SHCS sensors show a highly linear spectral response to temperature. The positions of the spectral dips and their sensitivity to perturbations are independent of the length of the HCF, which could facilitate the miniaturization and design of compact sensors [1-3]. However, the loss within the HCF is high, and the hollow core is prone to collapse during fusion splicing with the SMFs, which can affect the spectrum and reduce the manufacturing yield [2,6].

An optical fiber interferometer for use as a temperature sensor can be based on the multimode interference (MMI) effect [7-9]. The interferometer can be a hetero-structure, such as an SMF-multimode fiber-SMF (SMS), where the multimode fiber can be replaced by a no-core fiber (NCF), small-core fiber (SCF), or any other fiber supporting multiple guided modes. The transmission spectrum of an interferometer is highly dependent on the length of the middle section fiber, where light is guided by total internal reflection. The sensitivity of temperature sensors based on a silica SMS [10], SMF-NCF-SMF (SNCS) [11], and SMF-SCF-SMF [12] is less than 40 pm/°C. An optical fiber interferometer for use as a temperature sensor can be based on the multimode interference (MMI) effect [7-9]. The interferometer can be a hetero-structure, such as an SMS, where the multimode fiber can be replaced by a NCF, SCF or any other fiber supporting multiple guided modes. Light in a multimode fiber is guided by the total internal reflection effect, and the transmission spectrum of the interferometer is highly dependent on the length of the middle section fiber. The reported sensitivity of temperature sensors based on a silica SMS [10], SMF-NCF-SMF (SNCS) [11], and SMF-SCF-SMF [12] is less than 40 pm/°C.

In this chapter, a new type of temperature sensor consisting of a bent high-index polymer-coated SNCS (PC-SNCS, SMF-PC-NCF-SMF) is proposed and demonstrated, which is based on an AR effect similar to that in an SHCS instead of the MMI effect present in an SNCS. The Chapter 6 has shown that periodic broad dips can appear in the transmission spectra of straight PC-SNCSs with a long or bent PC-NCF (length > 50 mm) [13]. It has been demonstrated that periodic sharp dips can be achieved for the PC-SNCSs with a millimeter order length (< 10 mm) subjected to bending. The spectral response of the PC-SNCSs to temperature is investigated in this chapter.

## 7.2 The modal properties of the PC-SNCS

In the experiment undertaken, SMF28 fiber (from Corning) was used as the SMF, and FG125LA fiber (from Thorlabs) was used as the NCF. Figs. 7.1(a) and 7.1(b) show the schematic diagrams of the SNCS and PC-SNCS, respectively, for simplicity sake without bending. The length of the middle section fibers is  $L$ . The diameter of the silica NCF is 125  $\mu\text{m}$ . The polymer coating is the original acrylate coating as supplied by the manufacturer of the NCF and has a thickness ( $t$ ) of 62.5  $\mu\text{m}$ . The refractive indices of the NCF, the polymer coating, and the surrounding air are assumed as  $n_1 = 1.445$ ,  $n_2 = 1.51$ , and  $n_3 = 1$  at a wavelength ( $\lambda$ ) of 1550 nm, respectively, with  $n_2 > n_1 > n_3$ .

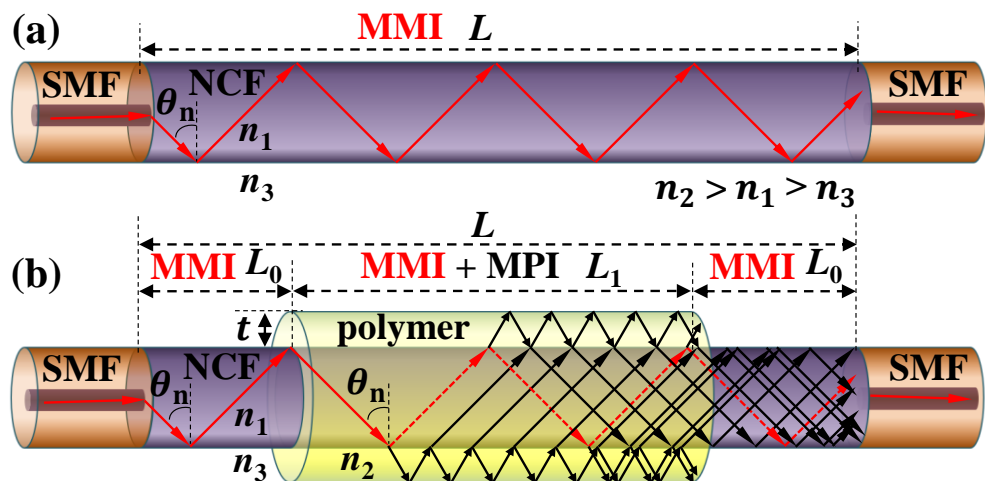


**Figure 7.1** Schematic diagrams: (a) SMF-NCF-SMF (SNCS) structure, (b) SMF-polymer coated NCF-SMF (PC-SNCS) structure.

For the SNCS in Fig. 7.1(a), when the fundamental mode of the lead-in (left) SMF is coupled into the NCF, multiple modes  $\text{LP}_{0,n}$  are excited due to the on-axis alignment, which propagate through the NCF and are then coupled into the lead-out SMF. The NCF is where the MMI takes place, which determines the transmission spectrum. The ray trajectory of one  $\text{LP}_{0,n}$  mode, with the effective refractive index  $n_{\text{eff}} = n_1 * \sin\theta_n$ , is indicated by the red arrows, which are confined to the NCF by total internal reflection.

In the PC-SNCS shown in Fig. 7.1(b), the lengths  $L_0$  of the polymer coating ( $\sim 1.5$  mm) at both ends of the PC-NCF are removed in order to enable the automatic splicing process with the SMFs. The length of the remaining polymer coating is  $L_1$  ( $< 7$  mm). Using geometrical optics to illustrate propagation in the PC-NCF section, the behaviour of the ray in NCF on the left side is the same as that in Fig. 7.1(a), as indicated by the red arrows. The ray in the PC-NCF section is partially reflected at the inner boundary of the polymer coating and totally reflected at its outer boundary, resulting in multi-path interference (MPI). The partially reflected ray indicated by the dashed red arrows retains the same angle ( $\theta_n$ ) with the radial direction, as that in Fig. 7.1(a). The field in the straight PC-NCF section can be considered as a combination of MMI and MPI. The field in the NCF on the right side is dominated by MMI.

The MPI will cause AR effect in the PC-NCF, and its dispersion diagram ( $n_{\text{eff}}$  vs.  $\lambda$ ) is different from that of the NCF [14]. Fig. 7.2 shows the dispersion curves of the modes  $\text{HE}_{1,N}$  ( $N = 34, 35, \dots, 38$ ) in the PC-NCF and the modes  $\text{HE}_{1,1}$  ( $\text{LP}_{0,1}$ ) and  $\text{HE}_{1,2}$  ( $\text{LP}_{0,2}$ ) in the NCF, calculated using an analytical method [14]. The parts with  $n_{\text{eff}} > n_1$  denote the cladding modes  $\text{HE}_{1,N}$  in the PC-NCF, showing a strong index dispersion. On the same curve, as the  $\lambda$  increases the  $\text{HE}_{1,N}$  will change into the anti-resonant core modes  $\text{HE}_{1,n+(N-n)}$ ,  $n = 1, 2, \dots$ , where the subscript ‘n’ denotes the radial number in the core while the ‘ $N-n$ ’ denotes the radial number in the cladding. The  $\text{HE}_{1,n+(N-n)}$  modes have moderate index dispersion similar to that of the  $\text{HE}_{1,n}$  modes in NCF, where their dispersion curves intersect with each other. The resonant bands are indicated by the vertical black and red dashed lines, whose positions are approximated as the cutoff wavelengths of the  $\text{TM}_N$  and  $\text{TE}_N$  modes, respectively, in an equivalent asymmetric planar waveguide [14]:

$$\lambda_{N,c} = \frac{2t\sqrt{n_2^2 - n_1^2}}{\left[N-1 + \frac{1}{\pi}\tan^{-1}\left(\kappa\sqrt{\frac{n_1^2 - n_3^2}{n_2^2 - n_1^2}}\right)\right]}, \kappa = \begin{cases} 1, & \text{TE}_N \\ \frac{n_2^2}{n_3^2}, & \text{TM}_N \end{cases} \quad (7.1)$$

where,  $N = 34, 35, \dots, 38$ . The  $n_{\text{eff}}$  of the modes  $\text{HE}_{1,n+(N-n)}$  in AR bands can be approximated as that of  $\text{HE}_{1,n}$  ( $\text{LP}_{0,n}$ ) in NCF.

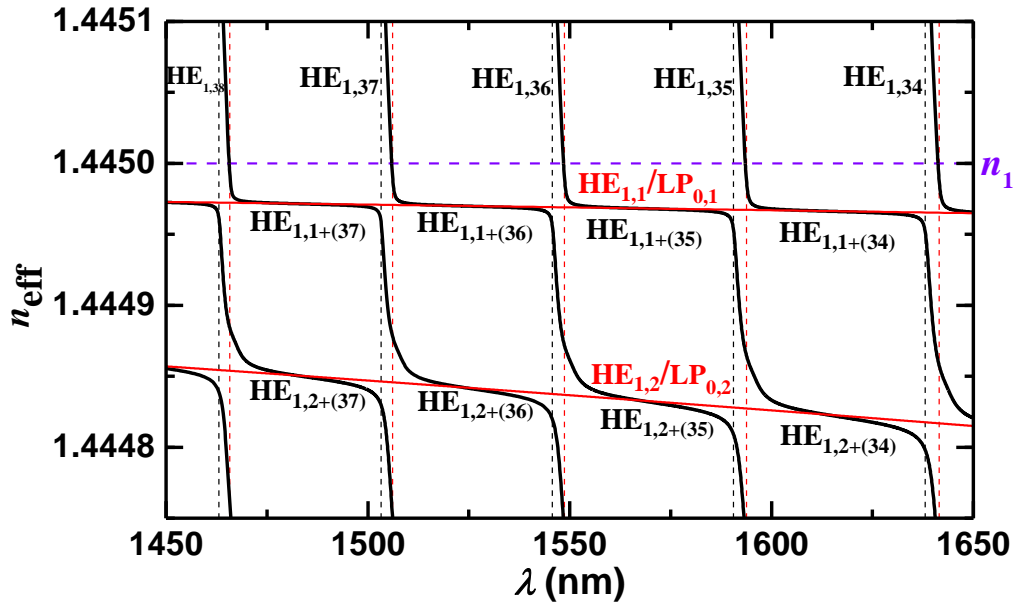


**Figure 7.2** Dispersion curves for  $\text{HE}_{1,1+(N-1)}$  and  $\text{HE}_{1,2+(N-2)}$  ( $N = 34, 35, \dots, 38$ ) in the PC-NCF (black lines) and  $\text{HE}_{1,1}$  ( $\text{LP}_{0,1}$ ) and  $\text{HE}_{1,2}$  ( $\text{LP}_{0,2}$ ) in NCF (red lines).

### 7.3 The transmission spectra of the PC-SNCS

The transmission efficiency of the straight SNCS is calculated by [7,8]:

$$I_{\text{MMI}} = 10 \log_{10} \left( \left| \sum \eta_{0,n} \exp \left( j \frac{2\pi n_{\text{eff}} (\text{LP}_{0,n}) L}{\lambda} \right) \right|^2 \right) \quad (7.2)$$

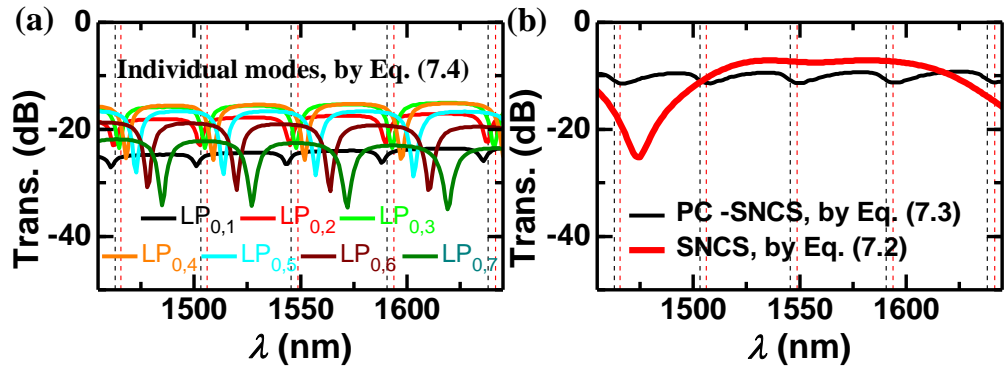
where  $\eta_{0,n}$  denotes the power coupling coefficient between the fundamental mode of the SMF and the excited modes  $\text{LP}_{0,n}$  of the NCF. The transmission efficiency of the straight PC-SNCS due to the AR can be calculated based on an asymmetric planar reflection model described in Ref. [13]:

$$I_{\text{AR}} = 10 \log_{10} (\sum \eta_{0,n}^2 \bar{R}_{0,n}) \quad (7.3)$$

where  $\bar{R}_{0,n}$  is the ratio of reflection intensity of a ray ( $LP_{0,n}$ ) impinging on the asymmetric planar waveguide, which is independent of the length. The transmission efficiency of an individual  $LP_{0,n}$  mode can be calculated by:

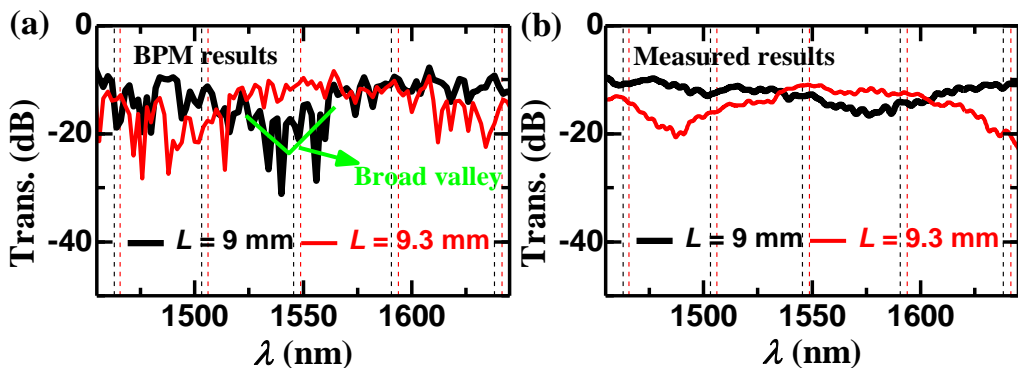
$$I_{0,n} = 10 \log_{10} (\eta_{0,n}^2 \bar{R}_{0,n}) \quad (7.4)$$

Figure 7.3(a) shows the transmission spectra of the individual modes  $LP_{0,n}$  ( $n = 1, 2, \dots, 7$ ) calculated by Eq. (7.4), which exhibit periodic dips and windows. Higher mode orders show a red spectral shift, accompanied by a change of the depth of the dips. The intensity of the transmission windows increases at first and then reduces in accordance with the power coupling coefficient as shown in Ref. [7]. The superposition of the spectra of individual modes  $LP_{0,n}$  by Eq. (7.3) results in a relatively flat spectrum for the straight PC-SNCS, as shown by the black curve in Fig. 7.3(b), where the periodic broad dips are indicated by the vertical black and red dashed lines (same to Fig. 7.2). The spectrum with periodic broad dips was achieved experimentally in a long PC-SNCS ( $L > 50$  mm) in Ref. [13].



**Figure 7.3** Simulated transmission spectra of (a) individual modes  $LP_{0,n}$  calculated by Eq. (7.4); (b) straight PC-SNCS calculated by Eq. (7.3) and SNCS with  $L = 9$  mm calculated by Eq. (7.2).

Equations (7.3) and (7.4) consider only the AR effect, but the actual light field in the straight PC-NCF also includes MMI as discussed. In order to better describe the situation with both AR and MMI, the Beam Propagation Method (BPM) was employed to simulate the transmission spectra of straight PC-SNCSs with  $L = 9$  mm and 9.3 mm [9]. The results are shown in the Fig. 7.4(a). The spectrum of the PC-SNCS with  $L = 9$  mm shows a fringe pattern with multiple random dips and a broad valley located around 1550 nm. The valley blue-shifts towards around 1475 nm for the PC-SNCS with a larger  $L = 9.3$  mm in Fig. 7.4(a). The PC-SNCS with  $L = 9.3$  mm shows similar spectral features to those of the SNCS with  $L = 9$  mm in Fig. 7.3(b), where a broad valley around 1475 nm is related to the destructive interference of modes in the NCF. The blue spectral shift for the PC-SNCSs with an increased  $L$  in Fig. 7.4(a) is consistent with the trend in an MMI-based optical fiber interferometer as shown in Ref. [8]. The simulated results are confirmed by the experiments as shown in Fig. 7.4(b). Compared to the simulated results, the multiple random dips are highly suppressed in the measured spectra, which may be due to the internal defects and the surface roughness of the polymer coating [15].



**Figure 7.4** (a) Transmission spectra simulated by BPM for straight PC-SNCSs with  $L = 9$  mm and 9.3 mm. (b) Measured transmission spectra for straight PC-SNCSs with  $L = 9$  mm and 9.3 mm (at  $\sim 25$  °C).

The similarity of spectral characteristics of the straight PC-SNCS with those for the straight SNCS and the dependence of the spectral shift on the length indicate that the MMI effect dominates in the straight PC-SNCS with a short  $L$ .

The resonance in PC-NCF results from the coupling between the core and the cladding modes. The resonant wavelengths depend only on the thickness and the refractive index of the high-index cladding as indicated by Eq. (7.1). It can be deduced that AR effect in PC-SNCS is less dependent on the collective behaviour of the  $LP_{0,n}$  modes, compared to MMI. When any individual  $LP_{0,n}$  mode meets the coupling condition with a corresponding cladding mode, resonance will happen. The phase and the coherence of the spatial eigenmodes is sensitive to the fiber bends and twists, which induce mode coupling and the redistribution of energy among modes in multimode fibers [16,17]. Therefore, the bending or twisting may break the superimposed spectrum of the multiple  $LP_{0,n}$  modes in the straight fiber structures indicated by Eqs. (7.2) and (7.3). The AR spectrum of an individual  $LP_{0,n}$  mode owning high energy and the resonant condition may stand out while the others are hidden, and thus result in periodic sharp dips as shown in Fig. 7.3(a).

Figure 7.5 shows the experimental setup used to investigate the effect of fiber bending and temperature. The PC-SNCS fiber sample is fixed on two translation stages in contact with the surface of the temperature stage, with these three stages located in the same plane. To allow for the PC-SNCS to be bent in a controlled fashion, the bending curvature of the sample can be tuned by adjusting the distance between two translation stages. The bend radius ( $R$ ) was calculated based on the displacement of the translation stages [13]. After adjustment of the bending states, two K-type thermocouples ( $T_1$  and  $T_2$ ) were fixed closely to the PC-NCF middle section. The measured temperature is an

average of the two temperatures:  $T = (T_1+T_2)/2$ . The samples and the stages were located in a sealed box, with small openings for the lead-in/lead-out wires for the temperature controller ( $25\text{ }^\circ\text{C} - 50\text{ }^\circ\text{C}$ ), thermometer (RS 206-3738), broadband light source (BBS, Thorlabs S5FC1005s) and optical spectrum analyzer (OSA, Agilent 86142B).

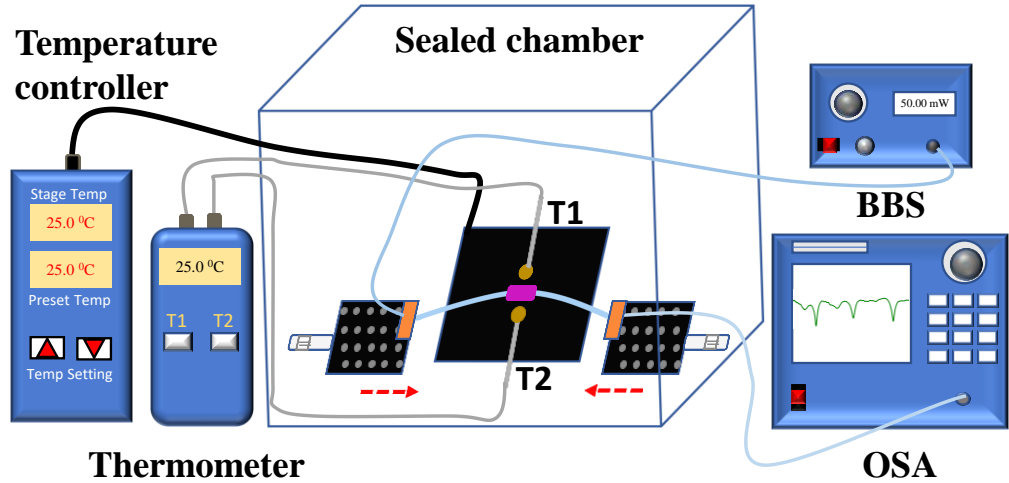


**Figure 7.5** Experimental setup for temperature and transmission spectrum measurement.

Figure 7.6(a) shows the spectral response of the PC-SNCS with  $L = 9.3\text{ mm}$  under the influence of different fiber bend radii. The changes in the bend radius result in various spectral responses, corresponding to the changes of modal phases and the redistribution of energy among modes. Due to the AR nature of the PC-NCF, periodic dips are clearly observed in the spectral responses, as indicated by the vertical black and red dashed lines. The periodic dips for the PC-SNCS with  $R = 16.4\text{ cm}$  are broad, similar to those for the long PC-SNCS in Ref. [13]. The broad dips are related to the superposition of the AR spectra of multiple  $\text{LP}_{0,n}$  modes. The spectrum for  $R = 10.2\text{ cm}$  has two separate dip pairs around  $1470\text{ nm}$ ,  $1500\text{ nm}$  and  $1550\text{ nm}$ , which are expected to be related to two modes with distinct resonant wavelengths. After a slight adjustment of the bend radius, the spectrum of the PC-SNCS with  $R = 10\text{ cm}$  shows periodic sharp dips (redrawn in

Fig. 7.6(b)), similar to the simulated spectra for the individual modes in Fig. 7.3(a). For a reduced bend radius  $R = 6.5$  cm, the dips become broad again, corresponding to a further change in the modal phase and energy redistribution. The experimental results indicate that the superposition of the AR spectra of multiple modes led to broadening of dips while separate individual modes caused sharper dips.

The spectra of the straight and bent ( $R = 10$  cm) PC-SNCS with  $L = 9.3$  mm are redrawn in Fig. 7.6(b), allow comparison with those of the straight and bent ( $R = 11$  cm) PC-SNCS with  $L = 9$  mm in Fig. 7.6(c) and those of the straight and bent ( $R = 15$  cm) PC-SNCS with  $L = 7.5$  mm in Fig. 7.6(d). The results suggest that periodic sharp dips can be achieved for all the three bent PC-SNCSs with different  $L$ , even though their spectra for the straight fiber states are different. This result indicates that for fabrication the repeatability with respect to the length of PC-NCF is relatively robust.

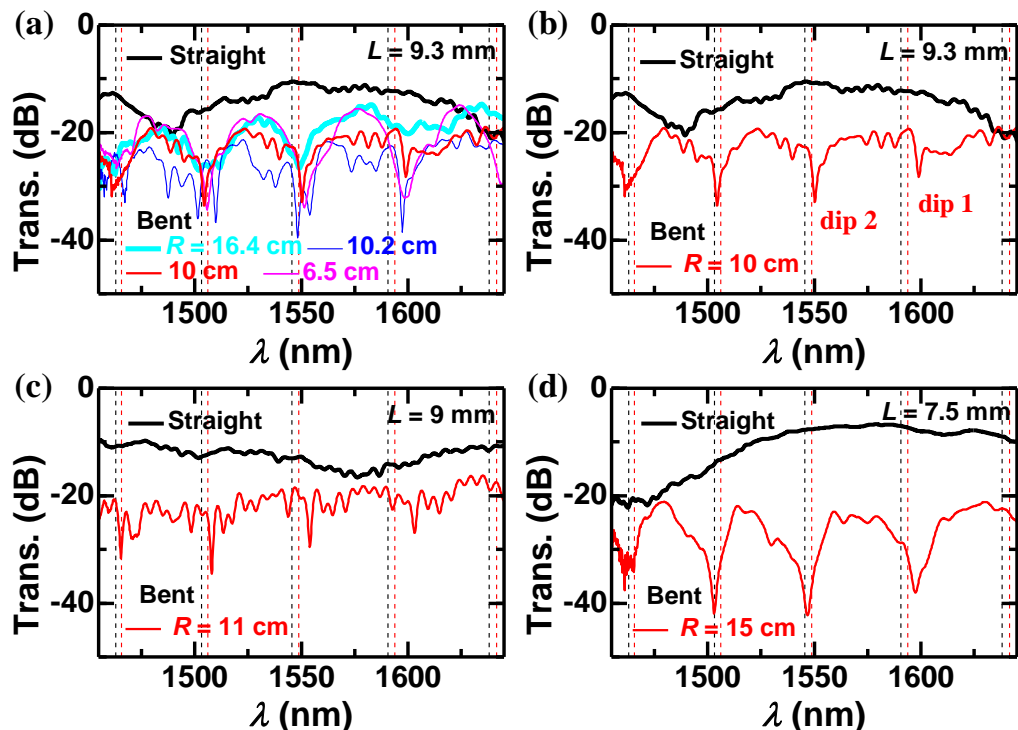


**Figure 7.6** Measured transmission spectra for bent and straight PC-SNCSs with (a) and (b)  $L = 9.3$  mm, (c)  $L = 9$  mm, and (d)  $L = 7.5$  mm (at  $\sim 25^\circ\text{C}$ , ‘ $R$ ’ = bend radius).

## 7.4 Sensing performance of the temperature sensor

The transmission spectra of the straight PC-SNCS with  $L = 9.3$  mm at  $24.75$  °C and  $31.6$  °C are shown in Fig. 7.7(a). As the temperature changes the position of the spectral valley around  $1475$  nm is almost unchanged. The results indicate that the spectral valley due to the MMI is less sensitive to temperature.

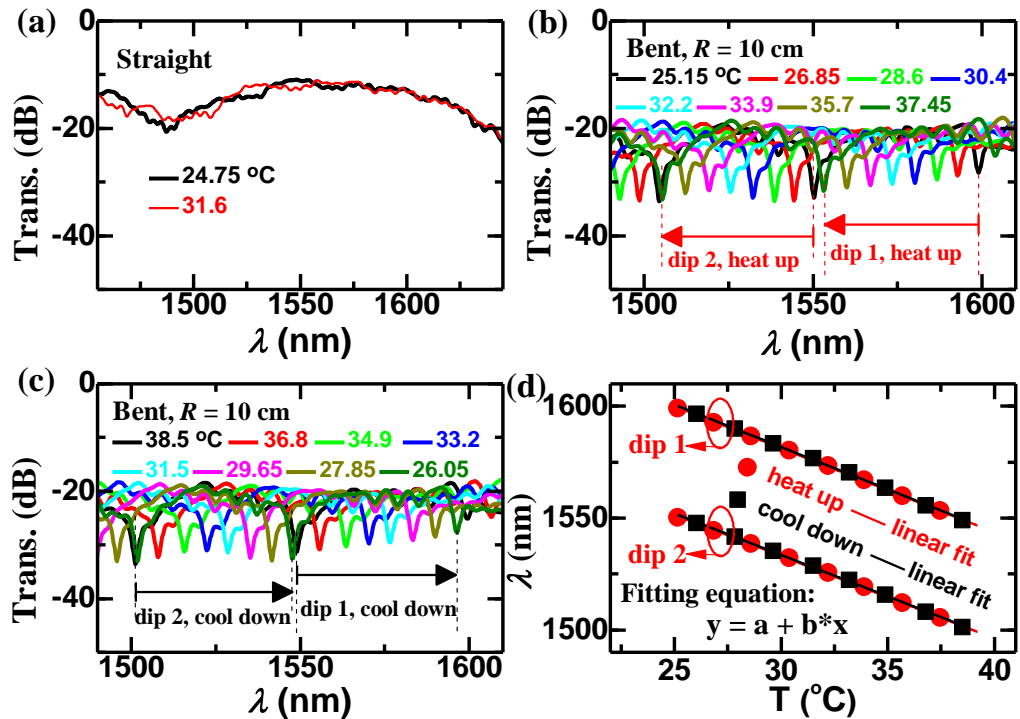


**Figure 7.7** Measured transmission spectra of (a) the straight, (b) and (c) the bent ( $R = 10$  cm) PC-SNCS with  $L = 9.3$  mm, at different temperatures as indicated; (d) shows the spectral shifts and the linear fittings of dip 1 and dip 2 in (b) and (c).

The PC-SNCS with  $L = 9.3$  mm and  $R = 10$  cm is employed for temperature measurement, as shown in Fig. 7.6(b), where the free spectral range between dip 1 and dip 2 is about  $50$  nm. The measurements were taken with a step size of about  $2$  °C. The spectrum blue shifts within one free spectral range as the temperature increases as shown in Fig. 7.7(b). As the temperature continues to increase, dip 1 will shift to the starting position (at  $25.15$  °C) of dip 2 and the spectral shift will continue and repeat

periodically. Conversely, the spectrum red shifts as the temperature decreases as shown in Fig. 7.7(c). Fig. 7.7(d) shows the linear fittings of results in Figs. 7.7(b) and 7.7(c). The R-squared value and the sensitivity (the slope) for dip 1 in the heating process are  $R^2 = 0.99941$  and  $-3.757 \text{ nm}^\circ\text{C}$  respectively, which are quite close to the values of  $R^2 = 0.99912$  and  $-3.784 \text{ nm}^\circ\text{C}$  in the cooling process. The  $R^2$  and the sensitivity of the dip 2 in the heating process are 0.99890 and  $-3.694 \text{ nm}^\circ\text{C}$  respectively, which are also quite close to the values of  $R^2 = 0.99875$  and  $-3.703 \text{ nm}^\circ\text{C}$  during the cooling process. The highly linear response is similar to that observed in the AR-based SHCS [1-3]. The sensitivity achieved with the PC-SNCS in this work is about 19 times higher than that of the PDMS-coated SHCS reported in Ref. [3].

## 7.5 Conclusion

In conclusion, a novel type of temperature sensor based on a bent PC-SNCS has been presented and demonstrated in this chapter. The sensor has a transmission spectrum with periodic sharp dips caused by the AR effect of an individual mode, attributed to breaking of the superposition effect of the multiple guided modes induced by the fiber bending. The sensor is easy to fabricate and has a highly linear temperature response with the sensitivity of up to  $-3.784 \text{ nm}^\circ\text{C}$ . This study shows that the different degrees of dependence of the MMI and the AR effects on the multimode property (the number of guided modes) can open new avenues in the design of AR-based devices such as sensors and filters with high-index claddings.

## 7.6 Reference

- [1] B. Feng, Y. Liu, and S. Qu, “High-temperature sensor based on resonant reflection in hollow core fiber,” Opt. Eng., vol. 55, no. 10, p. 106127, 2016.

- [2] N. Cai, L. Xia, and Y. Wu, “Multiplexing of anti-resonant reflecting optical waveguides for temperature sensing based on quartz capillary,” *Opt. Express*, vol. 26, no. 25, pp. 33501-33509, 2018.
- [3] S. Liu, Y. Ji, L. Cui, W. Sun, J. Yang, and H. Li, “Humidity-insensitive temperature sensor based on a quartz capillary anti-resonant reflection optical waveguide,” *Opt. Express*, vol. 25, no. 16, pp. 18929-18939, 2017.
- [4] N. M. Litchinitser, A. K. Abeeluck, C. Headley, and B. J. Eggleton, “Antiresonant reflecting photonic crystal optical waveguides,” *Opt. Lett.* vol. 27, no. 18, pp. 1592-1594, 2002.
- [5] L. Vincetti and V. Setti, “Waveguiding mechanism in tube lattice fibers,” *Opt. Express*, vol. 18, no. 22, pp. 23133-23146, 2010.
- [6] X. Zhang, H. Pan, H. Bai, M. Yan, J. Wang, C. Deng, and T. Wang, “Transition of Fabry–Perot and antiresonant mechanisms via a SMF-capillary-SMF structure,” *Opt. Lett.* vol. 43, no. 10, 2268-2271, 2018.
- [7] W. S. Mohammed, A. Mehta, and E. G. Johnson, “Wavelength tunable fiber lens based on multimode interference,” *J. Lightw. Technol.*, vol. 22, no. 2, p. 469, 2004.
- [8] Q. Wang, G. Farrell, and W. Yan, “Investigation on single-mode–multimode–single-mode fiber structure,” *J. Lightw. Technol.*, vol. 26, no. 5, pp. 512-519, 2008.
- [9] X. Lian, Q. Wu, G. Farrell, C. Shen, Y. Ma, and Y. Semenova, “Discrete self-imaging in small-core optical fiber interferometers,” *J. Lightw. Technol.* vol. 37, no. 9, pp. 1873-1884, 2019.
- [10] Q. Wu, Y. Semenova, A. M. Hatta, P. Wang, and G. Farrell, “Bent SMS fiber structure for temperature measurement,” *Electron. Lett.*, vol. 46, no. 16, pp. 1129-1130, 2010.
- [11] S. Susana, E. G. P. Pachon, M. A. R. Franco, P. Jorge, J. L. Santos, F. X. Malcata, C. M. B. Cordeiro, and O. Frazão, “Curvature and temperature discrimination using multimode interference fiber optic structures—A proof of concept,” *J. Lightw. Technol.*, vol. 30, no. 23, pp. 3569-3575, 2012.
- [12] J. Wu, Y. Miao, B. Song, W. Lin, K. Zhang, H. Zhang, B. Liu, and J. Yao, “Simultaneous measurement of displacement and temperature based on thin-core fiber modal interferometer,” *Opt. Commun.*, vol. 340, pp. 136-140, 2015.

- [13] X. Lian, G. Farrell, Q. Wu, W. Han, C. Shen, Y. Ma, and Y. Semenova, “Spectral dependence of transmission losses in high-index polymer-coated no-core fibers,” *J. Lightw. Technol.*, vol. 38, no. 22, pp. 6352-6361, 2020.
- [14] X. Lian, G. Farrell, Q. Wu, W. Han, C. Shen, Y. Ma, and Y. Semenova, “Anti-resonance, inhibited coupling and mode transition in depressed-core fibers,” *Opt. Express*, vol. 28, no. 11, pp. 16526-16541, 2020.
- [15] C. C. Katsidis and D. I. Siapkas, “General transfer-matrix method for optical multilayer systems with coherent, partially coherent, and incoherent interference,” *Appl. Opt.* vol. 41, no. 19, pp. 3978-3987, 2002.
- [16] D. Marcuse, *Theory of Dielectric Optical Waveguides*, 2nd ed, (Academic, New York, 1991).
- [17] J. M. Kahn, K. Ho, and M. B. Shemirani, “Mode coupling effects in multimode fibers,” Optical Fiber Communication Conference, OFC ‘12, OW3D.3, 2012.

# **Chapter 8**

## **Conclusions and Future Research Work**

This chapter presents a comprehensive review of the key outcomes and conclusions of the research work described in this PhD thesis. Future research work as an extension of this thesis is also discussed.

### **8.1 Conclusions from the research**

The primary aim of this thesis, as stated in Chapter 1, was to **investigate the three-layer step-index optical fibers and the three-layer depressed-core fibers from a modal and spectral perspective and to develop high performance fiber optic devices based on these types of fibers.**

The major conclusions and insights of this thesis can be divided into five areas, as follows:

#### **1) Conclusions regarding the calculation and analysis of mode properties of the three-layer step-index fibers**

The effective refractive indices ( $n_{\text{eff}}$ ) and modal profiles of both core and the cladding modes in three-layer step-index optical fibers as a function of core radius ( $r_1$ ) were calculated independently by the analytical method, scalar BPM and the full-vector FEM, as demonstrated in Chapters 3 and 4. The key conclusions from the studies in this area can be drawn as follows:

- For the first time a complete dispersion diagram for the dispersion curves ( $n_{\text{eff}}$  vs.  $r_1$ ) of the core and the cladding modes for a three-layer step-index optical fiber was developed.
- It was shown in the dispersion diagram that the transition between cladding-type and core-type modes occurs as a result of the changes in the core radius for a three-layer step-index fiber.
- It was found that the cladding modes possess different dispersion characteristics compared to those of the core modes in three-layer step-index fibers, based on the mode reorganization phenomenon of the cladding modes in the dispersion diagram.

## **2) Conclusions regarding the investigation of the self-imaging phenomenon of pure cladding modes in three-layer step-index small-core fibers**

The self-imaging of cladding modes in three-layer step-index small-core fiber was analytically and numerically calculated and confirmed by experiments, as demonstrated in Chapter 4. The key conclusions from the studies in this area can be drawn as follows:

- It was shown by calculation and experimental investigations that the self-imaging of cladding modes only appears at a set of discrete positions along the interferometer axis with an equal spacing corresponding to certain discrete values of the fiber core radius.
- It was deduced that the research demonstrates that the small-core fiber is a discrete multimode physical system.
- It was demonstrated by calculation and experiment that the self-imaging period of the cladding modes is an exponential function of the core radius,

in contrast to the quadratic relationship in the case of core modes in conventional multimode fibers.

- It was found that the light field in small-core fibers with micro/nano- core is characterized by combinations of the Bessel functions  $J_0$  and  $Y_0$ , unlike the field characterized only by Bessel function  $J_0$  in the core region of a conventional multimode fiber.

### **3) Conclusions regarding the calculation and analysis of the mode properties of three-layer depressed-core fibers**

The dispersion diagram and modal profiles of a depressed-core fiber were obtained by solving the full-vector eigenvalue equations and analysed, as demonstrated in Chapter 5. The key conclusions drawn from the research in regard to the depressed-core fibers are as follows:

- It was demonstrated theoretically that the waveguiding in a depressed-core fiber is governed by anti-resonance, inhibited coupling and the total internal reflection effects.
- It was shown by calculation that the anti-resonant core modes of the depressed-core fiber have disc-like transverse field profiles while the cladding modes have annular-like transverse field profiles.
- For the first time a complete dispersion diagram for the dispersion curves ( $n_{\text{eff}}$  vs.  $\lambda$ ) of the core and the cladding modes in the depressed-core fibers was developed by calculation.
- It was demonstrated that a depressed-core fiber has the non-leaky anti-resonant core modes, unlike the tube-type hollow-core fiber, whose core modes have a leaky nature.

- The research demonstrates that the resonant bands in the dispersion diagram of a depressed-core fiber can be determined with a proposed asymmetric anti-resonant reflecting optical waveguide (ARROW) model.
- It was demonstrated that the anti-resonant core modes exhibit similar qualitative and quantitative behaviour to those of conventional step-index fibers.

#### **4) Conclusions regarding the investigation of the spectral dependence of transmission losses in high-index polymer-coated no-core fibers**

A high-index polymer-coated no-core fiber (PC-NCF) was studied as an example of a depressed-core fiber. The transmission spectra of the straight and bent PC-NCFs (length > 5 cm) were measured and analyzed from a modal dispersion perspective, as demonstrated in Chapter 6. The key conclusions from the studies in this area can be drawn as follows:

- It was demonstrated that a PC-NCF is effectively a depressed-core fiber, where the light is guided by the anti-resonant, inhibited coupling and total internal reflection effects and the dispersion diagram shows periodic resonant and anti-resonant bands.
- It was deduced that depressed-core fiber with multiple non-leaky core modes are likely to exhibit multimode interference characteristics in the transmission spectrum, where the anti-resonance effect is suppressed.
- It was demonstrated by simulation that the fractional power in the cladding for the modes in the resonant bands is higher than that for the modes in the anti-resonant bands in straight PC-NCFs, and that deliberate fiber bending can enhance this difference.

- It was demonstrated experimentally that periodic loss dips can be detected in the transmission spectra of PC-NCFs with a longer length or under bending conditions.
- It was determined that the wavelength positions of the transmission dips can be predicted based on the proposed asymmetric ARROW model.
- It was demonstrated that the anti-resonant transmission spectra of the PC-NCFs can be determined based on multiple reflections from an asymmetric planar waveguide.

## **5) Conclusions regarding the design of temperature sensors based on high-index polymer-coated optical fiber interferometers.**

A novel type of highly sensitive temperature sensor based on a bent optical fiber interferometer with SMF-PC-NCF-SMF hetero-structure was demonstrated, as shown in Chapter 7. The main conclusions from the studies in this area are as follows:

- It was shown experimentally that periodic sharp transmission dips in the transmission spectrum can be achieved with a bent SMF-PC-NCF-SMF hetero-structure.
- It was shown experimentally that a bent SMF-PC-NCF-SMF hetero-structure can implement a compact (< 10 mm), high sensitivity and linear response temperature sensor with the sensitivity as high as  $-3.784 \text{ nm}^{\circ}\text{C}$  in a range of  $25^{\circ}\text{C} - 50^{\circ}\text{C}$ .

- It was found that the different degrees of dependence of the MMI and the AR on the multimode properties can open new directions in the design of AR-based devices such as sensors and filters with high-index claddings.
- It was shown that the temperature sensor is relatively easy to fabricate and the repeatability with respect to length of PC-NCF is relatively robust.

Overall, this thesis has demonstrated for the first time the complete modal dispersion diagrams, the modal properties, and the transmission characteristics of two basic fiber types: the three-layer step-index optical fiber and the three-layer depressed-core fiber. Based on this fundamental knowledge and insights, additional novel devices based on these two types of fiber are expected to be designed in the future.

## **8.2 Future research work**

The research carried out to date has given complete full-vector modal dispersion diagrams for both the three-layer step-index fibers and the DCFs. The research also demonstrated the discrete self-imaging phenomenon of pure cladding modes in SCFs, and the anti-resonant and inhibited coupling effects in DCFs. These findings could form a basis of future research, such as:

### **1) Development of optical devices using the pure cladding-type mode fields in small-core fibers.**

The unique light field of multiple cladding-type modes in an SCF, distinct from that of multiple core-type modes in the commonly used MMFs, can be further explored in many applications. For example, compared to the Bessel beams generated by a MMF and characterized by the function  $J_0$ , the pure cladding

modes in a SCF can be used to generate a new kind of Bessel beams characterized by the combinations of  $J_0$  and  $Y_0$ . Bessel beams based on a truncation of  $Y_0$  having higher energy over a longer range than that of  $J_0$  Bessel beams were theoretically predicted in Ref. [1]. Indeed, the micro/nano- core in SCFs can strongly modify the on-axis intensity, which is critically important to the performance of Bessel beams used for optical manipulation [2, 3]. Therefore the  $Y_0$  modulated  $J_0$  Bessel beams generated with SCFs may offer an improved performance in optical manipulation applications.

The discrete self-imaging effect indicates that the SCF may also be a discrete multimode physical system. The SCF with pure cladding modes may be a valuable platform for studies of multimode nonlinear fiber optics. It is also expected that multimode solitons, which so far have been only experimentally observed in a graded-index MMF, could be achieved in a SCF.

**2) Development of multimode optical devices based on the rule of the discrete self-imaging phenomenon.**

The discrete self-imaging effect in a small-core optical fiber interferometer can be regarded as the first discrete self-imaging phenomenon found in multimode waveguides, which may provide new insights and rules for the design of the multimode interference devices such as optical couplers, optical modulators, multimode fiber lasers and space-division multiplexing systems.

**3) Development of optical devices based on the anti-resonance effect in multimode waveguides with high-index claddings.**

The application of high-index coatings to the surface of conventional step-index fiber changes its original index distribution and results in the anti-resonance phenomenon. Compared to the multimode interference effect, the anti-resonance effect does not rely on the multimode properties of the optical waveguide. The bending can suppress the multimode interference and can break the superposition of anti-resonant spectra of multiple modes. This results in the dominance of the anti-resonance of an individual mode and consequently in periodic sharp transmission dips in the spectrum of a high-index coated waveguide. Therefore, simple technologies such as high-index coating and bending can be used in the design of anti-resonant based devices for a variety of applications.

### 8.3 Reference

- [1] L. Vicari, “Truncation of non-diffracting beams,” Opt. Commun., vol. 70, no. 4, pp. 263-266, 1989.
- [2] D. McGloin and K. Dholakia, “Bessel beams: diffraction in a new light,” Contemporary Physics, vol. 46, no. 1, pp. 15-28, 2005.
- [3] T. Čižmár, V. Kollárová, Z. Bouchal, and P. Zemánek, “Sub-micron particle organization by self-imaging of non-diffracting beams,” New J. Phys., vol. 8, no. 3, p. 43, 2006.

## Appendix A

# Eigenvalue Equations for Vector Modes TE, TM, HE and EH in Three-Layer Optical Fibers

This section introduces the eigenvalue equations for modes in a three-layer step-index fiber shown in Fig. 1(b) with  $n_3 < n_2 < n_1$  and a three-layer depressed-core fiber with  $n_3 < n_1 < n_2$  shown in Fig. 1(d).

The eigenvalue equations used to calculate the effective refractive index of the cladding modes with  $n_3 < n_{\text{eff}} < n_2$  in three-layer step-index fiber (or the core modes with  $n_3 < n_{\text{eff}} < n_1$  in three-layer depressed-core fiber) are as follows [1]:

for the  $\text{TE}_{0,n}$  modes:

$$\hat{J} \left( K p_m + \frac{r_m}{\alpha_2 U_2} \right) = \frac{1}{U_2} \left( \hat{K} q_m + \frac{s_m}{\alpha_2 U_2} \right), m = 0 \quad (\text{A.1})$$

for the  $\text{TM}_{0,n}$  modes with:

$$\hat{J} \left( \hat{K} p_m + s_{23} \frac{r_m}{\alpha_2 U_2} \right) = \frac{s_{21}}{U_2} \left( \hat{K} q_m + s_{23} \frac{s_m}{\alpha_2 U_2} \right), m = 0 \quad (\text{A.2})$$

for the  $\text{HE}_{m,n}$  and the  $\text{EH}_{m,n}$  modes with:

$$\begin{aligned}
& p_m^2 + 2 \left( \frac{2}{\pi \alpha_2 U_2^2} \right)^2 \left( \frac{n_2^2}{n_1 n_3} \right) x_1 x_2 \\
& + x_1^2 x_2^2 \left[ \hat{J} \left( \hat{K} p_m + \frac{r_m}{\alpha_2 U_2} \right) - \frac{1}{U_2} \left( \hat{K} q_m + \frac{s_m}{\alpha_2 U_2} \right) \right] \\
& \times \left[ \hat{J} \left( \hat{K} p_m + s_{23} \frac{r_m}{\alpha_2 U_2} \right) - \frac{s_{21}}{U_2} \left( \hat{K} q_m + s_{23} \frac{s_m}{\alpha_2 U_2} \right) \right] \\
& = x_1^2 \left( \hat{J} p_m - \frac{q_m}{U_2} \right) \left( \hat{J} p_m - s_{21} \frac{q_m}{U_2} \right) \\
& + x_2^2 \left( \hat{K} p_m + \frac{r_m}{\alpha_2 U_2} \right) \left( \hat{K} p_m + s_{23} \frac{r_m}{\alpha_2 U_2} \right)
\end{aligned} \tag{A.3}$$

The fiber parameters of the depressed-core fibers shown in Fig. 2.10 are  $r_1$ ,  $r_2$ ,  $n_1$ ,  $n_2$  and  $n_3$ . The wavenumber in vacuum is:  $k_0 = 2\pi/\lambda$ , where  $\lambda$  is the wavelength. The longitudinal propagation constant is:  $\beta = k_0 n_{\text{eff}}$ . In the Eqs (A.1), (A.2) and (A.3), the parameters used are as follows:

$$\alpha_2 = \frac{r_2}{r_1}, \tag{A.4}$$

$$u_1 = \sqrt{k_0^2 n_1^2 - \beta^2}, \tag{A.5}$$

$$u_2 = \sqrt{k_0^2 n_2^2 - \beta^2}, \tag{A.6}$$

$$\omega_3 = \sqrt{\beta^2 - k_0^2 n_3^2}, \tag{A.7}$$

$$U_1 = u_1 r_1, \quad U_2 = u_2 r_1, \quad W_3 = \omega_3 r_2, \tag{A.8}$$

$$\hat{J} = \frac{J'_m(U_1)}{u_1 J_m(U_1)}, \tag{A.9}$$

$$\hat{K} = \frac{K'_m(W_3)}{W_3 K_m(W_3)}, \tag{A.10}$$

$$p_m = J_m(u_2 r_2) Y_m(u_2 r_1) - J_m(u_2 r_1) Y_m(u_2 r_2), \tag{A.11}$$

$$q_m = J_m(u_2 r_2) Y'_m(u_2 r_1) - J'_m(u_2 r_1) Y_m(u_2 r_2), \tag{A.12}$$

$$r_m = J'_m(u_2 r_2) Y_m(u_2 r_1) - J_m(u_2 r_1) Y'_m(u_2 r_2), \quad (A.13)$$

$$s_m = J'_m(u_2 r_2) Y'_m(u_2 r_1) - J'_m(u_2 r_1) Y'_m(u_2 r_2), \quad (A.14)$$

$$s_{23} = \frac{n_2^2}{n_3^2}, s_{21} = \frac{n_2^2}{n_1^2}, \quad (A.15)$$

$$V_{12}^2 = k_0^2 r_1^2 (n_1^2 - n_2^2), V_{23}^2 = k_0^2 r_2^2 (n_2^2 - n_3^2), \quad (A.16)$$

$$x_1^2 = \frac{n_1^2 U_1^4 U_2^4}{\sigma_0^2 V_{12}^4}, x_2^2 = \frac{n_3^2 \alpha_2^4 U_2^4 W_3^4}{\sigma_0^2 V_{23}^4}, \quad (A.17)$$

$$\sigma_0^2 = \left( \frac{\beta_m}{k_0} \right)^2. \quad (A.18)$$

The parameters  $u_1, u_2, \omega_3, U_1, U_2, W_3$  are phase parameters. The functions  $J_m$ ,  $Y_m$  and  $K_m$  denote the Bessel function of the first kind, the Bessel function of the second kind and the modified Bessel function of the second kind.  $J'_m$ ,  $Y'_m$ , and  $K'_m$  denote the derivatives of the corresponding Bessel functions.

To calculate the core modes with  $n_2 < n_{eff} < n_1$  in three-layer step-index fibers (or the cladding modes with  $n_1 < n_{eff} < n_2$  in three-layer depressed-core fibers), the phase parameter  $u_1$  in the Eq. (A.5) needs to be modified as:

$$u_1 = \sqrt{\beta^2 - k_0^2 n_1^2} \quad (A.19)$$

and  $\hat{J}$  in the Eq. (A.9) need to be modified as:

$$\hat{J} = -\frac{I'_m(U_1)}{U_1 I_m(U_1)}, \quad (A.20)$$

where  $I_m$  and  $I'_m$  denote the modified Bessel function of the first kind and its derivative.

The modal intensity and electric field vector distributions can be calculated with the field functions shown in Refs. [1-3].

## Reference

- [1] C. Tsao, *Optical Fiber Waveguide Analysis*, (Oxford University Press, New York, 1992).
- [2] T. Erdogan, “Cladding-mode resonances in short- and long-period fiber grating filters,” J. Opt. Soc. Am. A, vol. 14, no. 8, pp. 1760-1773, 1997.
- [3] Z. Zhang and W. Shi, “Eigenvalue and field equations of three-layered uniaxial fibers and their applications to the characteristics of long-period fiber gratings with applied axial strain,” J. Opt. Soc. Am. A, vol. 22, no. 11, pp. 2516–2526, 2005.

## Appendix B

### Eigenvalue Equations for Scalar Modes LP<sub>m,n</sub> in Three-Layer Optical Fibers

In a three-layer step-index optical fiber the field profiles of the scalar modes LP<sub>m,n</sub> are used as in Ref. [1]:

$$E_{m,n}(r) = \begin{cases} A_0 J_m\left(u \frac{r}{r_1}\right), & r \leq r_1 \\ A_1 J_m\left(u' \frac{r}{r_2}\right) + A_2 Y_m\left(u' \frac{r}{r_2}\right), & \text{if } n_{\text{eff}} < n_2 \\ A_3 K_m\left(v \frac{r}{r_2}\right), & r \geq r_2 \end{cases}$$
(B.1)

and

$$E_{m,n}(r) = \begin{cases} A'_0 J_m\left(u \frac{r}{r_1}\right), & r \leq r_1 \\ A'_1 I_m\left(v' \frac{r}{r_2}\right) + A'_2 K_m\left(v' \frac{r}{r_2}\right), & \text{if } n_{\text{eff}} > n_2 \\ A'_3 K_m\left(v \frac{r}{r_2}\right), & r \geq r_2 \end{cases}$$
(B.2)

where  $J_m$ ,  $Y_m$ ,  $I_m$  and  $K_m$  are usual Bessel and modified Bessel functions,  $A_0$ ,  $A'_0$ , are the normalization coefficients and  $u$ ,  $u'$ ,  $v$ ,  $v'$ ,  $A_1$ ,  $A'_1$ ,  $A_2$ ,  $A'_2$ ,  $A_3$  and  $A'_3$  are defined as follows:

$$u = r_1 [k_0^2 n_1^2 - (n_{\text{eff}} k_0)^2]^{1/2} \quad (\text{B.3-1})$$

$$u' = r_2[k_0^2 n_2^2 - (n_{\text{eff}} k_0)^2]^{1/2} \quad (\text{B.3-2})$$

$$v' = r_2[(n_{\text{eff}} k_0)^2 - k_0^2 n_2^2]^{1/2} \quad (\text{B.3-3})$$

$$v = r_2[(n_{\text{eff}} k_0)^2 - k_0^2 n_3^2]^{1/2}. \quad (\text{B.3-4})$$

$$A_1 = \frac{\pi A_0}{2}[u J_{m+1}(u) Y_m(u'c) - u' c J_m(u) Y_{m+1}(u'c)] \quad (\text{B.4-1})$$

$$A_2 = \frac{\pi A_0}{2}[u' c J_{m+1}(u'c) J_m(u) - u J_{m+1}(u) J_m(u'c)] \quad (\text{B.4-2})$$

$$A_3 = \frac{1}{K_m(v)}[A_1 J_m(u') + A_2 Y_m(u')] \quad (\text{B.4-3})$$

$$A'_1 = A'_0[v' c J_m(u) K_{m+1}(v'c) - u J_{m+1}(u) K_m(v'c)] \quad (\text{B.5-1})$$

$$A'_2 = A'_0[v' c J_m(u) I_{m+1}(v'c) + u J_{m+1}(u) I_m(v'c)] \quad (\text{B.5-2})$$

$$A'_3 = \frac{1}{K_m(v)}[A'_1 I_m(v') + A'_2 K_m(v')] \quad (\text{B.5-3})$$

The  $n_{\text{eff}}$  ( $\text{LP}_{m,n}$ ) is the solution of the eigenvalue equations as below:

$$\frac{[\hat{J}_m(u) - \hat{Y}_m(u'c)][\hat{R}_m(v) - \hat{J}_m(u')]}{[\hat{J}_m(u) - \hat{J}_m(u'c)][\hat{R}_m(v) - \hat{Y}_m(u')]} = \frac{J_{m+1}(u'c) Y_{m+1}(u')}{J_{m+1}(u') Y_{m+1}(u'c)} \quad \text{if } n_{\text{eff}} < n_2 \quad (\text{B.6})$$

and

$$\frac{[\hat{J}_m(u) - \hat{R}_m(v'c)][\hat{R}_m(v) + \hat{I}_m(v')]}{[\hat{J}_m(u) + \hat{I}_m(v'c)][\hat{R}_m(v) - \hat{R}_m(v')]} = \frac{I_{m+1}(v'c) K_{m+1}(v')}{I_{m+1}(v') K_{m+1}(v'c)} \quad \text{if } n_{\text{eff}} > n_2 \quad (\text{B.7})$$

where

$$\hat{F}_0(x) = \frac{F_0(x)}{xF_1(x)} \quad (\text{B.8})$$

( $F$  representing the Bessel functions  $J$ ,  $Y$ ,  $I$ , or  $K$ ) and

$$c = \frac{r_1}{r_2} \quad (\text{B.9})$$

## Reference

- [1] M. Monerie, "Propagation in doubly clad single-mode fibers," IEEE J. Quantum Electron., vol. QE-18, no. 4, pp. 535-542, 1982.

## Appendix C

# Multiple Reflections of an Unpolarized Incident Beam on an Asymmetric Planar Waveguide

The multiple reflections of one beam incident on an asymmetric planar waveguide are considered in this section. The asymmetric planar waveguide consists of three regions with refractive indices of  $n_1$ ,  $n_2$  and  $n_3$  ( $n_2 > n_1 > n_3$ ) as indicated in Fig. C.1(a). The angle of incidence is  $\theta_1$  within  $n_1 > n_1 \sin \theta_1 > n_3$ , which ensures that Fresnel's refraction and reflection at the interface between

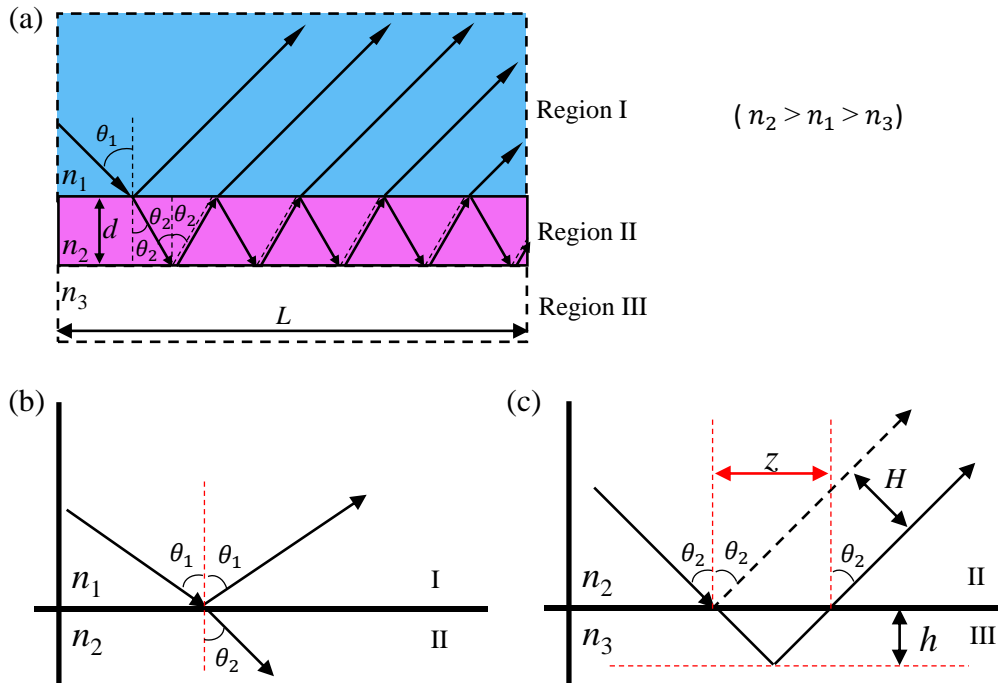


**Figure C.1** (a) Ray trajectory of a beam with angle of incidence  $\theta_1$  ( $n_1 > n_1 \sin \theta_1 > n_3$ ) impinging on the interface of an asymmetric planar waveguide. (b) Fresnel's refraction and reflection at the interface between regions I and II. (c) Total reflection at the interface between regions II and III, where 'z', 'H', and 'h' denote the Goos-Hänchen shift, the deviation of the reflection light, and the penetration depth of the evanescent wave, respectively.

regions I and II is as shown in Fig. C.1(b) while total reflection at the interface between regions II and III is as shown in Fig. C.1(c).

The Fresnel's (intrinsic) transmission ( $t$ ) and reflection ( $r$ ) coefficients for TE beams are [1]:

$$r_{\perp ij} = \frac{n_i \cos \theta_i - n_j \cos \theta_j}{n_i \cos \theta_i + n_j \cos \theta_j}, t_{\perp ij} = \frac{2n_i \cos \theta_i}{n_i \cos \theta_i + n_j \cos \theta_j} \quad (\text{C.1})$$

and for TM beams are:

$$r_{\parallel ij} = \frac{n_j \cos \theta_i - n_i \cos \theta_j}{n_j \cos \theta_i + n_i \cos \theta_j}, t_{\parallel ij} = \frac{2n_i \cos \theta_i}{n_j \cos \theta_i + n_i \cos \theta_j} \quad (\text{C.2})$$

where indices  $i = 1$  (2) and  $j = 2$  (1), denote the incident region and transmission region, respectively.

The intrinsic reflection coefficient ( $r$ ) and the phase change ( $\phi$ ) in the total reflection case are as follows. For the TE beams:

$$r_{\perp ij} = e^{i2\phi_{\perp}}, \phi_{\perp} = \tan^{-1} \left( \frac{\sqrt{\sin^2 \theta_i - n_j^2/n_i^2}}{\cos \theta_i} \right) \quad (\text{C.3})$$

For the TM beams:

$$r_{\parallel ij} = e^{i2\phi_{\parallel}}, \phi_{\parallel} = \tan^{-1} \left( \frac{n_i^2 \sqrt{\sin^2 \theta_i - n_j^2/n_i^2}}{n_j^2 \cos \theta_i} \right) \quad (\text{C.4})$$

where index  $i = 2$  and  $j = 3$  denote regions II and III, respectively.

The total amplitude of multiple reflections for TE (or TM) beams in the region II can be calculated as:

$$\begin{aligned}
A^{(r)} &= [r_{12} + t_{12}r_{23}t_{21}e^{i\delta} + t_{12}r_{23}(r_{21}r_{23})t_{21}e^{i2\delta} + t_{12}r_{23}(r_{21}r_{23})^2t_{21}e^{i3\delta} \\
&\quad + \dots + t_{12}r_{23}(r_{21}r_{23})^{p-2}t_{21}e^{i(p-1)\delta}] A^{(i)} \\
&= \left\{ r_{12} + t_{12}r_{23}t_{21} \left[ \frac{1 - (r_{21}r_{23}e^{i\delta})^{p-1}}{1 - r_{21}r_{23}e^{i\delta}} \right] e^{i\delta} \right\} A^{(i)}
\end{aligned} \tag{C.5}$$

where  $\delta$  is the phase difference between the two adjacent reflected beams in region I:  $\delta = \frac{4\pi n_2 d \cos \theta_2}{\lambda}$ .  $p$  is number of reflected beams:  $p = \frac{L}{2d \tan \theta_2}$ .  $A^{(i)}$  is the amplitude of the incident beam. Given  $d = 62.5 \mu\text{m}$ ,  $n_1 = 1.445$ ,  $n_2 = 1.51$ , and a waveguide length  $L > 0.5 \text{ cm}$ , the  $p$  is large enough for the total reflected amplitude to be approximated as:

$$A^{(r)} = \left( r_{12} + \frac{t_{12}r_{23}t_{21}}{1 - r_{21}r_{23}e^{i\delta}} e^{i\delta} \right) A^{(i)} \tag{C.6}$$

And the ratio of reflection intensity can be calculated as:

$$R = \frac{A^{(r)} A^{(r)*}}{A^{(i)} A^{(i)*}} = \left| r_{12} + \frac{t_{12}r_{23}t_{21}}{1 - r_{21}r_{23}e^{i\delta}} e^{i\delta} \right|^2 \tag{C.7}$$

Substituting the intrinsic reflection and refraction coefficient for the TE (or TM) beams calculated by Eqs. (C.1)-(C.4) into Eqs. (C.6) and (C.7), the ratio of reflection intensity of the TE and TM beams are calculated respectively as  $R_{\perp}$  and  $R_{\parallel}$ . The ratio of reflection intensity of an unpolarized incident beam is the average of  $R_{\perp}$  and  $R_{\parallel}$  thus:

$$\bar{R} = \frac{R_{\perp} + R_{\parallel}}{2}. \tag{C.8}$$

## Reference

- [1] M. Born, and E. Wolf, *Principles of Optics: Electromagnetic Theory of Propagation, Interference and Diffraction of Light*, (Elsevier, 2013).

## **Appendix D**

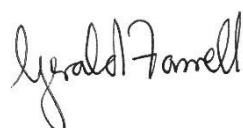
### **Statement of Contribution**

For the publications presented within this thesis, the co-authors listed below certify that:

1. Xiaokang Lian is the first author for the first listed four journal publications and the first listed four conference papers in the publication list.
2. As first author for the first listed four journal publications and the first listed four conference papers in the publication list, Xiaokang Lian undertook all aspects of the research described in each publication, including preparation and submission of the publications and the preparation of any revisions requested by referees, with the support and advice of the co-authors.
3. The co-authors agree to the use of the publications in this thesis.



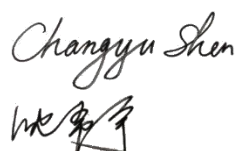
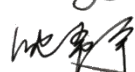
**Prof. Yuliya Semenova**



**Prof. Gerald Farrell**



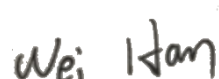
**Prof. Qiang Wu**

**Prof. Changyu Shen**



**Dr. Youqiao Ma**



**Mr. Wei Han**